博士論文

Operando microbio-electrochemical study of deca-heme flavocytochrome under non-equilibrium condition

（非平衡で駆動する多核ヘムフラボシトクロムの微生物電気化学的研究）

徳納　吉秀

Table of Contents

Chapter 1

General introduction

1-1. Overview and objective of this study

Electron transport processes sustain the energy production in live organisms. As it was suggested that aerobic organisms obtain energy from molecular oxygen over 200 years ago, redox reactions of chemicals such as oxygen and organics coupled with sequential electron transport through intracellular respiratory chain produce energy available to life [1]. Since cells possess insulative membranes, it has been assumed that the biological electron transfer reactions occur inside cells, and that electron donors and acceptors are limited to soluble chemicals permeable to membranes. However, in 1980s, it has been found that some bacteria are able to exchange electrons with extracellular solid minerals such as iron oxides and manganese oxides (Details in 1-2) [2-5]. Since energy metabolism can be driven even in soluble nutrient-limited conditions, this interfacial electron transport process, extracellular electron transport (EET) through electron transport proteins localized on outer-membrane (OM), expands the limitation of bacterial habitat and living strategies as well as has an impact on environmental elemental cycling (Details in 1-3) [6-10]. Furthermore, electrodes can be served as electron donors or acceptors for EET-capable bacteria instead of minerals, which enabled development of various bio-electrochemical technologies (Details in 1-4) [11-13]. While the EET process has been

assumed to be limited to specific bacterial strains (iron-reducing bacteria), recently EET-coupled respiration was found outside the context of mineral-based respiration, e.g. sulfate reducing bacteria which is one of the most widely distributed bacterial species in the world [14-17], gut bacteria which potentially affect the health of mammal, and so on (Details in 1-5) [18-19]. Due to those significance of EET in the environment and industrial applications, and generality of EET as a bacterial respiratory strategy, the mechanisms and kinetics of EET process have been extensively studied in molecular-level.

The mechanisms of EET have been extensively studied using a model bacterium, *Shewanella oneidensis* MR-1, which possesses multi-heme cytochromes complex on OM (OM *c*-Cyts) as electron conduits (Details in 1-6) [20-22]. Accumulating studies have revealed that, in nature, the respiratory electrons conveyed from cell interior are exported by the combination of OM *c*-Cyts and a self-secreted redox molecule, flavin [23-31]. The role of flavin in EET is not limited to *S. oneidensis* MR-1, but also used by a variety of bacteria such as *Geobacter* which is another model EET-capable bacterium [27, 32] and over 100 strains of Gram-positive bacteria including representative gut bacteria, *Lactobacillus*, and food-borne bacterial pathogen, *Listeria* [18-19]. Furthermore, the involvement of flavins enhances the rate of EET compared with that in flavin-limited condition, with implications for the development of emerging bioelectrochemical technologies as well as the ecophysiology of EET-capable bacteria [23-24, 33]. Thus, the molecular mechanisms for involvement of flavins to accelerate EET has been the focal point.

Because flavins have been believed to shuttle electrons between OM *c*-Cyts and extracellular solids by molecular diffusion as two-electron reduced state, the electron transport between OM *c*-Cyts and flavins has been studied from the viewpoint of redox potential and diffusion constant [33-34]. However, recently it was found that flavins are

stabilized as one-electron reduced semiquinone form and bound with OM *c*-Cyts as non-covalent redox-active cofactor molecules [26-28]. The bound flavins pass electrons from OM *c*-Cyts to extracellular solids without diffusion, which predominantly contribute on EET acceleration rather than shuttling mechanism (Details in 1-7) [26, 35]. However, the redox cycling of the bound flavin has a redox potential of about −150 mV versus standard hydrogen electrode (SHE), which is about 200 mV lower than that of heme groups in OM *c*-Cyts on average [26, 36-37]. The electron transfer from OM *c*-Cyts to flavin is thermodynamically unfavorable, conflicting with the rate enhancement of EET; thereby, it is still unclear about the mechanisms underlying the EET acceleration and the potential for further enhancement of the rate of EET. Given that flavin and analogous molecules are key players in metabolic redox reactions (e.g. those of the Q-cycle), and that (both bound and free) flavins of several types are major factors in many kinds of anaerobic electron bifurcation reaction (all involving flavins as semiquinone intermediates) [38-39], an understanding of the mechanisms in flavin-mediated EET enhancement is of fundamental importance.

Flavin acts as an electron carrier in EET process. However, when thinking about functions of redox molecules as cofactors of electron transport proteins, it is notable that bound cofactor plays roles not only as an electron carrier but also as a regulator to induce functional and structural change of proteins. For example, in ubiquinol-cytochrome-*c* reductase (complex III) in respiratory electron transport chain, bound ubiquinone molecule acts as a proton carrier as well as an electron carrier [40-41]. Protonation/deprotonation reaction of ubiquinone coupled with redox cycling endows complex III with the function of proton translocation across inner-membrane. In addition, such redox molecules induce local conformational change of proteins as ligands, which

enhance the electron flow. Based on this background, in this thesis, it was hypothesized that the act of bound flavin as a regulator to couple proton transport and induce structural change of OM *c*-Cyts leads to EET rate enhancement.

Since biochemical analysis of purified OM *c*-Cyts is one of the most direct approaches to test the role of flavins on EET acceleration, the interaction with flavins has been extensively studied using OM *c*-Cyts dissolved in solution or embedded in artificial lipid bilayer [29, 42]. Although those approaches demonstrated the complex formation [29], the observation of stabilized semiquinone state of flavins has been limited to whole-cell system [26, 28]; thereby experiments with purified OM *c*-Cyts have failed to exhibit the semiquinone-based stable rate enhancement of EET [42]. Therefore, in this thesis, the author examined the mechanisms in EET acceleration caused by bound flavins with OM *c*-Cyts, using whole-cell of *S. oneidensis* MR-1, i.e. "Microbio-electrochemistry".

This thesis comprises five chapters. In this chapter 1, the general background of this research was described. In detail, in chapter 1-2 ~ 1-5, the importance in exploiting EET reaction was mentioned from the viewpoint of bacterial respiration, environmental elemental cycling, emerging bio-electrochemical technologies, and relevance to various bacterial phenomena occurring in nature. Then, in chapter 1-6 ~ 1-7, the mechanisms in EET mediated by the combination of OM *c*-Cyts and flavins are reviewed mainly focusing on *S. oneidensis* MR-1 as a model system. In chapter 2, the role of proton transport in flavin-mediated EET enhancement was examined using microbio-electrochemistry. Because whole-cell approaches limit accesses to molecular-level information regarding specific enzymes, a variety of techniques were combined with microbio-electrochemistry to investigate the EET mechanisms, e.g. design of flavin analogues to bind with OM *c*-Cyts instead of flavin, kinetic isotope effect (KIE) on EET

using deuterated water, and impact of pH on EET kinetics. In chapter 3, the author developed a methodology to monitor the geometry of hemes inside OM *c*-Cyts in whole *S. oneidensis* MR-1 cells, and the acceleration mechanisms were investigated from the viewpoint of the structural change of OM *c*-Cyts. Based on the insight about flavin-mediated EET enhancement, in chapter 4, the author examined the mechanisms how bound flavin dictate the direction of electron flow through OM *c*-Cyts, i.e. forward and reverse electron transport. The conclusion and future perspective of this study are described in chapter 5.

1-2. Extracellular electron transport (EET) as an energy metabolism

One of the aspects of bacterial respiration is to convert energy from nutrients into chemicals available to life such as adenosine triphosphate (ATP). This biological energy conversion system can be considered as a coupling of redox reactions from the viewpoint of electrochemistry [43]. For example, aerobic respiration is coupled with oxidation of organics and reduction of molecular oxygen. Since oxygen has higher redox potential than organics (thermodynamically more stable to accept electrons), electrons produced from organics flows to oxygen following a thermodynamic gradient. Given that the energy generated by the electron flow can be converted into ATP using a gradient of protons across bacterial inner-membrane (IM), bacteria can survive within the area containing both electron donor and acceptors. Since bacteria have insulative OM, it has been assumed that the bacterial habitat is limited to the place with soluble redox pairs permeable to OM.

However, in 1986, M. R. Hoffman *et al*, isolated a bacterium, *Pseudomonas* sp. 200, and revealed that *Pseudomonas* sp. 200 can reduce insoluble iron-oxide [2]. This is the first report to suggest extracellular electron transport (EET) across bacterial OM, conflicting with the conventional concept that respiratory electron transfer reactions complete inside bacterial cells. In 1988, C. R. Mayer and K. H. Nealson reported that *Alteromonas putrefaciens* MR-1 (Later, this bacterium is identical with *Pseudomonas* sp. 200 and named as *Shewanella oneidensis* MR-1) can reduce manganese-oxide and grow without any soluble electron acceptors (Figure 1-1), suggesting the a novel bacterial survival strategy that the electron transfer beyond bacterial OM generate energy to sustain bacterial life [3]. In the same year, D. R. Lovely and E. J. P. Phillips discovered another

EET-capable bacterium, *Geobacter sulfurreducens* (Figure 1-2), which supports the EET-based respiration as a general strategy for bacteria to gain energy in soluble-nutrient limited conditions [4]. Recently, it was found that EET-capable bacteria are not limited to *Shewanella* and *Geobacter*, but exist in a diverse environment with a wide range of lifestyles in both Gram negative and positive bacteria [18]. The generality of EET-capable bacteria on the earth demonstrates that EET is one of the common process involved in energy metabolisms and highlights the importance in investigation of EET process.

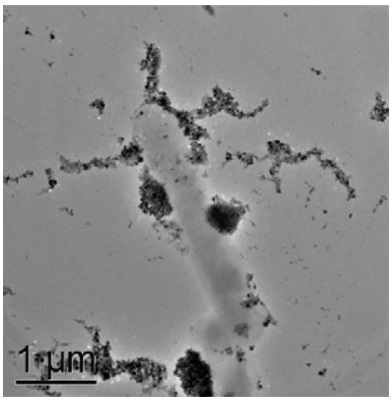

Figure 1-1. Transmission electron microscopic image of *Shewanella oneidensis* MR-1 in the presence of silica ferrihydrite [44]. (Copyright 2006, National Academy of Sciences.)

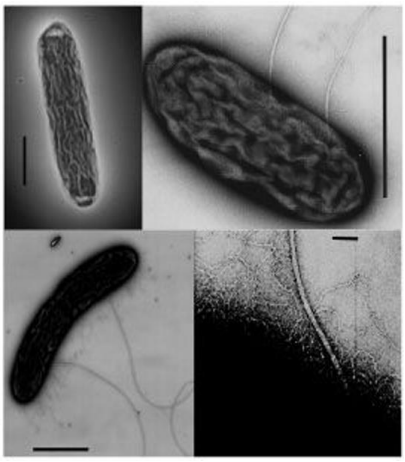

Figure 1-2. Transmission electron microscopic images of *Geobacter* species. Scale bars represent 1 µm. (Reprinted with permission from ref. [45]. Copyright 2002, Nature Publishing Group)

1-3. Impact of EET on elemental cycling

One of the roles of EET in nature is elemental cycling. Given that the total amount of matter on the earth is limited, elemental cycle is essential to realize sustainable environment. Since metal elements such as iron and manganese exhibit several orders lower solubility in oxidized form than that in reduced form, in the ocean, metal oxides precipitate at the sea bottom once metals in reduced state react with dissolved oxygen. Therefore, available metal elements on the earth should be diminished without reduction reaction of metal oxides at the sea bottom. While the metal cycling in the ocean has been assumed to be driven by abiotic reaction, e.g. reduction of metal by sulfide, the finding of EET-capable bacteria demonstrated that iron and manganese are reduced by EET-capable bacteria coupled with oxidation of organic compounds, driving the geochemical cycling of metal elements [6-7, 46]. Due to the diversity of habitat for EET-capable bacteria, the impact of EET on mineral cycling may not be limited to ocean but a variety of environments such as a high pH serpentinizing spring [8].

1-4. Emerging bio-electrochemical technologies with EET-capable bacteria

Since electrodes can be served as electron donors or acceptors for bacteria instead of minerals, EET-capable bacteria can be utilized for emerging bio-electrochemical systems (BES). Here two representative EET-utilizing technologies, microbial fuel cells (MFCs) and microbial electrosynthesis (MES), are described.

(A) Microbial fuel cells (MFCs)

Microbial fuel cells (MFCs) are devices that exploits microbial EET to generate electrical energy (Figure 1-3). Since the EET processes are catalyzed by bacterial respiration coupled with oxidation and catabolism of organics, the MFCs are the only technologies to generate energy from waste without external energy [13, 47-48]. Thus, the main motives for development of MFCs are 1) the potential to complement the existing wastewater treatment systems with huge cost, and 2) the potential to act as sustainable energy system. Conventional wastewater treatment system also utilizes bacterial respiration and metabolism, which degrade waste coupled with oxygen reduction; thereby significant costs for oxygen supply and removal of dead bacterial cells were problematic. MFCs are advantageous because of low running-cost by the diminishment of oxygen and dead cells, in addition to the gain of electrical energy by EET process [13, 49]. Furthermore, the MFCs system can potentially operate with optional functions such as production of hydrogen as bio-fuel in microbial electrolysis cells and desalination of water in microbial desalination cells [50-52].

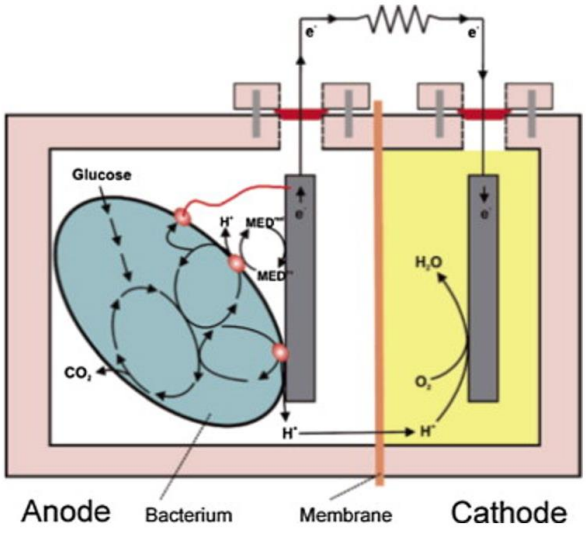

Figure 1-3. Schematic illustration of MFCs system. (Reprinted with permission from ref. [13]. Copyright 2006, American Chemical Society.)

(B) Microbial electrosynthesis (MES)

Given that the EET process is linked with intracellular enzymatic reactions, EET-capable bacteria can be utilized as catalysts to produce bio-fuels and bio-chemicals from electrical energy [12, 53]. Thus, cathodic bio-chemical production associated with reverse EET (bacterial uptake of electrons from electrode) has been developed as microbial electrosynthesis (MES). One of the examples of biochemical products in MES system is elongation of hydrocarbons (Figure 1-4). It was reported that low-grade chemicals such as acetate and butylate can be anabolized into valuable fuels like alcohols and caproate associated with cathodic EET [54]. Another study demonstrated production of valerate with 5-carbon chain from propionate with 3-carbon chain [55]. In addition, fixation of carbon dioxide in MES system has been also tested in a variety of EET-capable bacteria [56-57]. Although the MES system is still under development, the idea to utilize EET-capable bacteria as bio-catalyst for reduction reaction has been gaining wide interest with significant implications, e.g. immobilization of heavy metals for bioremediation [58-59].

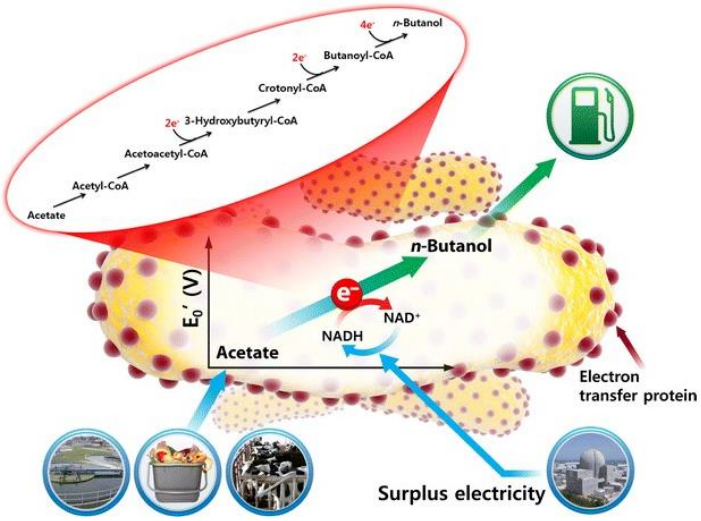

Figure 1-4. The upgrade of waste into value-added biofuels. The acetate from wastes, such as waste activated sludge, food waste, and animal manure, was feed stocks for biofuel production by electroactive microorganisms. The extracellular electron transfer from cathode to microbe via electron transfer protein could be used for the reduction of acetate to butanol. NADH the reduced form, NAD+ the oxidized form of nicotinamide adenine dinucleotide, respectively. [53] (Copyright 2015, BioMed Central.)

In addition to MFCs and MES, a variety of biotechnologies utilizing EET-capable bacteria are proposed. For example, utilization of EET-capable bacteria as nano- or micro- scale electronic components [60] or logic gates [61], and energy conversion from solar to electrical energy [62-63]. Thus, investigation of the mechanisms of EET in the molecular-level and development of techniques to accelerate EET is fundamentally important.

1-5. Diversity of phenomena related with EET-capable bacteria

Since the EET process had been recognized as a minor biological process limited to iron-reducing bacteria until 2000s, the attention about EET had been limited to understanding of elemental cycle on the earth and development of bio-electrochemical technologies. However, recently it has been discovered that EET is a common respiratory process utilized by a variety of bacteria and archaea. Therefore, understanding and controlling EET process has gained more importance to control diverse EET-related phenomena. Here, some of the EET-capable bacteria other than iron-reducing bacteria and related phenomena are described.

In 2004, a paper suggested that some of sulfate reducing bacteria (SRB) have an ability to grow with iron as a sole electron donor, i.e. ability to conduct cathodic EET [14]. Recently, some groups supported the electron extraction of SRB from extracellular metal [17, 64-65]. Given that SRB is one of the most ubiquitous bacteria on the earth and the genes corresponding electron conduits of SRB are broadly conserved in a variety of bacteria, the ubiquity of the EET in subsurface environments was indicated. In addition, recent studies suggested the EET of SRB is utilized to metabolically connect with anaerobic methane oxidation reaction in archaea (Figure 1-5) [15-16, 66]. Since this the aggregation of SRB and methanotrophic archaea is known to control the emission of the greenhouse gas, methane, from the ocean floor, the EET process may play significant roles in carbon cycle and global warming [67-68]. Furthermore, the EET of SRB is proposed to act a major role in anaerobic corrosion of iron and steel (Figure 1-6) [14, 17]. The anaerobic bio-corrosion of iron and steel has a significant economic and environmental damage, e.g. the economic loss caused by corrosion was estimated to be over 1 % of gross domestic production in

U.S.A., of which over 10 % was estimated to be induced by bacteria [69-70].

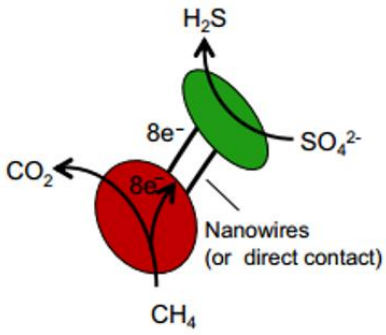

Figure 1-5. Schematic illustration of syntrophy constructed by SRB (illustrated in green) and anaerobic methanotrophic archaea (illustrated in red) sustained by EET-capability. (Reprinted with permission from ref. [15]. Copyright 2015, Nature Publishing Group)

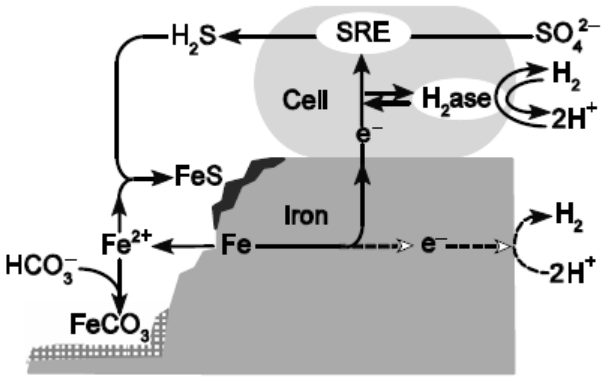

Figure 1-6. Schematic illustration of a proposed model of iron corrosion mechanism catalyzed by SRB. (Reprinted with permission from ref. [14]. Copyright 2004, Nature Publishing Group)

Recently, the EET-capability of cyanobacteria has also been reported [71]. Cyanobacteria have an ability to thrive in nutrient-limited condition by virtue of photosynthesis, where metabolisms can be driven by solar energy. Although detailed molecular mechanisms of EET are still under investigation, the EET-capability may convert a part of energy gained by photosynthesis into electricity by serving electrodes to

cyanobacteria [72]. Therefore, the elucidation of bacterial EET mechanisms has implications towards development of cyanobacteria-based electrical technologies such as bio-photovoltaics (microbial solar cells) and bio-sensors (Figure 1-7) [73-75].

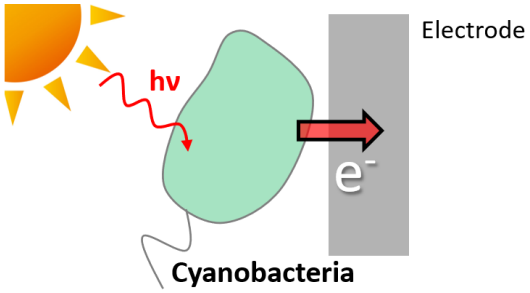

Figure 1-7. Schematic illustration of a bio-photovoltaics (microbial solar cells) using EET-capable cyanobacteria.

The EET-related respiration has been found even in pathogenic bacteria. In 1993, it was found that a food-borne bacterial pathogen, *Listeria monocytogenes*, can reduce extracellular iron oxide, suggesting the EET-capability [76]. In 2018, S. H. Light *et al*, reported that *L. monocytogenes* has electron conduit for EET and thrives dependent on EET-related respiration [18]. Given that *L. monocytogenes* frequently has a host-associated part of its life cycle in mammalian gut and gets associated with decaying plant matter [77], the EET process might be closely related with host-associated bacterial communities and diseases. Notably, S. H. Light *et al*, found that the genes corresponding with the proteins acting as electron conduits are phylogenetically widely distributed. Homologues of the genes were identified in hundreds of species of Gram-positive bacteria with a variety of lifestyle (Figure 1-8). Since those bacteria do not always starve with soluble nutrient in the habitats. Thus, those findings may indicate that EET is used not only to survive in soluble nutrient-limited condition but also to save the investment to synthesize proteins as life-sustaining infrastructure in nutrient-abundant environments [78].

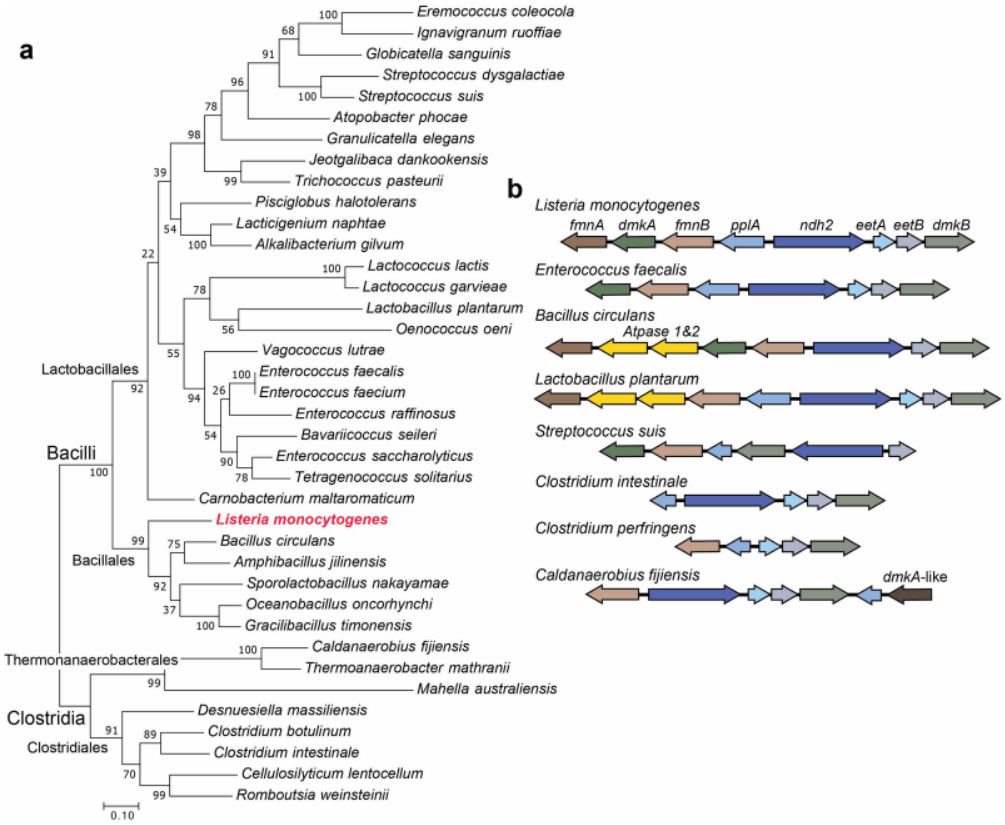

Figure 1-8. (a) Phylogenetic tree constructed based on a gene corresponding with EET conduit (Ndh2 homologue sequences). Labels on the branches refer to the percentage of replicate trees that gave the depicted branch topology in a bootstrap test of 1,000 replicates. (b) Distinct EET loci from select genomes. (Reprinted with permission from ref. [18]. Copyright 2018, Nature Publishing Group)

In 2013, G. Wanger *et al*, reported that biofilm in oral environments has a conductivity with the help of EET capability [79]. Oral biofilm formed on teeth causes oral diseases such as gingivitis and periodontitis promoting the dissolution of teeth. One of the central mechanisms of teeth dissolution is acidification of teeth surface caused by biofilm. Recently, it was suggested that an oral bacterium, *Streptococcus mutans*, conduct EET coupled with pH drop, suggesting the link of EET process with oral cavity (*Unpubilshed*).

Taken together, recent studies accumulate the evidence that a variety of bacteria and archaea such as SRB, methanotrophic archaea, cyanobacteria, mammalian pathogen, and oral bacteria, have an ability to conduct EET, and the EET process is related with wide range of bacterial phenomena such as anaerobic metal corrosion with huge economic and environmental damages, development of microbial solar cells, infectious diseases, and oral cavity. Those findings highlight the importance of understanding and controlling EET process.

1-6. Multi-heme cytochromes complex on outer-membrane (OM *c*-Cyts) act as an electron conduit for EET in a model bacterium, *Shewanella oneidensis* MR-1

Since *S. oneidensis* MR-1 is one of the EET-capable bacteria discovered in 1980s and easy to cultivate, the molecular mechanisms of EET were mainly studied using *S. oneidensis* MR-1. It was found that abundant cytochromes containing multi-heme redox centers are located on both IM and OM of *S. oneidensis* MR-1, which suggest cytochromes as potential respiratory electron transport pathways [80]. Accumulating genome analyses and biochemical experiments illustrated the detailed electron transfer pathway between cytoplasm (cell interior) to extracellular insoluble metal oxides [81]. The EET pathway of *S. oneidensis* MR-1 proposed in 2018 is as follows (Figure 1-9). First, electrons provided in a form of intracellular NADH are delivered into IM as quinone. The reduced quinone (quinol) transports electron to tetraheme cytochrome *c* (CymA), which is localized to the periplasmic side of the IM. The electrons are finally delivered to the cytochromes complex on OM (OM *c*-Cyts) acting as electron conduits for extracellular electron acceptors [20, 22, 82-83].

While several types of OM *c*-Cyts are found in *S. oneidensis* MR-1, MtrCAB complex is the most biosynthesized OM *c*-Cyts (Figure 1-9) [84]. This complex comprises of three proteins, MtrA and MtrC which contain ten heme redox centers, and a transmembrane protein MtrB [85]. The electrons delivered by CymA are accepted by MtrA, which is located to the periplasmic side of the complex, and then are passed to solid materials through MtrC. The ability of MtrCAB complex to transport electrons to metal oxides or electrodes has been demonstrated both in a purified system embedded in liposome (artificial lipid bilayer) and in whole cell system of *S. oneidensis* MR-1 [36-37, 86].

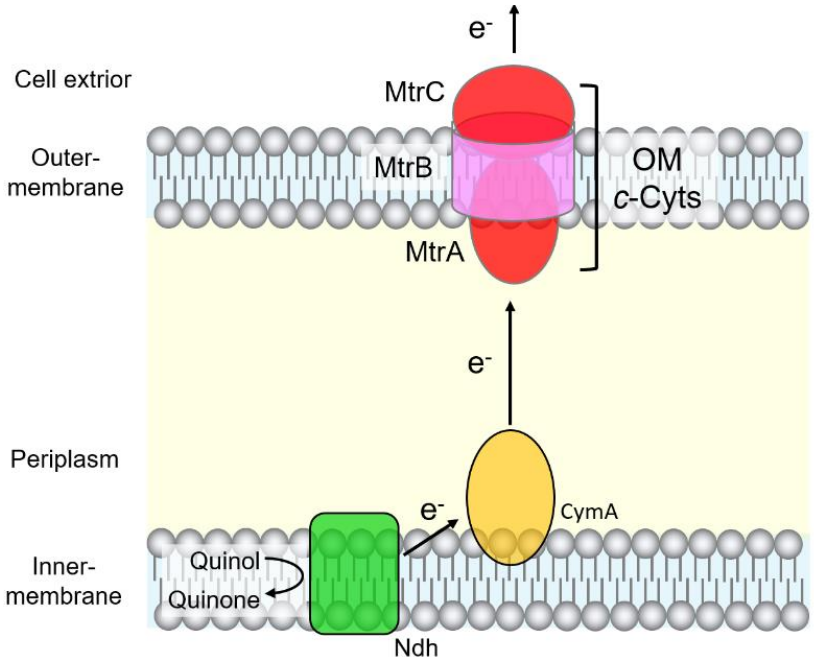

Figure 1-9. Schematic illustration of typical EET pathway of *S. oneidensis* MR-1 spanning from cell interior to extracellular electron acceptors.

The electron transport reactions through OM *c*-Cyts have been examined based on their crystal structure to clarify the EET mechanisms. In 2011, the crystal structure of MtrF, which is a homologous protein of MtrC was resolved, and subsequently that of MtrC was revealed in 2015 (Figure 1-10) [25, 29]. Since the structural information of MtrCAB complex is limited to the data of small-angle neutron scattering [85], the molecular mechanisms are usually discussed based on the crystal structures of MtrF/MtrC. The structure reveals that, 10 hemes are aligned in MtrC with approximate dimensions of 90 Å × 60 Å × 40 Å. MtrC is folded into four distinct domains (Domain I ~ IV indicated in Figure 1-10). Domains II and IV each contain 5 hemes attached to the cysteine residues. Domains I and III each contain seven antiparallel β-strands with Greek key topology forming a split-barrel structure. The 10 hemes of MtrC are organized into a so-called "staggered cross" configuration. 8 hemes (hemes 10, 9, 8, 6, 1, 3, 4, 5 in Figure 1-10b)

are aligned throughout the domains II and IV, and this penta-heme conduit is crossed at the middle by tetra-heme chain (hemes 2, 1, 6, 7 in Figure 1-10b) connecting with the Greek key split β-barrel domains I and III. Several theoretical studies have been conducted to estimate the electron transport mechanisms, and now it is proposed that electrons are conveyed through the penta-heme in domains II and IV [30, 87-89].

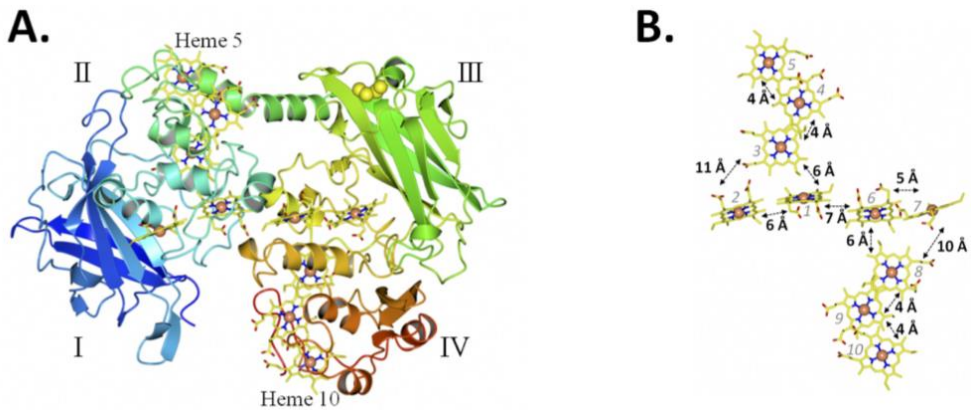

Figure 1-10. Crystal structure of MtrC at 1.8 Å resolution (PDB ID: 4LM8) referred from [29]. (A) Cartoon representation of MtrC. The four domains indicated by roman numerals. The polypeptide chain is shown in cartoon representation and colored from blue (N-terminus) to red (C-terminus). The iron atoms of the hemes are represented as orange spheres and the porphyrin rings of the hemes are shown as yellow sticks. The cysteines of the disulfide bond are represented as yellow spheres. (B) Heme packing and putative electron transfer distances between porphyrin rings. The numbers of hemes are indicated. Ref. [29]. (Copyright 2015, Nature Publishing Group)

In addition to the theoretical simulation, electron transfer mechanisms have been tested using purified MtrC/MtrF. For example, conductive AFM and STM experiments or *I -V* measurements in solid state have been conducted [90-92]. In both theoretical simulations based on the crystal structures and biochemical experiments suggested that electron hopping among hemes is the major mechanisms to proceed EET through

MtrC/MtrF [93]. This highlights the importance of inter-hemes coupling and the redox potential of hemes are critical to the EET mechanisms and kinetics. In contrast, OmcA, another homologous protein of MtrC, flexibly change its conformation. For example, one study with small-angle X-ray scattering showed that upon being reduced, the overall length of OmcA is shortened by nearly 8 % [94]. In addition, the structural changes of OmcA associated with physical contact with grapheme oxide was monitored by circular dichroism spectroscopy combined with infrared spectroscopy techniques, probably shortening the electron-transfer distance to mitigate the energy barrier [95]. Those data imply that OM *c*-Cyts potentially change their structure with distinct heme geometry and inter-hemes coupling in whole-cell. However, the detailed electron transport mechanisms through OM *c*-Cyts in whole-cell is still under debate due to the limitation of methodology to examine the structure of OM *c*-Cyts using *S. oneidensis* MR-1.

1-7. Flavins act as redox centers in EET pathway

While the electron transport mechanisms through OM *c*-Cyts has been extensively studied, it was found that in nature, the EET is usually not mediated only by OM *c*-Cyts, but also the combination of OM *c*-Cyts and a self-secreted redox molecule, flavin [23-24]. Furthermore, the involvement of flavins to the EET pathway enhances the rate of EET (Figure 1-11) [23, 33]. Therefore, the molecular mechanisms for the involvement of flavins to accelerate EET has major implications to ecophysiology of EET-capable bacteria as well as development of emerging bioelectrochemical technologies [23-24, 33]. In addition, the involvement of flavins in EET process is a universal phenomenon observed in not only *S. oneidensis* MR-1, but also another iron-reducing bacteria, *Geobacter*, [27, 32] and over 100 strains of Gram-positive bacteria including *Lactobacillus*, a representative gut bacterium [18-19], highlighting the fundamental importance in elucidation of mechanisms underlying flavin-mediated EET reactions.

In 2008, it was found that the supernatant after cultivation of *S. oneidensis* MR-1 contains riboflavin (RF) and riboflavin mononucleotide (FMN) in micromolar-order concentration in both aerobically and anaerobically condition [24]. In the same year, E. Marcili *et al*, reported that RF and FMN are secreted from biofilms of *Shewanella* during current production, and removal of flavins drops the rate of EET over 70 % [23]. In 2010, electrochemical experiments with gene-deleted *S. oneidensis* MR-1 demonstrated that flavins deliver electrons from OM *c*-Cyts to extracellular minerals and electrodes [96]. Therefore, it has been assumed that flavins shuttle electrons between OM *c*-Cyts and extracellular solids by molecular diffusion [97]. Namely, it was believed that self-secreted flavins increase the current production by increasing the number of current-contributing

cells, since flavins may deliver electrons from *S. oneidensis* MR-1 cells lacking direct contact with solids by molecular diffusion (Figure 1-12a).

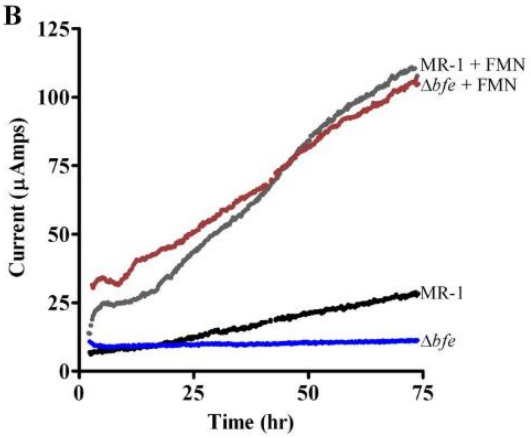

Figure 1-11. Time course profile of current production from *S. oneidensis* MR-1 referred from [33]. Bioreactors were continuously flushed with nitrogen gas, and electrodes were poised at a potential of +0.242 V versus a standard hydrogen electrode (SHE). Current measurement of *S. oneidensis* MR-1 (black), *S. oneidensis* MR-1 + 10 μM FMN (gray), the gene deletion mutant corresponding with FMN biosynthesis mutant (Δ*bfe*, blue), and the Δ*bfe* mutant + 10 μM FMN (red) in bioreactors is shown. (Copyright 2013, American Society for Microbiology)

However, in 2013, completely different mechanisms for flavin-associated EET was proposed [26]. It was proposed that flavins are bound with OM *c*-Cyts (MtrC) as non-covalent redox-active cofactor molecules, and that flavins deliver electrons without molecular diffusion (Figure 1-12b). In detail, it was found that the non-covalent bond formation with MtrC stabilizes flavin as a one-electron reduced form (semiquinone state, Sq, Equation 1-1), which is distinct from two-electron redox reaction of diffusing flavin molecule (Equation 1-2).

$$\text{Flavin (Ox)} + 1e^- + 1H^+ \rightleftarrows \text{Flavin (Sq)} \qquad \text{(Eq. 1-1)}$$

$$\text{Flavin (Ox)} + 2e^- + 2H^+ \rightleftarrows \text{Flavin (Hq)} \qquad \text{(Eq. 1-2)}$$

where Ox represents the oxidized form of flavin and Hq represents hydroquinone, the two-electrons reduced form of flavin.

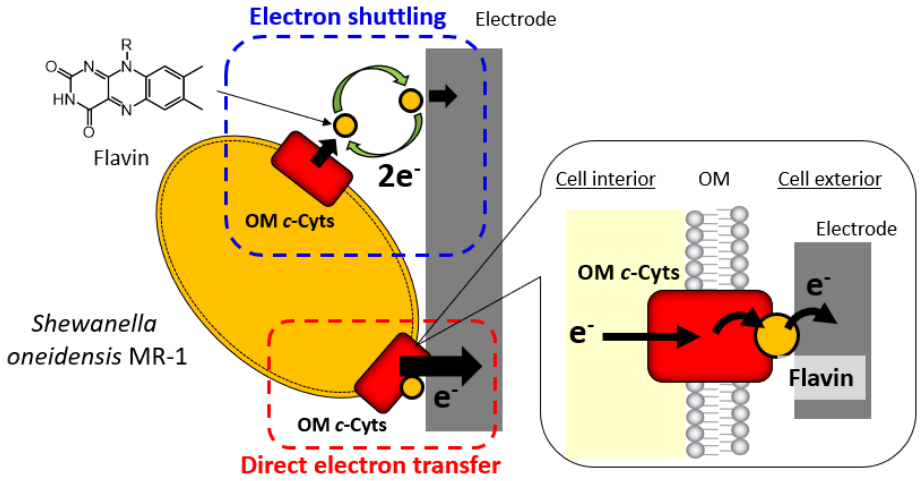

Figure 1-12. Schematic illustration of flavins mediating EET processes of *S. oneidensis* MR-1. Upper side: Electron shuttling process between OM *c*-Cyt complexes and electrodes by two-electron redox reaction of free-form flavins. Lower side: Direct EET process via a one-electron reaction of flavins that are associated with the flavin binding site in OM *c*-Cyt (MtrC protein).

This "bound cofactor model" is supported by several research group until now, e.g. it was demonstrated that purified MtrC in reduced state stably binds with flavins [29]. Furthermore, it was also proposed that the "bound cofactor model" predominantly contribute on EET acceleration rather than the shuttling mechanism (Details in 1-7) [26, 31, 35]. Although the detailed binding site of MtrC with flavins are still unclear, it was demonstrated that reductive cleavage of the disulfide bond in the domains III of MtrC resulted in the complex formation of MtrC/FMN, suggesting that the domain III, especially the Greek key split β-barrel is essential for the binding process (Figure 1-10) [29]. Since computational docking studies of MtrC and FMN has not yet been succeeded in the identification of binding site [98], crystallization of FMN-bound MtrC is greatly anticipated.

The bound flavin cofactor also act as an electron carrier in electron uptake process, i.e. reverse EET in *S. oneidensis* MR-1 with implications for development of MES as described in chapter 1-4 (Figure 1-13a). Since *S. oneidensis* MR-1 have IM-bound fumarate reductase, FccA, in periplasm, the OM *c*-Cyts can deliver electrons from cathode to FccA in the presence of fumarate [99]. The bound flavin stabilized as Sq state shows redox cycle of Sq/Hq during electron uptake as described in Equation 1-3, accelerating the electron transport [100].

Flavin (Sq) + $1e^-$ + $1H^+$ ⇄ Flavin (Hq) (Eq. 1-3)

Since Sq/Hq redox cycle shows about 300 mV lower redox potential than that of Ox/Sq (Figure 1-13b) [100], the electron uptake from cathode can be thermodynamically favored without additional gene expression or protein synthesis.

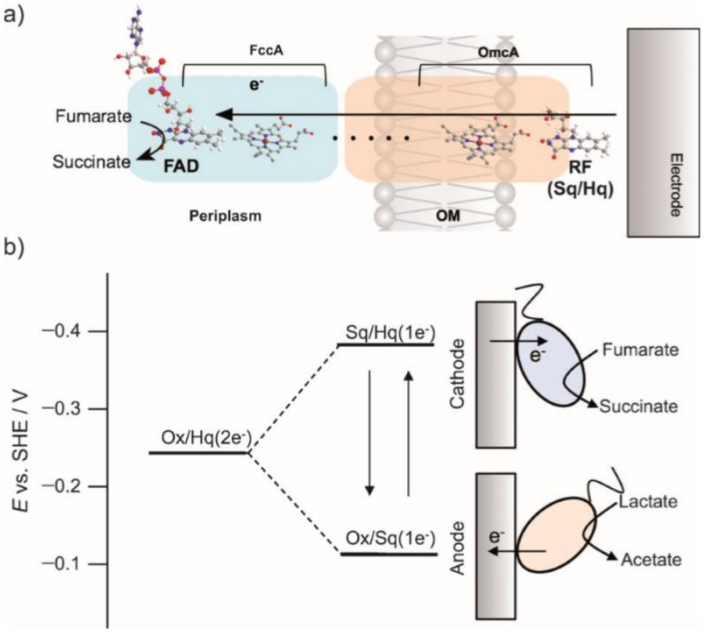

Figure 1-13. (a) Schematic illustration of reverse EET through OM *c*-Cyt, which is initiated by the semiquinone/hydroquinone (Sq/Hq) redox reaction of bound flavin. (b) Proposed model for switching the direction of the electron flow depending on the electrode potential owing to the flavin redox bifurcation. (Reprinted with permission from ref. [100]. Copyright 2014, WILEY-VCH Verlag GmbH & Co. KGaA, Weinheim)

Due to the role of flavins as electron carriers, the flux of electron import is almost identical with that of export. As shown the data of linear sweep voltammetry of *S. oneidensis* MR-1 in Figure 1-14, the absolute value of cathodic current (rate of electron import) around the peak potential of Sq/Hq was the same order with that of anodic current (rate of electron export) around the peak potential of Sq/Ox.

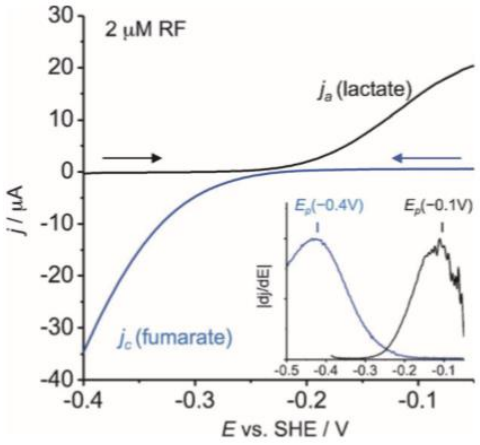

Figure 1-14. Linear sweep voltammograms of a monolayer biofilm of *S. oneidensis* MR-1 in the presence of 2 μM RF at a scan rate of 0.1 mVs^{-1} in the presence of 10 mM lactate (j_a) or 50 mm fumarate (j_c) as an electron donor or accepter, respectively. Inset: the absolute value of the first derivative of j_a and j_c. (Reprinted with permission from ref. [100]. Copyright 2014, WILEY-VCH Verlag GmbH & Co. KGaA, Weinheim)

While flavins also act as electron carriers in another iron-reducing bacterium, *Geobacter sulfurreducens* PCA [27, 32], the rate of electron import is over 10 times lower than that of export [101-104]. *Geobacter sulfurreducens* PCA conduct EET through OM *c*-Cyts (OmcB, OmcE, OmcS, and OmcT as major cytochromes on OM), and produces anodic current with highest efficiency reported so far [32]. Electrochemical voltammetric studies have exhibited that the flavins in the presence of *G. sulfurreducens* PCA have redox potential of about −0.20 V versus SHE, which is distinct from that of unbound

flavins of −0.27 V (Figure 1-15). The anodic current linearly increased with the amount of flavins with redox potential of −0.20 V, and the redox property of flavins altered by deletion of OmcBEST, suggesting that *G. sulfurreducens* PCA utilize flavins as bound Sq cofactors of OM *c*-Cyts as with the case of *S. oneidensis* MR-1 (Figure 1-15). Although *S. oneidensis* MR-1 proceed efficient bi-directional EET based on the bound cofactor model, *G. sulfurreducens* PCA have preference for electron export like a biological diode. It would be of great interest to test how the bound flavins control the bias in electron transport direction.

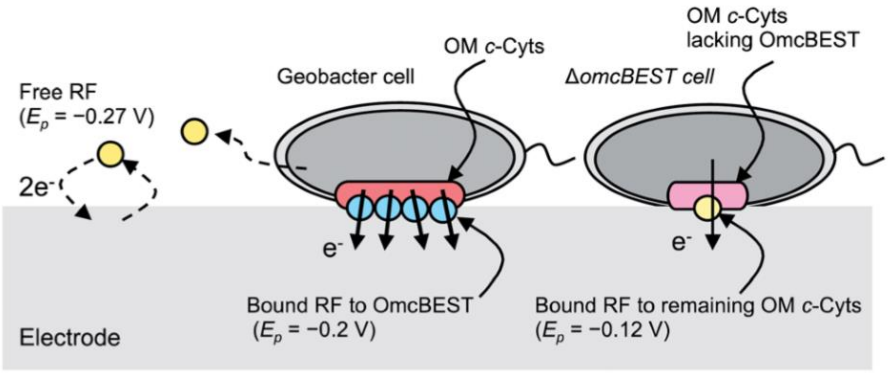

Figure 1-15. Schematic illustration of EET process in *Geobacter sulfurreducens* PCA referred from [32]. (Copyright 2014, Published by The Royal Society of Chemistry.)

The act of flavins as bound cofactor is even suggested in over 100 strains of Gram-positive bacteria including a Gram-positive food-borne bacterial pathogen, *L. monocytogenes* [18-19]. As mentioned in chapter 1-6, Light *et al.*, identified the proteins Ndh2, EetB, EetA and PplA as key proteins for the EET process using a combination of genetic and biochemical approaches (Figure 1-16) [18]. Notably, it was revealed that a membrane-bound protein, termed PplA, containing two bound flavin molecules enables the electron export through the cell wall in *L. monocytogenes* (Figure 1-16). In addition,

injection of flavin into *L. monocytogenes* showed a pronounced increase in anodic current in an electrochemical reactor.

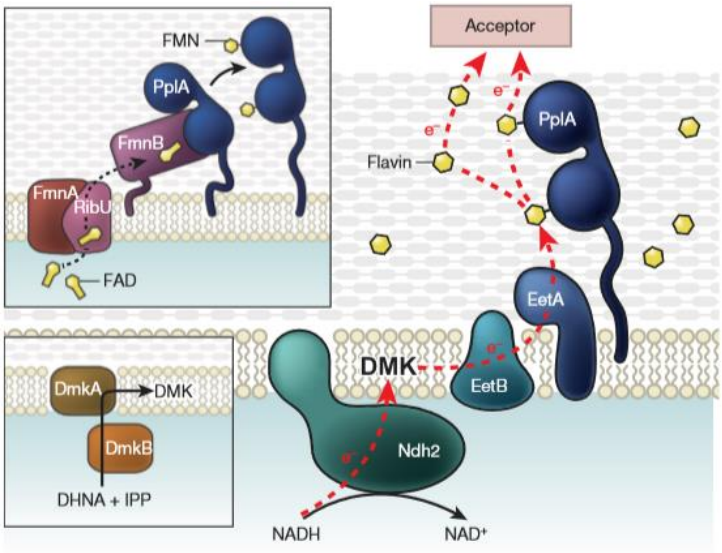

Figure 1-16. Schematic illustration of EET process in *Listeria monocytogenes* referred from [18]. (Reprinted with permission from ref. [18]. Copyright 2018, Nature Publishing Group)

Taken together, those studies indicate that the bound cofactor model is a universal EET mechanisms used by a variety of microorganisms including both Gram-negative and -positive bacteria. Notably, the bound cofactor mechanisms can be driven under micromolar-order concentrations of flavin, which is typical condition of nutrient-rich environments, such as the plant biomass and mammalian hosts [105-106]. Therefore, an understanding of the mechanisms in EET process mediated by bound flavin is of fundamental importance.

References in chapter 1

1. Ramirez, B. E.; Malmstrom, B. G.; Winkler, J. R.; Gray, H. B., The currents of life: The terminal electron-transfer complex of respiration. *Proc. Natl. Acad. Sci. U.S.A.* **1995,** *92* (26), 11949-11951.
2. Arnold, R. G.; Olson, T. M.; Hoffmann, M. R., Kinetics and Mechanism of Dissimilative Fe(III) Reduction by *Pseudomonas*-sp-200. *Biotechnol. Bioeng.* **1986,** *28* (11), 1657-1671.
3. Myers, C. R.; Nealson, K. H., Bacterial Manganese Reduction and Growth with Manganese Oxide as the Sole Electron-Acceptor. *Science* **1988,** *240* (4857), 1319-1321.
4. Lovley, D. R.; Phillips, E. J., Novel mode of microbial energy metabolism: organic carbon oxidation coupled to dissimilatory reduction of iron or manganese. *Appl. Environ. Microbiol.* **1988,** *54* (6), 1472-80.
5. Arnold, R. G.; Dichristina, T. J.; Hoffmann, M. R., Reductive Dissolution of Fe(III) Oxides by *Pseudomonas* sp 200. *Biotechnol Bioeng* **1988,** *32* (9), 1081-1096.
6. Nealson, K. H.; Saffarini, D., Iron and Manganese in Anaerobic Respiration - Environmental Significance, Physiology, and Regulation. *Annu. Rev. Microbiol.* **1994,** *48*, 311-343.
7. Risgaard-Petersen, N.; Revil, A.; Meister, P.; Nielsen, L. P., Sulfur, iron-, and calcium cycling associated with natural electric currents running through marine sediment. *Geochim. Cosmochim. Acta* **2012,** *92*, 1-13.
8. Rowe, A. R.; Yoshimura, M.; LaRowe, D. E.; Bird, L. J.; Amend, J. P.; Hashimoto, K.; Nealson, K. H.; Okamoto, A., In situ electrochemical enrichment and isolation of a magnetite-reducing bacterium from a high pH serpentinizing spring. *Environ. Microbiol.* **2017,** *19* (6), 2272-2285.
9. Fuller, S. J.; McMillan, D. G. G.; Renz, M. B.; Schmidt, M.; Burke, I. T.; Stewart, D. I., Extracellular Electron Transport-Mediated Fe(III) Reduction by a Community of Alkaliphilic Bacteria That Use Flavins as Electron Shuttles. *Appl. Environ. Microbiol.* **2014,** *80* (1), 128-137.
10. Emerson, D.; Moyer, C. L., Neutrophilic Fe-Oxidizing bacteria are abundant at the Loihi Seamount hydrothermal vents and play a major role in Fe oxide deposition. *Appl. Environ. Microbiol.* **2002,** *68* (6), 3085-3093.
11. Lovley, D. R., Bug juice: harvesting electricity with microorganisms. *Nat. Rev. Microbiol.* **2006,** *4* (7), 497-508.
12. Rabaey, K.; Rozendal, R. A., Microbial electrosynthesis - revisiting the electrical route for microbial production. *Nat. Rev. Microbiol.* **2010,** *8* (10), 706-716.
13. Logan, B. E.; Hamelers, B.; Rozendal, R. A.; Schrorder, U.; Keller, J.; Freguia,

S.; Aelterman, P.; Verstraete, W.; Rabaey, K., Microbial fuel cells: Methodology and technology. *Environ. Sci. Technol.* **2006,** *40* (17), 5181-5192.

14. Dinh, H. T.; Kuever, J.; Mussmann, M.; Hassel, A. W.; Stratmann, M.; Widdel, F., Iron corrosion by novel anaerobic microorganisms. *Nature* **2004,** *427* (6977), 829-832.

15. Wegener, G.; Krukenberg, V.; Riedel, D.; Tegetmeyer, H. E.; Boetius, A., Intercellular wiring enables electron transfer between methanotrophic archaea and bacteria. *Nature* **2015,** *526* (7574), 587-U315.

16. McGlynn, S. E.; Chadwick, G. L.; Kempes, C. P.; Orphan, V. J., Single cell activity reveals direct electron transfer in methanotrophic consortia. *Nature* **2015,** *526* (7574), 531-U146.

17. Deng, X.; Dohmae, N.; Nealson, K. H.; Hashimoto, K.; Okamoto, A., Multi-heme cytochromes provide a pathway for survival in energy-limited environments. *Sci. Adv.* **2018,** *4* (2).

18. Light, S. H.; Su, L.; Rivera-Lugo, R.; Cornejo, J. A.; Louie, A.; Iavarone, A. T.; Ajo-Franklin, C. M.; Portnoy, D. A., A flavin-based extracellular electron transfer mechanism in diverse Gram-positive bacteria. *Nature* **2018,** *562* (7725), 140-+.

19. Khan, M. T.; Duncan, S. H.; Stams, A. J. M.; van Dijl, J. M.; Flint, H. J.; Harmsen, H. J. M., The gut anaerobe Faecalibacterium prausnitzii uses an extracellular electron shuttle to grow at oxic-anoxic interphases. *ISME Journal* **2012,** *6* (8), 1578-1585.

20. Myers, C. R.; Myers, J. M., Outer membrane cytochromes of *Shewanella putrefaciens* MR-1: Spectral analysis, and purification of the 83-kDa *c*-type cytochrome. *Biochim. Biophys. Acta* **1997,** *1326* (2), 307-318.

21. Xiong, Y. J.; Shi, L.; Chen, B. W.; Mayer, M. U.; Lower, B. H.; Londer, Y.; Bose, S.; Hochella, M. F.; Fredrickson, J. K.; Squier, T. C., High-affinity binding and direct electron transfer to solid metals by the *Shewanella oneidensis* MR-1 outer membrane *c*-type cytochrome OmcA. *J. Am. Chem. Soc.* **2006,** *128* (43), 13978-13979.

22. Hartshorne, R. S.; Reardon, C. L.; Ross, D.; Nuester, J.; Clarke, T. A.; Gates, A. J.; Mills, P. C.; Fredrickson, J. K.; Zachara, J. M.; Shi, L.; Beliaev, A. S.; Marshall, M. J.; Tien, M.; Brantley, S.; Butt, J. N.; Richardson, D. J., Characterization of an electron conduit between bacteria and the extracellular environment. *Proc. Natl. Acad. Sci. U.S.A.* **2009,** *106* (52), 22169-22174.

23. Marsili, E.; Baron, D. B.; Shikhare, I. D.; Coursolle, D.; Gralnick, J. A.; Bond, D. R., *Shewanella* Secretes flavins that mediate extracellular electron transfer. *Proc. Natl. Acad. Sci. U.S.A.* **2008,** *105* (10), 3968-3973.

24. von Canstein, H.; Ogawa, J.; Shimizu, S.; Lloyd, J. R., Secretion of flavins by Shewanella species and their role in extracellular electron transfer. *Appl. Environ.*

Microbiol. **2008,** *74* (3), 615-623.
25. Clarke, T. A.; Edwards, M. J.; Gates, A. J.; Hall, A.; White, G. F.; Bradley, J.; Reardon, C. L.; Shi, L.; Beliaev, A. S.; Marshall, M. J.; Wang, Z. M.; Watmough, N. J.; Fredrickson, J. K.; Zachara, J. M.; Butt, J. N.; Richardson, D. J., Structure of a bacterial cell surface decaheme electron conduit. *Proc. Natl. Acad. Sci. U.S.A.* **2011,** *108* (23), 9384-9389.
26. Okamoto, A.; Hashimoto, K.; Nealson, K. H.; Nakamura, R., Rate enhancement of bacterial extracellular electron transport involves bound flavin semiquinones. *Proc. Natl. Acad. Sci. U.S.A.* **2013,** *110* (19), 7856-7861.
27. Okamoto, A.; Nakamura, R.; Nealson, K. H.; Hashimoto, K., Bound Flavin Model Suggests Similar Electron-Transfer Mechanisms in *Shewanella* and *Geobacter*. *Chemelectrochem* **2014,** *1* (11), 1808-1812.
28. Okamoto, A.; Kalathil, S.; Deng, X.; Hashimoto, K.; Nakamura, R.; Nealson, K. H., Cell-secreted Flavins Bound to Membrane Cytochromes Dictate Electron Transfer Reactions to Surfaces with Diverse Charge and pH. *Sci Rep* **2014,** *4*, 5628.
29. Edwards, M. J.; White, G. F.; Norman, M.; Tome-Fernandez, A.; Ainsworth, E.; Shi, L.; Fredrickson, J. K.; Zachara, J. M.; Butt, J. N.; Richardson, D. J.; Clarke, T. A., Redox Linked Flavin Sites in Extracellular Decaheme Proteins Involved in Microbe-Mineral Electron Transfer. *Sci Rep* **2015,** *5,* 11677.
30. Watanabe, H. C.; Yamashita, Y.; Ishikita, H., Electron transfer pathways in a multiheme cytochrome MtrF. *Proc. Natl. Acad. Sci. U.S.A.* **2017,** *114* (11), 2916-2921.
31. Xu, S.; Barrozo, A.; Tender, L. M.; Krylov, A. I.; El-Naggar, M. Y., Multiheme Cytochrome Mediated Redox Conduction through *Shewanella oneidensis* MR-1 Cells. *J. Am. Chem. Soc.* **2018,** *140* (32), 10085-10089.
32. Okamoto, A.; Saito, K.; Inoue, K.; Nealson, K. H.; Hashimoto, K.; Nakamura, R., Uptake of self-secreted flavins as bound cofactors for extracellular electron transfer in *Geobacter* species. *Energy Environ. Sci.* **2014,** *7* (4), 1357-1361.
33. Kotloski, N. J.; Gralnick, J. A., Flavin Electron Shuttles Dominate Extracellular Electron Transfer by *Shewanella oneidensis*. *Mbio* **2013,** *4* (1).
34. Jiang, J.; Kappler, A., Kinetics of microbial and chemical reduction of humic substances: Implications for electron shuttling. *Environ. Sci. Technol.* **2008,** *42* (10), 3563-3569.
35. Xu, S.; Jangir, Y.; El-Naggar, M. Y., Disentangling the roles of free and cytochrome-bound flavins in extracellular electron transport from *Shewanella oneidensis* MR-1. *Electrochim. Acta* **2016,** *198*, 49-55.
36. Okamoto, A.; Nakamura, R.; Ishii, K.; Hashimoto, K., *In vivo* Electrochemistry

of *C*-Type Cytochrome-Mediated Electron-Transfer with Chemical Marking. *Chembiochem* **2009,** *10* (14), 2329-2332.

37. Okamoto, A.; Nakamura, R.; Hashimoto, K., *In-vivo* identification of direct electron transfer from *Shewanella oneidensis* MR-1 to electrodes via outer-membrane OmcA-MtrCAB protein complexes. *Electrochim. Acta* **2011,** *56* (16), 5526-5531.

38. Buckel, W.; Thauer, R. K., Flavin-Based Electron Bifurcation, Ferredoxin, Flavodoxin, and Anaerobic Respiration With Protons (Ech) or NAD(+) (Rnf) as Electron Acceptors: A Historical Review. *Front. Microbiol.* **2018,** *9*.

39. Lubner, C. E.; Jennings, D. P.; Mulder, D. W.; Schut, G. J.; Zadvornyy, O. A.; Hoben, J. P.; Tokmina-Lukaszewska, M.; Berry, L.; Nguyen, D. M.; Lipscomb, G. L.; Bothner, B.; Jones, A. K.; Miller, A. F.; King, P. W.; Adams, M. W. W.; Peters, J. W., Mechanistic insights into energy conservation by flavin-based electron bifurcation. *Nat. Chem. Biol.* **2017,** *13* (6), 655-659.

40. Millett, F.; Havens, J.; Rajagukguk, S.; Durham, B., Design and use of photoactive ruthenium complexes to study electron transfer within cytochrome bc_1 and from cytochrome bc_1 to cytochrome *c*. *Biochim. Biophys. Acta* **2013,** *1827* (11-12), 1309-1319.

41. Xia, D.; Esser, L.; Tang, W. K.; Zhou, F.; Zhou, Y. H.; Yu, L. D.; Yu, C. A., Structural analysis of cytochrome bc_1 complexes: Implications to the mechanism of function. *Biochim. Biophys. Acta* **2013,** *1827* (11-12), 1278-1294.

42. Wang, Z. M.; Shi, Z.; Shi, L.; White, G. F.; Richardson, D. J.; Clarke, T. A.; Fredrickson, J. K.; Zachara, J. M., Effects of soluble flavin on heterogeneous electron transfer between surface-exposed bacterial cytochromes and iron oxides. *Geochim. Cosmochim. Acta* **2015,** *163*, 299-310.

43. Lane, N., What can't bacteria do? *Nature* **2006,** *441* (7091), 274-277.

44. Gorby, Y. A.; Yanina, S.; McLean, J. S.; Rosso, K. M.; Moyles, D.; Dohnalkova, A.; Beveridge, T. J.; Chang, I. S.; Kim, B. H.; Kim, K. S.; Culley, D. E.; Reed, S. B.; Romine, M. F.; Saffarini, D. A.; Hill, E. A.; Shi, L.; Elias, D. A.; Kennedy, D. W.; Pinchuk, G.; Watanabe, K.; Ishii, S.; Logan, B.; Nealson, K. H.; Fredrickson, J. K., Electrically conductive bacterial nanowires produced by *Shewanella oneidensis* strain MR-1 and other microorganisms. *Proc. Natl. Acad. Sci. U.S.A.* **2006,** *103* (30), 11358-11363.

45. Childers, S. E.; Ciufo, S.; Lovley, D. R., Geobacter metallireducens accesses insoluble Fe(III) oxide by chemotaxis. *Nature* **2002,** *416* (6882), 767-769.

46. Lovley, D. R.; Holmes, D. E.; Nevin, K. P., Dissimilatory Fe(III) and Mn(IV) reduction. *Adv. Microbial. Physiol.* **2004,** *49*, 219-286.

47. Santoro, C.; Arbizzani, C.; Erable, B.; Ieropoulos, I., Microbial fuel cells: From

fundamentals to applications. A review. *J. Power. Sources.* **2017,** *356*, 225-244.
48. Wang, H. M.; Park, J. D.; Ren, Z. J., Practical Energy Harvesting for Microbial Fuel Cells: A Review. *Environ. Sci. Technol.* **2015,** *49* (6), 3267-3277.
49. Watanabe, K., Recent Developments in Microbial Fuel Cell Technologies for Sustainable Bioenergy. *J. Biosci. Bioeng.* **2008,** *106* (6), 528-536.
50. Wang, H. M.; Ren, Z. Y. J., A comprehensive review of microbial electrochemical systems as a platform technology. *Biotechnol. Adv.* **2013,** *31* (8), 1796-1807.
51. Harnisch, F.; Schroder, U., From MFC to MXC: chemical and biological cathodes and their potential for microbial bioelectrochemical systems. *Chem. Soc. Rev.* **2010,** *39* (11), 4433-4448.
52. Liu, H.; Grot, S.; Logan, B. E., Electrochemically assisted microbial production of hydrogen from acetate. *Environ. Sci. Technol.* **2005,** *39* (11), 4317-4320.
53. Choi, O.; Sang, B. I., Extracellular electron transfer from cathode to microbes: application for biofuel production. *Biotechnol. Biofuels.* **2016,** *9*.
54. Van Eerten-Jansen, M. C. A. A.; Ter Heijne, A.; Grootscholten, T. I. M.; Steinbusch, K. J. J.; Sleutels, T. H. J. A.; Hamelers, H. V. M.; Buisman, C. J. N., Bioelectrochemical Production of Caproate and Caprylate from Acetate by Mixed Cultures. *ACS Sustain. Chem. Eng.* **2013,** *1* (5), 513-518.
55. Dennis, P. G.; Harnisch, F.; Yeoh, Y. K.; Tyson, G. W.; Rabaey, K., Dynamics of Cathode-Associated Microbial Communities and Metabolite Profiles in a Glycerol-Fed Bioelectrochemical System. *Appl. Environ. Microbiol.* **2013,** *79* (13), 4008-4014.
56. Hawkins, A. S.; McTernan, P. M.; Lian, H.; Kelly, R. M.; Adams, M. W. W., Biological conversion of carbon dioxide and hydrogen into liquid fuels and industrial chemicals. *Curr. Opin. Biotech.* **2013,** *24* (3), 376-384.
57. Ganigue, R.; Puig, S.; Batlle-Vilanova, P.; Balaguer, M. D.; Colprim, J., Microbial electrosynthesis of butyrate from carbon dioxide. *Chem. Commun.* **2015,** *51* (15), 3235-3238.
58. Xafenias, N.; Zhang, Y.; Banks, C. J., Enhanced Performance of Hexavalent Chromium Reducing Cathodes in the Presence of Shewanella oneidensis MR-1 and Lactate. *Environ. Sci. Technol.* **2013,** *47* (9), 4512-4520.
59. Gregory, K. B.; Lovley, D. R., Remediation and recovery of uranium from contaminated subsurface environments with electrodes. *Environ. Sci. Technol.* **2005,** *39* (22), 8943-8947.
60. Leung, K. M.; Wanger, G.; El-Naggar, M. Y.; Gorby, Y.; Southam, G.; Lau, W. M.; Yang, J., *Shewanella oneidensis* MR-1 Bacterial Nanowires Exhibit p-Type, Tunable

Electronic Behavior. *Nano Lett.* **2013,** *13* (6), 2407-2411.
61. Hu, Y. D.; Yang, Y.; Katz, E.; Song, H., Programming the quorum sensing-based AND gate in Shewanella oneidensis for logic gated-microbial fuel cells. *Chem. Commun.* **2015,** *51* (20), 4184-4187.
62. Rosenbaum, M.; He, Z.; Angenent, L. T., Light energy to bioelectricity: photosynthetic microbial fuel cells. *Curr. Opin. Biotech.* **2010,** *21* (3), 259-264.
63. Ng, F. L.; Phang, S. M.; Periasamy, V.; Yunus, K.; Fisher, A. C., Enhancement of Power Output by using Alginate Immobilized Algae in Biophotovoltaic Devices. *Sci Rep* **2017,** *7*, 16237.
64. Venzlaff, H.; Enning, D.; Srinivasan, J.; Mayrhofer, K. J. J.; Hassel, A. W.; Widdel, F.; Stratmann, M., Accelerated cathodic reaction in microbial corrosion of iron due to direct electron uptake by sulfate-reducing bacteria. *Corros. Sci.* **2013,** *66*, 88-96.
65. Enning, D.; Garrelfs, J., Corrosion of Iron by Sulfate-Reducing Bacteria: New Views of an Old Problem. *Appl. Environ. Microbiol.* **2014,** *80* (4), 1226-1236.
66. Scheller, S.; Yu, H.; Chadwick, G. L.; McGlynn, S. E.; Orphan, V. J., Artificial electron acceptors decouple archaeal methane oxidation from sulfate reduction. *Science* **2016,** *351* (6274), 703-707.
67. Reeburgh, W. S., Oceanic methane biogeochemistry. *Chem. Rev.* **2007,** *107* (2), 486-513.
68. Boetius, A.; Wenzhofer, F., Seafloor oxygen consumption fuelled by methane from cold seeps. *Nat. Geosci.* **2013,** *6* (9), 725-734.
69. Beech, W. B.; Sunner, J., Biocorrosion: towards understanding interactions between biofilms and metals. *Curr. Opin. Biotech.* **2004,** *15* (3), 181-186.
70. Uhlig, H. H., *Uhlig's corrosion handbook*. John Wiley & Sons: 2011; Vol. 51.
71. Pisciotta, J. M.; Zou, Y.; Baskakov, I. V., Light-Dependent Electrogenic Activity of Cyanobacteria. *Plos One* **2010,** *5* (5).
72. Sekar, N.; Umasankar, Y.; Ramasamy, R. P., Photocurrent generation by immobilized cyanobacteria via direct electron transport in photo-bioelectrochemical cells. *Phys. Chem. Chem. Phys.* **2014,** *16* (17), 7862-7871.
73. De Schamphelaire, L.; Verstraete, W., Revival of the Biological Sunlight-to-Biogas Energy Conversion System. *Biotechnol. Bioeng.* **2009,** *103* (2), 296-304.
74. McCormick, A. J.; Bombelli, P.; Bradley, R. W.; Thorne, R.; Wenzel, T.; Howe, C. J., Biophotovoltaics: oxygenic photosynthetic organisms in the world of bioelectrochemical systems. *Energy Environ. Sci.* **2015,** *8* (4), 1092-1109.
75. McCormick, A. J.; Bombelli, P.; Scott, A. M.; Philips, A. J.; Smith, A. G.; Fisher, A. C.; Howe, C. J., Photosynthetic biofilms in pure culture harness solar energy in a

mediatorless bio-photovoltaic cell (BPV) system. *Energy Environ. Sci.* **2011,** *4* (11), 4699-4709.

76. Deneer, H. G.; Boychuk, I., Reduction of Ferric Iron by Listeria-Monocytogenes and Other Species of Listeria. *Can. J. Microbiol.* **1993,** *39* (5), 480-485.

77. Freitag, N. E.; Port, G. C.; Miner, M. D., Listeria monocytogenes - from saprophyte to intracellular pathogen. *Nat. Rev. Microbiol.* **2009,** *7* (9), 623-628.

78. Cahoon, L. A.; Freitag, N. E., The electrifying energy of gut microbes. *Nature* **2018,** *562* (7725), 43-44.

79. Wanger, G.; Gorby, Y.; El-Naggar, M. Y.; Yuzvinsky, T. D.; Schaudinn, C.; Gorur, A.; Sedghizadeh, P. P., Electrically conductive bacterial nanowires in bisphosphonate-related osteonecrosis of the jaw biofilms. *Oral Surg. Oral Med. Oral Pathol. Oral Radiol.* **2013,** *115* (1), 71-8.

80. Myers, C. R.; Myers, J. M., Localization of Cytochromes to the Outer-Membrane of Anaerobically Grown *Shewanella-Putrefaciens* MR-1. *J. Bacteriol.* **1992,** *174* (11), 3429-3438.

81. Heidelberg, J. F.; Paulsen, I. T.; Nelson, K. E.; Gaidos, E. J.; Nelson, W. C.; Read, T. D.; Eisen, J. A.; Seshadri, R.; Ward, N.; Methe, B.; Clayton, R. A.; Meyer, T.; Tsapin, A.; Scott, J.; Beanan, M.; Brinkac, L.; Daugherty, S.; DeBoy, R. T.; Dodson, R. J.; Durkin, A. S.; Haft, D. H.; Kolonay, J. F.; Madupu, R.; Peterson, J. D.; Umayam, L. A.; White, O.; Wolf, A. M.; Vamathevan, J.; Weidman, J.; Impraim, M.; Lee, K.; Berry, K.; Lee, C.; Mueller, J.; Khouri, H.; Gill, J.; Utterback, T. R.; McDonald, L. A.; Feldblyum, T. V.; Smith, H. O.; Venter, J. C.; Nealson, K. H.; Fraser, C. M., Genome sequence of the dissimilatory metal ion-reducing bacterium *Shewanella oneidensis*. *Nat. Biotechnol.* **2002,** *20* (11), 1118-1123.

82. Hartshorne, R. S.; Jepson, B. N.; Clarke, T. A.; Field, S. J.; Fredrickson, J.; Zachara, J.; Shi, L.; Butt, J. N.; Richardson, D. J., Characterization of *Shewanella oneidensis* MtrC: a cell-surface decaheme cytochrome involved in respiratory electron transport to extracellular electron acceptors. *J. Biol. Inorg. Chem.* **2007,** *12* (7), 1083-1094.

83. Ross, D. E.; Brantley, S. L.; Tien, M., Kinetic Characterization of OmcA and MtrC, Terminal Reductases Involved in Respiratory Electron Transfer for Dissimilatory Iron Reduction in Shewanella oneidensis MR-1. *Appl. Environ. Microbiol.* **2009,** *75* (16), 5218-5226.

84. Kasai, T.; Kouzuma, A.; Nojiri, H.; Watanabe, K., Transcriptional mechanisms for differential expression of outer membrane cytochrome genes *omcA* and *mtrC* in *Shewanella oneidensis* MR-1. *BMC Microbiol.* **2015,** *15*.

85. Edwards, M. J.; White, G. F.; Lockwood, C. W.; Lawes, M. C.; Martel, A.; Harris, G.; Scott, D. J.; Richardson, D. J.; Butt, J. N.; Clarke, T. A., Structural modeling of an outer membrane electron conduit from a metal-reducing bacterium suggests electron transfer via periplasmic redox partners. *J. Biol. Chem.* **2018,** *293* (21), 8103-8112.
86. White, G. F.; Shi, Z.; Shi, L.; Wang, Z. M.; Dohnalkova, A. C.; Marshall, M. J.; Fredrickson, J. K.; Zachara, J. M.; Butt, J. N.; Richardson, D. J.; Clarke, T. A., Rapid electron exchange between surface-exposed bacterial cytochromes and Fe(III) minerals. *Proc. Natl. Acad. Sci. U.S.A.* **2013,** *110* (16), 6346-6351.
87. Breuer, M.; Zarzycki, P.; Blumberger, J.; Rosso, K. M., Thermodynamics of Electron Flow in the Bacterial Deca-heme Cytochrome MtrF. *J. Am. Chem. Soc.* **2012,** *134* (24), 9868-9871.
88. Breuer, M.; Rosso, K. M.; Blumberger, J., Electron flow in multiheme bacterial cytochromes is a balancing act between heme electronic interaction and redox potentials. *Proc. Natl. Acad. Sci. U.S.A.* **2014,** *111* (2), 611-616.
89. Barrozo, A.; El-Naggar, M. Y.; Krylov, A. I., Distinct Electron Conductance Regimes in Bacterial Decaheme Cytochromes. *Angew. Chem. Int. Ed.* **2018,** *57* (23), 6805-6809.
90. Wigginton, N. S.; Rosso, K. M.; Lower, B. H.; Shi, L.; Hochella, M. F., Electron tunneling properties of outer-membrane decaheme cytochromes from *Shewanella oneidensis*. *Geochim. Cosmochim. Acta* **2007,** *71* (3), 543-555.
91. Byun, H. S.; Pirbadian, S.; Nakano, A.; Shi, L.; El-Naggar, M. Y., Kinetic Monte Carlo Simulations and Molecular Conductance Measurements of the Bacterial Decaheme Cytochrome MtrF. *Chemelectrochem* **2014,** *1* (11), 1932-1939.
92. Garg, K.; Ghosh, M.; Eliash, T.; van Wonderen, J. H.; Butt, J. N.; Shi, L.; Jiang, X. Y.; Zdenek, F.; Blumberger, J.; Pecht, I.; Sheves, M.; Cahen, D., Direct evidence for heme-assisted solid-state electronic conduction in multi-heme *c*-type cytochromes. *Chem. Sci.* **2018,** *9* (37).
93. Blumberger, J., Recent Advances in the Theory and Molecular Simulation of Biological Electron Transfer Reactions. *Chem. Rev.* **2015,** *115* (20), 11191-11238.
94. Johs, A.; Shi, L.; Droubay, T.; Ankner, J. F.; Liang, L., Characterization of the Decaheme c-Type Cytochrome OmcA in Solution and on Hematite Surfaces by Small Angle X-Ray Scattering and Neutron Reflectometry. *Biophys. J.* **2010,** *98* (12), 3035-3043.
95. Yu, S. S.; Chen, J. J.; Liu, X. Y.; Yu, H. Q., Interfacial Electron Transfer from the Outer Membrane Cytochrome OmcA to Graphene Oxide in a Microbial Fuel Cell: Spectral and Electrochemical Insights. *ACS Energy Lett.* **2018,** *3* (10), 2449-2456.

96. Coursolle, D.; Baron, D. B.; Bond, D. R.; Gralnick, J. A., The Mtr Respiratory Pathway Is Essential for Reducing Flavins and Electrodes in *Shewanella oneidensis*. *J. Bacteriol.* **2010,** *192* (2), 467-474.
97. Brutinel, E. D.; Gralnick, J. A., Shuttling happens: soluble flavin mediators of extracellular electron transfer in *Shewanella*. *Appl. Microbiol. Biotechnol.* **2012,** *93* (1), 41-48.
98. Breuer, M.; Rosso, K. M.; Blumberger, J., Flavin Binding to the Deca-heme Cytochrome MtrC: Insights from Computational Molecular Simulation. *Biophys. J.* **2015,** *109* (12), 2614-2624.
99. Ross, D. E.; Flynn, J. M.; Baron, D. B.; Gralnick, J. A.; Bond, D. R., Towards Electrosynthesis in Shewanella: Energetics of Reversing the Mtr Pathway for Reductive Metabolism. *Plos One* **2011,** *6* (2).
100. Okamoto, A.; Hashimoto, K.; Nealson, K. H., Flavin Redox Bifurcation as a Mechanism for Controlling the Direction of Electron Flow during Extracellular Electron Transfer. *Angew. Chem. Int. Ed.* **2014,** *53* (41), 10988-10991.
101. Bond, D. R.; Lovley, D. R., Electricity production by *Geobacter sulfurreducens* attached to electrodes. *Appl. Environ. Microbiol.* **2003,** *69* (3), 1548-1555.
102. Gregory, K. B.; Bond, D. R.; Lovley, D. R., Graphite electrodes as electron donors for anaerobic respiration. *Environ. Microbiol.* **2004,** *6* (6), 596-604.
103. Yang, G.; Huang, L.; You, L.; Zhuang, L.; Zhou, S., Electrochemical and spectroscopic insights into the mechanisms of bidirectional microbe-electrode electron transfer in *Geobacter soli* biofilms. *Electrochem. Commun.* **2017,** *77*, 93-97.
104. Strycharz, S. M.; Glaven, R. H.; Coppi, M. V.; Gannon, S. M.; Perpetua, L. A.; Liu, A.; Nevin, K. P.; Lovley, D. R., Gene expression and deletion analysis of mechanisms for electron transfer from electrodes to *Geobacter sulfurreducens*. *Bioelectrochemistry* **2011,** *80* (2), 142-150.
105. Powers, H. J., Riboflavin (vitamin B-2) and health. *Am. J. Clin. Nutr.* **2003,** *77* (6), 1352-1360.
106. Huhner, J.; Ingles-Prieto, A.; Neususs, C.; Lammerhofer, M.; Janovjak, H., Quantification of riboflavin, flavin mononucleotide, and flavin adenine dinucleotide in mammalian model cells by CE with LED-induced fluorescence detection. *Electrophoresis* **2015,** *36* (4), 518-525.

Chapter

2

Flavin enhances the rate of extracellular electron transport by acceleration of coupled proton transport

In chapter 1, the importance and generality of flavin-mediated EET was reviewed. Flavin is stabilized as one-electron reduced semiquinone form (Sq) and is bound with OM *c*-Cyts as a non-covalent redox-active cofactor molecule [1-3]. Although the flavin Sq has modified redox potential of about −145mV (vs standard hydrogen electrode, SHE), however, it is lower than that of OM *c*-Cyts (about 50mV on average) [1, 4-5]. The flavin-mediated EET process involves up-hill electron transfer reaction with about 200 mV (Figure 2-1), thus, it remains questionable how the involvement of flavin Sq accelerates the EET process through OM *c*-Cyts.

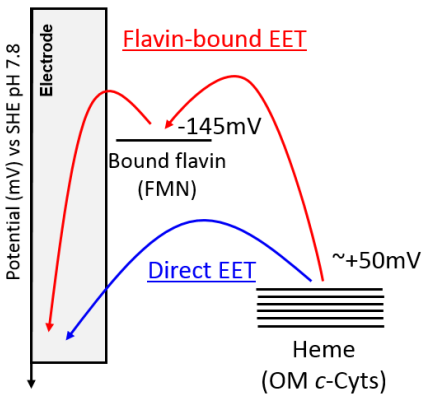

Figure 2-1. Energy diagrams for EET process in *S. oneidensis* MR-1.

Although the EET process has been studied from the viewpoint of energetics of

electrons [1, 6-8], little attention has been given to the alternative roles of counter cations, e.g. protons. Proton transport is essential for biological energy conversion driven by enzymes that catalyze electron transfer. For example, sequential electron transfer in bacterial inner-membrane or mitochondrial membrane is coupled with formation of proton gradient or proton motive force (PMF) [9-10]. However, the role of protons in EET process is still unclear, thus, protons have been primarily considered to promote chemiosmotic ATP production [11]. Importantly, those proton transfer reactions are kinetically coupled with biological electron transfer, potentially limiting the rate of electron transfer. Thus, in chapter 2, it was hypothesized that proton transport reaction is coupled with EET through OM *c*-Cyts, and flavin enhances the rate of EET by acceleration of coupled proton transport. To test this hypothesis, in chapter 2-1, the impact of the basicity of bound cofactor on EET kinetics was tested. Bound-flavin cofactor was replaced with its analogous molecules with different pK_a, and the current production through OM *c*-Cyts was compared using microbio-electrochemistry. In chapter 2-2, the solvent kinetic isotope effect (KIE) and the effect of pH change on EET kinetics were examined as one of the most critical ways to study the contribution of proton transfer on the kinetics of EET. The author also discusses about the PMF generation and proton translocation during EET process.

Figures in chapter 2 are reprinted with permission from WILEY-VCH Verlag GmbH & Co. KGaA and The Chemical Society of Japan.

A. Okamoto+, Y. Tokunou+, S. Kalathil, K. Hashimoto, *Angew. Chem. Int. Ed.*, **2017**, 56, 9082-9086. +: Equal contribution

Y. Tokunou, K. Hashimoto, and A. Okamoto, *Bull. Chem. Soc. Jpn*, **2015**, 88, 690–692.

2.1

Basicity of N(5) in flavin semiquinone dictates the rate of extracellular electron transport through the outer-membrane *c*-type cytochromes

2.1.1 Introduction

Extracellular electron transport (EET) is the process whereby prokaryotes move electrons between the inner membrane and cell exterior, such that redox reactions can occur with otherwise unavailable extracellular electron donors or acceptors [12-13]. Microbes exhibiting EET molecular machinery are thus capable of innovative metabolic processes not available to microbes without EET machinery, e.g., redox reactions with solid minerals [12-13], intercellular electron transfer [14-15], and even surface interactions with electrodes for application to novel energy-production and environmental technologies [16-18]. One controversial aspect is the role of redox molecules as enhancers of bacterial current production. High concentrations (10 μM or above) of exogenous quinone and flavin analogues (QFAs) enhance EET via an electron shuttling mechanism (a two-electron redox process) [8, 19-20]. In contrast, low levels (1 μM or below) of endogenous riboflavin (RF) or flavin mononucleotide (FMN) accumulate in cultures of EET-capable bacteria, and these molecules non-covalently bind specific sites of OM *c*-Cyts as cofactors [1, 21-22]. This leads to formation of single-electron reduced semiquinone (Sq), which strongly enhances the EET rate to the same extent as the exogenous quinone-mediated shuttling mechanism, despite the 100-fold lower endogenous concentration [1-2, 22-25]. Given that

QFAs are the major redox molecules in various environments such as sediments, waters, and soils typically at micromolar concentration [19, 26], EET-coupled metabolisms must be strongly influenced by QFAs in nature. The knowledge on the spectrum of QFAs that highly accelerate EET in a few micromolar concentration remains a challenge. Therefore, understanding the mechanism(s) by which QFAs enhance the rate of EET and controlling the EET rate is central to understanding the role of EET in microbial eco-physiology.

In this chapter 2-1, the author has used microbio-electrochemistry using *S. oneidensis* MR-1 as a model system to estimate rates of EET enhancement by various QFAs, taking into consideration the pK_a value of QFAs as calculated using a quantum chemical approach [27-28]. These data showed that the nitrogen atom located at the same position with flavins termed as N(5) is critical for QFAs to bind with OM *c*-Cyts stabilizing semi-reduced state (SR, analogous with Sq) and its extent of protonation is a key regulatory factor for EET (Figure 2-2).

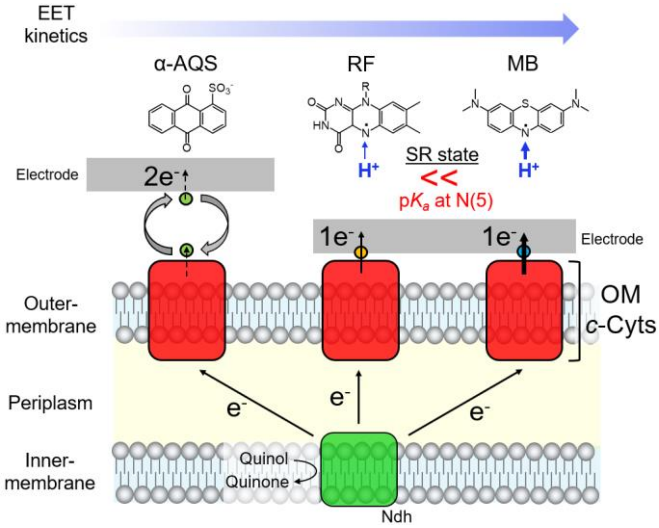

Figure 2-2. Schematic illustration of molecular control for extracellular electron transport in *S. oneidensis* MR-1 mediated by flavin, flavin analogues and quinones. α-AQS, anthraquinone-1-sulfonate; RF, riboflavin; MB, methylene blue.

2.1.2 Methods

Strains and culture conditions

Shewanella oneidensis MR-1 cells were grown aerobically in 15 mL of Luria-Bertani (LB) medium (20 g L^{-1}) at 30°C for 24 hours. The cell suspension was then centrifuged at 6,000 *g* for 10 min, and the resultant cell pellet was resuspended in 15 mL of defined medium (pH 7.8) (DM: $NaHCO_3$ [2.5 g], $CaCl_2 \cdot 2H_2O$ [0.08 g], NH_4Cl [1.0 g], $MgCl_2 \cdot 6H_2O$ [0.2 g], NaCl [10 g], yeast extract [0.5 g], and (2-[4-(2-hydroxyethyl)-1-piperazinyl] ethanesulfonic acid [HEPES; 7.2 g] [per liter]) supplemented with 10 mM lactate as the source of carbon for *S. oneidensis* MR-1[29]. The cells were further cultivated aerobically at 30°C for 12 hours and centrifuged again at 6,000 *g* for 10 min. The resultant cell pellet was then washed twice with DM medium by centrifugation for 10 min at 6,000 *g* before electrochemical experiment.

Electrochemical measurements for the catalytic current of microbial lactate oxidation (i_c) from *S. oneidensis* MR-1 with each redox molecule

A single-chamber, three-electrode system for whole-cell electrochemistry was constructed as shown in Figure 2-3. An indium tin-doped oxide (ITO) substrate (surface area: 3.1 cm^2) placed at the bottom of the reactor was used as the working electrode, and Ag/AgCl (sat. KCl) and a platinum wire (approximate surface area: 10 mm^2) were used as the reference and counter electrodes, respectively. 4.0 mL DM (pH 7.8) containing each redox molecule (Figure 2-4) with 10 mM lactate as a sole electron donor was deaerated by bubbling N_2 more than 20 min and added to the electrochemical cell as an electrolyte. The concentration of small redox molecule was set as 2.0 μM unless noted.

The reactor was maintained at a temperature of 30°C and was not stirred during measurements. Cell suspensions with an optical density of 0.1 at 600 nm (OD_{600}) were inoculated in the reactor with the working electrode poised at +0.4 V versus SHE.

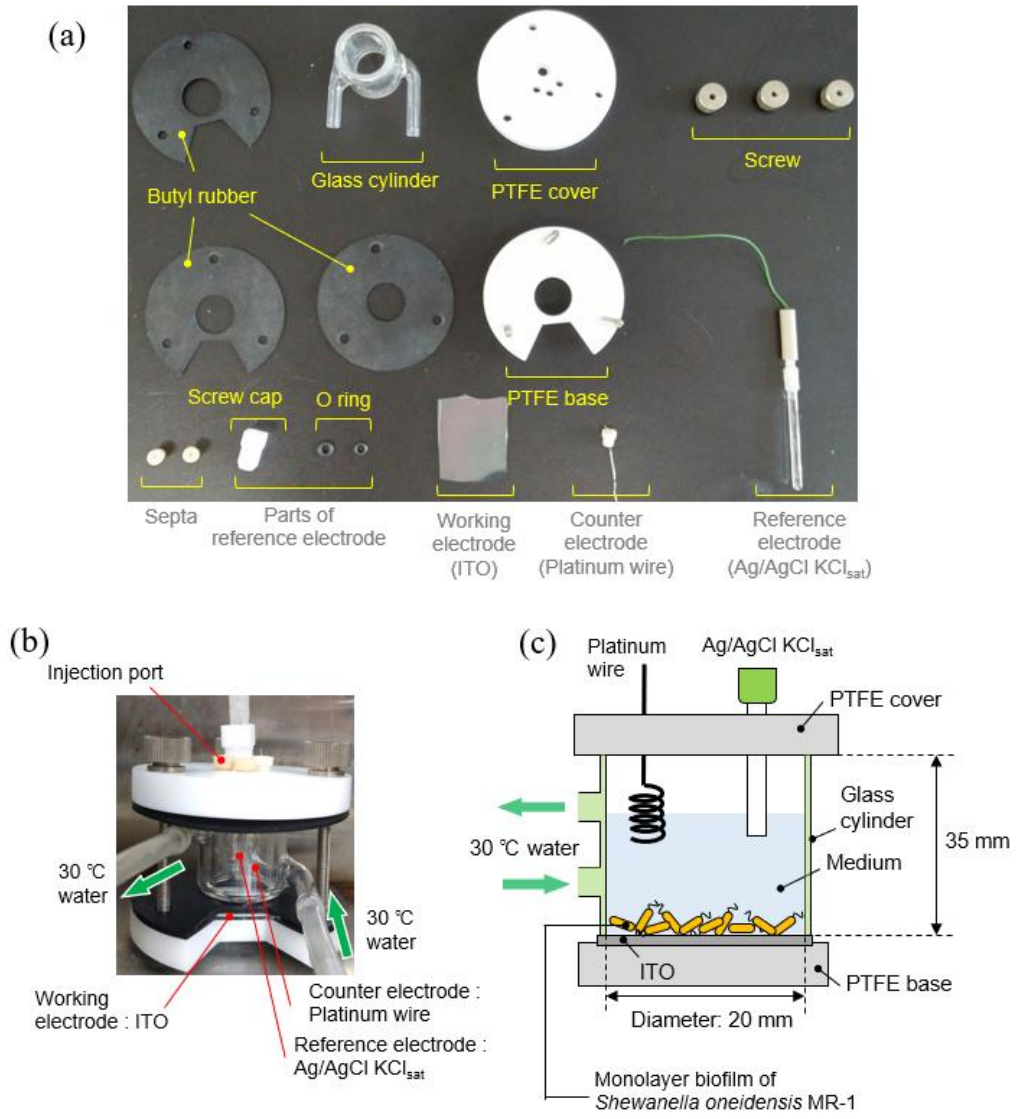

Figure 2-3. Electrochemical reactor used in this study. Photograph of the electrochemical cell before construction (a) and after construction (b). (c) Schematic illustration of the electrochemical reactor.

Voltammetric techniques

Cyclic voltammetry (CV) and differential pulse voltammetry (DPV) was conducted to examine electrochemical property of small redox molecules and a monolayer biofilm of *S. oneidensis* MR-1 using an automatic polarization system (VMP3, Bio Logic). DPV was conducted under the following conditions: 5.0 mV pulse increments, 50 mV pulse amplitude (ΔE_{pa}), 300 ms pulse width, and a 5.0 s pulse period. As a redox potential (E_0) is approximated with the equation $E_0 = E_p + (\Delta E_{pa}/2)$[30], E_0 is estimated to be 25 mV more positive than peak potential (E_p) observed in DPV. In order to correctly determine the peak potential (E_p), half-width ($\Delta E_{p/2}$), and intensity of oxidation peak in DPV, the background current was subtracted by fitting the baseline from regions sufficiently far from the peak and assuming the continuation of a similar and smooth charging current throughout the peak region. The subtraction was performed using the open source program, SOAS [31].

Estimation of current production from *S. oneidensis* MR-1 mediated by diffusion of redox molecules

The catalytic current of lactate oxidation (i_c) mediated by diffusion of redox molecules originates from sequential redox reaction steps and diffusion step as follows [32]:

Step. 1 Incorporation of lactate into *S. oneidensis* MR-1

Step. 2 Reduction of OM *c*-Cyts by metabolic electrons generated by oxidation of lactate

Step. 3 Reduction of redox mediators associated with oxidation of OM *c*-Cyts

Step. 4 Diffusion of reduced mediators from cell to electrode

Step. 5 Electron transfer from reduced mediator to electrode

In this study, we assumed the maximum i_c values (I_c) in the 10 h measurements are limited

by the diffusion of α-AQS between cell and electrode (Step. 4) in the range of 2~800 μM. A linear relationship between I_c and concentration of α-AQS was depicted in Figure 2-11a because current density under diffusion-controlled condition linearly increases with the concentration of diffusive molecule in Fick's laws.

Condition of circular dichroism (CD) spectroscopy in far-UV region

CD spectroscopy was performed on J-1500 (JASCO) CD spectrometer at room temperature (25 ± 1°C). Purified MtrC protein was dissolved in phosphate buffer at pH 7.4 (5.7 mM K_2HPO_4 + 3.3 mM KH_2PO_4). The spectra are collected in a quartz cuvette with path length of 1.0 mm under following conditions: 100 nm min^{-1} scan rate, 0.1 nm data pitch, and 1.0 nm bandwidth.

Estimation of dissociation constant (K_d) for complex formation between OM *c*-Cyts and cofactor

The dissociation constant (K_d) for complex formation between OM *c*-Cyts and a redox cofactor for each redox molecule was estimated using the following equation.

$$K_d = \frac{[P][L]}{[PL]} \qquad (Eq\ 2-1)$$

where [P] is the concentration of OM *c*-Cyts, [L] is the concentration of unbound redox molecule in solution, and [PL] is the concentration of the OM *c*-Cyts complex with the molecule. Because the [PL] associates with the intensity of the oxidation peak current for the bound cofactor in DPV in the concentration range of several μM as demonstrated in Figure 2-6, K_d can be estimated from the peak intensity at different concentration of each redox molecule. When the peak intensity increased about α times with increase of the concentration of redox molecules from $[L]_1$ to $[L]_2$, K_d can be described as below,

assuming the sum of [P] and [PL] is constant throughout the measurement as previously described

$$\alpha - 1 = \mathrm{K_d}\left(\frac{1}{[\mathrm{L}]_1} - \frac{\alpha}{[\mathrm{L}]_2}\right) \quad (\mathrm{Eq}\ 2-2)$$

The K_d for complex formation between OM *c*-Cyts and each cofactor was estimated via linear regressions obtained from the plot of $\alpha - 1$ against $\frac{1}{[\mathrm{L}]_1} - \frac{\alpha}{[\mathrm{L}]_2}$, in the range of 2~10 μM redox molecule.

Quantification of EET capability for each redox molecule, normalized by the amount of complex of OM *c*-Cyts and cofactor molecule

EET capability of each molecule was approximated as the maximum i_c value (I_c) in the 10 h measurements for each 2.0 μM N(5) molecules, normalized by the amount of cofactor-bound OM *c*-Cyts complex. When the produced current is proportionally related to the amount of binding redox cofactor, the rate of EET per unit concentration of complex of OM *c*-Cyts and cofactor, β, can be described as follows.

$$\beta = \frac{I_c}{[\mathrm{PL}]} \qquad (\mathrm{Eq}\ 2-3)$$

where [PL] represents the concentration of the OM *c*-Cyts complex with the molecule. Incorporation of K_d provides:

$$\beta = \frac{([\mathrm{L}]+\mathrm{K_d})I_c}{[\mathrm{L}]([\mathrm{P}]+[\mathrm{PL}])} \quad (\mathrm{Eq}\ 2-4)$$

In order to compare β among cofactors, [L] was set as 2.0 μM and the sum of [P] and [PL] was assumed to be the same among each reactor. Normalization by the β for RF (β_{RF}) provides EET capability for each redox molecule shown below.

$$\text{EET capability} : \frac{\beta}{\beta_{RF}}$$

Calculation of the acid-base equilibrium dissociation constants (pK_a) in redox active molecules.

To compute the absolute pK_a values, a quantum chemical approach was employed [27]. In the deprotonation reaction of the protonated state (AH) to deprotonated state (A^-) in aqueous solution, pK_a is defined as

$$pK_a = \frac{\Delta G_{aq}}{2.303\,RT} \qquad (\mathbf{Eq\ 2-5})$$

where ΔG_{aq} is the free energy difference between AH and ($A^- + H^+$) in water (i.e., $\Delta G_{aq} = G_{aq}(A^-) + G_{aq}(H^+) - G_{aq}(AH)$), R is the gas constant, and T is the temperature. ΔG_{aq} can also be written as

$$\Delta G_{aq} = \Delta G_{gas} + \Delta G_{solv}(A^-) + \Delta G_{solv}(H^+) - \Delta G_{solv}(HA) \qquad (\mathbf{Eq\ 2-6})$$

$$\Delta G_{gas} = G_{gas}(A^-) + G_{gas}(H^+) - G_{gas}(AH) \qquad (\mathbf{Eq\ 2-7})$$

The free energy G_{gas} in vacuum can be obtained, using the following equation;

$$G_{gas} = E_0 + ZPE + \Delta G_{0\rightarrow 298K} \qquad (\mathbf{Eq\ 2-8})$$

where E_0 is the ground-state energy in vacuum, ZPE is the zero-point vibrational energy, and $\Delta G_{0\rightarrow 298K}$ is the thermal vibrational free energy at 298 K. For proton, the free energy $G_{gas}(H^+)$ of 6.28 kcal/mol and $\Delta G_{solv}(H^+)$ of 265.74 kcal/mol[27] were used. To obtain E_0, ZPE, and $\Delta G_{0\rightarrow 298K}$, full geometry optimizations were carried out using the restricted DFT method for the non-radical states and the unrestricted DFT method for the radical states with the B3LYP functional and 6-31g** basis sets, and we used the Jaguar program code [33]. Vibrational frequencies and electrostatic potentials were calculated using the

geometry-optimized structures at the same level of theory. To calculate the ground-state electronic energy E_0, we employed cc-pvqz basis sets for accuracy.

The solvation energy ΔG_{solv} was calculated by solving the Poisson equation using the Solvate module from MEAD [34], where van der Waals radii for H, N, O, Cl, and titratable H^+ are 1.2, 1.4, 1.4, 1.9, and 1.0 Å, respectively; C for $-CH_3$ and $-CH_2-$ groups are 2.0 Å, whereas C for others are 1.2 Å [35]. Atomic partial charges used for ΔG_{solv} were determined by the restraint-electrostatic-potential (RESP) method [36-38].

To evaluate the accuracy of the method, calculatioin of pK_a values was conducted for 28 compounds whose experimentally measured pK_a values are reported (i.e., ref. [39] for H_2O and NH_4^+ and ref. [35] for other compounds) (Figure 2-17). The experimentally measured pK_a values were reproduced with a root-mean square deviation of 0.94 and a maximum error of 1.77 in pK_a units (Figure 2-17).

Estimation of nucleophilicity at N(5) site of cofactor by Hammett substituent parameter (σ parameter)

Because methylene blue (MB), toluidine blue (TB), new methylene blue (NMB), and thionine (TN) have the same backbone except for the substituent at para- and ortho-position to N(5), the electronic characteristics at N(5) site of each molecule can be estimated by the sum of Hammett substituent parameters, σ_{para} and σ_{ortho}[40].

2.1.3 Results and discussion

N(5) in isoalloxazine ring in flavin is essential to bind with OM *c*-Cyts

The author first identified key molecular structure of QFAs to work as potential cofactors bound with OM *c*-Cyts by checking the EET kinetics. Redox molecules not acting as bound cofactors can also accelerate EET by diffusing and shuttling electrons between OM *c*-Cyts and electrode. QFAs acting as shuttling mediator have often been used at several tens or hundreds μM to demonstrate enhancement of EET in microbial electrode systems [19, 41]. In contrast, *S. oneidensis* MR-1 can utilize FMN at micromolar or submicromolar concentrations, leading to a similar rate enhancement of EET [1-2, 22]. The fundamental difference between these two alternatives is that at low concentrations RF binds to an extracellular part of OM *c*-Cyts where it is stabilized as one-electron reduced form of FMN (semi-reduced state, SR) to enhance the rate of EET, while at higher concentrations, RF reduction in solution can proceed via a two-electron reaction [1, 8]. To determine the key molecular structure required for bound cofactor of OM *c*-Cyts, Therefore, the catalytic current produced during lactate oxidation (i_c) by *S. oneidensis* MR-1 was measured in the presence of 12 different QFAs including FMN (Figure 2-4), fixing the concentration at 2.0 μM, in which FMN strongly enhances i_c from *S. oneidensis* MR-1 as a bound cofactor via the formation of a SR intermediate state, but not as a shuttling molecule [1, 19]. Simultaneously, differential pulse voltammetry (DPV) was conducted to electrochemically support the act of bound cofactors by tracking the SR form during i_c generation.

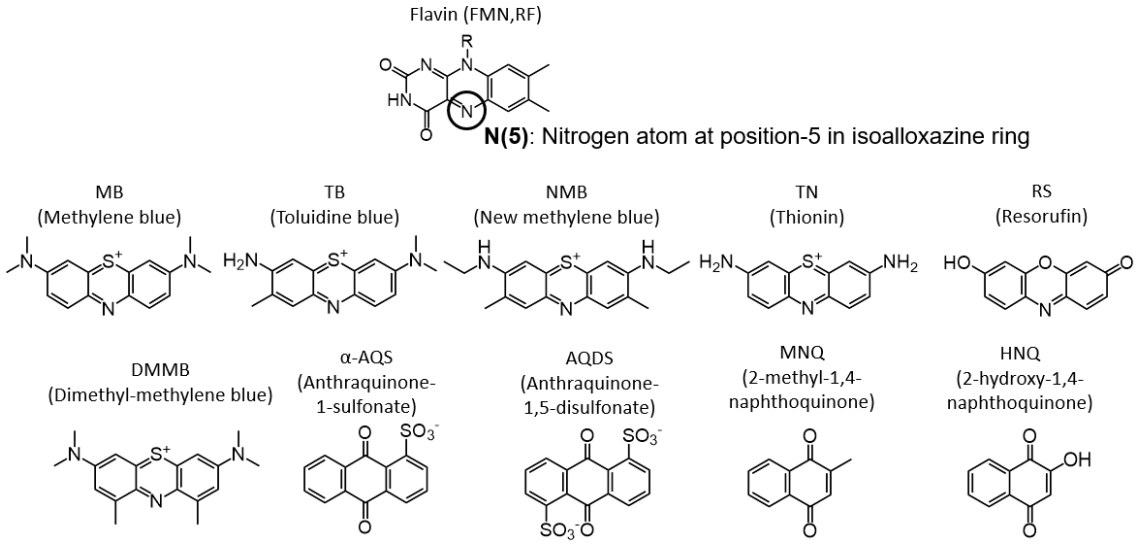

Figure 2-4. The chemical structure of redox molecules used in this study. Nitrogen atom at position 5 (N(5)) in isoalloxazine ring is highlighted in the chemical structure of flavin.

The QFAs with a nitrogen atom in position 5 of the isoalloxazine ring (N(5)) in their polycyclic backbone, all enhanced i_c at a rate equal to, or higher than that seen with FMN at a concentration of 2.0 μM (Figure 2-5a and b), suggesting the act as bound cofactors in OM *c*-Cyts. In accordance with the analysis of i_c measurements, stabilization of these N(5) compounds as SR forms in OM *c*-Cyts was confirmed by the number of electrons involved in the redox reaction of all N(5) molecules via DP voltammetry. After the addition of 0.5, 1.0, 1.5 and 2.0 μM MB (possessing N(5)) to the electrochemical reactor containing *S. oneidensis* MR-1, the peak anodic current was observed at +25 mV vs SHE and increased with increasing MB concentration (Figures 2-6 and 2-7), indicating that the anodic peak at +25 mV is assignable to the redox reaction mediated by MB. The half-width potential ($\Delta E_{p/2}$) for the peak was approximately 120 mV (Figure 2-7), which is close to the characteristics of the one-electron redox reaction in bound FMN with MtrC[1]. In contrast, the two-electron redox reaction of unbound MB in a cell-free system has $\Delta E_{p/2}$ and E_p values of approximately 55 mV and −25 mV, respectively (Figure 2-7). These

redox profiles strongly suggest that MB mediates one-electron redox reactions in the presence of *S. oneidensis* MR-1, similar to the bound FMN cofactor in MtrC[1]. To support the assignment of E_p of +25 mV to the SR state of MB, the effect of the addition of the free radical scavenger, α-tocopherol, on the DPV signals was further examined. The addition of 0.1 mM α-tocopherol showed approximately 10% of decrease in the peak intensity at +25 mV decrease, and subsequently added α-tocopherol further decreased the anodic peak as previously demonstrated in FMN (Figure 2-8)[1]. Consistently with the bound-cofactor model, the anodic DP peak at E_p of +25 mV gradually shifted to negative direction, which suggests that MB also acts as shuttling electron mediator at the concentration of several tens or hundreds μM (Figure 2-9). As the same with MB, other QFAs possessing N(5) showed DP voltammograms consistent with bound-cofactor model (Figure 2-10). The DPV of QFAs in the presence or absence of *S. oneidensis* MR-1 showed redox profiles characteristic of one- or two-electron redox reactions, respectively (Figure 2-10).

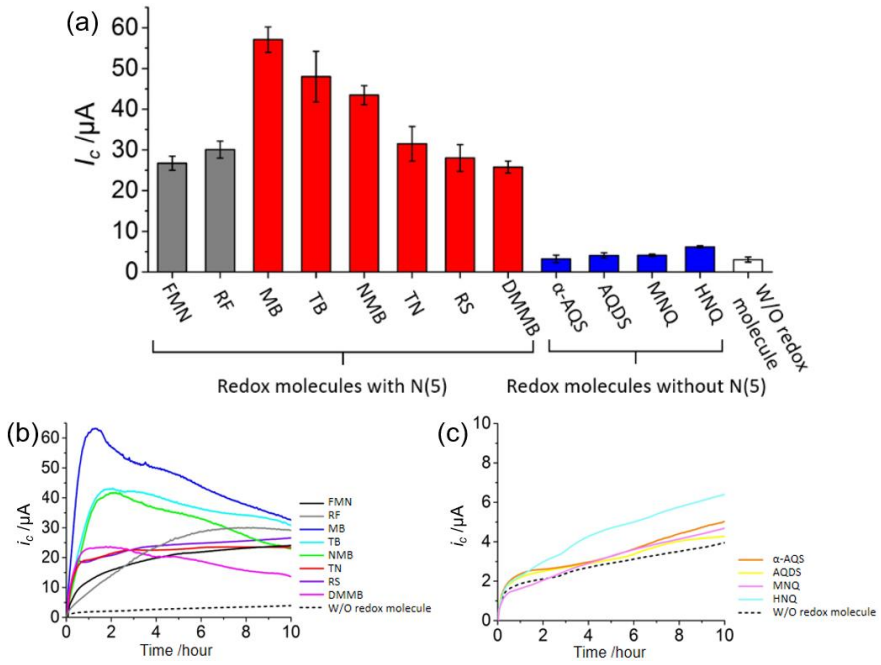

Figure 2-5. (a) The maximum catalytic current of microbial lactate oxidation from *S. oneidensis* MR-1 (I_c) in 10 hours measurement in the presence of each molecule shown in (b) and (c). The I_c in the presence of flavin, flavin analogues, and quinones are represented as gray, red, and blue bars, respectively. The concentration of each redox molecule was set as 2.0 μM. The error bars represent mean ± SEM obtained from at least three times individual experiments in separate reactors. (b, c) Representative time courses of current generation from *S. oneidensis* MR-1 (i_c) in the presence of QFAs.

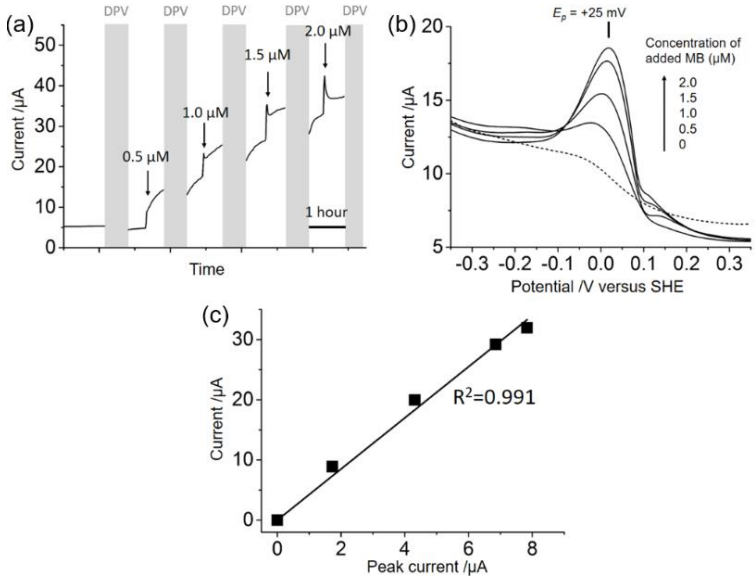

Figure 2-6. (a) Time course for a current production from *S. oneidensis* MR-1. The arrows and the gray regions indicate the timing at which MB was added and DPV was conducted, respectively. (b) DPV for *S. oneidensis* MR-1 containing 0.5, 1.0, 1.5, 2.0 μM MB (solid lines) and in the absence of MB (dotted line), which were obtained during the measurement in (a). (c) Plots of the current production from *S. oneidensis* MR-1 obtained in (a) against the peak current of MB in DPV obtained in (b). Both the current production and the peak current are subtracted by the value obtained in the absence of MB. The square of the correlation coefficients, $R^2 = 0.991$, includes the point of origin.

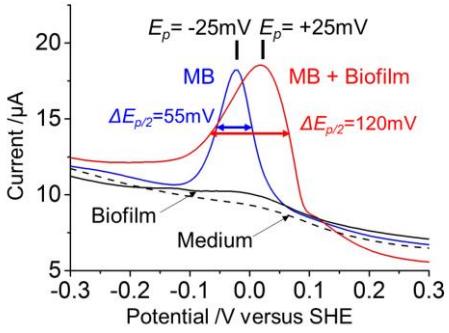

Figure 2-7. A representative data of DPV for DM medium with 10 mM lactate (DM-L, dotted line), DM-L with a monolayer biofilm of *S. oneidensis* MR-1 (black line), DM-L containing 2.0 μM MB (blue line), and DM-L with a monolayer biofilm of *S. oneidensis* MR-1 containing 2.0 μM MB (red line). The half width ($\Delta E_{p/2}$) and the peak potential (E_p) of the oxidation peak for MB in DPV measurement are indicated.

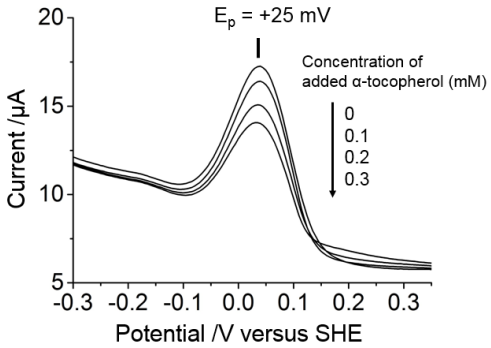

Figure 2-8. The effect of α-tocopherol addition on the DPV for *S. oneidensis* MR-1 on an ITO electrode in the presence of 2.0 μM MB. The concentrations of α-tocopherol added into the reactor are indicated.

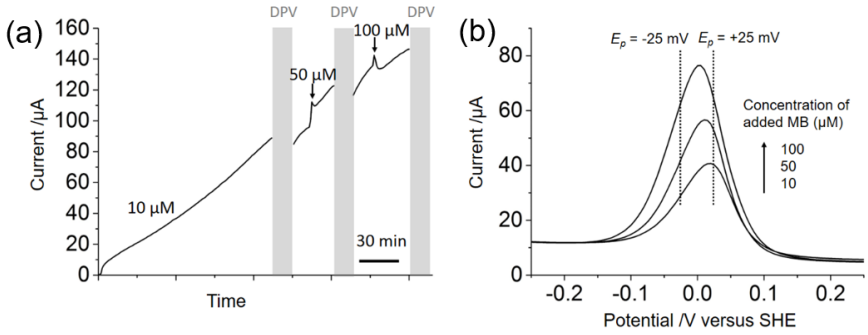

Figure 2-9. (a) Time course for a current production from *S. oneidensis* MR-1. The arrows and the gray regions indicate the timing at which MB was added and DPV was conducted, respectively. (b) DPV for *S. oneidensis* MR-1 containing 10, 50, 100 μM MB, which were obtained during the measurement in (a).

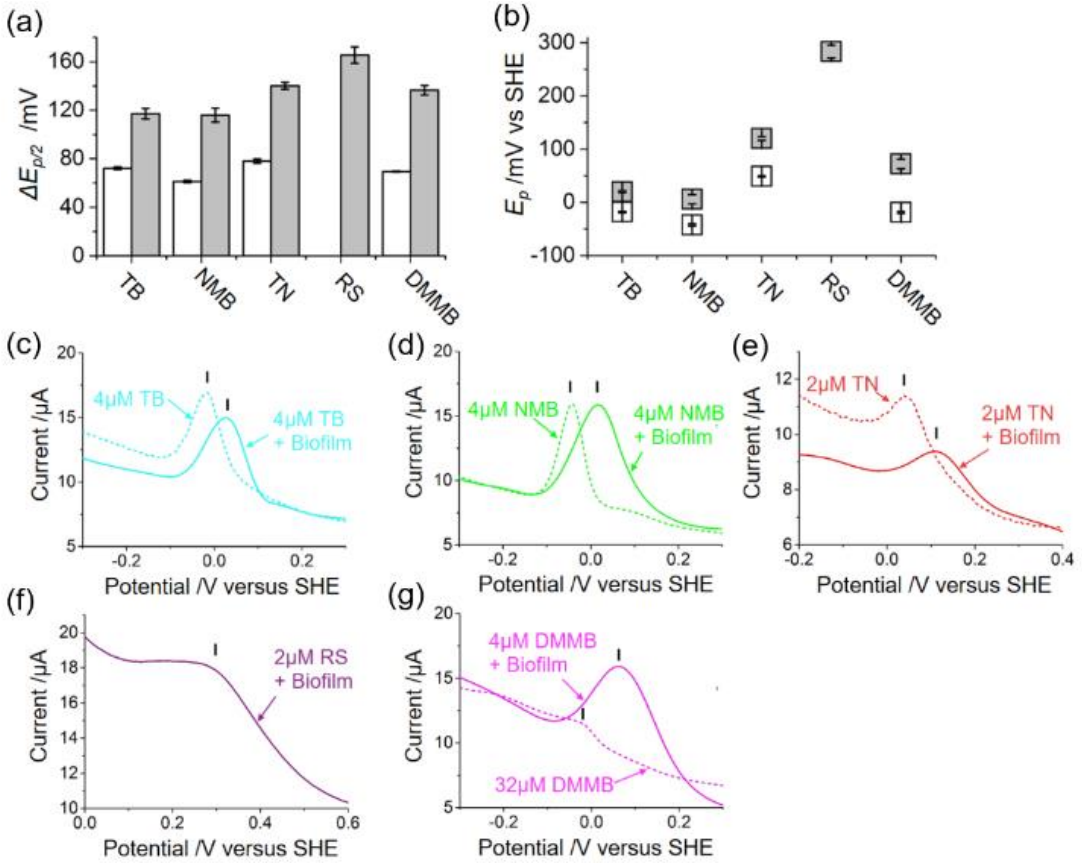

Figure 2-10. DPV for QFAs containing N(5). The half width ($\Delta E_{p/2}$) (a) and the peak potential (E_p) (b) of the oxidation peak for small redox molecules containing N(5) in DPV measurement in cell-free medium (white bar and plot), in the presence of monolayer biofilm of *S. oneidensis* MR-1 (light gray bar and plot). The oxidation peak for RS in cell-free condition was not detected. The standard errors in the $\Delta E_{p/2}$ and E_p are obtained from at least three individual DPV measurements in separate reactors. The representative data of DPV for TB (c), NMB (d), TN (e), RS (f), DMMB (g) in the presence (solid lines) and absence (dotted lines) of a monolayer biofilm of *S. oneidensis* MR-1. The concentration of each molecule and the position of the oxidation peak are indicated.

In contrast, much less enhancement was observed in the presence of the quinones that lack the N(5) atom (Figure 2-5 a and c). For example, α-AQS showed about 4 μA of I_c, which is over 10 times less current of that with MB. When the concentration of α-AQS was increased, the i_c increased following the diffusion kinetics of α-AQS estimated by

Fick's law, and 100 μM α-AQS was required to reach the i_c to the level achieved with 2.0 μM RF (Figure 2-11). This diffusion-limited features of α-AQS are consistent with undetectable SR state formation in DPV analysis (Figure 2-12). In contrast, the same analysis on the N(5)-containing compounds (RF and MB) showed that their electron transport process to the electrode occurred at low concentrations, indicating the N(5) molecules localized at cell-electrode interface and predominantly worked as bound cofactors (Figure 2-13). Taken together, these results suggest that the N(5) atom in their polycyclic backbone is the critical structural feature in the QFAs, allowing them to function in the SR state as a bound cofactor in OM *c*-Cyts.

The formation of the SR state, with the enhancement of electron flow is reminiscent of the SR states observed in electron bifurcation reactions for a number of microbial reactions [42], some of which have now been confirmed with detailed analysis of the crystal structure of the bound flavins in flavodoxins [42-43]. While similar studies have not yet been possible with the OM *c*-Cyts, our data suggest that the N(5) atom in RF and other flavin analogues plays a critical role in binding with OM *c*-Cyts probably through hydrogen bond formation at N(5) of RF in the protein scaffold, similar to that seen with the formation of Sq (SR) state in representative flavodoxins [43].

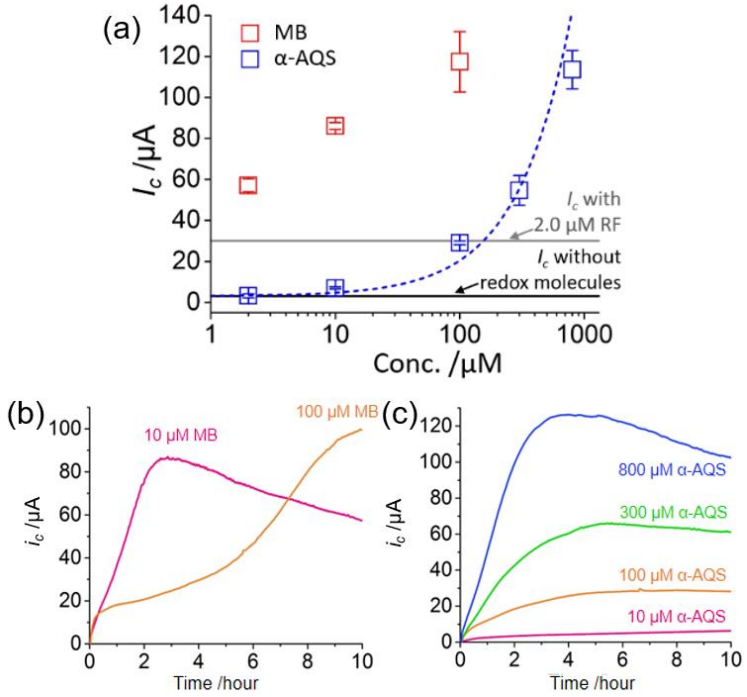

Figure 2-11. (a) The I_c against the concentration of MB or α-AQS in the reactor. Blue dotted line represents the estimated I_c by Fick's laws following the diffusion kinetics of α-AQS between cell and electrode. The error bars represent mean ± SEM obtained from at least three times individual experiments in separate reactors. Representative time courses of i_c in the presence of MB (b) and α-AQS (c) at various concentrations.

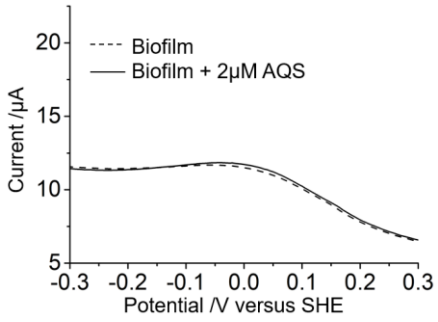

Figure 2-12. The representative data of DPV for a monolayer biofilm of *S. oneidensis* MR-1 in the absence (dotted line) and presence of 2.0 μM α-AQS.

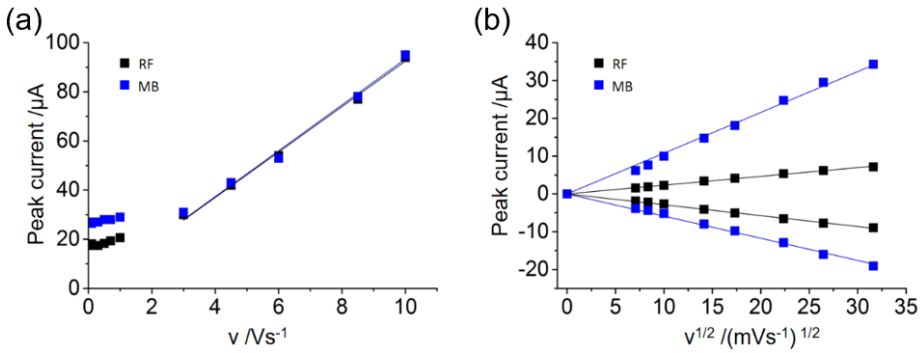

Figure 2-13. (a) Plots of peak current obtained in CV for 4.0 μM RF (black plots) or 4.0 μM MB (blue plots) in the presence of a monolayer biofilm of *S. oneidensis* MR-1 as a function of a scan rate. When the scan rate is fast enough to neglect metabolic current, both plots showed a linear relationship, demonstrating that both RF and MB are adsorbed and localized at the interface between cell membrane and electrode[44]. (b) Plots of peak current obtained in CV for 4.0 μM RF (black plots) or 4.0 μM MB (blue plots) in the absence of a monolayer biofilm of *S. oneidensis* MR-1 as a function of as a function of the square root of a scan rate, demonstrating that both RF and MB proceeds redox reaction as diffusing species without a monolayer biofilm of *S. oneidensis* MR-1.

Comparison of binding machinery between FMN and MB using purified MtrC

In order to confirm that the QFAs containing N(5) binds with MtrC at the same site with that of flavins, circular dichroism (CD) spectra of purified MtrC protein were compared in the presence of FMN or MB. Since the CD spectra at far-UV region correspond with the excitation of electronic transitions in amide groups, the content of secondary structure can be estimated. The CD spectra of MtrC in reduced state changed by the addition of 80 μM FMN, indicating that the binding reaction of FMN with MtrC causes secondary structural changes (Figure 2-14). In order to quantitatively estimate the changes of secondary structure, the CD spectra were analyzed using BeStSel, which improved the accuracy of estimations in the secondary structure content by taking the conformation of β-sheet into account [45-46]. Four types of secondary structures, an α-helix, a β-sheet, a turn

motif, and others (including random coil), were identified, and their contents are summarized in Table 2-1. Notably, the content of β-sheet decreased upon the binding reaction. Considering that the binding site is proposed to be the domain I or III composed of β-sheet[22, 47], the decrease of β-sheet content indicates that the binding reaction causes local conformational change around the binding site. The change was also observed in the content of α-helix, which is located not around the binding site but in domain II and IV including 10 hemes in MtrC, indicating that the structural change caused by FMN is not limited near the binding site, but also whole-protein including electron transfer pathway. Addition of MB also showed the same tendency, decrease of both α-helix and β-sheet. Furthermore, MB changed the twisting angle of β-sheet in a same way with FMN. In both cases, the content of relaxed β-sheet decreased, and instead, the ratio of left-twisted β-sheet increased. The same tendency of secondary structural change in both the content and conformation strongly suggest that the binding reaction of MB occurs in a same manner with FMN. The content of both α-helix and β-sheet lost by binding reaction was smaller in MB than FMN, probably suggesting that not only the N(5) but also other part of FMN is partly associated with the binding reaction as demonstrated in flavodoxin[43].

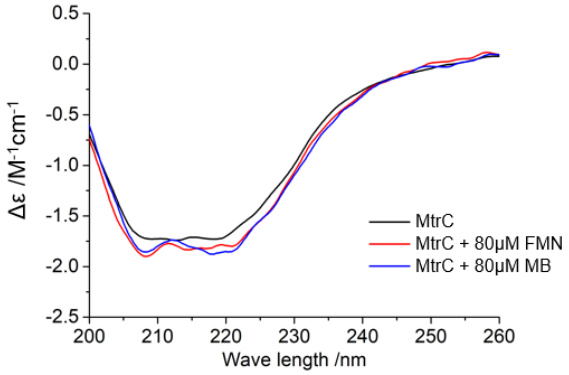

Figure 2-14. CD spectra of purified MtrC protein reduced by 0.7 mM $Na_2S_2O_4$. Red and blue lines were obtained by addition of 80 μM of FMN or MB to the reduced MtrC, respectively. Those spectra were obtained after subtraction by that of 0.7 mM $Na_2S_2O_4$ and FMN or MB. The Δε was divided by the number of amino acids in the MtrC protein. The maintenance of reduced state after addition of FMN or MB was confirmed by CD spectra in the Soret region.

Table 2-1. Estimation of secondary structure of reduced MtrC*

	Reduced MtrC /%	Reduced MtrC + 80 μM FMN /%	Reduced MtrC + 80 μM MB /%
α-helices	8.4	6.2	7.4
β-sheet	31.8	27.3	28.8
Turn	13.2	14.9	14.2
Others including random coil	46.6	51.6	49.6
Left-twisted β-sheet	4.4	5.9	5.8
Relaxed β-sheet	13	4.6	6.8
Right-twisted β-sheet	12.4	13.1	12.5
Parallel β-sheet	2.1	3.7	3.7

*Estimated by a software, BeStSel [45-46].

Correlation of EET kinetics with pK_a suggests rate limitation by protonation at N(5)

Given that the flavins receive electrons from the heme groups of OM *c*-Cyts, the N(5) molecules with more positive redox potential should be more favorable for the

acceleration of EET in the experimental condition (+0.4 V versus SHE) [1, 5]. To this end, it is clear from the data shown in Figure 2-5 that the level of enhancement is not the same for all of N(5)-containing compounds. However, the relationship between i_c values produced and their redox potentials (E_0) was different from what was predicted (Figure 2-15a). EET capability was approximated as the max i_c value (I_c) in the 10 h measurements for each of the N(5) molecules per the concentration of OM *c*-Cyts complex with bound cofactors (Figure 2-16 and Table 2-2) and their redox potential was estimated by DPV (Figures 2-7 and 2-10). As shown in Figure 2-15a, while the rate of EET increased with the redox potential for those N(5) molecules with redox potentials below about 50 mV versus SHE, this tendency diminished with N(5)-containing molecules with higher redox potentials. The cut off was almost identical with the redox potential of OM *c*-Cyts [E_0 = ~40 mV versus SHE][5]. The N(5) molecules with redox potential over 50 mV accept electrons from OM *c*-Cyts with thermodynamically favorable down-hill reaction, suggesting that the rate suppression might be caused by some other process. Given that the SR species of RF is known to form a hydrogen bond at the N(5) site with flavodoxin associated with electron transfer reaction [43], the author reasoned that the rate of EET in bound RF with OM *c*-Cyts could be limited by the rate of protonation reaction of the N(5). Thus, it was hypothesized that the N(5) atom is not only critical for the stabilization of SR state, but also its proton uptake capability may be rate limiting for EET.

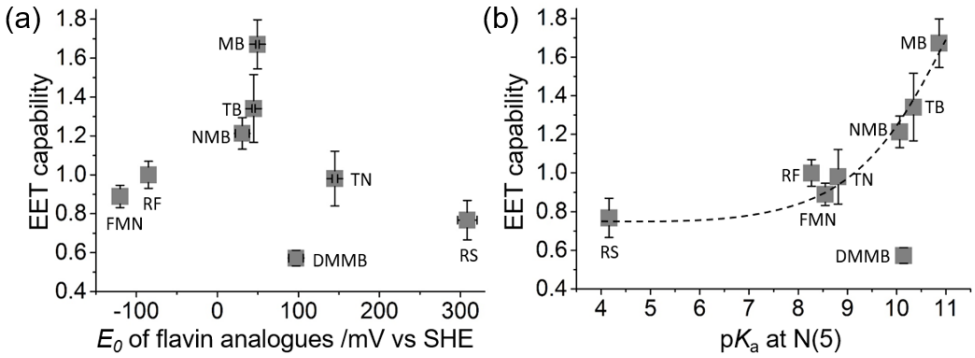

Figure 2-15. Correlation between current production from *S. oneidensis* MR-1 and redox property of QFAs. Plots of the EET capability of *S. oneidensis* MR-1 with each N(5) molecule as a function of the redox potential (E_0) of each cofactor (a) and pK_a at N(5) in one-electron reduced form (b). The E_0 of each cofactor, bound with OM *c*-Cyts, were obtained by DPV (Figures 2-7 and 2-10), except for FMN and RF, of which E_0 were quoted from refs.[1-2]. The pK_a at N(5) were calculated by quantum chemical approach using 28 compounds as reference (Figure 2-17). Note that pK_a at N(5) of FMN and RF were quoted from ref.[48]. The error bars represent mean ± SEM from at least three individual experiments. Dotted line is a guide to the eye.

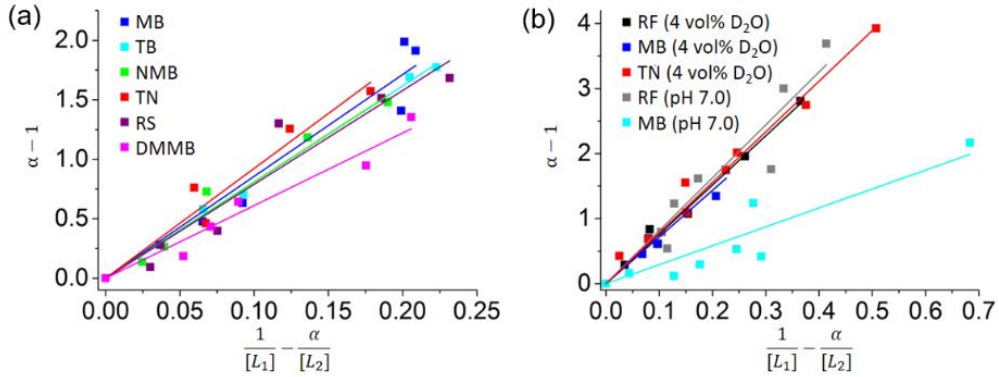

Figure 2-16. Estimation of dissociation constant (K_d) for complex formation between OM *c*-Cyts and cofactor. K_d for complex formation between OM *c*-Cyts and each cofactor was estimated via linear regressions, setting $\frac{1}{[L]_1} - \frac{\alpha}{[L]_2}$ and $\alpha - 1$ as horizontal and vertical axis, respectively as described in eq. 2-2. (a) K_d for complex formation at pH 7.8. The linear regressions are as follows; MB: b = 8.560a, R^2 = 0.939; TB: b = 8.079a, R^2 = 0.997; NMB: b = 8.071a, R^2 = 0.949; TN: b = 9.227a, R^2 = 0.949; RS: b = 7.890a, R^2 = 0.927; DMMB: b = 6.013a, R^2 = 0.958. (b) K_d for complex formation at pH 7.0 or in the presence of 4% (v/v) D_2O at pH 7.8. The linear regressions are as follows; RF with 4 vol% D_2O: b = 7.579a, R^2 = 0.987; MB with 4 vol% D_2O: b = 7.172a, R^2 = 0.972; TN with 4 vol% D_2O: b = 7.781a, R^2 = 0.977; RF at pH 7.0: b = 8.137a, R^2 = 0.906; MB at pH 7.0; b = 2.910a, R^2 = 0.854. Each K_d with standard error is summarized in Table 2-2.

Table 2-2. Quantification of EET capability with each redox molecule normalized by the amount of cofactor-bound OM *c*-Cyts

	Maximum current production with 2.0 μM molecule (I_c) /μA	Dissociation constant (K_d) /μM	EET capability
FMN	26.73±1.72	10*	0.89±0.06
RF	30.07±2.08	10*	1.00±0.07
MB	57.15±3.12	8.56±0.55	1.67±0.13
TB	48.03±6.22	8.08±0.12	1.34±0.17
NMB	43.47±2.32	8.07±0.41	1.21±0.08
TN	31.51±4.24	9.23±0.57	0.98±0.14
RS	28.08±3.30	7.89±0.59	0.77±0.10
DMMB	25.78±1.46	6.01±0.34	0.57±0.04

*Values from [1, 3]

To test this prediction, the author compared pK_a of the N(5) with the EET capability for each N(5)-containing quinone. The pK_a at the N(5) site in the SR state was calculated using a quantum chemical approach (Figure 2-17) [27-28]. As shown in Figure 2-15b, the larger EET capability was observed with the molecules having higher pK_a at the N(5) site in the SR form. Since the N(5) with a higher pK_a rapidly accepts a proton, the increase of current production by higher pK_a suggests that the protonation reaction at N(5) in one-electron reduced cofactor controls the EET kinetics. Consistent with this, the increase of nucleophilicity at N(5) estimated by Hammett substituent parameters, σ_{para} and σ_{ortho}, increased the current production (Figure 2-18 and Table 2-3). Furthermore, introduction of a methyl group near to the N(5) suppressed the EET capability by about 65% likely due to the prevention of protonation at N(5) (Figure 2-15b). In contrast, there was no clear relationship between the current production and pK_a of any of the two-electron reduced forms (Figure 2-19).

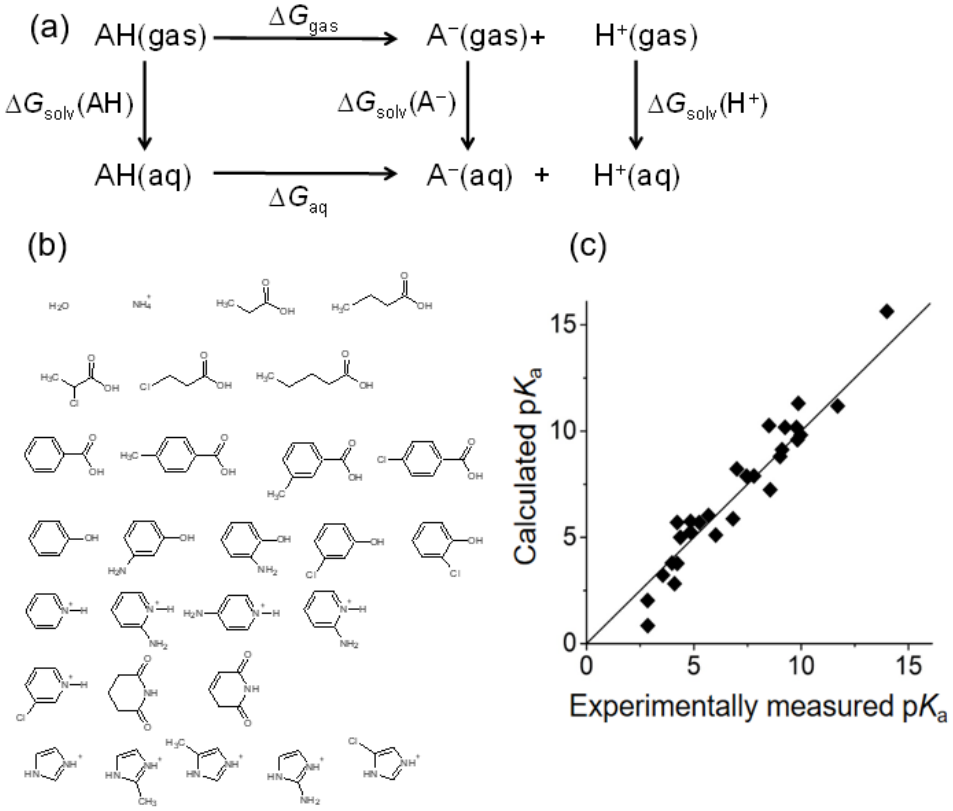

Figure 2-17. (a) Thermodynamic cycle for obtaining ΔG_{aq}, according to eqs. 2-6 and 2-7. (b) 28 compounds evaluated in Figure c (c) Correlation between experimentally measured and calculated pK_a values of 28 compounds in (b). The root-mean-square deviation and the maximum error were 0.94 and 1.77 in pK_a units, respectively

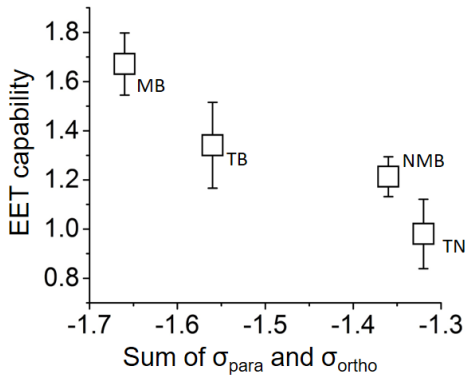

Figure 2-18. Correlation of the EET capability and the nucleophilicity at N(5) site, estimated by the sum of the Hammett σ_{para} and σ_{ortho} parameters for MB, TB, NMB, and TN. The molecule possessing more negative σ shows higher nucleophilicity at N(5). Hammett σ_{para} and σ_{ortho} parameters of each substituent and numeric data for the sum of σ_{para} and σ_{ortho} are provided in Table 2-3.

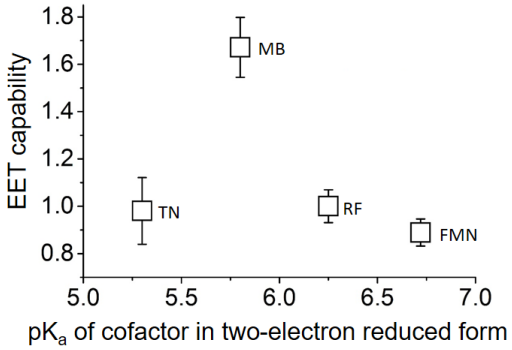

Figure 2-19. Plots of the EET capability of *S. oneidensis* MR-1 with each N(5) molecule as a function of the pK_a of cofactor in two-electron reduced form. The pK_a of each cofactor was obtained by refs. [48-50].

Table 2-3. Hammett parameter (σ_{para} and σ_{ortho}) and the sum of σ_{para} and σ_{ortho} ($\Sigma\sigma$) to N(5) site of MB, TB, NMB, and TN

	σ_{para}	σ_{ortho}	$\Sigma\sigma$
MB	-1.66	0	-1.66
TB	-1.49	-0.07	-1.56
NMB	-1.22	-0.14	-1.36
TN	-1.32	0	-1.32

σ_{para} for NH_2: -0.66; σ_{para} for $N(CH_3)_2$: -0.83; σ_{para} for $NH(C_2H_5)$: -0.61; σ_{ortho} for CH_3: -0.07

2.1.4 Conclusion

The results presented here demonstrated that the variation in the enhancement of EET of *S. oneidensis* MR-1 by flavins and flavin analogues is due to variation in the ability of these electron carriers to bind with OM *c*-Cyts, and is also a function of their proton uptake capability (Figure 2-2). Given that the redox potential and pK_a of N(5) atom in the polycyclic backbone is potentially tunable, the flow of protons, could well be a key control point for the regulation of EET. Whether similar activities are also involved with uptake of electrons (and protons) via EET is now under investigation [51-52].

2.2

Coupled proton transport limits the rate of extracellular electron transport

2.2.1 Introduction

The iron-reducing bacterium, *S. oneidensis* MR-1, is capable of moving electrons from the respiratory chain to the cell exterior by a process called EET [53]. Respiratory electrons are transported extracellularly via OM *c*-Cyts [54], which have implications for iron and manganese circulation in nature [53] and for microbial technologies such as microbial fuel cells [55] and electrode biosynthesis [56]. Direct interfacial electron transport to extracellular solids is terminated either by a covalent heme center in OM *c*-Cyts or a non-covalently bound flavin Sq cofactor with OM *c*-Cyts (Figure 2-20) [1-2, 6, 8, 22, 57]. While the kinetic aspect has been the focal point of EET process, however, the mechanisms underlying the flavin-mediated EET enhancement has remained questionable due to the limited approaches to investigate the OM *c*-Cyts/electrode interface using intact cell. In chapter 2-1, it was revealed that the pK_a value as well as the redox potential of flavin Sq is critical for flavin-mediated EET kinetics by means of molecular design of 10 flavin analogues, suggesting that the protonation reaction at N(5) in flavin dictates the rate of EET.

Thus, in chapter 2-2, it was hypothesized that proton transport reaction is coupled with EET through OM *c*-Cyts, and flavin enhances the rate of EET by acceleration of coupled proton transport. To test this hypothesis, the solvent kinetic isotope effect (KIE) on EET through OM *c*-Cyts was compared with that of flavin-mediated EET, because the extent of the KIE reflects the molecular characteristics of a rate-limiting proton transfer

process. Furthermore, the effect of pH change on EET kinetics was tested to clarify the significance of proton transport on EET process. In addition, the author discussed about the relationship of the EET-coupled proton transport on biological energy production (PMF generation) with implications to bacterial ecophysiology.

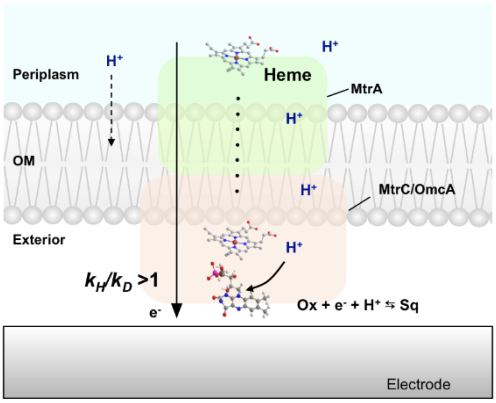

Figure 2-20. Schematic illustration of extracellular electron transport via outer-membrane flavocychrome complex in *S. oneidensis* MR-1 and the non-covalent flavin cofactor that involves in a rate-limiting proton transport. Ox and Sq represents fully oxidized flavin and semiquinone, respectively.

2.2.2 Methods

Formation of a monolayer biofilm of *S. oneidensis* MR-1 on ITO electrode

S. oneidensis MR-1 was grown as described in chapter 2-1, and the electrochemical experiments were conducted using the same reactor with chapter 2-1. For the formation of a monolayer biofilm, 4.0 mL of DM (pH 7.8) with 10 mM lactate was added into the electrochemical cell as an electrolyte and was deaerated by bubbling with N_2 for more than 20 min. Cell suspension of *S. oneidensis* MR-1 with OD_{600} = 0.1 was cultivated in the reactor with the working electrode poised at +0.4 V versus SHE in the presence of 10 mM lactate as a sole electron donor at 30°C with no agitation for 25 hours. The formation of a monolayer biofilm was confirmed by in situ confocal fluorescence microscopy as previously described [5].

Addition of deuterated water (D_2O) to the electrochemical reactor in the presence of a monolayer biofilm of *S. oneidensis* MR-1

After formation of a monolayer biofilm of *S. oneidensis* MR-1 on ITO electrode, the supernatant solution was refreshed with anaerobic DM with 10 mM lactate containing either 2.0 μM methylene blue (MB) or 2.0 μM thionine (TN) at pH 7.8. Then D_2O was sequentially added to the reactor at final concentrations ranging from 0.5 % to 4% (v/v).

Quantification of the kinetic isotope effect (KIE) on EET, normalized by the amount of cofactor-bound OM *c*-Cyts complex

The extent of kinetic isotope effect (KIE) on EET was evaluated from the difference between the current production 10 minutes after the addition of 4 % (v/v) D_2O and H_2O

($i_c(H_2O)/i_c(D_2O)$) to the electrochemical system in the presence of a monolayer biofilm of *S. oneidensis* MR-1, followed by normalization of the amount of cofactor-bound OM *c*-Cyts complex using dissociation constant (K_d) in the presence of 4% D_2O and in the absence of D_2O as below:

$$\mathrm{KIE} = \frac{i_c(\mathrm{H_2O})}{i_c(\mathrm{D_2O})} \cdot \frac{[\mathrm{PL}]_\mathrm{D}}{[\mathrm{PL}]_\mathrm{H}} \quad (\mathrm{Eq}\ 2-9)$$

where $[PL]_D$ and $[PL]_H$ show the concentration of the OM *c*-Cyts complex with cofactor in the presence of 4% (v/v) D_2O and in the absence of D_2O, respectively. [PL] can be described from the definition of dissociation constant (K_d) (Eq. 2-1) as follows.

$$[\mathrm{PL}] = \frac{[\mathrm{P}]_\mathrm{total}[\mathrm{L}]}{\mathrm{K_d}+[\mathrm{L}]} \quad (\mathrm{Eq}\ 2-10)$$

where $[P]_{total}$ is the sum of the concentration of OM *c*-Cyts unbound by cofactor and OM *c*-Cyts bound with cofactor, [L] is the concentration of unbound redox molecule in solution. Assuming that $[P]_{total}$ is constant before and after the addition of D_2O, the KIE can be described as follows.

$$\mathrm{KIE} = \frac{i_c(\mathrm{H_2O})}{i_c(\mathrm{D_2O})} \cdot \frac{\mathrm{K_d}(\mathrm{H_2O})+[\mathrm{L}]}{\mathrm{K_d}(\mathrm{D_2O})+[\mathrm{L}]} \qquad (\mathrm{Eq}\ 2-11)$$

$K_d(D_2O)$ and $K_d(H_2O)$ represent the dissociation constant in the presence of 4% (v/v) D_2O and in the absence of D_2O, respectively. [L] was set as 2.0 μM for KIE experiment.

Monitoring the current production from *S. oneidensis* MR-1 in several pH

After formation of a monolayer biofilm of *S. oneidensis* MR-1 on ITO electrode, the supernatant solution was refreshed with anaerobic DM with 10 mM lactate containing 2.0 μM riboflavin (RF), 2.0 μM methylene blue (MB), or 100 μM 2-hydroxy-1,4-naphthoquinone (HNQ), whose pH was adjusted at 8.17. The micro-electrode of the pH meter (D-73, pH meter, Horiba, Japan) was directly introduced into the electrochemical

reactor. HCl was added into the reactor to change the pH.

Protein Content Assay

To determine total protein content, ITO electrodes with attached cells after 24 h of I_c measurements were gently washed once with an aqueous buffer solution consisting of 4.3 mM Na_2HPO_4 and 1.4 mM KH_2PO_4 (pH 7.5). The washed electrodes were carefully broken into small pieces, placed in a 2 ml tube containing 300 μl phosphate buffered saline (PBS), and then vortexed for 5 min. The protein concentration was determined using a Micro BCA Protein Assay Kit (Pierce) according to the manufacturer's instructions.

Fluorescence measurements

Flavin concentration in the cell suspensions was quantified by fluorescence in supernatant after centrifugation of cell suspension with an optical density of 1.0 at 600nm (OD_{600}) in the presence of polymyxin B (PMB) and 10 mM lactate as a sole electron donor. We performed fluorescence measurement experiment two times separately and shown data is representative one. Fluorescence measurement was performed in a plate reader (SH-9000Lab, Corona-el). The wavelength of excitation and emission was 445nm and 525nm, respectively.

2.2.3 Results and discussion

Flavin changes the kinetics and pathway of proton transport coupled with EET through OM *c*-Cyts

To test the role of proton transfer in the kinetics of EET, the kinetic isotope effect (KIE) of deuterium on EET was examined using a 3-electrode electrochemical system with an ITO electrode. To utilize the KIE to examine whether proton transport determines the rate of EET via OM *c*-Cyts *in vivo* measurements, the rate of EET via the OM *c*-Cyts must limit or reflect the catalytic current (i_c) production. For this reason, the experiments were conducted in an electrochemical system containing sufficient lactate as an electron donor and under pH and temperature conditions that support oxidative lactate metabolism, thereby limiting the i_c to EET via OM *c*-Cyts, as confirmed in previous reports [1-2, 58]. The measurements were conducted following the electrochemical cultivation of *S. oneidensis* MR-1 as a monolayer biofilm on an ITO electrode, poised at +0.4 V [vs. the standard hydrogen electrode (SHE)]. The supernatant solution in the electrochemical cell was refreshed before the addition of deuterated water (D_2O) to maximize the cellular metabolic activity for lactate oxidation and to minimize the involvement of motile bacteria.

Upon the addition of D_2O to the electrochemical system, the i_c sharply decreased within 10 s; the further addition of D_2O, up to a final concentration of 4%, resulted in a further decrease in the i_c, whereas almost no reduction in the i_c was observed following the addition of H_2O (Figure 2-21 a and d). To confirm that the large current reduction was not attributable to the slower diffusion of deuterium ions compared to protons, the author examined the effect of D_2O on I_c in the presence of anthraquinone-1-sulfonate (α-AQS),

which functions as a shuttling mediator for the transport of both electrons and protons that are in the electron transport chain and are located in the inner membrane or periplasm [59]. In the presence of 100 μM α-AQS, the i_c was limited by diffusion (Figure 2-22) and the addition of D_2O had minimal impact on the i_c (Figure 2-21b and d), indicating that the potential delay of the upstream reactions by deuterium ions did not cause the large KIE. Based on these results, the large KIE could be attributed to the EET process via OM *c*-Cyts, indicating that the EET is limited by proton transport. It is notable that even 0.5 % D_2O largely decreased i_c, and the magnitude was gradually buffered in higher concentration of D_2O (Figure 2-21d). This non-linear bowed-shaped relationship of i_c-D_2O concentration is characteristics of multiple protonic sites related with rate-limiting proton transfer [60-62]. Therefore, it is plausible that the OM *c*-Cyts possess hydrogen bond networks related with rate-limiting proton transfer.

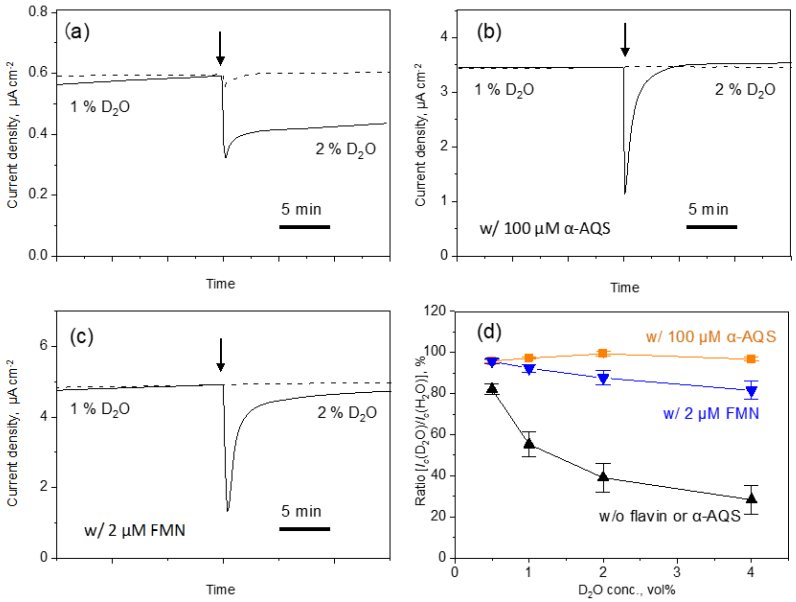

Figure 2-21. Time versus current production (i_c) for a monolayer biofilm of *S. oneidensis* MR-1 in an electrochemical system containing 10 mM lactate (a), and additionally 100 μM anthraquinone-1-sulfonate (α-AQS) (b), or 2 μM flavin mononucleotide (FMN) (c). The arrow indicates the time of the addition of D_2O (solid line) or H_2O (dotted line). The data corresponding to the dotted line were normalized to the data point just prior to the addition of D_2O in the solid line data. (d) The ratio of i_c before and 10 min after the addition of D_2O versus the D_2O concentration up to 4% (v/v). The data are shown as the means ± standard error of the mean (n > 3).

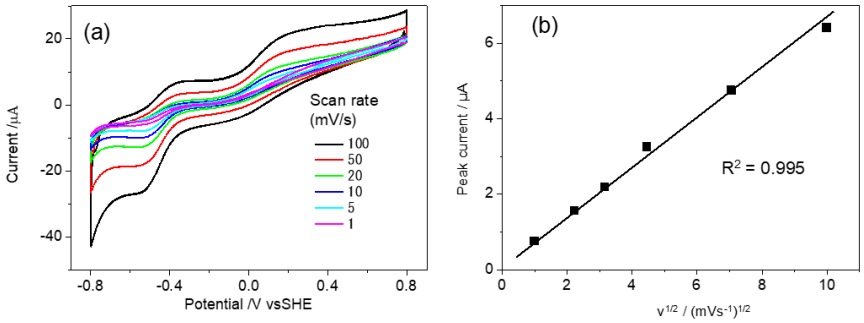

Figure 2-22. (a) Cyclic voltammograms (CV) of the cell-attached electrode for *S. oneidensis* MR-1 at 30 ℃ in the presence of 100 μM α-AQS measured at scan rates (ν) of 1, 5, 10, 20, 50, and 100 mVs^{-1} (pH 7.8). (b) Plot of peak current in the CVs in panel (a) as a function of the square root of ν. The same trend was observed in more than two independent experiments.

The observation that proton transport limits the rate of EET is in accordance with the acceleration of EET via OM *c*-Cyts in the presence of flavins, RF or FMN. The Sq state of these non-covalently bound cofactors in OM *c*-Cyts [1-2, 22] have an unfavorable energy level for accepting electrons from heme redox centers. Because the bound Sq cofactor has a more negative redox potential than heme cofactors in OM *c*-Cyts, the rate of electron transport should not be enhanced compared with the highly efficient electron transport circuit of hemes in the OM *c*-Cyts complex. Therefore, it is likely that the association of flavins with OM *c*-Cyts, i.e., the formation of an OM flavocytochrome complex, enhances the rate of proton, not electron transport, resulting in an apparent enhancement in the rate of EET. To directly test the hypothesis that flavin-bound OM *c*-Cyts operate with a rate-limiting proton pathway, the KIE on EET by the *S. oneidensis* MR-1 strain in the presence and absence of flavins was examined, because the extent of the KIE reflects the molecular characteristics of a rate-limiting proton transfer pathway. In contrast to the effects of α-AQS, in the presence of 2.0 μM FMN, the i_c was significantly reduced following the addition of D_2O, but the KIE in the presence of FMN was largely reduced compared with that in the absence of FMN (Figure 2-21c and d), indicating that the binding of FMN by OM *c*-Cyts altered the rate-limiting proton transport pathway. Since the reduction of the bound FMN (Ox/Sq) is coupled with protonation at physiological pH as described in chapter 2-1 [48], the protonation of bound FMN might alter the proton transport kinetics associated with EET. The relationship of i_c-D_2O concentration was still non-linear bowed-shaped in the presence of FMN, which suggests the existence of multiple protonic sites in FMN-bound OM *c*-Cyts [60-62]. Therefore, the result indicates that protons are transported inside flavin-bound OM *c*-Cyts, and the kinetics and pathway of proton transport in OM *c*-Cyts are altered by bound Sq

flavin.

To support the alteration of proton transport pathway by bound flavin, the involvement of protonation at the N(5) site in rate-limiting proton transport through flavocytochromes was examined by the KIEs in the presence of other redox molecules containing N(5). The extent of the KIE on the rate of EET was evaluated from the difference between the current production 10 minutes after the addition of D_2O and H_2O ($i_c(H_2O)/i_c(D_2O)$) to the electrochemical system, followed by normalization of the amount of cofactor-bound OM *c*-Cyts complex using dissociation constant (K_d) in the presence of 4% D_2O and in the absence of D_2O (Figure 2-16). The addition of D_2O decreased the current production within 10 s in the presence of TN, and further addition of D_2O up to a final concentration of 4% resulted in a further decrease, whereas the current inversely increased in the presence of MB by D_2O addition (Figure 2-23). However, upon the normalization by K_d, KIE for the complex of OM *c*-Cyts and MB became normal KIE value of 1.06 ± 0.07, and RF and TN showed KIE as 1.35 ± 0.03 and 1.46 ± 0.10, respectively (Figure 2-24a, b and Table 2-4). The large KIE difference observed with the different cofactors is consistent with the involvement of the N(5) site as proton transport pathway, suggesting that bound flavin accelerates EET by alteration of proton transport kinetics.

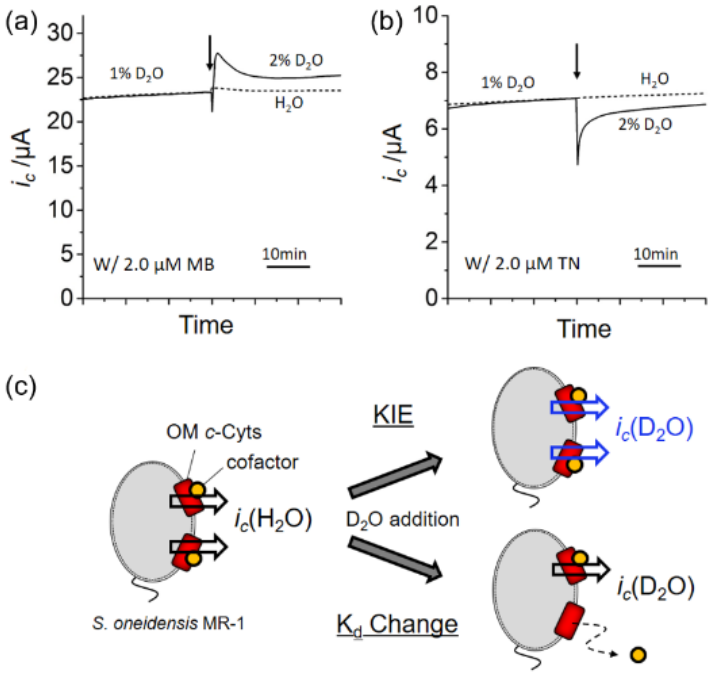

Figure 2-23. Effect of deuterium ion on extracellular electron transport. The representative time course for the current production from a monolayer biofilm of *S. oneidensis* MR-1 in the presence of 2.0 μM MB (a) and TN (b). The arrow indicates the point for addition of D_2O (solid line) or H_2O (dotted line). The data corresponding to the dotted line was normalized to the data point just prior to the addition of D_2O in the solid line data. (c) Schematic illustration of D_2O effect on EET. D_2O alter the i_c by the kinetic isotope effect (KIE) in the cofactor-bound OM *c*-Cyts (upper image) and K_d change (lower image). Therefore, the observed $i_c(D_2O)$ should be normalized by K_d to clarify the KIE in the cofactor-bound OM *c*-Cyts.

Table 2-4. Quantification of kinetic isotope effect (KIE) on EET via single-Cyts-cofactor complex for 4.0 vol% D_2O

	$i_c(H_2O)/i_c(D_2O)$	Dissociation constant in the presence of 4.0 vol% D_2O ($K_d(D_2O)$) /μM	KIE on EET via single-Cyts-cofactor complex
RF	1.08±0.01	7.58±0.22	1.35±0.03
MB	0.92±0.02	7.17±0.32	1.06±0.07
TN	1.27±0.05	7.78±0.23	1.46±0.10

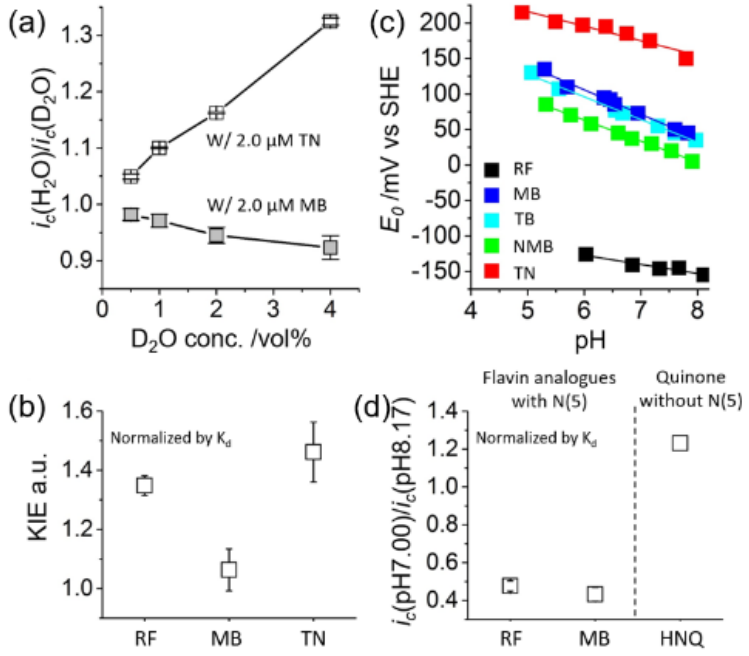

Figure 2-24. Effect of deuterium ion and pH change on extracellular electron transport kinetics in the presence of redox molecules. (a) The effect of D_2O addition on i_c in the presence of 2.0 μM MB or TN under subtoxic concentration (up to 4% v/v). The error bars represent mean ± SEM obtained from three individual experiments in separate reactors. (b) The KIE on EET per unit concentration of cofactor-bound OM *c*-Cyts complex in 4% (v/v) D_2O. The error bars represent mean ± SEM. (c) The redox potential (E_0) of bound cofactor (RF, MB, TB, NMB, and TN) determined by DPV as a function of pH in bulk solution. The slopes for the plots are as follows: RF: −13 mV pH^{-1}; MB: −34 mV pH^{-1}; TB: −32 mV pH^{-1}; NMB: −30 mV pH^{-1}; TN: −21 mV pH^{-1}. (d) The effect of pH decrease in bulk solution on i_c in the presence of 2.0 μM RF, 2.0 μM MB and 100 μM HNQ. The pH was altered from 8.17 to 7.00 ± 0.05. Note that the i_c is normalized by unit concentration of cofactor-bound OM *c*-Cyts in the case of RF and MB. The error bars represent mean ± SEM of K_d.

Furthermore, the pH dependency of i_c and E_0 supports the proton donation from OM *c*-Cyts to N(5) associated with EET. Although acidification of the supernatant solution significantly decreased i_c in the presence of 2.0 μM RF and MB, the pH decrease caused linear positive shift of E_0 with slope value of −13 mV and −34 mV per pH at 303

K, respectively (Figures 2-24 c, d and 2-25). Assuming that protons are supplied to the N(5) from the bulk solution, such pH-dependency of redox potential should facilitate the rate of electron transport at lower pH as demonstrated for the quinones lacking the N(5), e.g., HNQ (Figures 2-24d and 2-25). This clear inconsistency of pH dependency between i_c and E_0 of redox cofactor strongly suggests the existence of an internal source of protons for the cofactor-bound OM *c*-Cyts complex associated with EET [63-64].

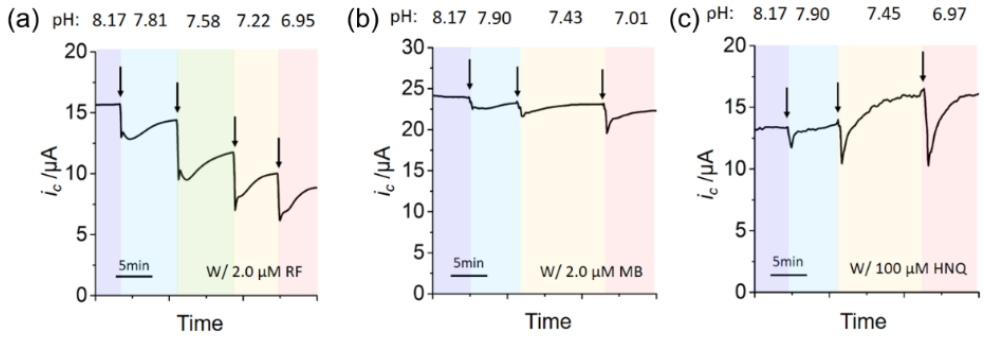

Figure 2-25. Representative time course for current production from a monolayer biofilm of *S. oneidensis* MR-1 in the presence of 2.0 μM RF (a), 2.0 μM MB (b) and 100 μM HNQ (c). At the beginning of the measurement, the pH in the bulk solution was adjusted at 8.17, HCl was then added into the reactor to change the pH in the physiological range at timings arrows indicate. The bulk pH is indicated above each data for current production.

Furthermore, the author examined the mutant strains Δ*mtrC* and Δ*omcA*, which lack key multi-heme protein components of the OM *c*-Cyts complex, but while this complex still retains the capacity to bind RF and FMN, respectively, there is potentially an altered hydrogen bonding network structure. Δ*mtrC* and Δ*omcA* displayed a two-fold greater reduction in the i_c upon the addition of D_2O than did the WT cells in the presence of RF and FMN, respectively (Figures 2-26 and 2-27), indicating that the proton transport pathway is significantly influenced by the lack of the multi-heme protein components in

the OM *c*-Cyts complex. The non-linearly increasing KIE against D_2O concentration is characteristic to multiple protonic sites, further supporting the proton transport pathway inside the OM *c*-Cyts complex (Figures 2-26 and 2-27)[60-62].

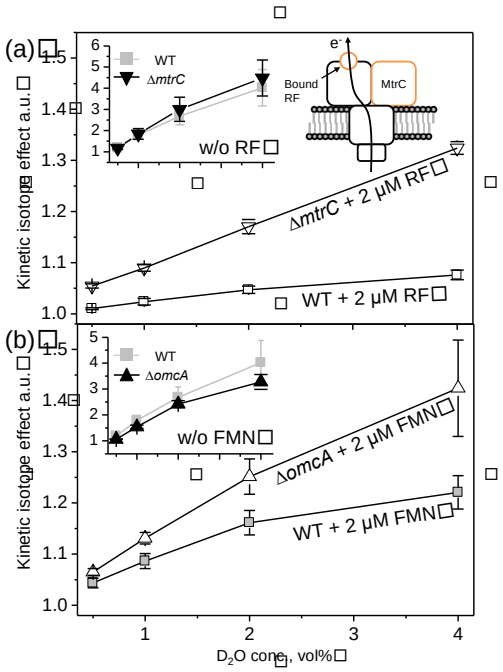

Figure 2-26. Effect of mutation of the MtrC or OmcA multi-heme protein (strains Δ*mtrC* and Δ*omcA*, respectively) on kinetic isotope effect (KIE) values. The KIE was estimated as the reciprocal of the ratio of i_c before and after the addition of D_2O. The i_c was monitored before and after the addition of D_2O at concentrations up to 4% (v/v) in systems containing WT, Δ*mtrC*, or Δ*omcA* cells in the presence 2.0 μM riboflavin (RF) (a) or flavin mononucleotide (FMN) (b). The data are presented as the means ± standard error of the mean (n > 3). The inset panels and figure represent the KIE data obtained in the absence of flavins with the same range of D_2O concentrations and the schematic illustration for EET via the RF-bound OM Cyt *c* complex, respectively.

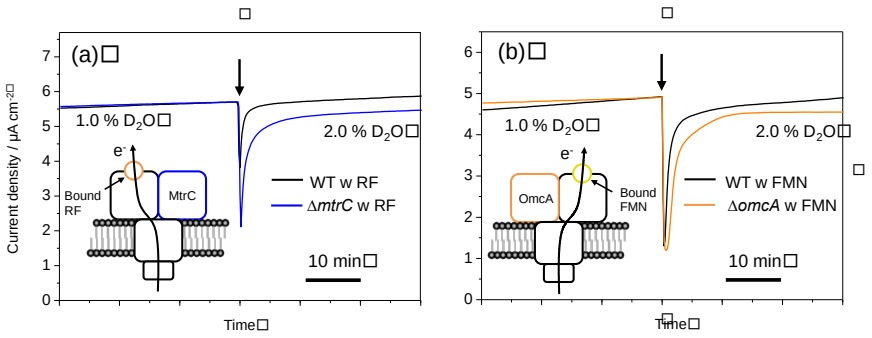

Figure 2-27. Effect of flavin molecules and mutation of the MtrC and OmcA proteins (strains Δ*mtrC* and Δ*omcA*, respectively) on the kinetic isotope effect (KIE) for microbial current production. (a) Time versus current production (i_c) for a monolayer biofilm of wild-type (WT; black line) and Δ*mtrC* (blue line) strains of *S. oneidensis* MR-1 in systems containing 10 mM lactate and 2.0 μM riboflavin (RF). (b) Time versus current production (i_c) for a monolayer biofilm of WT (black line) and Δ*omcA* (orange line) strains of *S. oneidensis* MR-1 in systems containing 10 mM lactate and 2.0 μM flavin mononucleotide (FMN). Data for the mutant strains Δ*mtrC* and Δ*omcA* were normalized to the tine point just prior to the addition of D_2O in the data for WT. The normalized i_c values for Δ*mtrC* and Δ*omcA* were 1.94 and 0.47 μA cm^{-2}, respectively. Inset scheme describes the location of RF, FMN, MtrC, and OmcA in the OM Cyts complex.

Although the KIE values clearly differed between the WT and Δ*mtrC* and Δ*omcA* strains in the presence of flavins, the KIE was nearly identical among the three strains in the absence of flavins (Figure 2-26, insets), indicating that the proton transport pathway in OM *c*-Cyts complex without the bound flavin cofactor is not involved in the deleted parts, which is distinct from that with flavin cofactor. Taken together, the significant increase of KIE by removal of flavin cofactors or key components of the OM *c*-Cyts and pH dependency strongly suggest that the bound flavin cofactor alters the kinetics and pathways of proton transport inside OM *c*-Cyts and accelerates rate-limiting proton transport.

Proton exportation model across OM

Since EET is the electron export process from periplasmic space to cell exterior, continuous EET may cause accumulation of positive charge in periplasm sandwiched by insulative outer- and inner- membranes. The author, then, reasoned that the observed large KIE may be assignable to proton export through OM *c*-Cyts to maintain the charge neutrality in the periplasm. Although the OM of Gram-negative bacteria is considered to be permeable to ions, the same number of cations and electrons must be removed from the periplasm to prevent charge accumulation once the rate of electron transport exceeds that of proton diffusion across the OM. Therefore, a significant KIE on the EET via the OM *c*-Cyts complex may indicate that the rate of proton removal from the periplasm limits the rate of EET. This idea is in accordance with previous experiments that compared the rate of EET in whole-cell systems with that of purified OM *c*-Cyts complexes. The EET rate by whole *S. oneidensis* MR-1 cells per OM *c*-Cyts complex was estimated about 20~300 electrons s^{-1}, [4-5, 65-66] which is at least 10-fold lower than that in a purified system (10^3~10^4 electrons s^{-1}) [67-68] (See details in **Estimation of electron flux for a single OM *c*-Cyts complex**). Given that the electron transport rate in a purified system is nearly equal to the theoretical value estimated from the crystal structure of MtrF [69-70] and based on an inter-heme electron-hopping model [71] (~10^4 electrons s^{-1}), the lower EET rate that was observed in whole *S. oneidensis* MR-1 cells may be attributable to the slower removal of protons from the periplasm. Although such a proton transfer pathway has not been identified in the crystal structures of OM *c*-Cyts in the oxidized state [22, 72], it may be possible that the hydrogen network in the OM *c*-Cyts complex is rearranged during electron flow *in vivo*.

In order to test the proton export model, the two points listed below were

examined (Figure 2-28).

1. ATP generation by proton motive force (PMF) is inactive during EET process.
2. Protons are not accumulated in the periplasmic space during EET process.

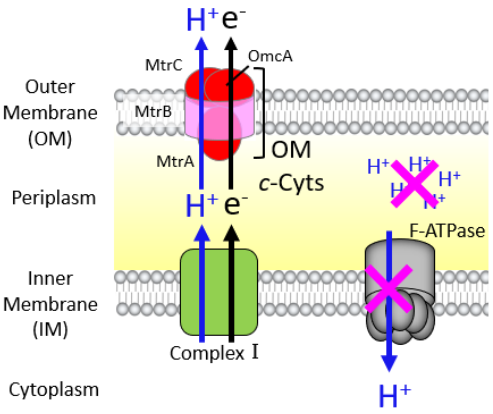

Figure 2-28. Hypothetical model of proton export during EET. If protons are exported by OM *c*-Cyts, ATP generation by F-ATPase should be inactive due to the removal of proton motive force (PMF), and simultaneously protons should not be accumulated in periplasm.

Although EET is considered to be coupled with the generation of PMF, the removal of protons from the periplasm during EET may hamper the PMF accumulation and scarcely accumulate protons inside periplasm. To test such a possibility, the growth and i_c coupled with lactate oxidation in the WT strain and the mutant strain of *S. oneidensis* MR-1 that lacks the sole F-type ATP synthase (ATPase; SO4746 to SO4754). Nearly identical i_c values were obtained for the WT and ΔATPase strains at +0.40 V (Figure 2-29a), suggesting that proton uptake by ATPase is not involved in the kinetics of EET. Protein quantification assays performed before and after the i_c measurements indicated that the significant anaerobic growth of the ΔATPase strains was nearly identical to that of the WT strain (Figure 2-29b and Table 2-5), whereas the aerobic growth rate of MR-1 was greatly reduced by the lack of F-ATPase. These results suggest that the EET process is not associated with the formation of PMF under the experimental conditions.

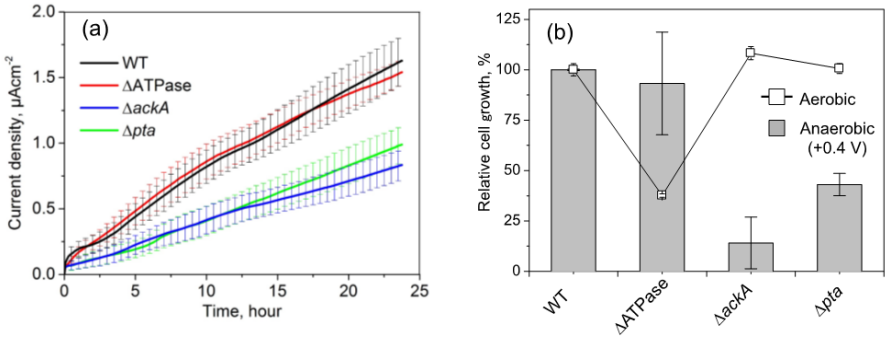

Figure 2-29. (a) Current production (i_c) from lactate oxidation in wild-type (WT) and mutant strains of *S. oneidensis* MR-1 lacking F-type ATP synthase (ΔATPase), SO2915 (Δ*ackA*) or SO2916 (Δ*pta*) measured at +0.4 V versus SHE in the presence of 10 mM lactate. (b) The cell growth on the electrode was estimated by the difference in protein content before and 24 h after the electrode inoculation. The i_c and growth data are presented as the means ± standard error of the mean (n = 5 and > 2, respectively).

Table 2-5. Growth data of WT, ΔATPase, Δ*pta* and Δ*ackA* strains of *S. oneidensis* MR-1 under anaerobic electrochemical or aerobic culture conditions.

Strain	**Δμg/cm^2 (Anaerobic)[a]**	**ΔOD$_{600}$ (Aerobic)[b]**
WT	12.0 ± 0.03 (n = 2)	1.50 ± 0.05 (n = 2)
ΔATPase	11.3 ± 3.09 (n = 3)	0.56 ± 0.01 (n = 2)
Δ*pta*	5.20 ± 0.67 (n = 2)	1.51 ± 0.04 (n = 2)
Δ*ackA*	1.70 ± 1.55 (n = 2)	1.62 ± 0.05 (n = 2)

a. Cell growth on the electrode was estimated by the difference in protein content before and 24 h after electrode inoculation. As the initial protein content was ~36 μg and the electrode surface area was 3.1 cm^2, the protein content of WT approximately doubled in 24 h with the electrode-cultivation.

b. Difference in the OD$_{600}$ after 24 h of aerobic cultivation. The initial OD$_{600}$ of all strains were 10^{-3}.

The author further confirmed that EET decouples chemiosmotic ATP synthesis by F-ATPase and, instead, promotes substrate-level ATP synthesis as an alternative path to ATP formation, which has been previously suggested for the anaerobic reduction of

fumarate located in the periplasm of *S. oneidensis* MR-1 [73]. Under the present current-producing conditions, it was further tested that the growth of WT and mutant strains lacking either the acetate kinase [*ackA* (SO2915)] or phosphotransacetylase [*pta* (SO2916)] genes, which are required for acetate production and substrate-level ATP production, respectively. Both the Δ*ackA* and Δ*pta* mutants exhibited significantly lower i_c and growth rate than those of the WT strain, suggesting the slower growth or suppression of NADH or formate production from lactate oxidation (Figure 2-29). In addition, because the concentration of formate had no impact on either the i_c or cell growth of the WT strain (Figure 2-30), the EET appeared to enhance the regeneration of NAD^+ to oxidize lactate and sustain substrate-level ATP production. These findings indicate that the role of the proton is not to generate a PMF but rather to regulate the flow of respiratory electrons, supporting the hypothesis that the removal of protons from the periplasm limits the rate of EET.

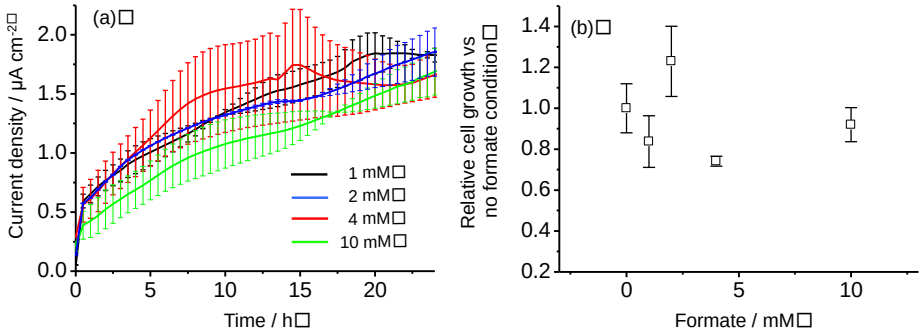

Figure 2-30. Effect of formate on current production (i_c) and growth of *S. oneidensis* MR-1 on a potential-poised electrode. Time course of current production (i_c) during lactate oxidation (a) and the growth rate (b) measured at +0.4 V (vs. SHE) in the presence of 10 mM lactate and 1, 2, 4, or 10 mM formate. The cell growth on the electrode was estimated by determining the difference in protein content before and after 24 h of cultivation. The i_c and growth data are shown as the mean ± standard error of mean (n = 2).

Given that F-ATPase was not functional and did not participate in the EET kinetics, rate-limiting proton transport in the absence of flavin could be either to the cytoplasm or to the extracellular environment across the OM via certain proton channels. However, the large KIE observed in the absence of flavins is distinct from that of active and passive transporters [74-79]. These results imply the proton export through OM *c*-Cyts. Thus, next, the periplasmic pH (pH_p) was tested to confirm that protons are not accumulated in the periplasmic space during EET process.

To monitor the pH_p during EET, a new method that uses the OM permeability of a biosynthesized flavin molecule was developed. Flavins are synthesized in the cytoplasm of *S. oneidensis* MR-1, transported to the periplasm via an IM transporter, and secreted to the cell exterior [20]. In the periplasm, flavins are in the reduced hydroquinone state (HQ) when a sufficient amount of electron donors is supplemented to the microbes. When pH_p increases higher than the pK_a of HQ, the deprotonation reaction of HQ proceeds, producing anionic hydroquinone (AHQ) in the periplasmic space (Figure 2-31a). Negatively charged AHQ likely accumulates in the periplasm due to low membrane permeability originating from electrostatic repulsion against OM composed of negatively charged acidic phospholipids and lipopolysaccharides (Figure 2-31b) [80]. Therefore, the author hypothesized that if the regents to enhance the permeability of OM was added, the AHQ that accumulated in the periplasmic space should be released under high pH_p conditions (Figure 2-31c). In contrast, at pH_p lower than 6.5, neutral hydroquinone (NHQ) permeates the OM (Figure 2-31b). Therefore, increasing the membrane permeability does not enhance the efflux of flavin through the OM. Thus, by increasing membrane permeability and monitoring flavin concentration, one can determine whether the pH_p is higher or lower compared with pK_a under in live conditions.

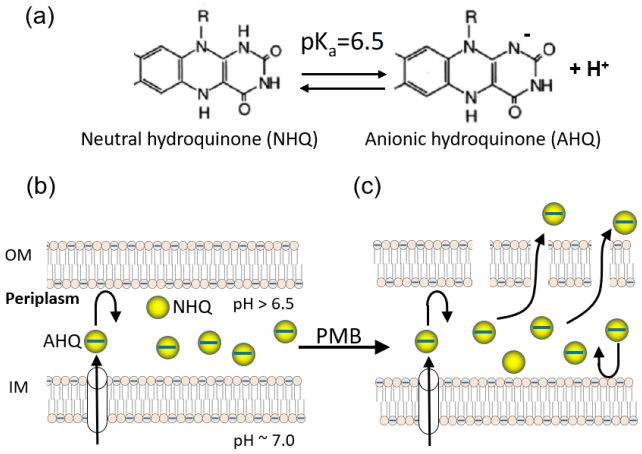

Figure 2-31. (a) Deprotonation reaction of neutral hydroquinone (NHQ) to anionic hydroquinone (AHQ). At pH_p higher than 6.5, AHQ accumulates in the periplasm (b) therefore, PMB enhances the outflow of flavin (c).

First, whether our assay could produce results consistent with previous reports was examined. It has been demonstrated that at pH 7.2, the sole F-type ATP synthase (F-ATPase) in *S. oneidensis* MR-1 is inactive when fumarate acts as an electron acceptor for anaerobic respiration, suggesting that PMF was not accumulated to drive F-ATPase [81]. This suggests that fumarate respiration caused minimal proton accumulation, shifting pH_p as high as the bulk pH to localize AHQ in the periplasm. To examine whether AHQ accumulates in the periplasm, the time course of flavin outflow promoted by polymyxin B (PMB) [82] was monitored in the anaerobic culture of *S. oneidensis* MR-1 with 10 mM lactate and 20 mM fumarate as the electron donor and acceptor, respectively. As shown in Figure 3-32a, the flavin concentration gradually increased with time as a function of cellular flavin secretion, even in the absence of PMB, which is consistent with previous observations [83]. Although 1.0 gmL^{-1} PMB addition did not have an effect, more PMB addition resulted in more rapid increase in flavin concentration compared with the no-PMB control (Figure 2-32a): i.e., the flavin concentration was 25 ± 2% higher in the

presence of 10 gmL^{-1} PMB. Assuming only AHQ was released from the periplasm, the amount of flavin excreted by PMB was sufficient for accounting higher pH_p value than the HQ pK_a. In contrast, under aerobic conditions with lactate as an electron donor, PMB addition up to 10 gmL^{-1} did not result in an increase in flavin concentration (Figure 2-32b). Fast increase in the bulk flavin concentration at the beginning in Figure 2-32b is likely attributed to higher growth rate in the aerobic conditions compared with the anaerobic fumarate conditions [83]. As PMB concentrations less than 20 gmL^{-1} perturb the OM but not the IM under conditions similar to those with Escherichia coli [82], these results suggest that AHQ accumulates in the periplasm during anaerobic fumarate respiration but not during aerobic respiration. These observations are consistent with previous reports that PMF drives ATP formation via the F-ATPase under aerobic conditions but not during anaerobic fumarate respiration [81]. One of the possible explanations is that pH_p is maintained at the bulk pH at 7.8 by the produced succinate because this weak acid (pK_a ~ 5.6) could increase pH_p to a value close to the bulk pH by exporting protons across the OM.

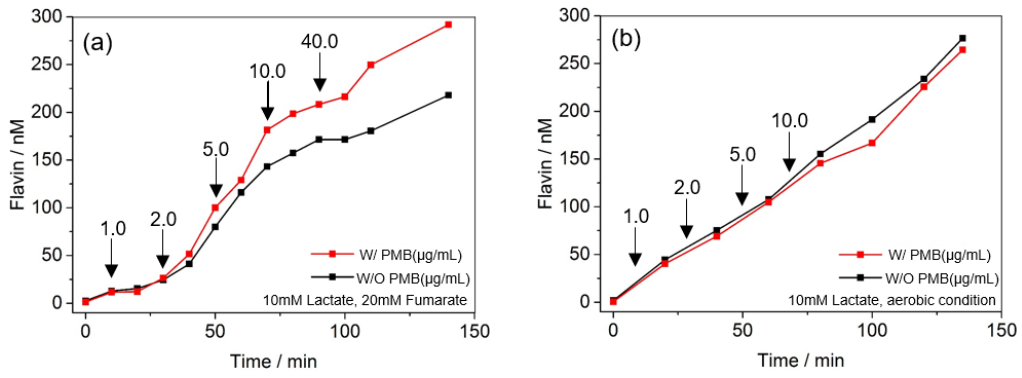

Figure 2-32. Effect of PMB for time course of bulk flavin concentration in fumarate anaerobic culture (a) and aerobic culture in the presence of lactate (b). PMB was added after sampling at timing of arrows.

Next, the effect of PMB addition on EET in *S. oneidensis* MR-1 to the ITO electrode surface was examined. Flavin molecules are known to enhance the rate of EET by binding to OM *c*-Cyts [1-2]. Therefore, the outflow of flavin will increase the microbial current production and the concentration of flavin bound to OM *c*-Cyts at the electrode surface, which is detectable by differential pulse (DP) voltammetry measurements as chapter 2-1. Figure 2-33 represents the time course of current production in *S. oneidensis* MR-1 in the presence of 10mM lactate as a sole electron donor at +0.4 V vs. SHE. In the absence of PMB, approximately 1.5 μAcm^{-2} current was observed. Upon the addition of 3.0 and 5.0 gmL^{-1} PMB, more current production was observed at the higher PMB concentration (Figure 2-33a). The current increased by an average of 22% in response to the addition of 5.0 gmL^{-1} PMB (Figure 2-33a inset), which is comparable to the anaerobic fumarate system shown in Figure 2-32a. DP voltammetry measured after PMB addition showed a current increase in the shoulder adjacent to a peak at approximately 0 mV that was determined to be the redox cycling of hemes in OM *c*-Cyts (Figure 2-33b) [1-2]. The difference between before and after PMB addition was observable as a peak at a current of −140 mV (Figure 2-33b inset). For this peak, the potential is almost identical with that of FMN but not with RF (110 mV) bound to OM *c*-Cyts [2]. Thus, these voltammetric results indicate that the electrode surface density of bound FMN in OM *c*-Cyts increased. The outflow of FMN, but not RF, is consistent with the proposed flavin secretion scenario whereby biosynthesized FAD is hydrolyzed to FMN in the periplasm and RF is formed in cell exterior after secretion [83]. These results demonstrate that EET causes AHQ accumulation in the periplasm. pH_p would remain as high as the anaerobic fumarate conditions, which is consistent with inactivation of F-ATPase during EET and proton

exportation model proposed herein.

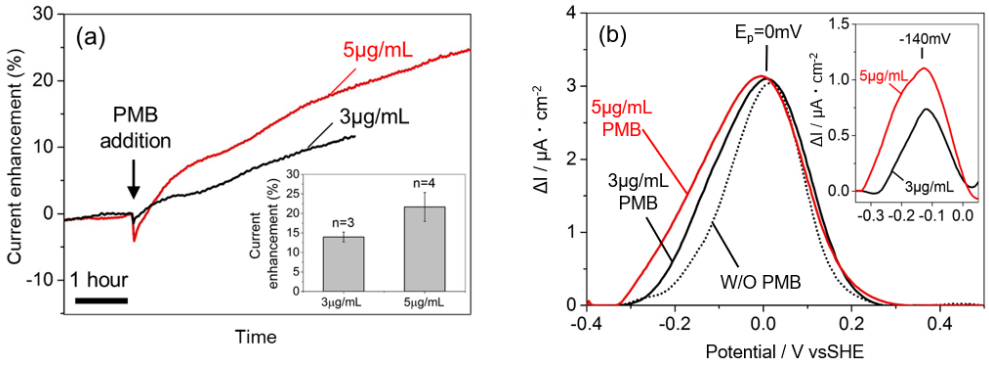

Figure 2-33. Effect of PMB addition in current generation (a) and DP voltammograms in *S. oneidensis* MR-1 (b). Peak current values in panel (b) were normalized to compare their peak shoulders. Inset (a): Averaged current enhancement by PMB. Inset (b): Differential current (ΔI) between DP voltammograms before and after PMB addition

Taken together, the inactivation of F-ATPase and un-accumulated protons in periplasmic space during EET were electrochemically confirmed. Those data strongly suggest that protons are exported to cell exterior. This possibility should be further explored in a proteoliposome system [67] or by a quantum chemical approach [69] once the crystal structure of flavin-bound OM *c*-Cyts is obtained. If true, the EET process may represent a novel form of respiratory metabolism, in which rapid electron outflow associated with proton export across the OM sustains the regeneration of NAD^+ to promote substrate-level phosphorylation like fermentation processes, which expel protons in the form of hydrogen or reduced organics for ATP formation.

Estimation of electron flux for a single OM *c*-Cyts complex

The author estimated the electron flux in single OM *c*-Cyts complexes in both whole-cell system and purified system. The electron flux in whole *S. oneidensis* MR-1 cell for a single OM *c*-Cyts complex was estimated using single-cell current production data at a

poised electrode potential of +0.4 V (vs. SHE) [65]. A previous study observed current production from single *Shewanella* cell using optical tweezer, which showed about 1.2×10^6 electrons s^{-1}. [65] Given that the content of OM *c*-Cyts per cell is approximately 4.0×10^3, [84] the electron flux per single OM *c*-Cyts complex is about 3.0×10^2 electrons s^{-1}. Other whole-cell electrochemical study showed that the current production of 1.8×10^5 electrons s^{-1} and 4.9×10^3 OM *c*-Cyts complex per cell, indicating that the electron flux per single OM *c*-Cyts complex is about 37 electrons s^{-1}.[5]

On the other hand, regarding the electron flux for purified OM *c*-Cyts complex embedded in proteoliposomes, White *et al*. reported that about 8.5×10^3 electrons s^{-1} are transported to γ-FeOOH [85]. The electron flux through OM *c*-Cyts complex was over 1.0×10^3 electrons s^{-1} for other kinds of iron oxides (α−Fe_2O_3 and α−FeOOH). Taken together, the EET rate by whole *S. oneidensis* MR-1 cells per OM *c*-Cyts complex is estimated to be over 10 times lower than that in purified system.

2.2.4 Conclusion

In this study, the author investigated the solvent KIE of deuterium in whole-cell electrochemical assays and demonstrated that proton transport in flavin-bound OM *c*-Cyts limits the rate of EET in *S. oneidensis* MR-1. Given that the removal of a flavin cofactor or key components of the OM *c*-Cyts complex significantly altered the KIE, the acceleration of EET by the Sq intermediate occurs most likely due to the rate enhancement of proton transfer that couples with EET. This novel proton-coupling property will expand the available strategies to control the kinetics of EET in iron-reducing bacteria and make the OM *c*-Cyts complex a model system for studying biological proton-coupled electron transfer reactions *in vivo* [86]. Additionally, considering that EET is observed in other microbial strains and consortia, the idea of cation transport and charge balancing may have major implications for microbial respiration in anaerobic iron corrosion [87] and methane oxidation processes [88]. Bio-redox chemistry underlying bacterial energy management using protons appears to be more flexible than previously thought.

References in chapter 2

1. Okamoto, A.; Hashimoto, K.; Nealson, K. H.; Nakamura, R., Rate enhancement of bacterial extracellular electron transport involves bound flavin semiquinones. *Proc. Natl. Acad. Sci. U.S.A.* **2013,** *110* (19), 7856-7861.
2. Okamoto, A.; Kalathil, S.; Deng, X.; Hashimoto, K.; Nakamura, R.; Nealson, K. H., Cell-secreted Flavins Bound to Membrane Cytochromes Dictate Electron Transfer Reactions to Surfaces with Diverse Charge and pH. *Sci. Rep.* **2014,** *4*, 5628.
3. Okamoto, A.; Nakamura, R.; Nealson, K. H.; Hashimoto, K., Bound Flavin Model Suggests Similar Electron-Transfer Mechanisms in *Shewanella* and *Geobacter*. *Chemelectrochem* **2014,** *1* (11), 1808-1812.
4. Okamoto, A.; Nakamura, R.; Ishii, K.; Hashimoto, K., *In vivo* Electrochemistry of *C*-Type Cytochrome-Mediated Electron-Transfer with Chemical Marking. *Chembiochem* **2009,** *10* (14), 2329-2332.
5. Okamoto, A.; Nakamura, R.; Hashimoto, K., *In-vivo* identification of direct electron transfer from *Shewanella oneidensis* MR-1 to electrodes via outer-membrane OmcA-MtrCAB protein complexes. *Electrochim. Acta* **2011,** *56* (16), 5526-5531.
6. von Canstein, H.; Ogawa, J.; Shimizu, S.; Lloyd, J. R., Secretion of flavins by Shewanella species and their role in extracellular electron transfer. *Appl. Environ. Microbiol.* **2008,** *74* (3), 615-23.
7. Clarke, T. A.; Edwards, M. J.; Gates, A. J.; Hall, A.; White, G. F.; Bradley, J.; Reardon, C. L.; Shi, L.; Beliaev, A. S.; Marshall, M. J.; Wang, Z. M.; Watmough, N. J.; Fredrickson, J. K.; Zachara, J. M.; Butt, J. N.; Richardson, D. J., Structure of a bacterial cell surface decaheme electron conduit. *Proc. Natl. Acad. Sci. U.S.A.* **2011,** *108* (23), 9384-9389.
8. Marsili, E.; Baron, D. B.; Shikhare, I. D.; Coursolle, D.; Gralnick, J. A.; Bond, D. R., Shewanella Secretes flavins that mediate extracellular electron transfer. *Proc. Natl. Acad. Sci. U.S.A.* **2008,** *105* (10), 3968-3973.
9. Kaila, V. R. I., Long-range proton-coupled electron transfer in biological energy conversion: towards mechanistic understanding of respiratory complex I. *J. R. Soc. Interface* **2018,** *15* (141).
10. Brzezinski, P., Redox-driven membrane-bound proton pumps. *Trends. Biochem. Sci.* **2004,** *29* (7), 380-387.
11. Myers, C. R.; Nealson, K. H., Respiration-Linked Proton Translocation Coupled to Anaerobic Reduction of Manganese(IV) and Iron(III) in *Shewanella-Putrefaciens* MR-1. *J. Bacteriol.* **1990,** *172* (11), 6232-6238.
12. Myers, C. R.; Nealson, K. H., Bacterial Manganese Reduction and Growth with

Manganese Oxide as the Sole Electron-Acceptor. *Science* **1988,** *240* (4857), 1319-1321.
13. Xiong, Y. J.; Shi, L.; Chen, B. W.; Mayer, M. U.; Lower, B. H.; Londer, Y.; Bose, S.; Hochella, M. F.; Fredrickson, J. K.; Squier, T. C., High-affinity binding and direct electron transfer to solid metals by the *Shewanella oneidensis* MR-1 outer membrane *c*-type cytochrome OmcA. *J. Am. Chem. Soc.* **2006,** *128* (43), 13978-13979.
14. Summers, Z. M.; Fogarty, H. E.; Leang, C.; Franks, A. E.; Malvankar, N. S.; Lovley, D. R., Direct Exchange of Electrons Within Aggregates of an Evolved Syntrophic Coculture of Anaerobic Bacteria. *Science* **2010,** *330* (6009), 1413-1415.
15. McGlynn, S. E.; Chadwick, G. L.; Kempes, C. P.; Orphan, V. J., Single cell activity reveals direct electron transfer in methanotrophic consortia. *Nature* **2015,** *526* (7574), 531-U146.
16. Logan, B. E.; Hamelers, B.; Rozendal, R. A.; Schrorder, U.; Keller, J.; Freguia, S.; Aelterman, P.; Verstraete, W.; Rabaey, K., Microbial fuel cells: Methodology and technology. *Environ. Sci. Technol.* **2006,** *40* (17), 5181-5192.
17. Busalmen, J. P.; Esteve-Nunez, A.; Berna, A.; Feliu, J. M., *C*-type cytochromes wire electricity-producing bacteria to electrodes. *Angew. Chem. Int. Ed.* **2008,** *47* (26), 4874-4877.
18. Leung, K. M.; Wanger, G.; El-Naggar, M. Y.; Gorby, Y.; Southam, G.; Lau, W. M.; Yang, J., *Shewanella oneidensis* MR-1 Bacterial Nanowires Exhibit p-Type, Tunable Electronic Behavior. *Nano Lett.* **2013,** *13* (6), 2407-2411.
19. Jiang, J.; Kappler, A., Kinetics of microbial and chemical reduction of humic substances: Implications for electron shuttling. *Environ. Sci. Technol.* **2008,** *42* (10), 3563-3569.
20. Kotloski, N. J.; Gralnick, J. A., Flavin Electron Shuttles Dominate Extracellular Electron Transfer by *Shewanella oneidensis*. *Mbio* **2013,** *4* (1).
21. Okamoto, A.; Saito, K.; Inoue, K.; Nealson, K. H.; Hashimoto, K.; Nakamura, R., Uptake of self-secreted flavins as bound cofactors for extracellular electron transfer in Geobacter species. *Energy Environ. Sci.* **2014,** *7* (4), 1357-1361.
22. Edwards, M. J.; White, G. F.; Norman, M.; Tome-Fernandez, A.; Ainsworth, E.; Shi, L.; Fredrickson, J. K.; Zachara, J. M.; Butt, J. N.; Richardson, D. J.; Clarke, T. A., Redox Linked Flavin Sites in Extracellular Decaheme Proteins Involved in Microbe-Mineral Electron Transfer. *Sci. Rep.* **2015,** *5*, 11677.
23. Xu, S.; Jangir, Y.; El-Naggar, M. Y., Disentangling the roles of free and cytochrome-bound flavins in extracellular electron transport from *Shewanella oneidensis* MR-1. *Electrochim. Acta* **2016,** *198*, 49-55.
24. Xu, S.; Barrozo, A.; Tender, L. M.; Krylov, A. I.; El-Naggar, M. Y., Multiheme

Cytochrome Mediated Redox Conduction through *Shewanella oneidensis* MR-1 Cells. *J. Am. Chem. Soc.* **2018,** *140* (32), 10085-10089.
25. Tokunou, Y.; Hashimoto, K.; Okamoto, A., Acceleration of Extracellular Electron Transfer by Alternative Redox-Active Molecules to Riboflavin for Outer-Membrane Cytochrome *c* of *Shewanella oneidensis* MR-1. *J. Phys. Chem. C* **2016,** *120* (29), 16168-16173.
26. Van Trump, J. I.; Sun, Y.; Coates, J. D., Microbial interactions with humic substances. *Adv. Appl. Microbiol.* **2006,** *60*, 55-96.
27. Schmidt am Busch, M.; Knapp, E. W., Accurate pK_a determination for a heterogeneous group of organic molecules. *Chemphyschem* **2004,** *5* (10), 1513-1522.
28. Matsui, T.; Baba, T.; Kamiya, K.; Shigeta, Y., An accurate density functional theory based estimation of pK_a values of polar residues combined with experimental data: from amino acids to minimal proteins. *Phys. Chem. Chem. Phys.* **2012,** *14* (12), 4181-7.
29. Roh, Y.; Gao, H. C.; Vali, H.; Kennedy, D. W.; Yang, Z. K.; Gao, W. M.; Dohnalkova, A. C.; Stapleton, R. D.; Moon, J. W.; Phelps, T. J.; Fredrickson, J. K.; Zhou, J. Z., Metal reduction and iron biomineralization by a psychrotolerant Fe(III)-reducing bacterium, *Shewanella* sp strain PV-4. *Appl. Environ. Microbiol.* **2006,** *72* (5), 3236-3244.
30. Rifkin, S. C.; Evans, D. H., Analytical Evaluation of Differential Pulse Voltammetry at Stationary Electrodes Using Computer-Based Instrumentation. *Anal. Chem.* **1976,** *48* (14), 2174-2180.
31. Fourmond, V.; Hoke, K.; Heering, H. A.; Baffert, C.; Leroux, F.; Bertrand, P.; Leger, C., SOAS: A free program to analyze electrochemical data and other one-dimensional signals. *Bioelectrochemistry* **2009,** *76* (1-2), 141-147.
32. Renslow, R.; Babauta, J.; Kuprat, A.; Schenk, J.; Ivory, C.; Fredrickson, J.; Beyenal, H., Modeling biofilms with dual extracellular electron transfer mechanisms. *Phys. Chem. Chem. Phys.* **2013,** *15* (44), 19262-19283.
33. Jaguar, v., **2008**, Schrodinger, LLC, New York, NY.
34. Bashford, D.; Gerwert, K., Electrostatic calculations of the pK_a values of ionizable groups in bacteriorhodopsin. *J. Mol. Biol.* **1992,** *224* (2), 473-86.
35. Schmidt am Busch, M.; Knapp, E.-W., Accurate pK_a determination for a heterogeneous group of organic molecules. *ChemPhysChem* **2004,** *5*, 1513-1522.
36. Besler, B. H.; Merz, J. K. M.; Kollman, P. A., *J. Comp. Chem.* **1990,** *11*, 431.
37. Bayly, C. I.; Cieplak, P.; Cornell, W. D.; Kollman, P. A., A well-behaved electrostatic potential based method using charge restraints for deriving atomic charges: the RESP model. *J. Phys. Chem.* **1993,** *97*, 10269-10280.
38. Breneman, C. M.; Wiberg, K. B., Determining atom-centered monopoles from

molecular electrostatic potentials. The need for high sampling density in formamide conformational analysis. *J. Comput. Chem.* **1990,** *11*, 361-373.

39. Lide, D. R., *Handbook of chemistry and physics (Chemical Rubber Publishing, Cleveland)* **2001**.

40. Hansch, C.; Leo, A.; Taft, R. W., A Survey of Hammett Substituent Constants and Resonance and Field Parameters. *Chem. Rev.* **1991,** *91* (2), 165-195.

41. Wu, Y. D.; Liu, T. X.; Li, X. M.; Li, F. B., Exogenous Electron Shuttle-Mediated Extracellular Electron Transfer of *Shewanella putrefaciens* 200: Electrochemical Parameters and Thermodynamics. *Environ. Sci. Technol.* **2014,** *48* (16), 9306-9314.

42. Buckel, W.; Thauer, R. K., Flavin-Based Electron Bifurcation, Ferredoxin, Flavodoxin, and Anaerobic Respiration With Protons (Ech) or NAD(+) (Rnf) as Electron Acceptors: A Historical Review. *Front Microbiol* **2018,** *9*.

43. Watt, W.; Tulinsky, A.; Swenson, R. P.; Watenpaugh, K. D., Comparison of the Crystal-Structures of a Flavodoxin in Its Three Oxidation-States at Cryogenic Temperatures. *J. Mol. Biol.* **1991,** *218* (1), 195-208.

44. Laviron, E., General Expression of the Linear Potential Sweep Voltammogram in the Case of Diffusionless Electrochemical Systems. *J. Electroanal. Chem.* **1979,** *101* (1), 19-28.

45. Micsonai, A.; Wien, F.; Kernya, L.; Lee, Y. H.; Goto, Y.; Refregiers, M.; Kardos, J., Accurate secondary structure prediction and fold recognition for circular dichroism spectroscopy. *Proc. Natl. Acad. Sci. U.S.A.* **2015,** *112* (24), 3095-3103.

46. Micsonai, A.; Wien, F.; Bulyaki, E.; Kun, J.; Moussong, E.; Lee, Y. H.; Goto, Y.; Refregiers, M.; Kardos, J., BeStSel: a web server for accurate protein secondary structure prediction and fold recognition from the circular dichroism spectra. *Nucleic Acids Res.* **2018,** *46*, W315-W322.

47. Breuer, M.; Rosso, K. M.; Blumberger, J., Flavin Binding to the Deca-heme Cytochrome MtrC: Insights from Computational Molecular Simulation. *Biophys. J.* **2015,** *109* (12), 2614-2624.

48. Draper, R. D.; Ingraham, L. L., A potentiometric study of the flavin semiquinone equilibrium. *Arch. Biochem. Biophys.* **1968,** *125* (3), 802-8.

49. Impert, O.; Katafias, A.; Kita, P.; Mills, A.; Pietkiewiez-Graczyk, A.; Wrzeszcz, G., Kinetics and mechanism of a fast leuco-Methylene Blue oxidation by copper(II)-halide species in acidic aqueous media. *Dalton. Trans.* **2003,** (3), 348-353.

50. Gordon, M., *The exciplex*. Elsevier: 2012.

51. Okamoto, A.; Hashimoto, K.; Nealson, K. H., Flavin Redox Bifurcation as a Mechanism for Controlling the Direction of Electron Flow during Extracellular Electron

Transfer. *Angew. Chem. Int. Ed.* **2014,** *53* (41), 10988-10991.
52. Rowe, A. R.; Rajeev, P.; Jain, A.; Pirbadian, S.; Okamoto, A.; Gralnick, J. A.; El-Naggar, M. Y.; Nealson, K. H., Tracking Electron Uptake from a Cathode into *Shewanella* Cells: Implications for Energy Acquisition from Solid-Substrate Electron Donors. *Mbio* **2018,** *9* (1).
53. Nealson, K. H.; Saffarini, D., Iron and manganese in anaerobic respiration: environmental significance, physiology, and regulation. *Annu. Rev. Microbiol.* **1994,** *48*, 311-343.
54. Hartshorne, R. S.; Reardon, C. L.; Ross, D.; Nuester, J.; Clarke, T. A.; Gates, A. J.; Mills, P. C.; Fredrickson, J. K.; Zachara, J. M.; Shi, L.; Beliaev, A. S.; Marshall, M. J.; Tien, M.; Brantley, S.; Butt, J. N.; Richardson, D. J., Characterization of an electron conduit between bacteria and the extracellular environment. *Proc. Natl. Acad. Sci. U.S.A.* **2009,** *106* (52), 22169-22174.
55. Schroder, U.; Niessen, J.; Scholz, F., A generation of microbial fuel cells with current outputs boosted by more than one order of magnitude. *Angew. Chem. Int. Ed.* **2003,** *42* (25), 2880-2883.
56. Rabaey, K.; Rozendal, R. A., Microbial electrosynthesis - revisiting the electrical route for microbial production. *Nat. Rev. Microbiol.* **2010,** *8* (10), 706-716.
57. Hong, G. Y.; Pachter, R., Bound Flavin-Cytochrome Model of Extracellular Electron Transfer in *Shewanella oneidensis*: Analysis by Free Energy Molecular Dynamics Simulations. *J. Phys. Chem. B* **2016,** *120* (25), 5617-5624.
58. Junki Saito, K. H., Akihiro Okmaoto, Flavin as an Indicator of the Rate-Limiting Factor for Microbial Current Production in *Shewanella oneidensis* MR-1. *Electrochim. Acta* **2016,** *216*, 261-265.
59. Guo, J. B.; Lian, J.; Xu, Z. F.; Xi, Z. H.; Yang, J. L.; Jefferson, W.; Liu, C.; Li, Z. X.; Yue, L., Reduction of Cr(VI) by *Escherichia coli* BL21 in the presence of redox mediators. *Bioresour. Technol.* **2012,** *123*, 713-716.
60. Schowen, K. B.; Schowen, R. L., Solvent Isotope Effects on Enzyme-Systems. *Method Enzymol.* **1982,** *87*, 551-606.
61. Cleland, W. W., The use of isotope effects to determine enzyme mechanisms. *J. Biol. Chem.* **2003,** *278* (52), 51975-51984.
62. Rohlfs, R. J.; Huang, L. X.; Hille, R., Prototropic Control of Intramolecular Electron-Transfer in Trimethylamine Dehydrogenase. *J. Biol. Chem.* **1995,** *270* (38), 22196-22207.
63. Hammes-Schiffer, S.; Stuchebrukhov, A. A., Theory of Coupled Electron and Proton Transfer Reactions. *Chem. Rev.* **2010,** *110* (12), 6939-6960.

64. Cleland, W. W., The Use of Ph Studies to Determine Chemical Mechanisms of Enzyme-Catalyzed Reactions. *Method Enzymol.* **1982,** *87*, 390-405.
65. Liu, H. A.; Newton, G. J.; Nakamura, R.; Hashimoto, K.; Nakanishi, S., Electrochemical Characterization of a Single Electricity-Producing Bacterial Cell of *Shewanella* by Using Optical Tweezers. *Angew. Chem. Int. Ed.* **2010,** *49* (37), 6596-6599.
66. McLean, J. S.; Wanger, G.; Gorby, Y. A.; Wainstein, M.; McQuaid, J.; Ishii, S. I.; Bretschger, O.; Beyenal, H.; Nealson, K. H., Quantification of Electron Transfer Rates to a Solid Phase Electron Acceptor through the Stages of Biofilm Formation from Single Cells to Multicellular Communities. *Environ. Sci. Technol.* **2010,** *44* (7), 2721-2727.
67. White, G. F.; Shi, Z.; Shi, L.; Wang, Z.; Dohnalkova, A. C.; Marshall, M. J.; Fredrickson, J. K.; Zachara, J. M.; Butt, J. N.; Richardson, D. J.; Clarke, T. A., Rapid electron exchange between surface-exposed bacterial cytochromes and Fe(III) minerals. *Proc. Natl. Acad. Sci. U.S.A.* **2013,** *110* (16), 6346-51.
68. Ross, D. E.; Brantley, S. L.; Tien, M., Kinetic Characterization of OmcA and MtrC, Terminal Reductases Involved in Respiratory Electron Transfer for Dissimilatory Iron Reduction in Shewanella oneidensis MR-1. *Appl. Environ. Microbiol.* **2009,** *75* (16), 5218-5226.
69. Breuer, M.; Rosso, K. M.; Blumberger, J., Electron flow in multiheme bacterial cytochromes is a balancing act between heme electronic interaction and redox potentials. *Proc. Natl. Acad. Sci. U.S.A.* **2014,** *111* (2), 611-616.
70. Breuer, M.; Zarzycki, P.; Blumberger, J.; Rosso, K. M., Thermodynamics of Electron Flow in the Bacterial Deca-heme Cytochrome MtrF. *J. Am. Chem. Soc.* **2012,** *134* (24), 9868-9871.
71. Polizzi, N. F.; Skourtis, S. S.; Beratan, D. N., Physical constraints on charge transport through bacterial nanowires. *Faraday Discuss* **2012,** *155*, 43-62.
72. Clarke, T. A.; Edwards, M. J.; Gates, A. J.; Hall, A.; White, G. F.; Bradley, J.; Reardon, C. L.; Shi, L.; Beliaev, A. S.; Marshall, M. J.; Wang, Z. M.; Watmough, N. J.; Fredrickson, J. K.; Zachara, J. M.; Butt, J. N.; Richardson, D. J., Structure of a bacterial cell surface decaheme electron conduit. *Proc. Natl. Acad. Sci. U.S.A.* **2011,** *108* (23), 9384-9389.
73. Hunt, K. A.; Flynn, J. M.; Naranjo, B.; Shikhare, I. D.; Gralnick, J. A., Substrate-Level Phosphorylation Is the Primary Source of Energy Conservation during Anaerobic Respiration of *Shewanella oneidensis* strain MR-1. *J. Bacteriol.* **2010,** *192* (13), 3345-3351.
74. Althoff, G.; Lill, H.; Junge, W., Proton channel of the chloroplast ATP synthase, CF_0: Its time-averaged single-channel conductance as function of pH, temperature,

isotopic and ionic medium composition. *J. Membr. Biol.* **1989,** *108* (3), 263-271.
75. Nikaido, H., Molecular basis of bacterial outer membrane permeability revisited. *Microbiol. Mol. Biol. Rev.* **2003,** *67* (4), 593-656.
76. Hirakura, Y.; Sugiyama, T.; Takeda, M.; Ikeda, M.; Yoshioka, T., Deuteration as a tool in investigating the role of protons in cell signaling. *Biochim. Biophys. Acta* **2011,** *1810* (2), 218-25.
77. Elsing, C.; Hirlinger, A.; Renner, E. L.; Lauterburg, B. H.; Meier, P. J.; Reichen, J., Solvent isotope effect on bile formation in the rat. *Biochem. J.* **1995,** *307*, 175-81.
78. Vasdev, S.; Gupta, I. P.; Sampson, C. A.; Longerich, L.; Parai, S., Deuterium oxide normalizes blood pressure and elevated cytosolic calcium in rats with ethanol-induced hypertension. *Can. J. Cardiol.* **1993,** *9* (9), 802-8.
79. Vasdev, S.; Prabhakaran, V. M.; Whelan, M.; Ford, C. A.; Longerich, L.; Parai, S., Fructose-induced hypertension, hypertriglyceridemia and elevated cytosolic calcium in rats: prevention by deuterium oxide. *Artery* **1994,** *21* (3), 124-47.
80. Beveridge, T. J., Structures of gram-negative cell walls and their derived membrane vesicles. *J. Bacteriol.* **1999,** *181* (16), 4725-4733.
81. Hunt, K. A.; Flynn, J. M.; Naranjo, B.; Shikhare, I. D.; Gralnick, J. A., Substrate-Level Phosphorylation Is the Primary Source of Energy Conservation during Anaerobic Respiration of *Shewanella oneidensis* Strain MR-1. *J. Bacteriol.* **2010,** *192* (13), 3345-3351.
82. Daugelavicius, R.; Bakiene, E.; Bamford, D. H., Stages of polymyxin B interaction with the Escherichia coli cell envelope. *Antimicrob. Agents Chemother.* **2000,** *44* (11), 2969-2978.
83. von Canstein, H.; Ogawa, J.; Shimizu, S.; Lloyd, J. R., Secretion of flavins by *Shewanella* species and their role in extracellular electron transfer. *Appl. Environ. Microbiol.* **2008,** *74* (3), 615-623.
84. Lower, B. H.; Shi, L.; Yongsunthon, R.; Droubay, T. C.; McCready, D. E.; Lower, S. K., Specific bonds between an iron oxide surface and outer membrane cytochromes MtrC and OmcA from *Shewanella oneidensis* MR-1. *J. Bacteriol.* **2007,** *189* (13), 4944-4952.
85. White, G. F.; Shi, Z.; Shi, L.; Wang, Z. M.; Dohnalkova, A. C.; Marshall, M. J.; Fredrickson, J. K.; Zachara, J. M.; Butt, J. N.; Richardson, D. J.; Clarke, T. A., Rapid electron exchange between surface-exposed bacterial cytochromes and Fe(III) minerals. *Proc. Natl. Acad. Sci. U.S.A.* **2013,** *110* (16), 6346-6351.
86. Huynh, M. H. V.; Meyer, T. J., Proton-coupled electron transfer. *Chem. Rev.* **2007,** *107* (11), 5004-5064.

87. Dinh, H. T.; Kuever, J.; Mussmann, M.; Hassel, A. W.; Stratmann, M.; Widdel, F., Iron corrosion by novel anaerobic microorganisms. *Nature* **2004,** *427* (6977), 829-832.
88. Stams, A. J. M.; Plugge, C. M., Electron transfer in syntrophic communities of anaerobic bacteria and archaea. *Nat. Rev. Microbiol.* **2009,** *7* (8), 568-577.

Chapter 3

In vivo-specific environments modulate the geometry of hemes in the outer-membrane *c*-type cytochromes

Electron transport reaction is one of the most essential and fundamental reaction in biology. Electron transport along a series of protein complexes located in membranes of mitochondria and bacteria is essential in the sense of energy conversion; the electron transport chain is coupled with proton translocation across membrane creating an electrochemical proton gradient that drives the synthesis of adenosine triphosphate (ATP), a molecule storing biological chemical energy [1]. Such efficient transports of electrons over several tens or hundreds angstroms along preferred pathways and directions have been accomplished by well-designed protein structure [2]. While electron transport in abiotic medium such as water occurs with Gaussian distribution and decay rapidly for larger values over short molecular distances, electrons move through proteins by means of quantum mechanical tunneling or hopping between metal redox centers [3-4]. The rate of electron transport and direction is defined by the electronic coupling between donor and acceptor, as well as the difference in redox potentials and the reorganization energy, thus, three-dimensional protein structure, especially architecture and interaction of metal redox centers, is the key determinants of biological electron transport rates and mechanisms [5-6].

The EET process has been also investigated based on the crystal structure, especially the heme geometry of some units of OM *c*-Cyts [7-10]. The redox potential and

electronic coupling among hemes estimated from the crystal structure obtained in oxidized state significantly contributed on the EET rates and pathways among hemes have been achieved as described in chapter 1 [11-16]. However, OM *c*-Cyts dynamically change their conformation and structure depending upon surrounding environments, which possibly dismisses conventional understandings of EET mechenisms through OM *c*-Cyts. For example, small-angle X-ray scattering revealed that reduction reaction decreases the overall length about 8% of OmcA, which is a homologue of MtrC protein [17]. Furthermore, a recent study using circular dichroism spectroscopy and Raman spectroscopy demonstrated the conformational change of some amino residues of OmcA associated with physical contact with solid materials [18]. Those studies have indicated that the structure and conformation of OM *c*-Cyts flexibly changes on the level of secondary structure or packings of amino acids. In addition, externally applied potential on *S. oneidensis* MR-1 varies the redox potentital of hemes in OM *c*-Cyts, which is linked with hemes environments [19]. Thus, in this study, the author hypothesized that the OM *c*-Cyts flexibly changes their conformation on the level of inter-heme interaction and geometry, with distinct EET mechanisms through OM *c*-Cyts in live *S. oneidensis* MR-1 from that estimated from the crystal structure (Figure 3-1).

Based on this hypothesis, in chapter 3, the author examined the heme geometry of OM *c*-Cyts in intact cell at various conditions and discussed about possible EET mechanisms via rearranged hemes centers. In chapter 3-1, the author developed a novel methodology to monitor the inter-heme interaction in a unit of OM *c*-Cyts, MtrC protein, in intact cell, termed whole-cell circular dichroism (CD) difference spectroscopy. In chapter 3-2, the use of whole-cell CD difference spectroscopy was extended to the association of OM *c*-Cyts with minerals, which has implicaitons to the EET mechanisms

in the presence of minerals in nature as well as the ecophysiology of EET-capable bacteria. In chapter 3-3, the whole-cell CD difference spectroscopy was finally combined with microbio-electrochemistry to obtain insights into the heme geometry during electron flow in the presence of bound flavin cofactors, which has structural implications to the mechanisms in EET acceleration caused by bound flavins, i.e., hemes may be rearranged by electron flow to enhance EET rate, which is consistent with proposed hydrogen-bond reorganization conveying rate-limiting protons described in chapter 2.

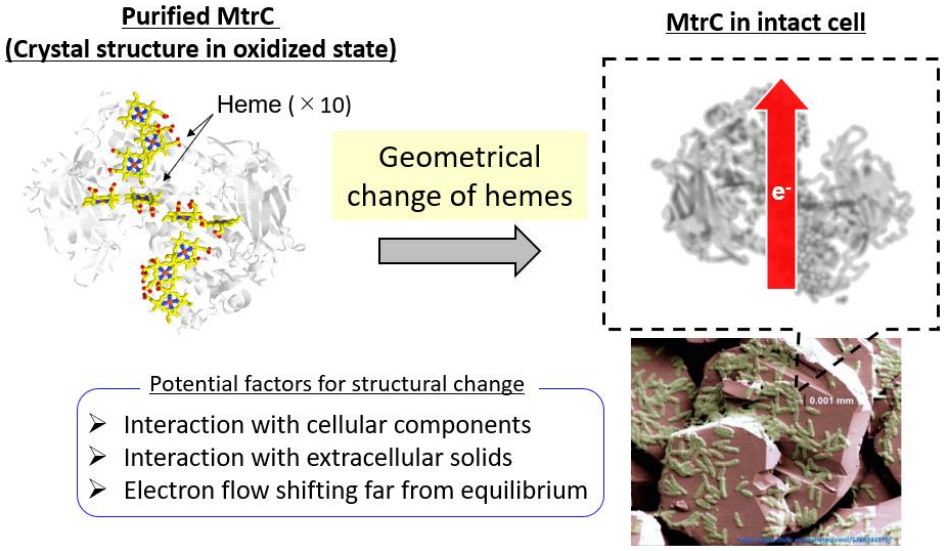

Figure 3-1. Schematic illustration of the hypothesis in chapter 3. Crystal structure was obtained by PDB code of 4LM8 [14].

Figures in chapter 3 are reprinted with permission from Royal Society of Chemistry and American Chemical Society.

Y. Tokunou, P. Chinotaikul, S. Hattori, T. A. Clarke, L. Shi, K. Hashimoto, K. Ishii, and A. Okamoto, *Chem. Commun.*, **2018**, 54, 13933-13936.

Y. Tokunou, and A. Okamoto, *Langmuir*, **2018**, DOI: 10.1039/c8cc06309e

3.1

Whole-cell circular dichroism difference spectroscopy reveals heme geometry in MtrC protein *in vivo*

3.1.1 Introduction

In this chapter 3-1, the author developed a novel methodology to monitor the inter-heme interaction in a unit of OM *c*-Cyts, MtrC protein, *in vivo* condition. Since determination of spatial conformation of hemes using whole-cell is a great challenge in life science, for example in-cell NMR has developed as the most promising technique to obtain structure of protein in atomic resolution. However, the magnitude of OM *c*-Cyts complexes (approximately 200 kDa) hampers the precise analysis of NMR spectrum [20].

As another technique, circular dichroism (CD) spectroscopy has been used to study the inter-heme conformation and interactions with purified peptides and proteins [21-23]. CD represents the difference between the absorption of left and right circularly polarized lights. When a couple of hemes allow electric transitions, the exciton coupling generates large Soret CD peak [22]. Given that the ten hemes with a minimal distance of 4 Å in MtrC (Figure 3-2) would provide a large amplitude in CD signal according to their exciton coupling between π-conjugated systems, which is inversely proportional to cube of the distance [14, 21, 24-25], the application of *S. oneidensis* MR-1 cells to CD spectroscopy might enable the direct observation of heme conformation in native MtrC. However, direct observation of heme protein encoded by single gene in an intact cell remains a challenge, often due to the presence of other heme proteins. Thus, the abundance of heme-

containing genes makes the characterization of MtrC particularly difficult in an intact cell of *S. oneidensis* MR-1 [24]. Here, the author established the whole-cell CD difference spectroscopy using *S. oneidensis* MR-1 wild type (WT) and mutant strain lacking MtrC to acquire the CD signal of MtrC under native conditions.

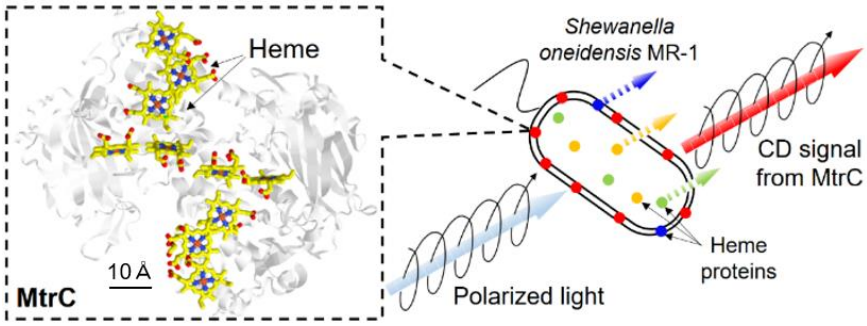

Figure 3-2. Schematic illustration of our whole-cell circular dichroism difference spectroscopy to reveal inter-hemes interaction in MtrC protein *in vivo*.

3.1.2 Methods

Preparation of MtrC protein

MtrC was purified as described previously [14, 26]. The concentration of purified MtrC was determined by UV-vis absorption spectroscopy of the air-equilibrated protein using the extinction coefficient $\varepsilon_{(410nm)}$ = 1.26×10^6 $/M^{-1}$ cm^{-1}.[26] Before the spectroscopic measurement, the MtrC solution was subjected to dialysis and pH was kept at 7.5 with 50 mM HEPES ((2-[4-(2-hydroxyethyl)-1-piperazinyl] ethanesulfonic acid) buffer.

Microbial strains and culture conditions

Shewanella oneidensis MR-1 and *Escherichia coli* K12 was aerobically cultured in 15 mL Luria-Bertani [25 gL^{-1}] medium shaking at 160 rpm for 24 hours at 30°C until stationary growth phase. Subsequently, the cell suspension was centrifuged at 6,000 × *g* for 10 min, and the resultant cell pellet was washed twice with 15 mL Defined Medium (15 mM Sodium succinate, 9.0 mM $(NH_4)_2SO_4$, 5.7 mM K_2HPO_4, 3.3 mM KH_2PO_4, 2.0 mM $NaHCO_3$, 1.0 mM $MgSO_4 \cdot 7H_2O$, and 0.49 mM $CaCl_2$; pH 7.4). Unless noted, the cell density was adjusted by optical density at 600 nm (OD_{600}) as 1.33 ± 0.02 just prior to the measurement. Mutant strains that lacked the *mtrC*, *cymA*, *fccA*, or *PEC* genes were constructed as previously described [27-28].

Instrumentation and conditions for CD spectroscopy and MCD spectroscopy

CD spectroscopy was performed on J-1500 (JASCO) CD spectrometer at room temperature (25 ± 1°C). The spectra are collected in a Pyrex cuvette with path length 1.0 cm under following conditions: 500 nm min^{-1} scan rate, 0.1 nm data pitch (0.5 nm data pitch for purified MtrC), and 5.0 nm bandwidth (1.0 nm bandwidth for purified MtrC).

The cell suspension was incubated for 10 minutes in the presence of oxygen or 30 mM lactate prior to spectral analysis to equilibrate the native MtrC to be oxidized or reduced state, respectively. No spectral change was confirmed over 30 minutes incubation. Unless noted, four and eight spectra were integrated for purified MtrC protein and bacterial cells, respectively. MCD spectroscopy was performed on E-250 (JASCO) spectrometer equipped with a JASCO electromagnet (+1.3~-1.3 T) using the same cuvette with CD spectroscopy under the condition of 600 nm min^{-1} scan rate, 0.5 nm data pitch, and 6.0 nm bandwidth (1.0 nm bandwidth for purified MtrC) at room temperature (25 ± 1°C).

Quantification of MtrC in *S. oneidensis* MR-1 by CD spectroscopy and sodium dodecyl sulfate-polyacrylamide gel electrophoresis (SDSPAGE)

S. oneidensis MR-1 and Δ*mtrC* were aerobically cultured in 200 mL bottle containing 100 mL Luria-Bertani (LB; 25 gL^{-1}) medium shaking at 160 rpm at 30°C and sampled about 15 mL at some timings during growth. The obtained cell suspension was washed twice with 10 mL defined medium. The half of the cell was applied to CD spectroscopy and the other was subjected to disruption by CelLytic B (Sigma-Aldrich) followed by quantification of MtrC in heme-dependent SDSPAGE. In detail, 400 μL of CelLytic B was added to the pellet made of 1.0 mL cell suspension of OD_{600} = 1.0 and the solution was gently mixed. After 15 minutes, the solution was diluted to appropriate concentration by sample buffer and applied to SDSPAGE as described previously [29]. Since the band intensity increases with the amount of heme [30], the author estimated the amount of MtrC from the band intensity measured by free-software, Image J, using the band from horse heart cytochrome *c* as standard curve. The position of band corresponding MtrC protein was confirmed by purification of MtrCAB complex as reported [31].

Electrochemical measurements of current generation from *S. oneidensis* MR-1

Electrochemical experiments were conducted in a single chamber, three-electrode system, as described in chapter 2. The three-electrode system comprised of an indium tin-doped oxide (ITO) substrate (surface area of 3.1 cm^2) as the working electrode at the bottom of the chamber, and Ag/AgCl (KCl saturated) and a platinum wire, which were used as reference and counter electrodes, respectively. *S. oneidensis* MR-1 cells aerobically cultured in 15 mL Luria-Bertani [25 gL-1] medium for 24 hour at 30°C was centrifuged at 6,000 × g for 10 min, and the resultant cell pellet was resuspended in 15 mL of electrochemical medium (pH 7.8) (EM: $NaHCO_3$ [2.5 g], $CaCl_2 \cdot 2H_2O$ [0.08 g], NH_4Cl [1.0 g], $MgCl_2 \cdot 6H_2O$ [0.2 g], NaCl [10 g], yeast extract [0.5 g], and (2-[4-(2-hydroxyethyl)-1-piperazinyl] ethanesulfonic acid [HEPES; 7.2 g] [per liter]) supplemented with 10 mM lactate as the source of carbon for *S. oneidensis* MR-1. The cells were further cultivated aerobically at 30℃ for 12 hours and centrifuged again at 6,000 × g for 10 min. The resultant cell pellet was then washed twice with EM medium by centrifugation for 10 min at 6,000 × g before electrochemical experiment. Four milliliters of EM containing lactate (10 mM), where pH was adjusted by NaOH or H_2SO_4, was deaerated by bubbling with N_2 and added into the electrochemical cell as an electrolyte. The reactor was maintained at a temperature of 303 K and was not agitated during the measurements. A cell suspension of *S. oneidensis* MR-1 in EM with OD_{600} of 0.1 was injected into the electrochemical cell with a potential of +0.4 V versus standard hydrogen electrode (SHE).

CD calculation based on the exciton chirality method

CD calculations based on the exciton chirality method were carried out in both oxidized and reduced MtrC. To calculate the CD spectra, the excited-state energies (ε) and the rotational strengths (R) were evaluated by a diagonalization of a determinant, in which off-diagonal terms (V_{ijkl}) were obtained by a point-dipole approximation. Here, electric transition dipole moments ($\boldsymbol{\mu}_{ij}$), which are necessary parameters for calculating V_{ijkl}, and excitation energies of hemes (σ_{ij}) were obtained by time-dependent density functional theory (TDDFT: Gaussian 09) calculations based on structures of hemes having two imidazole axial ligands in a crystal structure of the oxidized MtrC (PDB code: 4LB8). The TDDFT calculations of hemes of reduced MtrC were carried out by changing the total charge of hemes without changing structure of oxidized MtrC. In the TDDFT calculations, B3LYP correlation function was applied. We used the 6-31G* basis set for the hydrogen, carbon, nitrogen and oxygen atoms, the LANL2DZ basis set for iron ion [32]. In the case of porphyrin analogies, two transitions, whose electric transition dipole moments are degenerate and orthogonal to each other, exist in the Soret band region ($\boldsymbol{\mu}_{ix}$ and $\boldsymbol{\mu}_{iy}$ for unit i). Thus, the determinant of purified MtrC should be evaluated for calculating twenty excited-state energies, ε_n (n = 1−20), and twenty eigenfunctions, Ψ_n (n = 1−20), which is represented by the linear combination of the basis function ϕ_{ij}, which describes unit i (i = 1−10) in the excited state j (j = x, y) as follows.

$$\begin{vmatrix} \sigma_{1x}-\varepsilon & 0 & V_{2x1x} & V_{2y1x} & \cdots & V_{10y1x} \\ 0 & \sigma_{1y}-\varepsilon & V_{2x1y} & V_{2y1y} & \cdots & V_{10y1y} \\ V_{1x2x} & V_{1y2x} & \sigma_{2x}-\varepsilon & 0 & \cdots & V_{10y2x} \\ V_{1x2y} & V_{1y2y} & 0 & \sigma_{2y}-\varepsilon & \cdots & V_{10y2y} \\ \vdots & \vdots & \vdots & \vdots & \ddots & \vdots \\ V_{1x10y} & V_{1y10y} & V_{2x10y} & V_{2y10y} & \cdots & \sigma_{10y}-\varepsilon \end{vmatrix} = 0 \qquad (\mathbf{Eq\ 3-1})$$

Here, σ_{ij} is excitation energy of the heme. Off-diagonal term (V_{ijkl}) is represented under a point-dipole approximation as follows.

$$V_{ijkl} = \frac{\boldsymbol{\mu}_{ij} \cdot \boldsymbol{\mu}_{kl}}{|\mathbf{r}_{ik}|^3} - 3\frac{(\boldsymbol{\mu}_{ij} \cdot \mathbf{r}_{ik})(\boldsymbol{\mu}_{kl} \cdot \mathbf{r}_{ik})}{|\mathbf{r}_{ik}|^5} \qquad (\mathbf{Eq\ 3-2})$$

$\mathbf{r}_{ij}$ denoted the distance vector between i and j. The eigenvalues and eigenvectors were obtained by diagonalizing the matrix. Rotational strength (R_n) is expressed as follows.

$$R_n = \pi \sum_{j=x,y} \sum_{i=1}^{10} \sigma_{ij} c_{ij} \boldsymbol{\mu}_{ij} \cdot \sum_{j=x,y} \sum_{i=1}^{10} c_{ij} \mathbf{r}_i \times \boldsymbol{\mu}_{ij} \qquad (\mathbf{Eq\ 3-3})$$

3.1.3 Results and discussion

Extraordinarily large Soret CD intensity of purified MtrC protein

First, the author examined the extent of exciton coupling among the ten heme centers in MtrC using CD spectroscopy. Purified MtrC in HEPES buffer was added to a Pyrex cuvette with a 1.0 cm optical path length and exhibited a positive peak at 412 nm in the CD spectrum and Soret peak absorption at 410 nm, which was assigned to the hemes in MtrC (Figure 3-3) [26]. Upon MtrC reduction by 0.67 mM $Na_2S_2O_4$, the positive CD peak signal shifted to 420 nm, and relatively small negative signals appeared (Figure 3-3) [24-25]. The peak CD signal intensities in the oxidized and reduced MtrC ($\Delta\varepsilon$) were 1.19×10^3 and 3.86×10^3 $M^{-1}cm^{-1}$, respectively, which are two orders of magnitude larger than that of mono-heme horse heart cytochrome *c* (approximately 17 $M^{-1}cm^{-1}$) [33]. Considering that this intensity is even larger than that of the artificially synthesized bis-porphyrin compound ($\Delta\varepsilon$ is approximately 400 $M^{-1}cm^{-1}$) [24, 34-35], the $\Delta\varepsilon$ of MtrC is extraordinarily large.

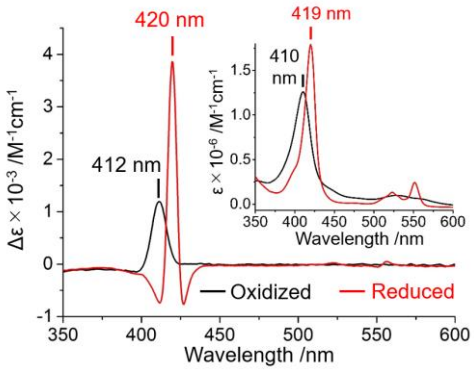

Figure 3-3. Circular dichroism (CD) spectra of purified MtrC in the visible range. Reduced MtrC is indicated by the red line and was achieved by the addition of 0.67 mM $Na_2S_2O_4$ to oxidized MtrC, which is depicted by the black line. Inset: Electronic absorption spectra of purified MtrC.

In order to confirm that exciton coupling among hemes contributes to the Soret CD peak intensity, we calculated the CD spectra with electric transition dipole moment of hemes in MtrC protein based on the exciton chirality method [21, 36]. Although the intensity of calculated Soret CD peak was larger than that of observed CD because of the over-estimation due to the point-dipole approximation, the order of the CD intensity was reproduced by calculation of exciton coupling (Figure 3-4), suggesting the substantial contribution of the exciton coupling to the observed CD intensity. This extraordinarily large CD intensity possibly enables CD spectroscopy of an intact cell to reveal the conformation of native MtrC.

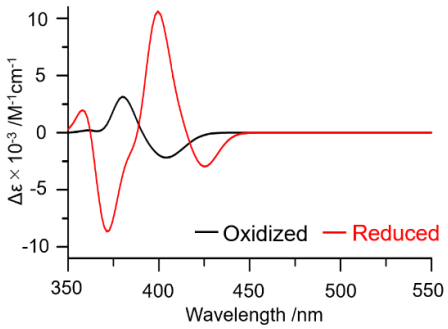

Figure 3-4. Calculated CD spectra of MtrC (oxidized form: black line, reduced form: red line).

Optimization of whole-cell CD spectroscopy enabled the assignment of Soret peaks to native MtrC protein

However, to accomplish the identification of the CD signal of the MtrC protein in intact *S. oneidensis* MR-1 cells, one had to overcome two problems concerning background signal: light scattering and interference from other cytochrome proteins [37]. In Figure 3-5, a broad peak throughout visible light wave range was observed in both cell suspensions of *S. oneidensis* MR-1 and *E. coli*, which diminished by chemical disruption of cells. This indicates that the broad background originates from the light scattering of microbial cell

surface. The author, thus, optimized CD measurement conditions as follows: the cell density was set as an optical density (OD) at 600 nm of 1.33±0.02, and the 1.0 nm bandwidth for purified MtrC was changed to 5.0 nm for intact cells (Figure 3-6).

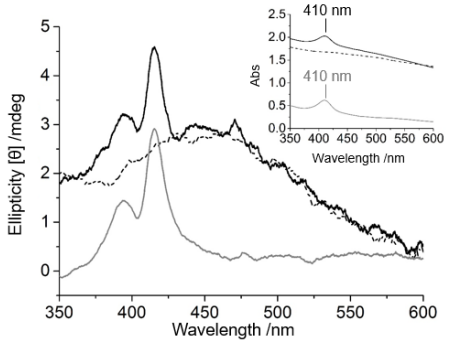

Figure 3-5. CD spectra of *S. oneidensis* MR-1 (black solid line), *E. coli* K12 (black dotted line), and *S. oneidensis* MR-1 broken by CelLytic B (gray solid line). While broad peak was observed throughout visible light wave range in *S. oneidensis* MR-1, almost identical peak appeared in the cell suspension of *E. coli* and diminished by chemical disruption of cells, indicating that the broad background originates from the light scattering of microbial cell surface. Inset: Absorption spectra obtained simultaneously with CD spectra.

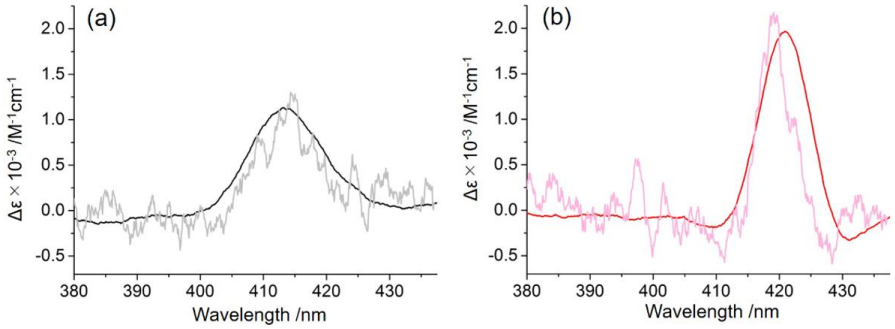

Figure 3-6. (a) Whole-cell CD difference spectra between WT and *ΔmtrC* strain of *S. oneidensis* MR-1 under aerobic condition in the absence of lactate (oxidized state) (a) and under anaerobic condition in the presence of lactate (reduced state) (b). Black and red lines were obtained with bandwidth as 5.0 nm and OD_{600} as 1.33±0.02. In contrast, when whole-cell CD spectra were measured at OD_{600} = 0.67±0.01 in the identical condition with purified MtrC (1.0 nm bandwidth, 50-time integration), the signal-to-noise ratio was poor as seen in gray and pink lines. To prevent the reduction of MtrC by metabolically generated electrons during measurement in (a), 30 mM fumarate was supplemented.

Second, the author minimized interference from the other cytochromes in *S. oneidensis* MR-1 cells by subtracting the CD spectrum from a mutant with a deletion in the gene encoding the MtrC protein (*ΔmtrC*) from the WT spectrum. The CD spectrum of WT suspended in defined-medium in a Pyrex cuvette with a 1.0 cm path length showed a strong signal near the Soret band, which was clearly diminished in *ΔmtrC* (Figure 3-7a). The difference in the CD spectrum between WT and *ΔmtrC* showed a large signal with a peak at 413 nm, which is almost identical in wavelength to the purified MtrC protein (Figure 3-7c). Furthermore, the reduction of native MtrC in *S. oneidensis* MR-1 by the addition of an electron donor, 30 mM lactate, under anaerobic condition shifted the peak to a longer wavelength centered at 421 nm with splitting signals (Figures 3-7b and c). The peak position and peak width in both the oxidized and reduced states were almost identical to the CD spectrum of the purified MtrC protein (Figure 3-7c).

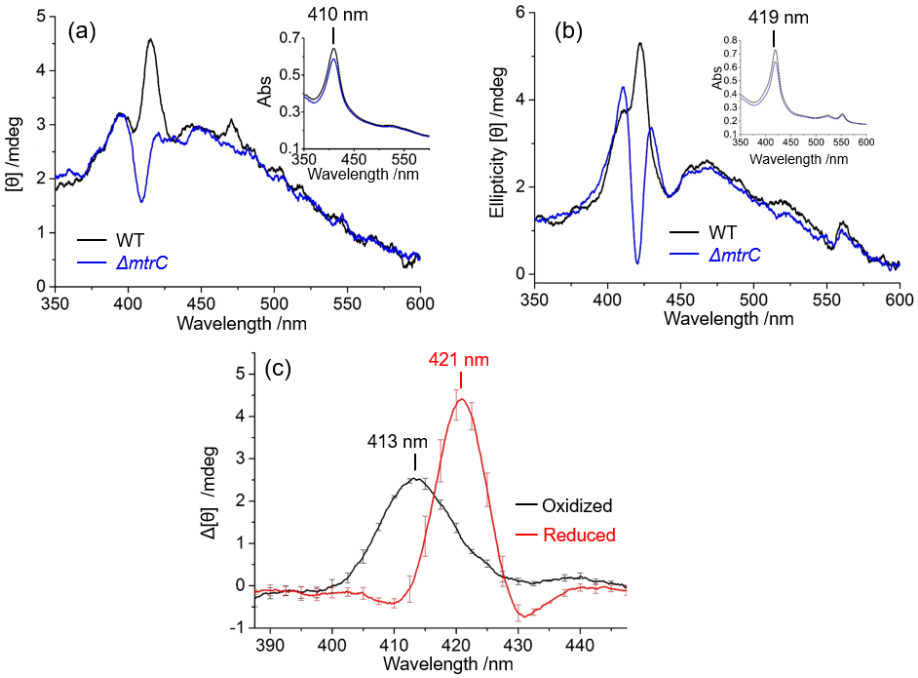

Figure 3-7. CD spectra of whole *S. oneidensis* MR-1 cells (wild-type, WT; black line) and a mutant strain deficient for the *mtrC* gene (*ΔmtrC*; blue line) under aerobic condition in the absence of lactate (oxidized state) (a) and under anaerobic condition in the presence of lactate (reduced state) (b). The cell density was adjusted to OD_{600}=1.33±0.02. Inset: Absorption spectra of the same samples in diffused transmission mode. (b) Differences in CD spectra between WT and *ΔmtrC* oxidized by oxygen (black line) and reduced by 30 mM lactate (red line). The error bars represent the mean±SEM obtained using three individual samples and eight measurements each.

Correlation of the intensity of the Soret CD peak with the concentration of the MtrC protein in cell suspension confirmed the assignment of the CD peak signals as native MtrC. Figure 3-8 shows the relationship between the intensity of the whole-cell CD difference spectrum at 413 nm ($\Delta[\theta]_{(413nm)}$) and the amount of MtrC in the cell suspension during various aerobic growth phases estimated by SDS-PAGE [29-30]. Consistent with a previous report [38], the MtrC concentration in the cell suspension increased depending on the growth phase and the deletion of *mtrC* gene had scarce impact on gene expression of other major proteins (Figures 3-8 and 3-9). While the Soret

absorption peak intensity indicates that the amount of MtrC is less than 20 % of total cytochrome proteins (Figure 3-7a and b inset), the $\Delta[\theta]_{(413nm)}$ linearly increased with MtrC concentration, and the squares of the correlation coefficient of 0.979 (black line in Figure 3-8) passed through the origin. This direct positive relationship strongly suggests that the whole-cell CD difference spectrum in the Soret region represents the signal from the native MtrC protein. In contrast, the amounts of other cytochromes in the cell fluctuate in each growth phase, as the absorption peak intensity at 410 nm showed poor correlation with the amount of the MtrC protein (Figure 3-8b inset, R^2=0.746), further supporting that the Soret CD signal is specific for the MtrC protein in native environment.

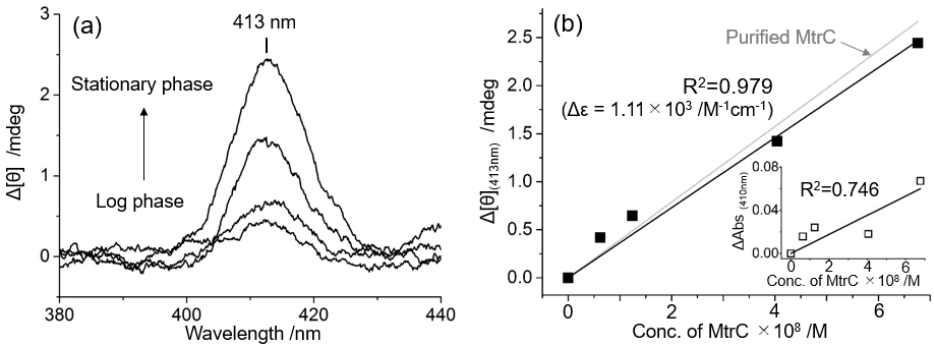

Figure 3-8. (a) The differences in CD spectra between WT and *ΔmtrC* at various growth phases in the oxidized state. (b) Plots of the changes in CD signal intensity at 413 nm observed in (a) ($\Delta[\theta]_{(413nm)}$) against the MtrC concentration in the cell suspension. The squares of the correlation coefficients (R^2=0.979, black line) include the point of origin. The gray line represents the CD signal intensity for purified MtrC at 412 nm estimated from $\Delta\varepsilon=1.19\times10^3$ $M^{-1}cm^{-1}$. Inset: The plots of ΔAbs at 410 nm between WT and *ΔmtrC* against the MtrC concentration.

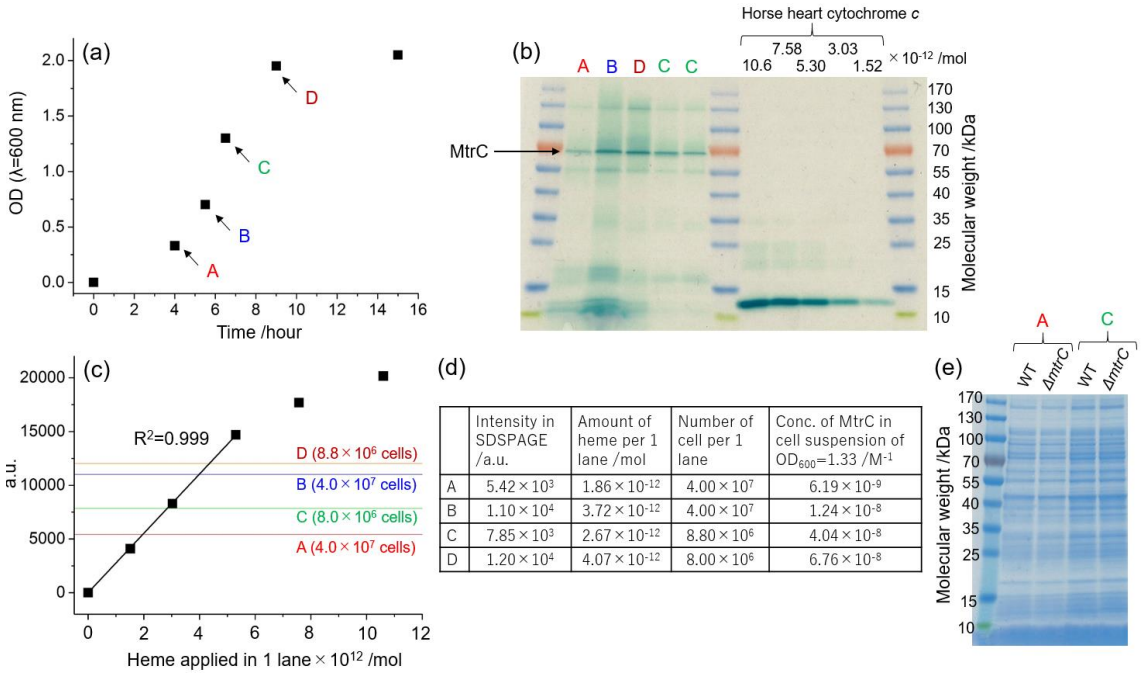

	Intensity in SDSPAGE /a.u.	Amount of heme per 1 lane /mol	Number of cell per 1 lane	Conc. of MtrC in cell suspension of OD_{600}=1.33 /M^{-1}
A	5.42×10^3	1.86×10^{-12}	4.00×10^7	6.19×10^{-9}
B	1.10×10^4	3.72×10^{-12}	4.00×10^7	1.24×10^{-8}
C	7.85×10^3	2.67×10^{-12}	8.80×10^6	4.04×10^{-8}
D	1.20×10^4	4.07×10^{-12}	8.00×10^6	6.76×10^{-8}

Figure 3-9. Quantification of MtrC by SDSPAGE. (a) Growth curve of *S. oneidensis* MR-1 during aerobic cultivation. The points from A to D were sampled and subjected to disruption followed by SDSPAGE. (b) SDSPAGE stained by a method specific for heme proteins. The samples from A to D in (a) and horse heart cytochrome *c* are tested. The arrow indicates the band for MtrC, which is confirmed by SDSPAGE for purified of MtrCAB complex from *S. oneidensis* MR-1. Note that the number of *S. oneidensis* MR-1 cells applied to each lane is different among the sample from A to D (A, 4.0×10^7 cells; B, 4.0×10^7 cells; C, 8.0×10^6 cells; D, 8.8×10^6 cells, assuming that OD_{600} = 1.0 represents 1.0×10^9 cells per mL) (c) The calibration curve for the intensity of the band for horse heart cytochrome *c* in (b) against the amount of hemes. The intensity was measured by free-software, Image J. (d) Estimation of MtrC concentration in each sample from A to D based on the calibration curve obtained in (c). (e) Comparison of SDSPAGE of wild type (WT) and *ΔmtrC* stained by Coomassie blue. The profile showed little difference between WT and *ΔmtrC*, suggesting that the deletion of *mtrC* gene has scarce impact on gene expression of major proteins other than MtrC.

CD spectra of mutant *S. oneidensis* MR-1 strains support the Soret peak assignment to native MtrC

The author also obtained the CD spectra of several mutant strains deleting genes corresponding with major cytochromes in *S. oneidensis* MR-1. Another Soret CD peak at 394 nm in the WT suspension in the presence of oxygen (Figure 3-7a) was completely absent in a mutant strain containing the complete deletion of the periplasmic electron carrier, termed *ΔPEC*, which lacked the *mtrA*, *mtrD*, *dmsE*, and *SO4360* genes that encode the periplasm-facing units of the OM *c*-Cyts (Figure 3-10 and 3-11). Deletion of the genes encoding representative intracellular cytochrome proteins (CymA or FccA: Figure 3-10), however, did not lead to the elimination of either of the two Soret CD peaks (Figure 3-12). These data indicate that the Soret peaks in whole-cell CD spectra predominantly originate from the OM *c*-Cyts, not cytochromes inside cells, further supporting our model that whole-cell CD difference spectra reflects the heme geometry in native MtrC protein.

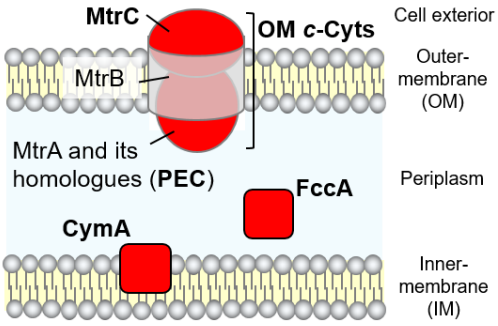

Figure 3-10. Location of OM *c*-Cyts, CymA, and FccA in *S. oneidensis* MR-1 cell. Heme-containing proteins are illustrated in red color.

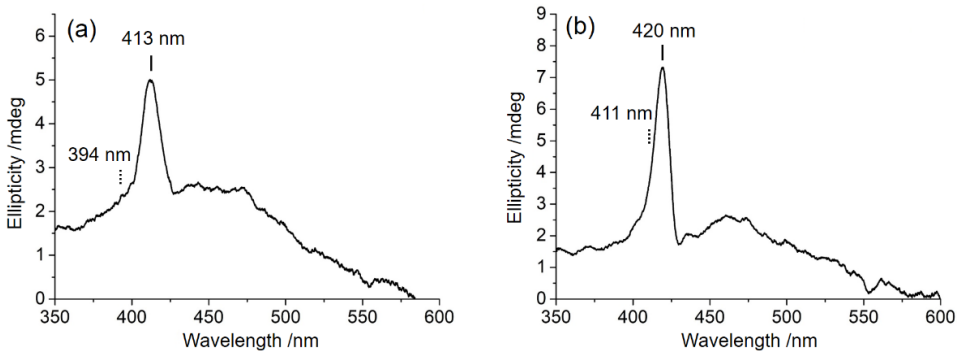

Figure 3-11. Whole-cell CD spectra of mutant *S. oneidensis* MR-1 strain named *ΔPEC*, lacking four genes of *mtrA*, *mtrD*, *dmsE*, and *SO4360* in the presence of 50 mM fumarate under aerobic condition (a) or 30 mM lactate under anaerobic condition (b).

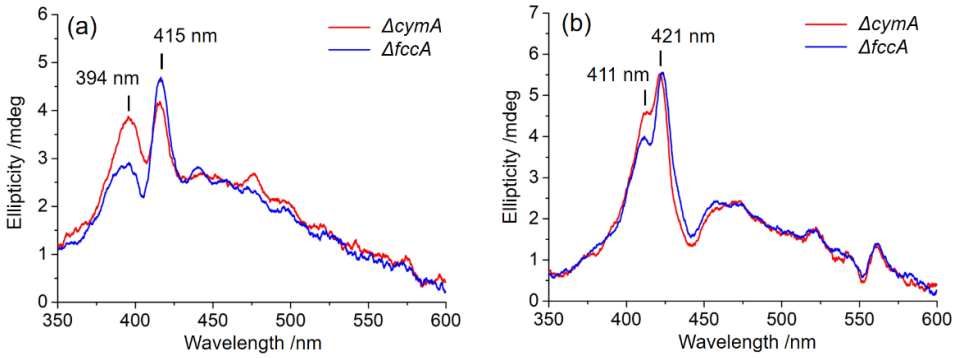

Figure 3-12. Whole-cell CD spectra of mutant *S. oneidensis* MR-1 strain lacking *cymA* gene (*ΔcymA*, red line) or *fccA* gene (*ΔfccA*, blue line) in the presence of 50 mM fumarate under aerobic condition (a) or 30 mM lactate under anaerobic condition (b).

Native MtrC shows distinct CD spectra from purified MtrC under reduced state

In order to obtain structural insights into hemes in native MtrC, the CD spactra of native MtrC and that of purified one were compared. The Soret CD peak intensity of oxidized native MtrC obtained from the slope in Figure 3-8b ($\Delta\varepsilon_{(413nm)}$=1.11×10^3 M^{-1}cm^{-1}) was almost identical to that of purified MtrC ($\Delta\varepsilon_{(412nm)}$=1.19×10^3 M^{-1}cm^{-1}), indicating that native MtrC maintains the arrangement of heme centers. In contrast, once native MtrC was reduced, the Soret CD intensity (whole-cell: $\Delta\varepsilon$ = 1.97×10^3 M^{-1}cm^{-1}) was

approximately twofold lower than that of purified MtrC ($\Delta\varepsilon = 3.86\times10^3\ M^{-1}cm^{-1}$), and the splitting signals around the positive peak at 420 nm were suppressed (Figure 3-13a), indicating the possibility of a conformational change in native MtrC associated with the reduction reaction. Furthermore, purified MtrC exhibited a Soret CD signal with a distinct pH dependency in the reduced state (Figure 3-13b). In the oxidized state, both purified and native MtrC maintained the Soret peak at a similar intensity throughout the physiological pH range. However, reduced native MtrC exhibited a drastic decrease in $\Delta\varepsilon$ of Soret CD peak at a pH of approximately 7 that was not observed in purified MtrC (Figure 3-13b). These distinct CD profiles suggest that the inter-heme interaction of reduced MtrC differs between in native and purified system. Consistently, it was confirmed that the extent of pH-dependent $\Delta\varepsilon$ decrease of native reduced MtrC was larger than that of absorption peak intensity (Figure 3-14), supporting that the change of electric transition dipole moment among hemes most likely occur at a pH of approximately 7 [21-22]. This is consistent with the conclusion that the decrease of $\Delta\varepsilon$ reflects the conformation change of hemes in MtrC dependent on pH.

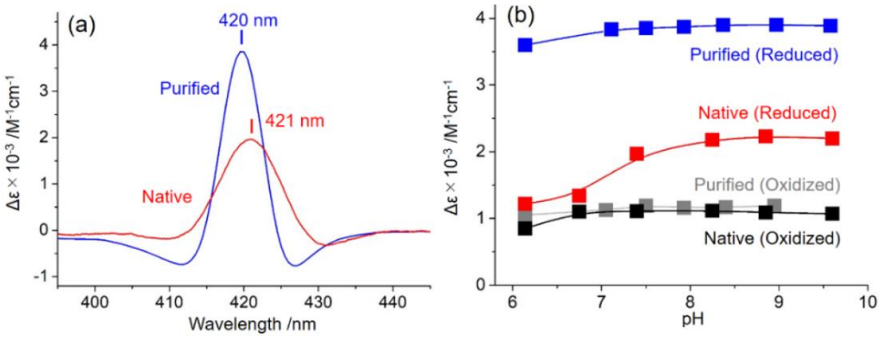

Figure 3-13. (a) CD spectra of purified MtrC (blue line) and native MtrC in whole cells (red line) in the reduced state at pH values of 7.5 and 7.4, respectively. The $\Delta\varepsilon_{(420nm)}$ for purified MtrC and the $\Delta\varepsilon_{(421nm)}$ for native MtrC are $3.86\times10^3\ M^{-1}cm^{-1}$ and $1.97\times10^3\ M^{-1}cm^{-1}$, respectively. (b) Soret peak intensities in the CD spectra of purified reduced MtrC ($\Delta\varepsilon_{(420nm)}$, blue), native reduced MtrC ($\Delta\varepsilon_{(421nm)}$, red), purified oxidized MtrC ($\Delta\varepsilon_{(412nm)}$, gray), and native oxidized MtrC ($\Delta\varepsilon_{(413nm)}$, black) as a function of pH.

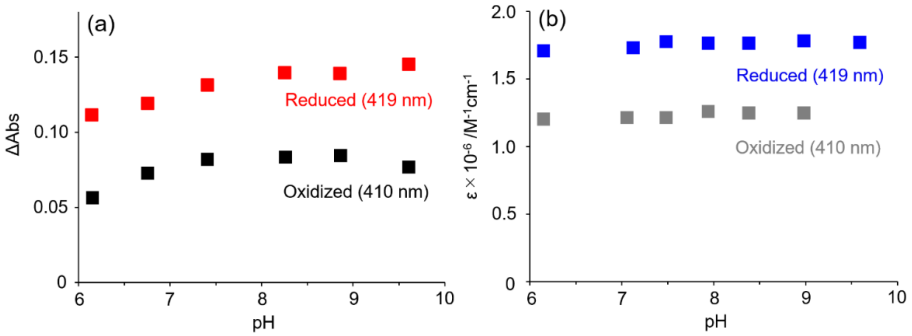

Figure 3-14. (a) Plots of the Soret ΔAbs between WT and *ΔmtrC* as a function of pH. Black and red plots represent the oxidized (410 nm) and reduced (419 nm) state, respectively. (b) Soret extinction coefficient of purified MtrC protein as a function of pH. The blue and gray plots represent the MtrC in reduced state and oxidized state, respectively.

Further analyses with magnetic CD spectroscopy and whole-cell electrochemistry support *in vivo*-specific inter-hemes interaction in MtrC

In addition to inter-heme interaction, aromatic amino acids in the vicinity of hemes, specifically bis-histidine coordinated to deca-hemes, potentially alter CD amplitude [39-40]. Therefore, the author conducted magnetic CD (MCD) spectroscopy to examine the coordination state of heme centers in reduced native and purified MtrCs (Figure 3-15). In oxidized state, both the purified MtrC and whole-cell showed a dispersion type Faraday A term at Soret region, which is consistent with the feature of two histidine residues as axial ligands reported as oxidized crystal structure [14]. After reduction, Faraday A term was observed with center wave length around 550 nm in both the purified and native MtrC, which is a characteristic of the low-spin ferrous state [41]. Notably, this spectral tendency is consistent with reduced heme with histidine residues as axial ligands, e.g. *c*-Cyt isolated from *Shewanella frigidimarina* NCIMB400 [41]. Furthermore, the positive CD signal observed at the Soret band of reduced MtrC in whole-cell (Figure 3-13a) is similar

to the CD spectra of c_3-Cyt purified from *Shewanella oneidensis* TSP-C, which has two histidine residues as axial ligands [42]. Thus, these MCD and CD spectra suggest that the reduced MtrC in whole-cell maintains the coordination of bis-histidine and has little effect on Soret CD peak intensity. Therefore, the CD signal decrease in reduced MtrC in native compared with purified system (Figure 3-13a) and at a pH of approximately 7 in native reduced MtrC (Figure 3-13b) are likely assignable to changes in inter-heme interaction.

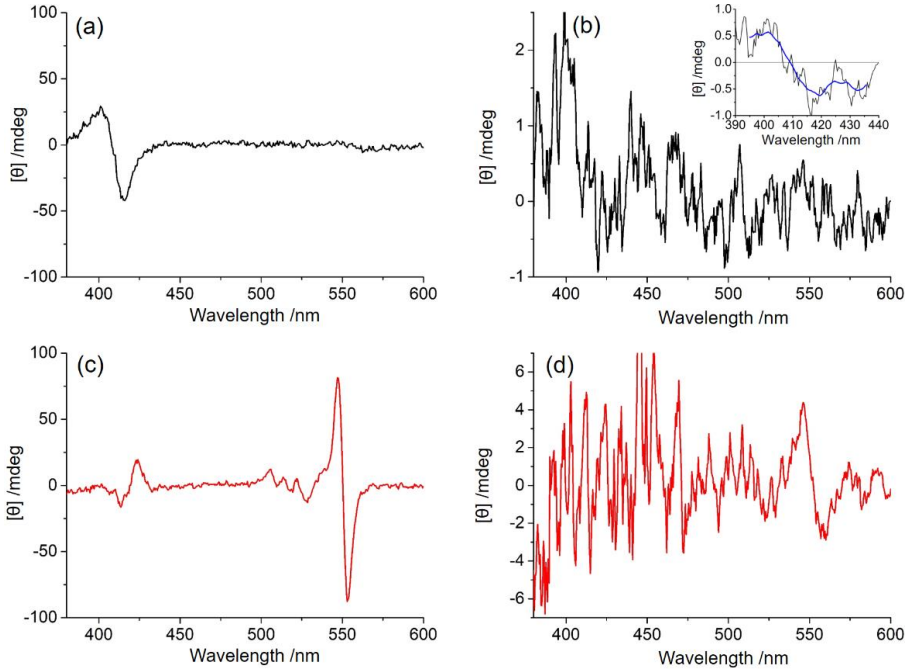

Figure 3-15. Magnetic circular dichroism (MCD) spectra of purified MtrC in oxidized state (a) and reduced state (c), and MCD difference spectra between WT and *ΔmtrC* in the absence of (oxidized state) (b) and the presence of lactate (reduced state) (d). 0.89 μM MtrC was used in (a) and (c), and the cell density was adjusted to OD_{600} = 0.60 ± 0.01 in (b) and 1.33 ± 0.02 in (d) prior to the measurement. Spectra were integrated 50 times in (b) and (d), and 200 times in inset (b), of which smoothed line is represented as blue. For maintaining oxidized state of MtrC during integration in (b), 50 mM fumarate was supplemented.

Accordingly, the electron transport kinetics through the heme centers in native MtrC represented a similar pH dependency with CD signal. A whole-cell electrochemical

assay was performed to probe the microbial lactate-oxidation current, which is limited by the rate of electron transport via OM *c*-Cyts under our experimental conditions (Figure 3-16) . At a pH below 7, current production at +0.4 V (versus a standard hydrogen electrode) significantly decreased compared with higher pH conditions (Figure 3-16), suggesting that the CD signal decrease at pH of between 7.4 and 6.8 corresponded with the rate of electron transport via the heme conduit in MtrC. In contrast, such pH dependency was not observed in the redox property of purified MtrC protein [26], which is also consistent with the pH susceptibility of CD signal in purified MtrC (Figure 3-13b). Assuming that the conformational change of hemes in reduced native MtrC decreases the electron flux, the critical conformational change may occur in T-shaped heme pairs (1,3 and 6,8) and coplanar heme pairs (2,1, 1,6 and 6,7) (Figure 3-17a) because they mediate slower electron transport reactions than other stacked heme pairs in MtrF, which is a homologue of MtrC [13]. Given that the orientation change in T-shaped heme pairs potentially alters the electron transfer matrix element over 1000 times [43], T-shaped heme pairs are the most likely candidates causing the decrease of electron transport rate. Similarly, the $\Delta\varepsilon$ calculation based on the exciton chirality method [21, 36] indicated that the T-shaped heme pairs have a larger impact on not only electron transport kinetics but also CD signal intensity compared with coplanar pairs (Figure 3-17b) [24, 34]. However, given the stacked heme pairs provided more significant contribution in $\Delta\varepsilon$ value, the pH dependent conformational change in reduced native MtrC may not be limited to T-shaped heme pairs but also heme conduit as a whole.

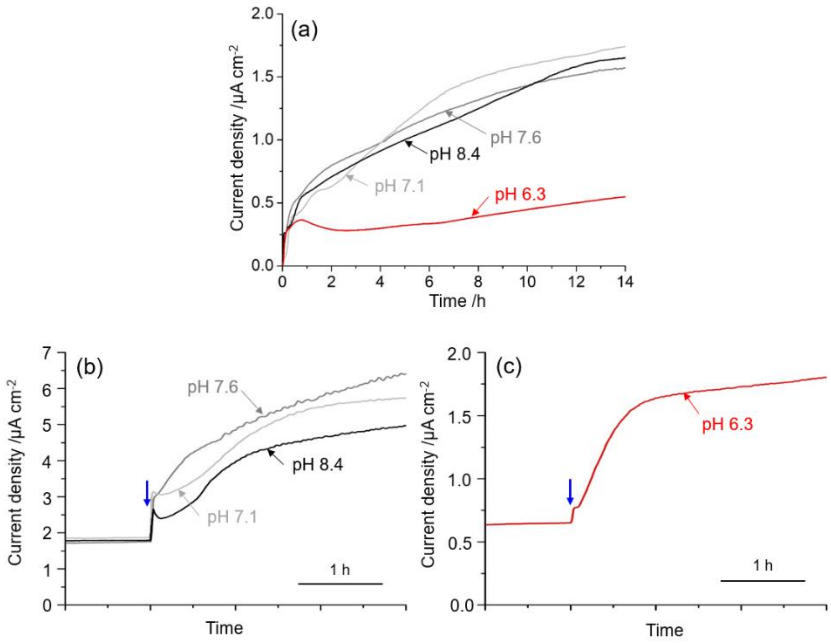

Figure 3-16. (a) Time course for the current production from *S. oneidensis* MR-1 cells in the presence of 10 mM lactate on an ITO electrode under +0.4 V (versus SHE) at various physiological pH. The cell suspension was injected into the electrochemical reactors at t = 0. The pH of the medium in the electrochemical reactors is indicated. The same tendency was observed in at least two individual experiments. (b), (c) Effect of 2.0 μM flavin mononucleotide (FMN) addition into the same electrochemical reactors with (a) on the current production. Blue arrows indicate the timing of FMN addition. The addition of FMN drastically increased the current production in all the condition, demonstrating that the electron transport via outer-membrane *c*-type cytochrome complex (OM *c*-Cyts) limits the current production as described in chapter 2.

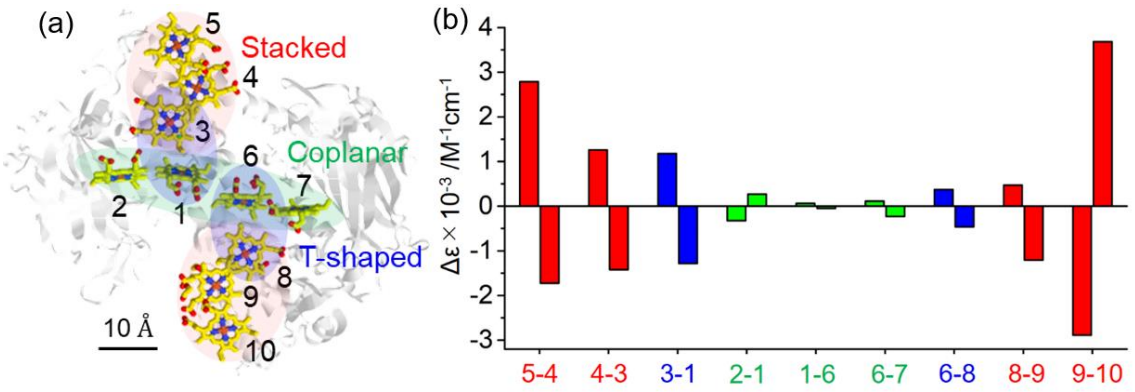

Figure 3-17. (a) Crystal structure of the MtrC protein highlighting the deca-hemes (PDB code: 4LM8) [14]. The heme numbers and heme pair motifs are indicated. (b) Calculated peak CD intensities based on the exciton interaction between adjacent heme pairs in the reduced MtrC. The bars are colored according to the inter-hemes orientation: stacked in red, T-shaped in blue, and coplanar in green. The dispersion-type peak CD signals are devided into shorter and longer wavelength parts, represented by left-side and right-side bars, respectively. In each CD calculation, the only off-diagonal term concerning the adjacent heme was considered.

Considering that the significant suppression in Soret CD signal in native MtrC was diminished in purified MtrCAB complex (Figure 3-18), the *in vivo*-specific conformational change is potentially caused by unfolding reaction of reduced MtrC assisted by other components of OM *c*-Cyts such as OmcA, other membrane proteins, and/or lipopolysaccharide [44]. It would be, therefore, interesting to further identify the critical molecular aspects using a combination of whole-cell CD spectroscopy and biochemical techniques such as point mutations.

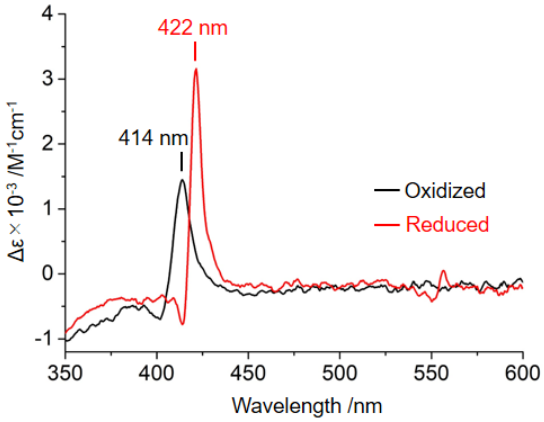

Figure 3-18. CD spectra of MtrCAB complex, which was purified as reported previously [31]. Reduced MtrCAB (red line) was achieved by the addition of 1.0 mM $Na_2S_2O_4$ to oxidized MtrCAB (black line).

Implications of pH-dependent conformational change of hemes on proton-limited electron transport through OM *c*-Cyts

In chapter 2, the deuterium experiments showed large kinetic isotope effect (KIE) on EET process through OM *c*-Cyts, indicating the rate limitation of EET by coupled proton transport reactions. However, it is still unclear which proteins have the rate-limiting proton transport pathways; OM *c*-Cyts, or other proteins located OM, IM, and periplasm. For identification of the proton pathway, KIE values of some of gene deletion mutants were tested in chapter 2, but no mutants showed distinct KIE from that of WT. In the viewpoint of proton pathway identification, the pH-dependent CD change in Figure 3-13b has contribution. Given that the EET rate decreased at pH below 7 as demonstrated in Figure 3-16, the pH value impacts on the rate-limiting proton transport coupled with EET. Together with the change in current production, the CD signal of reduced MtrC in intact cell decreased at pH of between 7.4 and 6.8 (Figure 3-13b). This correspondence of proton transport rate with CD signal intensity strongly suggests that the rate-limiting

proton pathway is involved in inter-heme interaction in MtrC, e.g. propion side chain of hemes or ligated histidines on hemes in MtrC.

This model fit well with the proposal that periplasmic protons are expelled across a proton conductive "wire" (exceeding 100 Å) across OM *c*-Cyts associated with EET to maintain charge neutrality as mentioned in chapter 2. While such a proton transfer pathway has not been identified in the crystal structures of OM *c*-Cyts in the oxidized state [14, 45], rearranged heme geometry and hydrogen-bond networks in the vicinity of hemes in intact cell suggested by the whole-cell CD difference spectroscopy may construct the proton "wire". It would be great interest to combine CD spectroscopy and point mutations from the viewpoint of identification of proton pathway in molecular-level.

3.1.4 Conclusion

In this chapter 3-1, the author established whole-cell difference CD spectroscopy to investigate inter-heme interactions in native MtrC protein by using wild-type and a mutant strain lacking MtrC in *S. oneidensis* MR-1. Comparisons of MtrCs in purified and native systems suggested that the heme conformation in reduced MtrC is altered in whole cells probably due to interactions with other components of OM *c*-Cyts such as OmcA, other membrane proteins, and/or lipopolysaccharide. Gaining insight into multi-heme cytochromes in an intact cell by using mutant strains has broad applicability beyond the bacterial species, such as *Geobacter sulfurreducens* PCA [46-47]. It is anticipated that the combination of this whole-cell CD spectroscopy method with electrochemistry would enable monitoring of MtrC conformation in a state where the equilibrium is shifted by continuous electron flow in a thermodynamically open system [37, 48], which is fundamental for understanding biological redox reactions.

3.2

Geometrical changes of the hemes in MtrC induced by minerals provide insight into the binding characteristic of microbe-mineral interaction

3.2.1 Introduction

Dissimilatory metal-reducing bacteria have the ability to sense physical contact with extracellular solid materials and thereby form an electrical connection. This connection provides an external microbial respiratory chain that incorporates environmental minerals, which enables microbes to generate energy and survive in a nutrient-limited environment [49]. The electrons that are transported from the microbes reduce and dissolve minerals, driving the geochemical cycling of various elements, such as Fe, Mn, S, and C [7, 50-51], in a variety of environmental settings [52-53]. This process can also be utilized with electrode surfaces [54-55], which has significant implications for the development of bioelectrochemical technologies, such as microbial fuel cells [54-55] and electrode biosynthesis [11]. The electrical connections are made via OM *c*-Cyts. Therefore, the molecular mechanisms underlying the interaction of OM *c*-Cyts and solid materials have been extensively studied.

One of the best-studied proteins is MtrC, which is a deca-heme *c*-type cytochrome that is a cell-exposed unit in OM *c*-Cyts within the metal-reducing bacterium *S. oneidensis* MR-1 [14, 56]. Various crystallographic and biochemical studies have revealed the molecular basis of the binding of MtrC and its homologues/paralogues (MtrF, OmcA,

and UndA) to minerals [8, 12, 45, 57-58]. Rapid electron transport between microbes and minerals is proposed to be mediated by MtrC via its binding to minerals by way of near-edge heme [56, 59]. However, these studies have been limited to the examination of purified protein dissolved in solution, instead of proteins within an intact cell. Given that MtrC in an intact cell may interact with minerals differently than MtrC suspended in solution due to the structural constraints imposed on the protein during the formation of OM *c*-Cyt complexes embedded in a fluid phospholipid membrane, it is essential to monitor the binding of MtrC protein to minerals within a living model system. Although the processes involved in adhesion in intact *S. oneidensis* MR-1 have been studied using a variety of techniques, such as atomic force microscopy [60-61], transmission electron microscopy [62-63] and attenuated total reflection infrared reflection spectroscopy [64-65], the chemical or physical mechanisms underlying the interaction of the MtrC protein with minerals in intact cells still remains unclear, mainly due to the complexity of the microbe-solid interface. *S. oneidensis* MR-1 localizes a variety of other biomolecules to the cell membrane in addition to OM *c*-Cyts. These biomolecules include lipopolysaccharides, extracellular polymeric substances, and other membrane proteins [66], which can interfere with the detection of the MtrC-mineral interaction in intact cells.

In chapter 3-1, the author has developed whole-cell CD difference spectroscopy, which can be used to measure the heme geometry of native MtrC proteins in intact *S. oneidensis* MR-1 cells. Given that mechanical interaction with a solid surface may potentially induce conformational changes in OM *c*-Cyts [8, 17, 67], changes in the CD signal may provide information about the characteristics of MtrC-mineral binding. Here, the author studied the binding mechanism of MtrC in both intact cells and in the purified state using CD spectroscopy. The CD spectra obtained in the presence and absence of minerals

were compared to obtain valuable molecular insights into the geometrical changes in the heme centers of the MtrC protein that occur upon its interaction with minerals. Moreover, CD spectra were obtained using various concentrations of mineral nanoparticles with both oxidized and reduced MtrC to further quantify the binding affinity of MtrC with minerals. The author also discusses the insights gained during this study regarding the flexibility of heme geometry and the binding affinity of MtrC associated with microbe-mineral interactions and speculate on their implications for our understanding of the microbial ecophysiology of the mineral surface and electron transport mechanisms.

3.2.2 Methods

CD spectroscopy to monitor the inter-heme interactions in MtrC in the presence or absence of hematite nanoparticles

Cultivation of *S. oneidensis* MR-1 and purification of MtrC protein were conducted as described in chapter 3-1. CD spectroscopy was performed on a J-1500 (JASCO) CD spectrometer, and the temperature was maintained at 20 ℃ by an accessory Peltier element. The parameter for CD measurements are identical with that in chapter 3-1. The mixture containing the cell suspension and hematite was stirred at 200 rpm in a Pyrex cuvette to prevent precipitation during subsequent measurements. The CD spectra were integrated 9 times, and the high tension (HT) voltage that was applied to the photomultiplier tube was maintained below 550 V during every measurement to guarantee the validity of the data. The CD spectra of the oxidized OM *c*-Cyts were obtained from a cell suspension under aerobic conditions in the presence of 50 mM fumarate, while those of the reduced OM *c*-Cyts were obtained under anaerobic conditions in the presence of 30 mM lactate [68]. The CD spectra of *ΔmtrC* strain bacteria were also obtained using the same conditions to calculate the whole-cell differences in CD spectra for the wild-type (WT) and *ΔmtrC* strains of *S. oneidensis* MR-1. The CD spectra of the purified MtrC protein at 0.20 μM were obtained in a solution of 50 mM HEPES buffer with 100 mM NaCl at pH 7.4.

Scanning transmission electron microscopy (STEM) to visualize the association of *S. oneidensis* MR-1 with hematite nanoparticles

Hematite nanoparticles at 13 mM were added into a cell suspension of *S. oneidensis* MR-1 in defined medium with an OD_{600} of 1.33±0.02. After incubation for 40 min at room temperature, the microbe-nanoparticle suspension was collected by centrifugation at 6000 × *g* for 5 min and immediately fixed in a mixture of 4% paraformaldehyde and 2.5% glutaraldehyde on ice. After fixation, the sample was centrifuged at 6000 × *g* for 5 min and was washed with 50 mM HEPES ((2-[4-(2-hydroxyethyl)-1-piperazinyl] ethanesulfonic acid) buffer at pH 7.4 three times. The sample was subsequently dehydrated in 25%, 50%, 75%, and 100% ethanol for 15 min each, then directly applied onto a 200 mesh copper grid coated with carbon-sputtered film (Nisshin EM). The sample was dried overnight and imaged with a JEM-ARM200F microscope operated at 80 kV.

Estimation of the free energy of binding of the reaction between purified MtrC protein and hematite nanoparticles

The author estimated the free energy of binding for the reaction between purified MtrC and hematite nanoparticles using a sedimentation assay. The standard Gibbs free energy ($\Delta G^{\circ\prime}$) of the binding reaction was calculated based on the Langmuir adsorption model. Hematite nanoparticles at 1.0 mM in 1.5 mL of solution containing 50 mM HEPES buffer and 100 mM NaCl at pH 7.4 were mixed with various concentrations of MtrC protein and then incubated at 293 K for 10 min to equilibrate the binding reaction. The mixture was then centrifuged at 15,000 × *g* for 3 min. The concentration of the unbound MtrC in solution ([MtrC]/M) and the amount of MtrC bound to hematite (Γ/mol) was determined using UV-vis absorption spectroscopy. Within the framework of the Langmuir isotherm, the standard Gibbs free energy, $\Delta G^{\circ\prime}$, can be determined as follows:

$$\frac{[\mathbf{MtrC}]}{\Gamma} = \frac{1}{\Gamma_M} \cdot [\mathbf{MtrC}] + \frac{1}{a \cdot \Gamma_M} \quad (\mathbf{Eq\ 3-4})$$

$$\Delta G^{\circ\prime} = -RT \cdot \ln(a) \quad (\mathbf{Eq\ 3-5})$$

where Γ_M is the theoretical maximum amount of MtrC that can be bound to hematite, and a is the adsorption/desorption equilibrium constant. Since the sedimentation assay provides the values of [MtrC] and Γ, the linear regression of [MtrC]/Γ against [MtrC] gives $\Delta G^{\circ\prime}$.

Estimation of the amount of MtrC-hematite complex at the intact cell surface in the presence of various concentrations of hematite nanoparticles

When it is assumed that a single hematite nanoparticle binds with each MtrC protein present on the intact cell surface, thereby altering the heme geometry of MtrC, the CD peak intensity relates to the ratio of MtrC bound to the nanoparticles according to the following equation:

$$(1-\theta) \cdot \Delta\varepsilon_0 + \theta \cdot \Delta\varepsilon_1 = \Delta\varepsilon_x \quad (\mathbf{Eq\ 3-6})$$

where θ is the ratio of MtrC bound to the hematite nanoparticle, and $\Delta\varepsilon_0$, $\Delta\varepsilon_1$, and $\Delta\varepsilon_x$ are the CD coefficients of unbound MtrC, bound MtrC, and a sample with a given concentration of hematite, respectively. Thus, the ratio of MtrC bound to hematite nanoparticles can be described by:

$$\theta = \frac{\Delta\varepsilon_x - \Delta\varepsilon_0}{\Delta\varepsilon_1 - \Delta\varepsilon_0} \quad (\mathbf{Eq\ 3-7})$$

In this study, $\Delta\varepsilon_0$ was set as $1.11\times10^3/M^{-1}\ cm^{-1}$ (at 413 nm) and $1.97\times10^3/M^{-1}\ cm^{-1}$ (at 421 nm) for MtrC in the oxidized and reduced states, respectively, as chapter 3-1. $\Delta\varepsilon_1$ was estimated based on Figure 3-26 to be $0.60\times10^3/M^{-1}\ cm^{-1}$ (at 413 nm) and $1.45\times10^3/M^{-1}$

cm^{-1} (at 421 nm) for the oxidized and reduced states, respectively. To quantify the coverage of MtrC during its association with a single hematite nanoparticle, a hematite nanoparticle was redefined as one molecule, and the concentration was recalculated as shown in Figure 3-27. Briefly, the number of hematite nanoparticles was calculated based on the average volume of a nanoparticle ($7.3\times10^3/nm^3$) as estimated using images obtained during transmission electron microscopy and subsequently divided by Avogadro's number to obtain an equivalent number of moles per liter [69]. The total amount of MtrC protein at the intact cell surface was calculated at 413 nm using the Soret CD intensity of the sample without hematite nanoparticles. The concentration of unbound hematite nanoparticles was estimated using the difference between the concentration of the added nanoparticles and that of MtrC bound to nanoparticles.

The curve derived from the Langmuir model using the identical $\Delta G^{\circ\prime}$ of the binding reaction between the purified MtrC proteins and the hematite nanoparticles that is superposed on Figure 3-27 was calculated according to the following equation:

$$\boldsymbol{\theta = \frac{a\cdot[\text{hematite}]}{1+a\cdot[\text{hematite}]}} \quad (\textbf{Eq 3 - 8})$$

where a is the constant calculated from Equation 3-4 that is related to the $\Delta G^{\circ\prime}$ of the binding reaction between the purified MtrC and the hematite nanoparticles obtained from Equation 3-5, and [hematite] is the concentration of the hematite nanoparticles that were not bound to MtrC.

3.2.3 Results and discussion

Hematite induces geometrical changes in the heme centers in OM *c*-Cyts in intact cells

The author first examined the inter-heme interaction in the oxidized MtrC protein in *S. oneidensis* MR-1 cells in both the presence and absence of hematite nanoparticles with a diameter of 20-40 nm using CD spectroscopy. Because the size of a nanoparticle is slightly larger than that of the MtrC protein (approximately 9 nm×6 nm×4 nm) [14] and is two orders of magnitude smaller than the cell length of a *S. oneidensis* MR-1 bacterium, the hematite nanoparticles were potentially able to bind all of the MtrC proteins on the cell surface. Both of the Soret peaks at 394 nm and 415 nm were clearly observed for all concentrations that were tested, but the signal-to-noise ratio worsened as the concentration increased under aerobic condition (Figure 3-19a). Although the addition of hematite nanoparticles at 2.0 to 4.8 mM had little effect on the CD spectra, the Soret peak at 415 nm was greatly diminished upon the addition of 9.1 mM hematite nanoparticles (Figure 3-19a). Since Soret peak intensity corresponds to the degree of exciton coupling that occurs during inter-heme interactions [21, 23, 40], the change in the Soret CD profile strongly suggests that binding to hematite altered the heme geometry of MtrC in intact *S. oneidensis* MR-1 cells. In contrast, the Soret CD peak at 415 nm for the *S. oneidensis* MR-1 cells showed little decrease upon the addition of hematite after chemical fixation (Figure 3-20), strongly suggesting that the significant decrease of CD signal intensity upon the addition of hematite before the fixation resulted from substantial structure alteration in the MtrC protein. Specifically, previous studies demonstrated that hematite nanoparticles with a diameter of 20-40 nm uniformly bind to the surface of *S. oneidensis*

MR-1 cells without aggregation [62-63]. The STEM images obtained in our study consistently showed that the nanoparticles were evenly dispersed on the cell surface, while the dehydration and drying process prior to measurement formed a few aggregations (Figure 3-21). Thus, conformational changes would be expected to occur in the cell surface-exposed MtrC protein. The intensity of the Soret peak at 394 nm also changed upon the addition of nanoparticles, suggesting that the MtrC-hematite interaction induced geometrical changes in the heme moieties present in PEC proteins as well (The location of PEC in *S. oneidensis* MR-1 cell is indicated in Figure 3-10). A Soret peak decrease was also observed in intact *S. oneidensis* MR-1 cells containing reduced OM *c*-Cyts. The author added 30 mM lactate to *S. oneidensis* MR-1 cells that were subjected to anaerobic conditions, resulting in the shift of the Soret peaks to longer wavelengths due to the reduction of the OM *c*-Cyts, as described in chapter 3-1 (Figure 3-19b). The addition of 4.8 mM hematite led to a clear decrease in the intensity of the Soret peak at 421 nm, which has an identical wavelength to that of the Soret CD peak corresponding to the MtrC protein, supporting the conclusion that the presence of hematite nanoparticles changes the heme geometry of MtrC in intact cells. Another peak, at 411 nm, assigned to the PEC proteins (Figure 3-11) also fluctuated upon the addition of hematite, further suggesting that physical contact between MtrC and the hematite nanoparticles induces geometrical changes in the heme centers that comprise the OM *c*-Cyts.

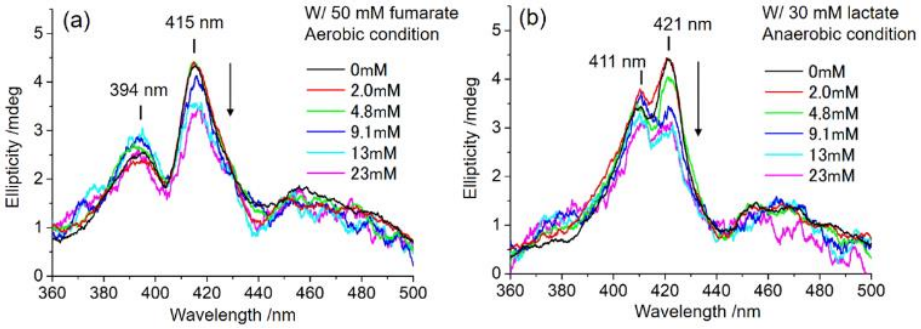

Figure 3-19. Whole-cell CD spectra of *S. oneidensis* MR-1 cells subjected to aerobic conditions in the presence of 50 mM fumarate (a) or 30 mM lactate under anaerobic conditions (b). These spectra were obtained upon the addition of various concentrations of hematite nanoparticles, as indicated by the legend. The arrows note the decrease of the Soret CD peak at 415 nm (a) and at 421 nm (b) upon the addition of hematite nanoparticles. The same tendency was reproduced in at least two separate experiments.

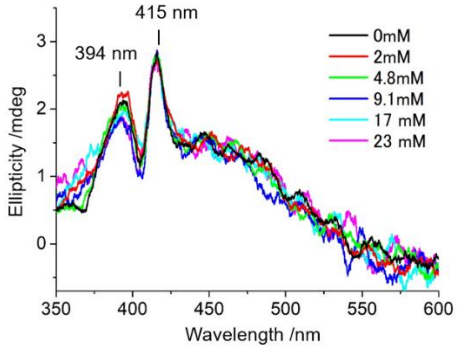

Figure 3-20. Whole-cell CD spectra of *S. oneidensis* MR-1 cells after chemical fixation of bacterial membranes and embedded proteins. Aerobically cultivated *S. oneidensis* MR-1 cells were fixed in 4% paraformaldehyde and 0.1% glutaraldehyde for 30 min [70], and subsequently washed twice with defined medium. The CD spectra were obtained in the presence of 50 mM fumarate and various concentrations of hematite nanoparticles as indicated by the legend. The same tendency was reproduced in two separate experiments.

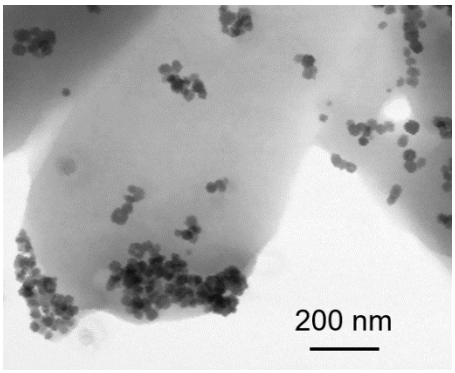

Figure 3-21. Bright-field STEM image of *S. oneidensis* MR-1 cells incubated under anaerobic conditions for 40 min in the presence of 13 mM hematite nanoparticles and 30 mM lactate.

The use of whole-cell CD difference spectra to quantify geometrical changes in the heme centers in MtrC

Since the data suggested that the changes in the whole-cell CD spectra originate from the MtrC-hematite interaction, the author quantified the intensity of the Soret peaks obtained from the MtrC protein within intact cells. In chapter 3-1, it was demonstrated that the difference between the CD spectra obtained from WT and deletion mutant (*ΔmtrC*) strains of *S. oneidensis* MR-1 provides a CD profile of the native MtrC protein present in intact cells. Thus, the whole cell CD difference spectra were quantified in the presence of hematite nanoparticles. The Soret peak of the native, oxidized MtrC at 413 nm clearly decreased in intensity upon the addition of 9.1 mM hematite, and the intensity increased by almost 40% upon the addition of 23 mM hematite (Figures 3-22~24), which demonstrates that the binding of hematite to oxidized MtrC alters its heme geometry in intact cells. Given that the local conformational changes in the amino acids surrounding the heme centers cause significant changes in the shape of the Soret peaks, including splitting effects [40, 71], the decrease in CD intensity while the shape of the CD spectra for

MtrC in intact cells is maintained (Figure 3-22) supports the conclusion that the interaction of bis-histidine residues with hemes is maintained during hematite binding. Consistently, the HT voltage profiles recorded during CD measurements indicated an almost identical Soret peak absorbance in both the presence and absence of hematite (Figure 3-23), which suggests that the decrease in the intensity of the Soret CD spectra caused by the addition of hematite stems from changes in the heme geometry, rather than from changes in the interaction with bis-histidines or artefacts within the CD measurements such as down-regulation of *mtrC* gene [39]. Based on the crystal structure, the 10 heme centers are aligned within the MtrC protein, and the heme on the edge, 5 or 10, is proposed to donate electrons to minerals [56, 59]. The contributions of heme 5 and 10 to Soret CD peak intensity were estimated to be below 25% and 35% of the total signal intensity derived from the MtrC protein, respectively [36], which are less than that of the observed suppression resulting from hematite binding. This finding indicates that the conformational changes induced by hematite binding are not limited to the heme center that is adjacent to the hematite nanoparticle but can take place in MtrC as a whole. Considering that the Soret CD peak intensity is inversely proportional to the square of the distance between hemes [21, 24], a decrease in the peak intensity suggests the occurrence of the unfolding of the MtrC protein, leading to an increase in the distance between the heme centers. Notably, the extent of the suppression of the Soret peak intensity originating from native, reduced MtrC was approximately 25% in the presence of 23 mM hematite, which differs from that of the oxidized species (Figure 3-22~24). This suggests that the inter-heme interactions within hematite-bound MtrC in a reduced state differ from those of oxidized MtrC likely facilitating the electron transfer reaction. Overall, the whole-cell CD difference spectra indicate that contact between hematite nanoparticles and *S. oneidensis*

MR-1 cells induces spatial arrangements of the deca-hemes in the MtrC protein.

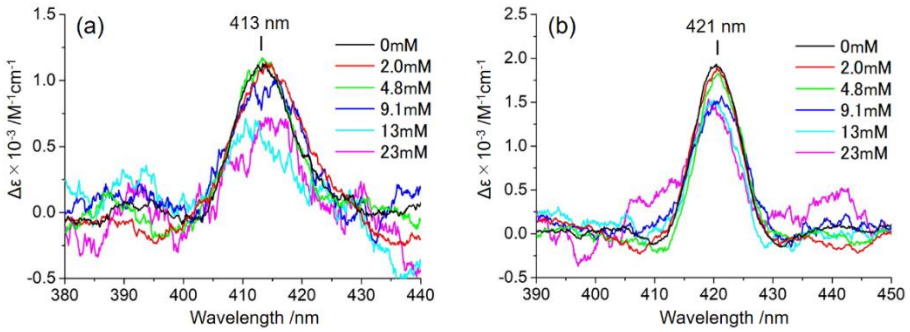

Figure 3-22. Whole-cell CD difference spectra between *S. oneidensis* MR-1 WT and *ΔmtrC* in the presence of 50 mM fumarate under aerobic condition (a) or 30 mM lactate under anaerobic condition (b). Hematite nanoparticle was added at the concentrations of 0 ~ 23 mM.

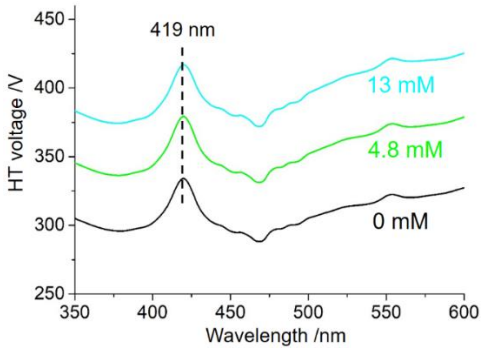

Figure 3-23. HT voltage profiles recorded during CD measurements of *S. oneidensis* MR-1 WT cells in the presence of 30 mM lactate under anaerobic condition. The concentrations of hematite nanoparticle added in the cuvette are indicated beside each spectrum. The fluctuations around 470 nm originate from the emission spectrum of xenon lamp equipped with the CD spectrometer.

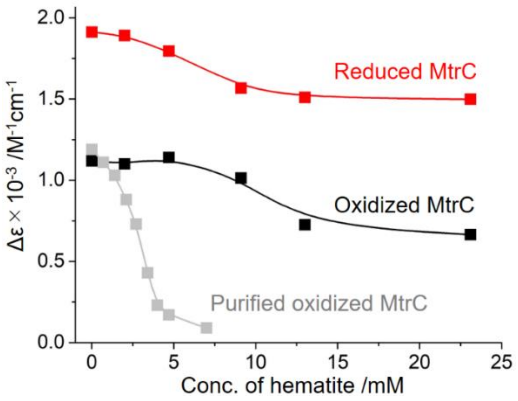

Figure 3-24. Soret peak intensity spectra obtained from whole-cell difference CD representing native, oxidized MtrC at 413 nm (black plot) and reduced MtrC at 421 nm (red plot) as a function of hematite concentration. The gray plot represents the intensity of purified, oxidized MtrC at 412 nm.

The author also examined the impact of hematite nanoparticles on heme geometry in the purified MtrC protein. As expected, the Soret CD peak obtained using 0.20 μM MtrC dissipated upon the addition of hematite, suggesting that binding of the nanoparticles causes geometrical changes in the heme centers of purified MtrC protein (gray plots in Figure 3-24 and Figure 3-25). However, localization of proteins to the surface of nanovesicles or nanoparticles flattens CD spectra [72], which distorts the quantification of changes in the Soret CD spectra induced by the spatial arrangement of hemes. The extent of the flattening effect depends upon the density of the proteins present on the surface of the materials. Whole-cell CD spectra in the presence of a phospholipid/MtrC ratio of approximately 2.0×10^3 (number of phospholipids per cell: ~2.0×10^7; number of MtrC proteins per cell: ~1.0×10^4) show little flattening effect [72-74]. On the other hand, purified MtrC protein is expected to densely cover the surface of a hematite nanoparticle, as reported in OmcA [8]; in this case, it would be expected that the CD spectra are greatly flattened. The decrease in Soret peak intensity derived from

purified MtrC in the presence of 7.0 mM hematite was approximately 90%; this exceeds the decrease that was previously reported for an extreme example of the flattening effect, in which bacteriorhodopsin that was densely embedded within a purple membrane at 75% (w/w) content resulted in an 80% decrease in the CD signal intensity [73]. The fact that the decrease in the Soret CD peak intensity of MtrC was greater than that of the flattening effect may suggest that the binding of hematite induces substantial arrangement of the heme centers in both the purified MtrC protein and in the native MtrC protein present in intact cells.

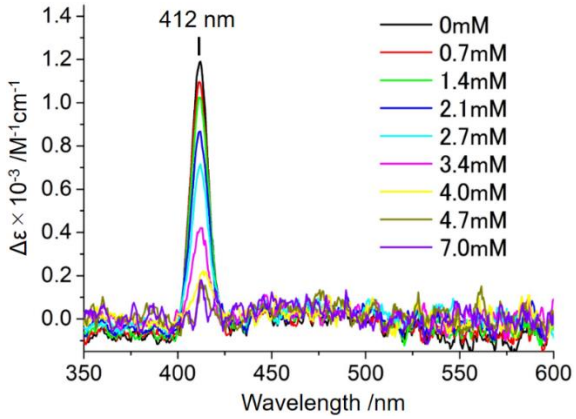

Figure 3-25. CD spectra of 0.20 μM MtrC protein solution in the presence of hematite nanoparticle at the concentration of 0 ~ 7.0 mM.

The binding affinity of MtrC with hematite depends on the redox state of MtrC and the concentration of hematite

Since the particle size of hematite is larger than that of the MtrC protein, it is plausible that the number of hematite nanoparticles that can bind with a single MtrC protein is limited to one. Based on the assumption that hematite binding leads to the unfolding of MtrC, the author plotted the ratio of hematite-bound MtrC and determined the concentration of hematite in solution (Figure 3-26), both of which were estimated using whole-cell CD difference spectra. Since hematite nanoparticles are subject to little

aggregation (Figure 3-21) [62-63], a hematite nanoparticle was redefined as one molecule, and the concentration was recalculated as described in the Method Section. For both the oxidized and reduced native MtrC, the coverage of the hematite nanoparticle increased as the particle concentration increased. In contrast, to cover 50% of the MtrC protein in the oxidized and the reduced states, approximately 5.5×10^{-8}/M and 2.5×10^{-8}/M hematite nanoparticles were required, respectively. Considering that the substantial concentration of hematite nanoparticles in the presence of native reduced MtrC would be lower than the apparent concentration due to the dissolution by reduction reaction, hematite nanoparticles with the concentration of less than 2.5×10^{-8}/M potentially cover 50% of the reduced MtrC protein. The substantially lower concentration of nanoparticles that was required for binding to reduced MtrC clearly indicates that the affinity of MtrC for the nanoparticles is increased when this protein is in the reduced state. Given that complementary electrostatic interactions are proposed to mediate binding between MtrF and hematite [58], redox-linked alteration of the charge distribution in MtrC would be the main factor contributing to the change in the binding affinity. Since the point of zero charge of hematite is approximately 8.5 [66], at pH 7.4, the positively-charged hematite would be more attracted to the reduced MtrC, which would be more negatively-charged than the oxidized MtrC. Given that, unlike oxidized MtrC, reduced MtrC requires contact with minerals to sustain microbial electrogenic respiration, redox-linked enhancement of binding affinity is probably necessary for the creation of an electrical connection between microbes and minerals, as suggested previously [60-61].

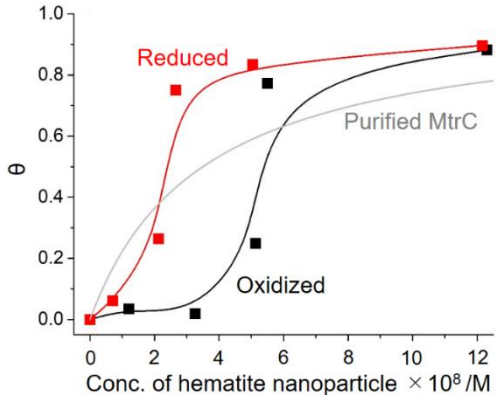

Figure 3-26. The fraction of native MtrC binding to hematite nanoparticles (θ) at various concentrations of nanoparticles in solution. The black and red plots represent oxidized and reduced MtrC, respectively. The gray line that is superposed on this graph represents a hyperbolic curve using a $\Delta G^{o'}$ value of −43 kJmol^{-1} following the Langmuir adsorption model, which is identical to the binding affinity of purified MtrC protein that was estimated in Figure 3-27. The θ was estimated from the Soret peak intensity of whole-cell CD difference spectra, assuming that a single hematite nanoparticle binds with each MtrC protein and alters the heme geometry. The concentration of hematite nanoparticles was redefined to be one molecule.

In addition to the redox chemistry-based binding model, allosteric effects also likely contribute to the curve profile shown in Figure 3-26. While the protein-mineral interaction is generally described by the Langmuir adsorption model, which depicts a relationship between coverage and mineral concentration that is characterized by a hyperbolic curve [8, 58], the interactions of native MtrC were represented by curves with distinct shapes. Coverage of the native, oxidized MtrC protein by hematite was limited to only approximately 5% in the presence of 3.0×10^{-8}/M nanoparticles but was significantly increased to approximately 70% in the presence of 6.0×10^{-8}/M nanoparticles. This dramatic increase in the bound ratio is typically observed for allosteric proteins, where the binding of the first ligand enhances the affinity of a protein for the second ligand. To

examine whether this unique allosteric behavior is due to the characteristics of the MtrC protein, the mechanisms of binding of the purified MtrC protein and hematite nanoparticles were examined using a sedimentation assay (Figure 3-27). It was found that the binding reaction proceeded according to a simple Langmuir adsorption model with a standard Gibbs free energy ($\Delta G^{\circ\prime}$) of −43 kJmol^{-1}, demonstrating that the presence of allostery is specific to the binding taking place in intact cells. In addition, the superposed curve utilizing a $\Delta G^{\circ\prime}$ value of −43 kJmol^{-1}, shown in Figure 3-26, demonstrates that a nanoparticle range on the same order of magnitude is present during binding, suggesting that the chemical bond formed between MtrC and hematite is the same in both the purified and native systems. Overall, it appears that the allosteric-like effect observed upon binding of the native MtrC originates not in the characteristics of the MtrC protein itself but in the specific functioning of MtrC when it is in membrane-bound protein complex conditions.

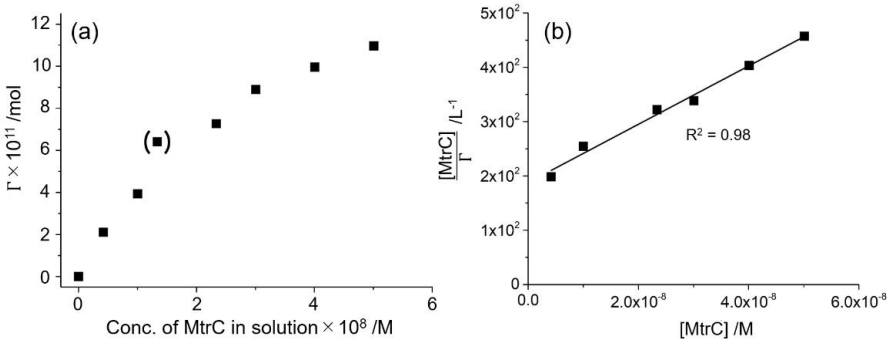

Figure 3-27. (a) The amount of MtrC protein bound in the presence of 1.0 mM hematite dispersed in 1.5 mL of solution (Γ/mol) at various concentrations of unbound MtrC protein as estimated using a sedimentation assay. This provides a standard Gibbs free energy ($\Delta G^{\circ\prime}$) value of −43 kJmol^{-1} for the binding of MtrC to the hematite surface. The data point in parentheses is not included in the estimation of $\Delta G^{\circ\prime}$. (b) Analysis of sedimentation assay data. The vertical axis represents the concentration of MtrC protein in solution ([MtrC] /M) divided by the amount of MtrC bound with hematite (Γ /mol), and the horizontal axis represents [MtrC]. The plots show a linear regression: [MtrC]/Γ = 5.37×10^9 [MtrC] + 187 with square of the correlation coefficient value of 0.98, which represents a $\Delta G^{\circ\prime}$ of −43 kJmol^{-1} for binding reaction of MtrC with hematite based on the Langmuir isotherm (Equations 3-4 and 3-5).

The physiological implications of the flexibility of the binding affinity of MtrC

Given that the attachment of *S. oneidensis* MR-1 cells to mineral surfaces is initiated by the formation of bonds between membrane proteins and hematite [65], the flexibility of the binding affinity modulated by the redox state and the hematite coverage of MtrC may assist in the attachment and detachment of cells from minerals. In particular, the redox state of MtrC is closely related to the status of the intracellular respiratory chain; thus, microbe-mineral interactions could be mediated by the metabolic condition of the cells. When *S. oneidensis* MR-1 cells actively produce NADH from lactate present in their environment, reduced MtrC tightly binds to the mineral surface, which allows for the

efficient regeneration of NAD^+ by extracellular electron transport and subsequent substrate-level ATP production as indicated in chapter 2. Furthermore, since OM *c*-Cyts are maintained in a reduced state during electron transport [75], *S. oneidensis* MR-1 cells are able to adhere stably onto mineral surfaces and continue substrate-level ATP production. Once the electron donor, lactate, is starved, the metabolic reduction of OM *c*-Cyts stops; thus, oxidized OM *c*-Cyts may assist in the detachment of *S. oneidensis* MR-1 cells from the mineral surface to obtain lactate from elsewhere in their environment. This redox-linked binding affinity allows microbes to reversibly and quickly switch between attachment to and detachment from the mineral surface, which would not be possible by utilizing the much slower and intensive processes involved in the production and localization of adhesive proteins and molecules; thus, this mechanism provides a method for microbes to survive using electrogenic respiration.

For cells to achieve redox-dependent flexibility in their attachment and detachment, electrostatically-controlled weak bond formation at the microbe-mineral interface would be preferable to tight adhesion. Consistently, the $\Delta G^{\circ\prime}$ of the binding reaction between purified MtrC protein and hematite was estimated to be −43 $kJmol^{-1}$ (Figure 3-27), which is much less than that of a typical bond formed during other biomineralization interactions, such as that of amelogenin with hydroxyapatite ($\Delta G^{\circ\prime}$ ~ −120 $kJmol^{-1}$) [58, 76]. Given that all of the reported $\Delta G^{\circ\prime}$ values for the other components in OM *c*-Cyts also suggest a weaker binding affinity than is typical for biomineral proteins (MtrF: −55 $kJmol^{-1}$; OmcA: −28 $kJmol^{-1}$)[8, 58], the observed features of MtrC may represent characteristics that are common to mineral-microbe interactions. To verify the generality of the redox-linked allosteric binding characteristics of microbe-mineral interactions, it would be of interest to conduct whole-cell CD spectroscopy using other

bacteria that possess OM *c*-Cyts, such as *Geobacter sulfurreducens*, especially as a component of the OM *c*-Cyts in *Geobacter sulfurreducens*, OmcS, exhibits a comparable Soret CD peak intensity to that of MtrC [77]. Consistently, the whole-cell spectroscopy of *Geobacter sulfurreducens* PCA revealed large Soret CD peaks (Figure 3-28). Given that OmcS is a major component of electrically conductive pili, which are required for direct electron exchange between microorganisms [78-79], the use of this technique could shed light on the structures involved in syntrophic respiration that is mediated by direct interspecies electron transfer.

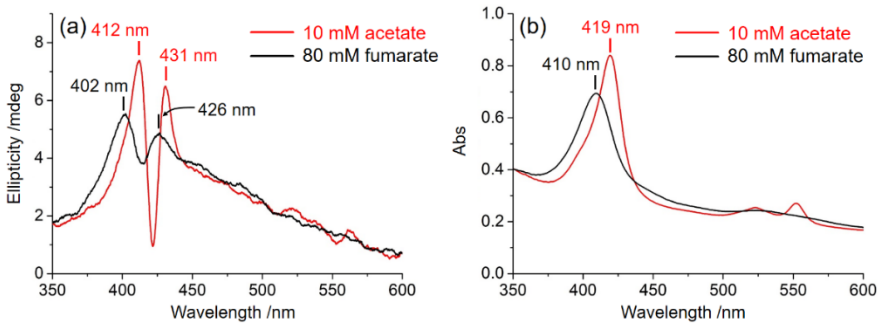

Figure 3-28. Whole-cell CD spectra (a) and absorption spectra in diffused transmission mode (b) of *Geobacter sulfurreducens* PCA cells with the optical density at 600 nm (OD_{600}) of 1.06. Red and black spectra were taken in the presence of 10 mM acetate or 80 mM fumarate as a sole electron donor or acceptor, anticipating reduction or oxidation of OM *c*-Cyts, respectively. *G. sulfurreducens* PCA was anaerobically cultivated at 303 K for 72 h in PSN medium as reported previously [80]. Cells were then collected and washed twice with PSN medium by centrifugation for 10 min at 5000 x g. The CD spectra were taken with a Pyrex cuvette with path length of 1.0 cm under anaerobic condition.

However, the use of whole-cell CD spectroscopy with minerals has limitations that depend on the size of the minerals. If the mineral size is comparable to or larger than that of the microbe, only a proportion of the OM *c*-Cyts will bind to minerals, resulting in only minute changes in the CD profile. Therefore, the application of whole-cell CD

spectroscopy would be limited to the study of microbe-nanoparticle associations, which are not representative of most biomineral interactions that occur in nature. However, the data obtained from microbe-nanoparticle interactions may still aid in understanding the interactions of microbes with large minerals. For example, when the interaction of *S. oneidensis* MR-1 cells with large minerals with rough surfaces is considered, the area of the surface with which an MtrC protein makes contact is expected to be small, which is reflected by conditions involving a low nanoparticle concentration, as shown in Figure 3-26. As a result, the bond between the *S. oneidensis* MR-1 cell and the cell surface may be lost due to the low binding affinity (Figure 3-26). The possibility of attachment and detachment behavior being influenced by the nano- or microtopography of the mineral surface is in good agreement with long-standing observations, such as that the roughness of the mineral surface impedes the adhesion of *S. oneidensis* MR-1 cells [81] as well as the dependence of the adhesiveness of cells to minerals on the crystal facets [82]. Those implications may contribute to measures to control the formation of biofilms on solid surfaces [83-85], which could also be used to accelerate the bio-reactions of metal-reducing bacteria. Given that the attachment and detachment of microbial cells are controlled by the surface property of minerals and electrodes [8] as well as the interactions of other cellular components such as lipopolysaccharides and membrane proteins [64, 66, 81], it would be of great interest to use whole-cell CD spectroscopy to further investigate the binding characteristics of mutant strains that lack those components with various minerals.

The implications of the structural flexibility of MtrC for extracellular electron transfer mechanisms

The whole-cell CD spectroscopy experiments in this study provided insights not only into the factors affecting the binding affinity of OM *c*-Cyts but also into the flexibility of heme geometry in OM *c*-Cyts. Although a homologous protein of MtrC, OmcA, has been proposed to undergo structural changes induced by mineral binding [8, 17], the author have provided the first evidence of the spatial rearrangement of the hemes during the electron flow and mineral binding. Inter-heme interactions strikingly affect the kinetics of the electron transfer reaction. Since hematite binding may cause the unfolding of MtrC in intact cells, weakening the inter-heme interactions, the rate of electron transport is expected to decrease; this is consistent with the relatively low electron transport rate that was observed between OM *c*-Cyts and hematite compared with other minerals [59]. This flexible alteration of heme geometry suggests the potential for OM *c*-Cyts to regulate the kinetics and pathways involved in electron transfer via the modulation of heme geometry based on the components and/or facets present in the bound minerals. Indeed, resonance Raman spectra obtained from purified MtrC have suggested that its binding with porous indium tin-doped oxide electrodes induces alteration of the bis-histidine residues that are adjacent to the heme centers, rather than a geometrical change in the hemes themselves [67]. This distinct structural change in MtrC that was observed in our experiments further supports the conclusion that MtrC forms different structures depending upon which mineral it binds.

Furthermore, the potential factors altering the heme geometry in OM *c*-Cyts are not limited to the presence of electron flow nor minerals. Small angle x-ray scattering measurements of purified OmcA proteins indicated that OmcA binding to a redox cofactor,

flavin, induces dimer formation and possible conformational changes [17]. Furthermore, the results in chapter 3-1 indicated that the inter-heme interactions in the MtrC protein are different in the purified system and the native whole-cell system. To gain a true understanding of the mechanisms underlying the control of long-range electron transport over 100 Å in OM *c*-Cyts in living cells, it would be essential to obtain molecular-level information about the formation of complexes between OM *c*-Cyts and minerals, electrodes and redox cofactors.

3.2.4 Conclusion

In this work, the author obtained the first evidence that microbe-mineral interactions induce geometrical changes in the heme centers in the MtrC protein as well as in whole OM *c*-Cyts, most likely associated with the unfolding of MtrC. These findings emphasize the structural flexibility of MtrC, in which the kinetics and pathways of electron transport potentially change depending on which molecules MtrC binds. To truly understand the electron transport mechanisms in OM *c*-Cyts in living cells, it would be essential to obtain molecular-level information about the formation of complexes between OM *c*-Cyts and minerals, electrodes and redox cofactors. Furthermore, the binding affinity of MtrC with hematite in intact cells was flexibly modulated by the redox state of MtrC and the ratio of MtrC bound to the mineral. Since these parameters are linked to intracellular metabolism and extracellular environmental conditions, the flexible regulation of electrical connections is expected to contribute to the ecophysiology of microbes that depend upon interactions with minerals.

The flexibility of OM *c*-Cyts may provide further understanding of the mechanisms underlying the electrical connections between microbes and minerals. As suggested in chapter 2 and 3-1, the OM *c*-Cyts are expected to export protons involved in the electron transport reaction; however, the crystal structures of MtrC and OmcA show no clear hydrogen-bond networks that could be involved in conveying protons [12, 14]. Considering the structural flexibility of MtrC, it is plausible that a proton wire is formed by structural change. To elucidate the biochemical mechanisms underlying the proton-coupled electron transport reaction occurring at the microbe-mineral interface, which is most likely a common feature shared with other electrogenic microbes [86], it is of great interest to obtain whole-cell CD spectra in the presence of cofactors such as flavins during electron flow with a combination with electrochemistry. The author hopes that these insights contribute to the improved efficiency of biotechnologies utilizing electrogenic respiration as well as to fundamental understanding of microbe-mineral interactions.

3.3

Acceleration of extracellular electron transport by flavin involves alteration of heme redox state in MtrC

3.3.1 Introduction

Metal-reducing bacteria have the ability to convey electrons to extracellular solid substrates across outer-membrane, termed extracellular electron transfer (EET) [8-10, 68, 87]. EET process extends the microbial respiratory chain towards cell exterior, enabling metal-reducing bacteria to survive in soluble oxidant-limited condition. In addition to the implications for geochemical elemental cycling, the EET-coupled respiration has significant implications for the development of bioelectrochemical technologies [54-55]. For understanding and utilizing the EET-based phenomena and technologies, the kinetics and molecular-level mechanisms of EET have been extensively studied.

The mechanisms of EET have been investigated using a model metal-reducing bacterium, *Shewanella oneidensis* MR-1, which conduct EET through multi-heme cytochromes complex on outer-membrane (OM *c*-Cyts) [14, 56]. One of the best-studied OM *c*-Cyts in *S. oneidensis* MR-1 is MtrABC complex, where MtrC acts as a terminal reductase at the cell surface. The X-ray structure revealed that the MtrC protein possesses 10 hemes in the arrangement of "staggered-cross" as shown in Figure 3-17. In addition to hemes, flavin mononucleotide (FMN) acts as a non-covalent redox cofactor of EET process, of which binding site is proposed to be near the heme 7 of MtrC [14-15, 45]. Based on those structural information about MtrC (and its paralogue, MtrF), quantum chemical

approaches have contributed on understanding the electron transfer pathways and kinetics.

One of the most intriguing findings is that the heme ion valence strikingly alters the profile of redox potential. Previous computational studies estimated that the heme valence change from 3+ to 2+ causes drastic negative redox potential shift about 300 mV in all hemes [15-16]. Notably, even the valence change of one heme (number 7) is proposed to alter the redox potential of all 10 hemes and changes the energy landscape of electron transport through MtrC [16], highlighting the importance in identification of heme ion valence during EET process in whole-cell. Given that continuous electron inflow and outflow are balanced in MtrC in living *S. oneidensis* MR-1, it may be possible that some of hemes are reduced and the others are oxidized, unlike conventional assumptions that all hemes in MtrC are oxidized during electron transport (or all reduced during hole transport), which is a stable state under equilibrium condition. Consistently, some of previous works reported that absorption spectra of metal-reducing bacteria show both ferric and ferrous heme peaks were obtained during EET process [37, 88]. However, it was not possible to implicate specific cytochromes, given that absorption spectra include the signals from all the hemes in bacteria other than OM *c*-Cyts. Especially, the abundance of heme-containing genes of *S. oneidensis* MR-1 makes the characterization of MtrC particularly difficult [89].

In chapter 3-1 and 3-2, the author demonstrated that whole-cell CD spectroscopy reflects the redox state of hemes in MtrC with minimum interferece from other heme proteins using intact cell. Here, the whole-cell CD difference spectroscopy was combined with microbio-electrochemistry to examine the redox state of hemes in FMN-bound MtrC in the presence of electron flow. The heme redox state in MtrC under non-equilibrium condition was compared with equilibrium condition by switching of the applied potential.

3.3.2 Methods

CD spectroscopy to monitor the inter-heme interactions in MtrC in the presence of flavin

Cultivation of *S. oneidensis* MR-1 and CD measurements were conducted under the same conditions with chapter 3-1 and 3-2. The CD spectra of the reduced OM *c*-Cyts binding with flavin were obtained under anaerobic conditions in the presence of 30 mM lactate and 10 μM FMN [68].

Attachment of *S. oneidensis* MR-1 on Pt mesh electrode

For attachment of *S. oneidensis* MR-1 on Pt-mesh electrode, a single-chamber, three-electrode system was constructed. 7.0 mm × 5.5 mm Pt 80 mesh (approximate surface area: 0.9 cm^2) was used as the working electrode, and Ag/AgCl (sat. KCl) and a platinum wire (approximate surface area: 10 mm^2) were used as the reference and counter electrodes, respectively. 4.0 mL defined medium (DM, pH = 7.8) containing 10 mM lactate as a sole electron donor was deaerated by bubbling N_2 more than 20 min and added to the electrochemical cell as an electrolyte. The reactor was maintained at a temperature of 30°C and was not stirred during measurements. Cell suspensions with an optical density of 0.1 at 600 nm (OD_{600}) were inoculated in the reactor with the working electrode poised at +0.4 V versus SHE for 36 hours.

Imaging of *S. oneidensis* MR-1 on Pt-mesh electrode

S. oneidensis MR-1 after electrochemical cultivation was taken out from the electrochemical reactor, and subsequently stained with DAPI (4',6-diamidino-2-

phenylindole) using a 0.5 μg/ml solution after gentle wash with phosphate buffer. Fluorescence microscopic images and bright field images were simultaneously obtained by an inverted microscope (Leica DMi8, Leica) combined with microcamera (Leica DFC9000, Leica) using 10× and 40× objective lenses.

Electrochemical CD measurement of *S. oneidensis* MR-1

CD spectroscopy was performed on J-1500 (JASCO) CD spectrometer at room temperature (25 ± 1°C). The CD spectra of Pt-mesh electrode after electrochemical cultivation was obtained in a quartz cuvette with path length of 1.0 mm containing anaerobic DM medium with 10 mM lactate. Parameters for CD measurements were set as follows: 100 nm min^{-1} scan rate, 0.1 nm data pitch, 5.0 nm bandwidth, and 10 times data integration.

Far-UV CD spectroscopy of purified MtrC protein

CD spectra of purified MtrC was obtained in the range of far-UV (190-260 nm) on J-1500 (JASCO) CD spectrometer at room temperature (25 ± 1°C). Purified MtrC protein was dissolved in phosphate buffer at pH 7.4 (5.7 mM K_2HPO_4 + 3.3 mM KH_2PO_4). Parameters for CD measurements were set as follows: 100 nm min^{-1} scan rate, 0.1 nm data pitch, 1.0 nm bandwidth, and 16 times data integration. 0.7 mM $Na_2S_2O_4$ was added for reduction of both hemes and disulfide bond, and 1.0 mM glutathione was used for specific reduction of disulfide bond in purified MtrC protein.

3.3.3 Results and discussion

Biofilm formation of *S. oneidensis* MR-1 on Pt mesh electrode

Biofilm of *S. oneidensis* MR-1 was formed on Pt mesh electrode by electrochemical cultivation as described in the Method Section. Figure 3-29 shows a representative time course of current production from *S. oneidensis* MR-1 during formation of biofilm on Pt electrode. The current production reached about 3 μA after 36 hours under +0.4 V versus SHE. Given that the approximate surface area of the Pt mesh electrode was about 0.9 cm^2, the current density was about twice higher than that from a monolayer biofilm of *S. oneidensis* MR-1 on ITO electrode shown in chapter 2 (Pt mesh: 3.3 μAcm^{-2}, monolayer on ITO: 1.6 μAcm^{-2}; about 5 μA from 3.1 cm^2 of ITO). This higher current density suggests that *S. oneidensis* MR-1 cells are attached onto Pt mesh forming multi-layers of biofilm.

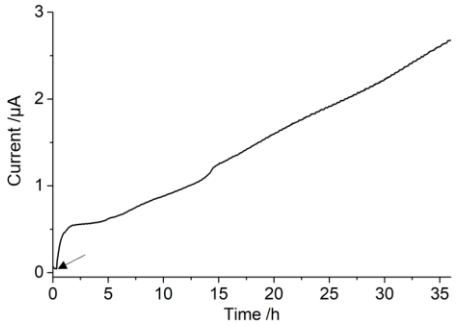

Figure 3-29. Representative current production from *S. oneidensis* MR-1 during the biofilm formation on Pt mesh electrode. An arrow indicates the time of the addition of the cell suspension into the electrochemical reactor. The same tendency was reproduced in at least three individual experiments.

To confirm the morphology of Pt mesh after electrochemical cultivation, fluorescence microscopic images and bright field images were simultaneously obtained after DAPI treatment which specifically stains microbial cells. Figure 2-30 are the images

obtained with 10× and 40× objective lenses. Bacterial cells were distributed on the surface of Pt mesh as well as among the gaps of Pt mesh forming some layers consistently with the current production shown in Figure 3-29.

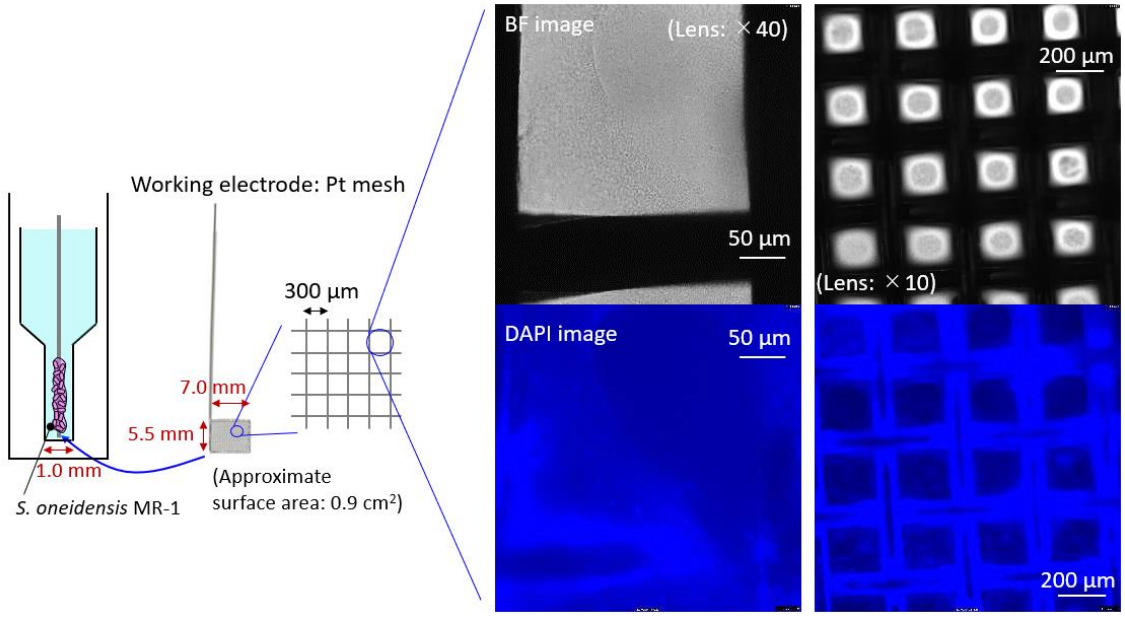

Figure 3-30. Experimental setup for electrochemical CD spectroscopy, and bright-field and fluorescence microscopic images of Pt-mesh electrode after electrochemical incubation of *S. oneidensis* MR-1. Those images were taken after DAPI staining.

Electrochemical whole-cell CD difference spectra indicate that electron flow induces geometrical changes in the heme centers in flavin-bound MtrC

To test the stability of CD signal from *S. oneidensis* MR-1, the CD signal of the Pt mesh electrode with biofilm of *S. oneidensis* MR-1 was obtained under open circuit voltage (V_{OC}) (approximately −350 mV versus SHE). After electrochemical cultivation, the electrode was moved to a cuvette with path length of 1.0 mm containing DM with 10 mM lactate and 10 µM FMN, and located in the CD spectrometer (Figure 3-30). The Pt mesh electrode was connected to potentiostat as the working electrode, and CD spectra of the electrode were obtained under V_{OC} condition (Figure 3-31). Given that electrons are

suppled by bacterial respiration under equilibrium of electron exchange between MtrC and electrode, it is reasonable that accumulated electrons reduces all the hemes in MtrC. The whole-cell CD spectra showed a clear Soret peak at 421 nm, which is characteristic to MtrC protein in reduced state as demonstrated in Figure 3-7, indicating that the hemes are maintained at reduced state under V_{OC} condition, and confirming that the content of *S. oneidensis* MR-1 on the Pt mesh electrode is enough to detect by CD spectrometer. Furthermore, almost identical CD spectrum was obtained after 30 min V_{OC} application to the electrode (Figure 3-31a, gray line), suggesting that the biofilm of *S. oneidensis* MR-1 is stably attached on the electrode with scarce removal.

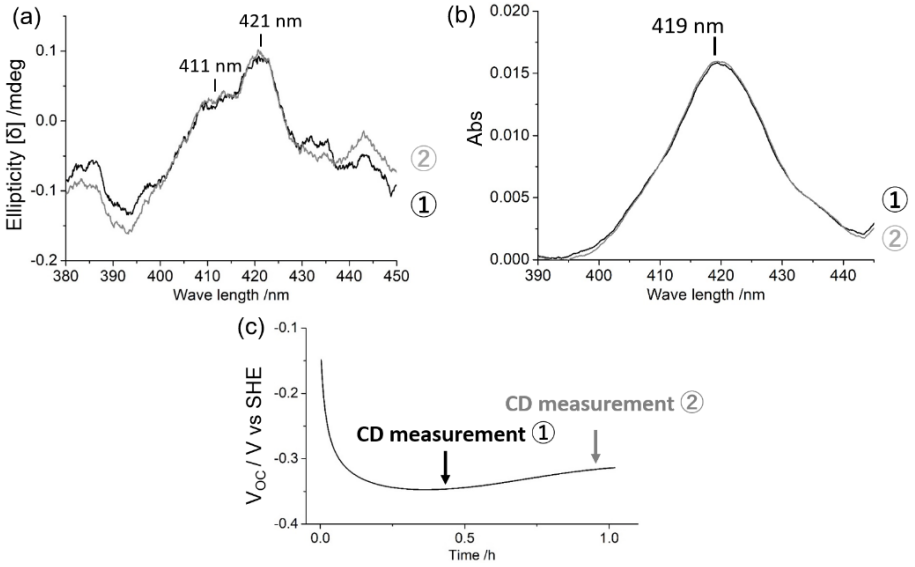

Figure 3-31. Electrochemical whole-cell CD spectra (a) and absorption spectra (b) of the biofilm of *S. oneidensis* MR-1 WT formed on Pt mesh electrode in the presence of 10 mM lactate and 15 μM FMN. Open circuit voltage (V_{OC}) (approximately −350 mV versus SHE) shown in panel (c) was applied during the measurements of both black and gray lines. The CD spectra of Pt mesh electrode without *S. oneidensis* MR-1 was used as the baseline.

Switch of applied potential to +0.4 V (versus SHE) largely diminished the Soret CD peak at 421 nm, initiating current production of about 5 μA mediated by FMN-bound

OM *c*-Cyts (Figure 3-32). Since the peak at 421 nm corresponds with the signal from MtrC protein in reduced state, the change in the Soret CD profile strongly suggests that the non-equilibrium condition caused by electron flow altered the heme redox state of MtrC in intact *S. oneidensis* MR-1 cells. Consistently, the absorption spectra showed decrease of peak intensity at 419 nm by +0.4 V (versus SHE) potential application. Since the alteration in the Soret CD peak intensity was repeatedly observed by switching of applied potential (Figure 3-32), strongly supporting that the decrease in the intensity of the Soret CD spectra originates from changes in the heme of MtrC, rather than from removal of biofilm or artefacts within the CD measurements such as down-regulation of *mtrC* gene. Another peak, at 411 nm, assigned to the PEC proteins (Figure 3-11) showed little change compared with that at 421 nm (Figure 3-32), suggesting that the redox state changes in the heme centers induced by electron flow mainly occurs in MtrC protein.

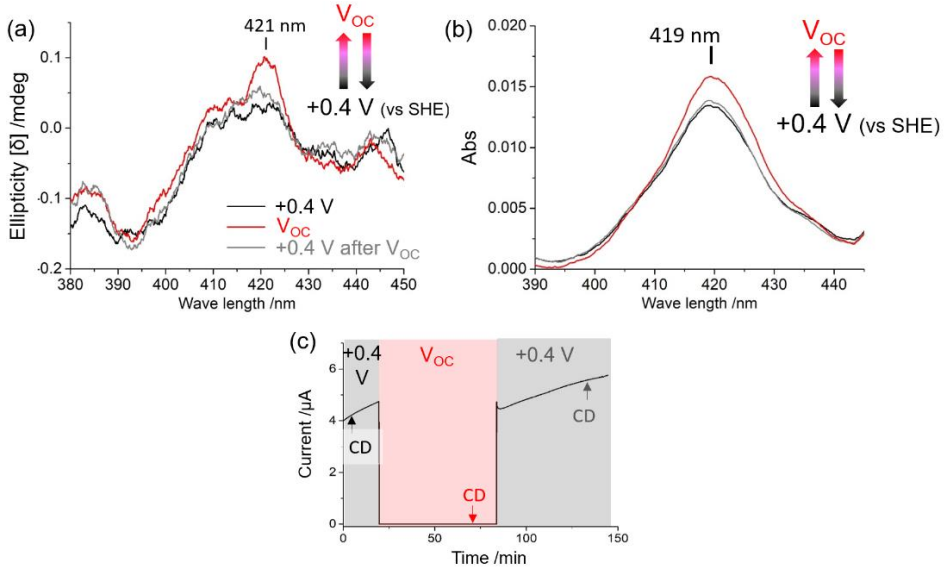

Figure 3-32. Electrochemical whole-cell CD spectra (a) and absorption spectra (b) of *S. oneidensis* MR-1 WT on Pt mesh electrode in the presence of 10 mM lactate and 15 μM FMN. The applied potential was either V_{OC} (red line) or +0.4 V (black and gray lines). (c) Time course of the current production from *S. oneidensis* MR-1 WT during the CD measurements. The arrow indicates the timing of CD measurements.

In order to quantify the Soret peak intensity from the MtrC protein during electron flow, whole-cell CD difference spectra were compared under V_{OC} and +0.4 V (versus SHE). The CD spectra of *ΔmtrC* strain grown on the Pt mesh electrode was used for subtraction from that of WT to obtain whole-cell CD difference spectra. The cell number was normalized by OD_{600}, and signal from FMN-bound MtrC was focused on using dissociation constant of complex formation. The whole-cell CD difference peak at 421 nm showed clear decrease about 60% upon potential switch from V_{OC} to +0.4 V (versus SHE) (Figure 3-33a), supporting that MtrC in intact cell conduct EET using both oxidized and reduced hemes. The absorption spectra obtained simultaneously showed increase in the peak at 409 nm which corresponds with oxidized heme as well as decrease at 419 nm (Figure 3-33b), further supporting the oxidation of partial hemes in MtrC during electron flow.

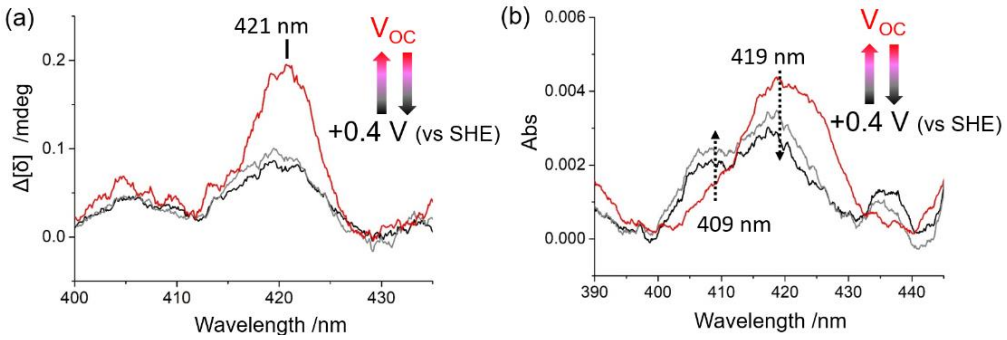

Figure 3-33. Electrochemical whole-cell CD difference spectra of *S. oneidensis* MR-1. The CD spectra of *ΔmtrC* strain grown on the Pt mesh electrode was used for subtraction from that of WT to obtain whole-cell CD difference spectra. The amount of *S. oneidensis* MR-1 on the Pt mesh was normalized by the absorption intensity at 600 nm under V_{OC} condition, and signal from FMN-bound MtrC was focused on using dissociation constant of complex formation.

Which hemes are most probably oxidized by electron flow?

As mentioned in chapter 2, molecular simulations based on the crystal structure of MtrC show two potential electron transfer pathways [14-16, 45]. Both initiate from aligned hemes, but one terminates with the bound flavin nearby heme 7 and the other terminates with heme 5 (Figure 3-34). Based on the experiments in chapter 2 demonstrated that the respiratory electron inlet into MtrC is enough fast than elctron outlet to bound FMN, suggesting that the hemes in electron transfer pathway are maintained in reduced state. In contrast, the electron pathway mediated by only heme centers is relatively inactive during EET, thus, it may be possible that electrons localized at the edge of hemes such as heme 5 and 4 move towards bound FMN associated with electron flow (Figure 3-34). Especially, the hemes 1, 3, 4, 5 are estimated to possess equivalent or lower redox potential than other hemes (average about + 50 mV and heme 1, 3, 4, 5 has about +45, + 60, −170, +80 mV versus SHE in oxidized state) [16], which are not thermodynamically unfavorable to deliver electrons towards heme 7.

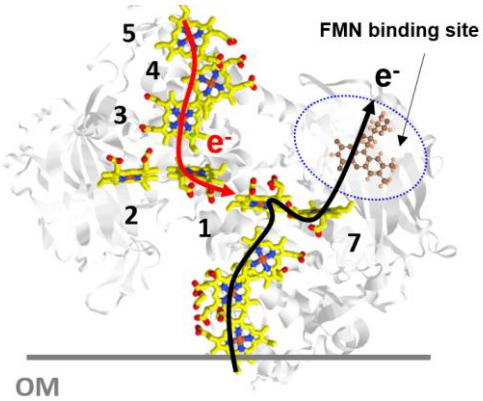

Figure 3-34. Oxidation of hemes possibly occurs associated with electron flow. Black arrow indicates the proposed active electron transport pathway in the presence of bound FMN [14-15, 45]. Red arrow indicates potential electron movement associated with electron flow causing heme oxidation. Crystal structure was obtained by PDB code of 4LM8 [14].

In order to confirm that the oxidation of hemes 1, 3, 4, 5 is consistent with the CD signal decrease about 60% observed in Figure 3-33a, the CD peak intensity from each adjacent heme pair in MtrC was calculated based on the exciton chirality method (Figure 3-17b). From the calculation, it was estimated that the hemes 1, 3, 4, 5 exhibit relatively high CD signal intensity, which reach about 55% of total signal from MtrC (Figure 3-17b). This estimation quantitatively corresponds with the CD signal decrease observed in whole-cell CD difference spectroscopy during electron flow, indicating that the oxidation reaction proceeds at hemes 1, 3, 4, 5 during EET process.

Implications for mechanisms of FMN-triggered EET acceleration

In chapter 2, it was demonstrated that the bound flavins with OM *c*-Cyts accelerate EET by enhancement of rate-limiting proton transport reaction and rearrangement of proton transport pathway. In addition, the whole-cell CD difference spectra of *S. oneidensis* MR-1 in chapter 3-1 suggested that the rate-limiting proton pathway is involved in local environments of hemes in MtrC, e.g. propion side chain of hemes or ligated histidines on hemes in MtrC. The heme redox state change in MtrC during EET may potentially explain the formation of proton transport pathway *in vivo*. Given that the heme valency change possibly alter the interaction of surrounding local amino residues, rearrangement of amino residues during electron flow might form proton transport pathways.

To test the rearrangement of amino residues around hemes, CD spectra of purified MtrC protein in both completely oxidized and reduced state were obtained in far-UV region, which represents the content of secondary structure in MtrC (Figure 3-35). The CD spectra of MtrC in oxidized state clearly changed upon reduction reaction by addition of 0.7 mM $Na_2S_2O_4$. For quantitative estimation of the secondary structure

change upon reduction, the CD spectra were analyzed using BeStSel, which improved the accuracy of estimations in the secondary structure content by taking the conformation of β-sheet into account as described in chapter 2 [90-91]. The reduction reaction decreased the content of α-helix from 11.1% to 8.4% (Table 3-1). Since α-helix is located in the domain II and IV aligning 10 hemes, this clear difference supports the redox-dependent rearrangement of amino residues around hemes in MtrC. While the content and conformation of β-sheet also changed by $Na_2S_2O_4$, the same tendency was observed in the presence of glutathione, which specifically reduce disulfide bond, not hemes (Table 3-1) [14], suggesting that the change in β-sheet is mainly caused by cleavage of disulfide bond located in the domain III. Consistently, the domain III is mainly composed of β-sheet [14] . Furthermore, the content of α-helix was unaffected by glutathione (Table 3-1), indicating that the rearrangement of amino residues around heme redox centers is driven by redox state of hemes.

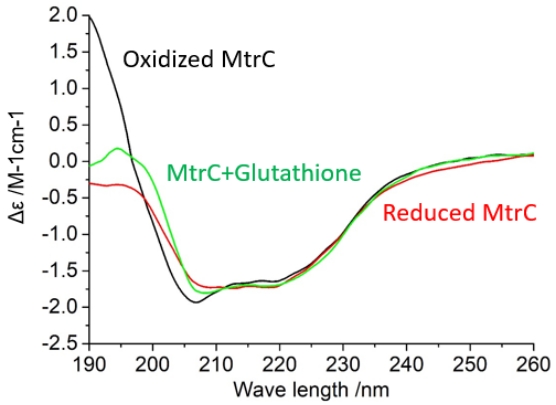

Figure 3-35. CD spectra of purified MtrC protein oxidized by dissolved oxygen (black line), reduced by 0.7 mM $Na_2S_2O_4$ (red line), and of which disulfide bond was specifically reduced by 1.0 mM glutathione (green line). Those spectra were obtained after subtraction by that of phosphate buffer and 0.7 mM $Na_2S_2O_4$ or 1.0 mM glutathione. The Δε was divided by the number of amino acids in the MtrC protein. The maintenance of oxidized or reduced state was confirmed by CD spectra in the Soret region.

Table. 3-1 Estimation of secondary structure of reduced MtrC*

	Oxidized MtrC /%	Reduced MtrC /%	MtrC + Glutation /%
α-helices	11.1	8.4	10.9
β-sheet	34.1	31.8	31.0
Turn	13.0	13.2	14.2
Others including random coil	41.7	46.6	43.1
Left-twisted β-sheet	2.7	4.4	6.0
Relaxed β-sheet	12.1	13	11.8
Right-twisted β-sheet	19.2	12.4	13.2
Parallel β-sheet	0	2.1	0.7

*Estimated by a software, BeStSel [90-91], using the CD spectra of 200 ~ 250 nm.

Possible heme geometrical alteration associated with electron flow

Since the CD signal intensity reflects the heme geometry as well as heme redox state, the decrease of Soret CD intensity in Figure 3-33a may indicate a possibility that heme geometry in MtrC is altered associated with electron flow. Once redox state of hemes are altered by electron flow, it is difficult to separate the effect of redox change from geometrical change. Thus, the electrochemical CD measurement was further conducted minimizing the change of hemes redox state.

In the absence of FMN, it is suggested that the pathway terminated with heme 5 proceeds EET and the pathway terminated with heme 2 and 7 are inactive (Figure 3-34) [14, 45, 56]. It is estimated that the heme 2 and 7 have relatively high redox potential compared with other hemes in oxidized state (average about +50 mV and heme 2 and 7 have about +180 mV and +110 mV versus SHE, respectively) [16], which is thermodynamically unfavorable to oxidize hemes 2 and 7. Thus, it is reasonable that MtrC is fully reduced during electron flow without FMN.

As expected, the absorption spectra of *S. oneidensis* MR-1 in the absence of FMN at +0.4 ~ 0.8 V (versus SHE) showed little difference from that under V_{OC} condition (Figure 3-36b), indicating that little hemes are oxidized associated with electron flow. The CD spectra showed little decrease at 421 nm during stable electron flow (Figure 3-36a and c), suggesting that heme geometry in MtrC is unaffected during electron flow without FMN cofactor, and supporting that the decrease in the intensity of the Soret CD spectra in the presence of FMN substantially originates from changes in the heme redox state.

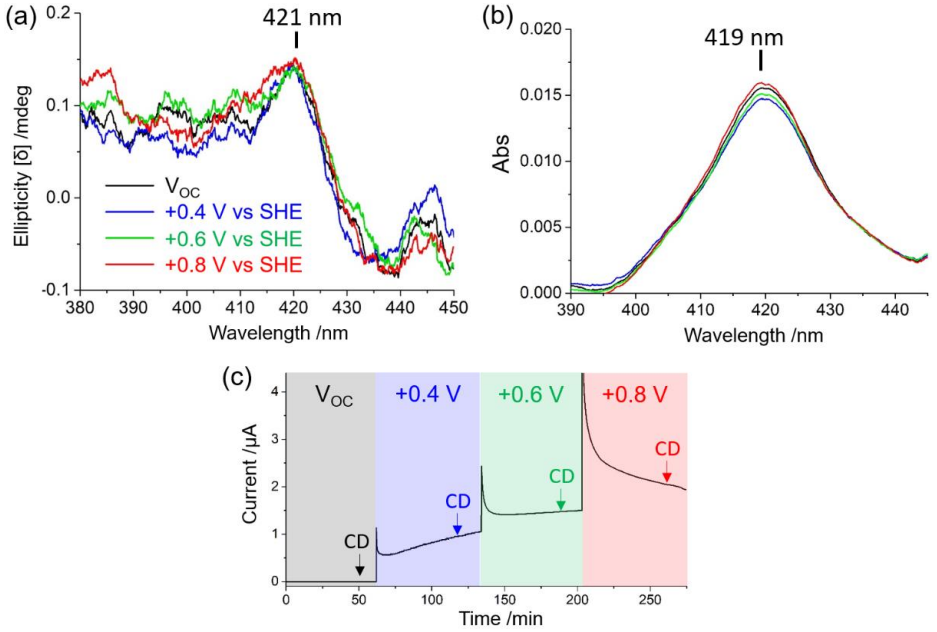

Figure 3-36. Electrochemical whole-cell CD spectra (a) and absorption spectra (c) of *S. oneidensis* MR-1 WT on Pt mesh electrode in the absence of FMN. (b) Time course of the current production from *S. oneidensis* MR-1during the CD measurements. The arrow indicates the timing of CD measurements.

3.3.4 Conclusion

In this chapter 3-3, the author combined whole-cell difference CD spectroscopy and electrochemistry to test the effect of electron flow on heme ion valence in MtrC in living system. The CD spectra at + 0.4V versus SHE showed decrease of Soret peak compared with that under V_{OC} condtion, suggesting oxidation of hemes 1, 3, 4, and 5 driven by non-equilibrium electron flow. Given that most of the conventional studies assumed that all redox centers in proteins are oxidized during electron transport (or all reduced during hole transport), which is a stable state under equilibrium condition, the present results may provide fundamental insight into understanding of biological electron transfer through metallo-proteins, where electron flow possibly rearrange redox state estimated from that of crystal structures. In addition, the results impled that the electron flow in MtrC reorganizes rate-limiting proton transport pathway in FMN-bound OM *c*-Cyts to accelerate EET. Given that the electron transport mechanisms in proteins have been discussed using crystal structures (in oxidized condition) based on the assumption that protein structures are scarcely affected by *in vivo* specific environments such as cellular components and electron flow, the whole-cell CD difference spectroscopy applicable to intact cells is an important first step in pioneering biological electron transfer providing insights into potential structural change in intact cell. The author hopes that electrochemical whole-cell CD difference spectroscopy further reveals the complicated proton-coupled EET process in living system.

References in chapter 3

1. Ramirez, B. E.; Malmstrom, B. G.; Winkler, J. R.; Gray, H. B., The currents of life: The terminal electron-transfer complex of respiration. *Proc. Natl. Acad. Sci. U.S.A.* **1995,** *92* (26), 11949-11951.

2. Marcus, R. A.; Sutin, N., Electron Transfers in Chemistry and Biology. *Biochim. Biophys. Acta* **1985,** *811* (3), 265-322.

3. Curry, W. B.; Grabe, M. D.; Kurnikov, I. V.; Skourtis, S. S.; Beratan, D. N.; Regan, J. J.; Aquino, A. J. A.; Beroza, P.; Onuchic, J. N., Pathways, Pathway Tubes, Pathway Docking, and Propagators in Electron-Transfer Proteins. *J. Bioenerg. Biomembr.* **1995,** *27* (3), 285-293.

4. Liu, J.; Chakraborty, S.; Hosseinzadeh, P.; Yu, Y.; Tian, S. L.; Petrik, I.; Bhagi, A.; Lu, Y., Metalloproteins Containing Cytochrome, Iron-Sulfur, or Copper Redox Centers. *Chem. Rev.* **2014,** *114* (8), 4366-4469.

5. Gray, H. B.; Winkler, J. R., Electron tunneling through proteins. *Q. Rev. Biophys.* **2003,** *36* (3), 341-372.

6. Blumberger, J., Recent Advances in the Theory and Molecular Simulation of Biological Electron Transfer Reactions. *Chem. Rev.* **2015,** *115* (20), 11191-11238.

7. Nealson, K. H.; Saffarini, D., Iron and Manganese in Anaerobic Respiration - Environmental Significance, Physiology, and Regulation. *Annu. Rev. Microbiol.* **1994,** *48*, 311-343.

8. Xiong, Y. J.; Shi, L.; Chen, B. W.; Mayer, M. U.; Lower, B. H.; Londer, Y.; Bose, S.; Hochella, M. F.; Fredrickson, J. K.; Squier, T. C., High-affinity binding and direct electron transfer to solid metals by the *Shewanella oneidensis* MR-1 outer membrane *c*-type cytochrome OmcA. *J. Am. Chem. Soc.* **2006,** *128* (43), 13978-13979.

9. Busalmen, J. P.; Esteve-Nunez, A.; Berna, A.; Feliu, J. M., *C*-type cytochromes wire electricity-producing bacteria to electrodes. *Angew. Chem. Int. Ed.* **2008,** *47* (26), 4874-4877.

10. Hartshorne, R. S.; Reardon, C. L.; Ross, D.; Nuester, J.; Clarke, T. A.; Gates, A. J.; Mills, P. C.; Fredrickson, J. K.; Zachara, J. M.; Shi, L.; Beliaev, A. S.; Marshall, M. J.; Tien, M.; Brantley, S.; Butt, J. N.; Richardson, D. J., Characterization of an electron conduit between bacteria and the extracellular environment. *Proc. Natl. Acad. Sci. U.S.A.* **2009,** *106* (52), 22169-22174.

11. Breuer, M.; Zarzycki, P.; Blumberger, J.; Rosso, K. M., Thermodynamics of Electron Flow in the Bacterial Deca-heme Cytochrome MtrF. *J. Am. Chem. Soc.* **2012,** *134* (24), 9868-9871.

12. Edwards, M. J.; Baiden, N. A.; Johs, A.; Tomanicek, S. J.; Liang, L. Y.; Shi, L.;

Fredrickson, J. K.; Zachara, J. M.; Gates, A. J.; Butt, J. N.; Richardson, D. J.; Clarke, T. A., The X-ray crystal structure of *Shewanella oneidensis* OmcA reveals new insight at the microbe-mineral interface. *FEBS Lett.* **2014,** *588* (10), 1886-1890.

13. Breuer, M.; Rosso, K. M.; Blumberger, J., Electron flow in multiheme bacterial cytochromes is a balancing act between heme electronic interaction and redox potentials. *Proc. Natl. Acad. Sci. U.S.A.* **2014,** *111* (2), 611-616.

14. Edwards, M. J.; White, G. F.; Norman, M.; Tome-Fernandez, A.; Ainsworth, E.; Shi, L.; Fredrickson, J. K.; Zachara, J. M.; Butt, J. N.; Richardson, D. J.; Clarke, T. A., Redox Linked Flavin Sites in Extracellular Decaheme Proteins Involved in Microbe-Mineral Electron Transfer. *Sci Rep* **2015,** *5,* 11677.

15. Watanabe, H. C.; Yamashita, Y.; Ishikita, H., Electron transfer pathways in a multiheme cytochrome MtrF. *Proc. Natl. Acad. Sci. U.S.A.* **2017,** *114* (11), 2916-2921.

16. Barrozo, A.; El-Naggar, M. Y.; Krylov, A. I., Distinct Electron Conductance Regimes in Bacterial Decaheme Cytochromes. *Angew. Chem. Int. Ed.* **2018,** *57* (23), 6805-6809.

17. Johs, A.; Shi, L.; Droubay, T.; Ankner, J. F.; Liang, L., Characterization of the Decaheme *c*-Type Cytochrome OmcA in Solution and on Hematite Surfaces by Small Angle X-Ray Scattering and Neutron Reflectometry. *Biophys. J.* **2010,** *98* (12), 3035-3043.

18. Yu, S. S.; Chen, J. J.; Liu, X. Y.; Yu, H. Q., Interfacial Electron Transfer from the Outer Membrane Cytochrome OmcA to Graphene Oxide in a Microbial Fuel Cell: Spectral and Electrochemical Insights. *ACS Energy Lett.* **2018,** *3* (10), 2449-2456.

19. Liu, H. A.; Matsuda, S.; Kawai, T.; Hashimoto, K.; Nakanishi, S., Feedback stabilization involving redox states of *c*-type cytochromes in living bacteria. *Chem. Commun.* **2011,** *47* (13), 3870-3872.

20. Sakakibara, D.; Sasaki, A.; Ikeya, T.; Hamatsu, J.; Hanashima, T.; Mishima, M.; Yoshimasu, M.; Hayashi, N.; Mikawa, T.; Walchli, M.; Smith, B. O.; Shirakawa, M.; Guntert, P.; Ito, Y., Protein structure determination in living cells by in-cell NMR spectroscopy. *Nature* **2009,** *458* (7234), 102-U10.

21. Harada, N.; Nakanishi, K., *Circular dichroic spectroscopy: exciton coupling in organic stereochemistry*. Univ Science Books: 1983.

22. Berova, N.; Di Bari, L.; Pescitelli, G., Application of electronic circular dichroism in configurational and conformational analysis of organic compounds. *Chem. Soc. Rev.* **2007,** *36* (6), 914-931.

23. Palmer, G.; Esposti, M. D., Application of Exciton Coupling Theory to the Structure of Mitochondrial Cytochrome-B. *Biochemistry* **1994,** *33* (1), 176-185.

24. Matile, S.; Berova, N.; Nakanishi, K.; Fleischhauer, J.; Woody, R. W., Structural studies by exciton coupled circular dichroism over a large distance: Porphyrin derivatives of steroids, dimeric steroids, and brevetoxin B. *J. Am. Chem. Soc.* **1996,** *118* (22), 5198-5206.
25. Heyn, M. P., Dependence of Exciton Circular-Dichroism Amplitudes on Oscillator Strength. *J Phys. Chem.* **1975,** *79* (22), 2424-2426.
26. Hartshorne, R. S.; Jepson, B. N.; Clarke, T. A.; Field, S. J.; Fredrickson, J.; Zachara, J.; Shi, L.; Butt, J. N.; Richardson, D. J., Characterization of Shewanella oneidensis MtrC: a cell-surface decaheme cytochrome involved in respiratory electron transport to extracellular electron acceptors. *J. Biol. Inorg. Chem.* **2007,** *12* (7), 1083-1094.
27. Okamoto, A.; Nakamura, R.; Hashimoto, K., *In-vivo* identification of direct electron transfer from *Shewanella oneidensis* MR-1 to electrodes via outer-membrane OmcA-MtrCAB protein complexes. *Electrochim. Acta* **2011,** *56* (16), 5526-5531.
28. Coursolle, D.; Gralnick, J. A., Modularity of the Mtr respiratory pathway of *Shewanella oneidensis* strain MR-1. *Mol. Microbiol.* **2010,** *77* (4), 995-1008.
29. Thomas, P. E.; Ryan, D.; Levin, W., Improved Staining Procedure for Detection of Peroxidase-Activity of Cytochrome-P-450 on Sodium Dodecyl-Sulfate Polyacrylamide Gels. *Anal. Biochem.* **1976,** *75* (1), 168-176.
30. Goodhew, C. F.; Brown, K. R.; Pettigrew, G. W., Heme Staining in Gels, a Useful Tool in the Study of Bacterial *C*-Type Cytochromes. *Biochim. Biophys. Acta* **1986,** *852* (2-3), 288-294.
31. Ross, D. E.; Ruebush, S. S.; Brantley, S. L.; Hartshorne, R. S.; Clarke, T. A.; Richardson, D. J.; Tien, M., Characterization of protein-protein interactions involved in iron reduction by *Shewanella oneidensis* MR-1. *Appl. Environ. Microbiol.* **2007,** *73* (18), 5797-5808.
32. Ming, X.; Fang, W. H., Mechanistic photodissociation of CO-ligated neuroglobin and subsequent rebinding processes: A theoretical study. *J. Phys. Chem. B* **2008,** *112* (3), 990-996.
33. Schweitzer-Stenner, R., Internal electric field in cytochrome *c* explored toy visible electronic circular dichroism spectroscopy. *J. Phys. Chem. B* **2008,** *112* (33), 10358-10366.
34. Pescitelli, G.; Gabriel, S.; Wang, Y. K.; Fleischhauer, J.; Woody, R. W.; Berova, N., Theoretical analysis of the porphyrin-porphyrin exciton interaction in circular dichroism spectra of dimeric tetraarylporphyrins. *J. Am. Chem. Soc.* **2003,** *125* (25), 7613-7628.

35. Borovkov, V. V.; Fujii, I.; Muranaka, A.; Hembury, G. A.; Tanaka, T.; Ceulemans, A.; Kobayashi, N.; Inoue, Y., Rationalization of supramolecular chirality in a bisporphyrin system. *Angew. Chem. Int. Ed.* **2004,** *43* (41), 5481-5485.
36. Hattori, S.; Akagawa, K.; Kudo, K.; Ishii, K., Determination of the Absolute Configuration of Side Chains of Basic Amino Acid Residues Using the Water-Soluble Porphyrin-Based Exciton Chirality Method. *J. Phys. Chem. B* **2016,** *120* (39), 10280-10287.
37. Nakamura, R.; Ishii, K.; Hashimoto, K., Electronic Absorption Spectra and Redox Properties of *C* Type Cytochromes in Living Microbes. *Angew. Chem. Int. Ed.* **2009,** *48* (9), 1606-1608.
38. Kasai, T.; Kouzuma, A.; Nojiri, H.; Watanabe, K., Transcriptional mechanisms for differential expression of outer membrane cytochrome genes *omcA* and *mtrC* in *Shewanella oneidensis* MR-1. *BMC Microbiol.* **2015,** *15*.
39. Woody, R. W.; Hsu, M.-C., Origin of the heme Cotton effects in myoglobin and hemoglobin. *J. Am. Chem. Soc.* **1971,** *93* (14), 3515-3525.
40. Blauer, G.; Sreerama, N.; Woody, R. W., Optical-Activity of Hemoproteins in the Soret Region - Circular-Dichroism of the Heme Undecapeptide of Cytochrome-*C* in Aqueous-Solution. *Biochemistry* **1993,** *32* (26), 6674-6679.
41. Field, S. J.; Dobbin, P. S.; Cheesman, M. R.; Watmough, N. J.; Thomson, A. J.; Richardson, D. J., Purification and magneto-optical spectroscopic characterization of cytoplasmic membrane and outer membrane multiheme *c*-type cytochromes from Shewanella frigidimarina NCIMB400. *J. Biol. Chem.* **2000,** *275* (12), 8515-8522.
42. Takayama, Y.; Kobayashi, Y.; Yahata, N.; Saitoh, T.; Hori, H.; Ikegami, T.; Akutsu, H., Specific binding of CO to tetraheme cytochrome *c(3)*. *Biochemistry* **2006,** *45* (10), 3163-3169.
43. Smith, D. M. A.; Rosso, K. M.; Dupuis, M.; Valiev, M.; Straatsma, T. P., Electronic coupling between heme electron-transfer centers and its decay with distance depends strongly on relative orientation. *J. Phys. Chem. B* **2006,** *110* (31), 15582-15588.
44. Bulieris, P. V.; Behrens, S.; Holst, O.; Kleinschmidt, J. H., Folding and insertion of the outer membrane protein OmpA is assisted by the chaperone Skp and by lipopolysaccharide. *J. Biol. Chem.* **2003,** *278* (11), 9092-9099.
45. Clarke, T. A.; Edwards, M. J.; Gates, A. J.; Hall, A.; White, G. F.; Bradley, J.; Reardon, C. L.; Shi, L.; Beliaev, A. S.; Marshall, M. J.; Wang, Z. M.; Watmough, N. J.; Fredrickson, J. K.; Zachara, J. M.; Butt, J. N.; Richardson, D. J., Structure of a bacterial cell surface decaheme electron conduit. *Proc. Natl. Acad. Sci. U.S.A.* **2011,** *108* (23), 9384-9389.

46. Bond, D. R.; Lovley, D. R., Electricity production by *Geobacter sulfurreducens* attached to electrodes. *Appl. Environ. Microbiol.* **2003,** *69* (3), 1548-1555.
47. Shi, L.; Squier, T. C.; Zachara, J. M.; Fredrickson, J. K., Respiration of metal (hydr)oxides by *Shewanella* and *Geobacter*: a key role for multihaem *c*-type cytochromes. *Mol. Microbiol.* **2007,** *65* (1), 12-20.
48. Tributsch, H.; Pohlmann, L., Electron transfer: Classical approaches and new frontiers. *Science* **1998,** *279* (5358), 1891-1895.
49. Myers, C. R.; Nealson, K. H., Bacterial Manganese Reduction and Growth with Manganese Oxide as the Sole Electron-Acceptor. *Science* **1988,** *240* (4857), 1319-1321.
50. Lovley, D. R.; Holmes, D. E.; Nevin, K. P., Dissimilatory Fe(III) and Mn(IV) reduction. *Advances in Microbial. Physiol.,* **2004,** *49*, 219-286.
51. Risgaard-Petersen, N.; Revil, A.; Meister, P.; Nielsen, L. P., Sulfur, iron-, and calcium cycling associated with natural electric currents running through marine sediment. *Geochim. Cosmochim. Acta* **2012,** *92*, 1-13.
52. Rowe, A. R.; Yoshimura, M.; LaRowe, D. E.; Bird, L. J.; Amend, J. P.; Hashimoto, K.; Nealson, K. H.; Okamoto, A., In situ electrochemical enrichment and isolation of a magnetite-reducing bacterium from a high pH serpentinizing spring. *Environ. Microbiol.* **2017,** *19* (6), 2272-2285.
53. Fuller, S. J.; McMillan, D. G. G.; Renz, M. B.; Schmidt, M.; Burke, I. T.; Stewart, D. I., Extracellular Electron Transport-Mediated Fe(III) Reduction by a Community of Alkaliphilic Bacteria That Use Flavins as Electron Shuttles. *Appl. Environ. Microbiol.* **2014,** *80* (1), 128-137.
54. Lovley, D. R., Bug juice: harvesting electricity with microorganisms. *Nat. Rev. Microbiol.* **2006,** *4* (7), 497-508.
55. Logan, B. E.; Hamelers, B.; Rozendal, R. A.; Schrorder, U.; Keller, J.; Freguia, S.; Aelterman, P.; Verstraete, W.; Rabaey, K., Microbial fuel cells: Methodology and technology. *Environ. Sci. Technol.* **2006,** *40* (17), 5181-5192.
56. Edwards, M. J.; White, G. F.; Lockwood, C. W.; Lawes, M. C.; Martel, A.; Harris, G.; Scott, D. J.; Richardson, D. J.; Butt, J. N.; Clarke, T. A., Structural modeling of an outer membrane electron conduit from a metal-reducing bacterium suggests electron transfer via periplasmic redox partners. *J. Biol. Chem.* **2018,** *293* (21), 8103-8112.
57. Edwards, M. J.; Hall, A.; Shi, L.; Fredrickson, J. K.; Zachara, J. M.; Butt, J. N.; Richardson, D. J.; Clarke, T. A., The Crystal Structure of the Extracellular 11-heme Cytochrome UndA Reveals a Conserved 10-heme Motif and Defined Binding Site for Soluble Iron Chelates. *Structure* **2012,** *20* (7), 1275-1284.
58. Fukushima, T.; Gupta, S.; Rad, B.; Cornejo, J. A.; Petzold, C. J.; Chan, L. J. G.;

Mizrahi, R. A.; Ralston, C. Y.; Ajo-Franklin, C. M., The Molecular Basis for Binding of an Electron Transfer Protein to a Metal Oxide Surface. *J. Am. Chem. Soc.* **2017,** *139* (36), 12647-12654.

59. Lower, B. H.; Lins, R. D.; Oestreicher, Z.; Straatsma, T. P.; Hochella, M. F.; Shi, L. A.; Lower, S. K., In vitro evolution of a peptide with a hematite binding motif that may constitute a natural metal-oxide binding archetype. *Environ. Sci. Technol.* **2008,** *42* (10), 3821-3827.

60. Lower, S. K.; Hochella, M. F.; Beveridge, T. J., Bacterial recognition of mineral surfaces: Nanoscale interactions between Shewanella and alpha-FeOOH. *Science* **2001,** *292* (5520), 1360-1363.

61. Lower, B. H.; Shi, L.; Yongsunthon, R.; Droubay, T. C.; McCready, D. E.; Lower, S. K., Specific bonds between an iron oxide surface and outer membrane cytochromes MtrC and OmcA from *Shewanella oneidensis* MR-1. *J. Bacteriol.* **2007,** *189* (13), 4944-4952.

62. Bose, S.; Hochella, M. F.; Gorby, Y. A.; Kennedy, D. W.; McCready, D. E.; Madden, A. S.; Lower, B. H., Bioreduction of hematite nanoparticles by the dissimilatory iron reducing bacterium *Shewanella oneidensis* MR-1. *Geochim. Cosmochim. Acta* **2009,** *73* (4), 962-976.

63. Glasauer, S.; Langley, S.; Beveridge, T. J., Sorption of Fe (hydr)oxides to the surface of *Shewanella putrefaciens*: Cell-bound fine-grained minerals are not always formed de novo. *Appl. Environ. Microbiol.* **2001,** *67* (12), 5544-5550.

64. Elzinga, E. J.; Huang, J. H.; Chorover, J.; Kretzschmar, R., ATR-FTIR Spectroscopy Study of the Influence of pH and Contact Time on the Adhesion of *Shewanella putrefaciens* Bacterial Cells to the Surface of Hematite. *Environ. Sci. Technol.* **2012,** *46* (23), 12848-12855.

65. Yan, W.; Wang, H. B.; Jing, C. Y., Adhesion of *Shewanella oneidensis* MR-1 to Goethite: A Two-Dimensional Correlation Spectroscopic Study. *Environ. Sci. Technol.* **2016,** *50* (8), 4343-4349.

66. Korenevsky, A.; Beveridge, T. J., The surface physicochemistry and adhesiveness of *Shewanella* are affected by their surface polysaccharides. *Microbiology* **2007,** *153*, 1872-1883.

67. Reuillard, B.; Ly, K. H.; Hildebrandt, P.; Jeuken, L. J. C.; Butt, J. N.; Reisner, E., High Performance Reduction of H2O2 with an Electron Transport Decaheme Cytochrome on a Porous ITO Electrode. *J. Am. Chem. Soc.* **2017,** *139* (9), 3324-3327.

68. Shibanuma, T.; Nakamura, R.; Hirakawa, Y.; Hashimoto, K.; Ishii, K., Observation of *In Vivo* Cytochrome-Based Electron-Transport Dynamics Using Time-

Resolved Evanescent Wave Electroabsorption Spectroscopy. *Angew. Chem. Int. Ed.* **2011,** *50* (39), 9137-9140.

69. Hitchcock, J. P.; Tasker, A. L.; Stark, K.; Leeson, A.; Baxter, E. A.; Biggs, S.; Cayre, O. J., Adsorption of Catalytic Nanoparticles onto Polymer Substrates for Controlled Deposition of Microcapsule Metal Shells. *Langmuir* **2018,** *34* (4), 1473-1480.

70. Kiernan, J. A., Formaldehyde, formalin, paraformaldehyde and glutaraldehyde: what they are and what they do. *Microscopy today* **2000,** *1* (5), 8-12.

71. Sugita, Y.; Nagai, M.; Yoneyama, Y., Circular dichroism of hemoglobin in relation to the structure surrounding the heme. *J. Biol. Chem.* **1971,** *246* (2), 383-388.

72. Miles, A. J.; Wallace, B. A., Circular dichroism spectroscopy of membrane proteins. *Chem. Soc. Rev.* **2016,** *45* (18), 4859-4872.

73. Swords, N. A.; Wallace, B. A., Circular-Dichroism Analyses of Membrane-Proteins - Examination of Environmental-Effects on Bacteriorhodopsin Spectra. *Biochem. J.* **1993,** *289*, 215-219.

74. Sohlenkamp, C.; Geiger, O., Bacterial membrane lipids: diversity in structures and pathways. *FEMS Microbiol. Rev.* **2016,** *40* (1), 133-159.

75. Okamoto, A.; Hashimoto, K.; Nealson, K. H.; Nakamura, R., Rate enhancement of bacterial extracellular electron transport involves bound flavin semiquinones. *Proc. Natl. Acad. Sci. U.S.A.* **2013,** *110* (19), 7856-7861.

76. Friddle, R. W.; Battle, K.; Trubetskoy, V.; Tao, J. H.; Salter, E. A.; Moradian-Oldak, J.; De Yoreo, J. J.; Wierzbicki, A., Single-Molecule Determination of the Face-Specific Adsorption of Amelogenin's C-Terminus on Hydroxyapatite. *Angew. Chem. Int. Ed.* **2011,** *50* (33), 7541-7545.

77. Qian, X. L.; Mester, T.; Morgado, L.; Arakawa, T.; Sharma, M. L.; Inoue, K.; Joseph, C.; Salgueiro, C. A.; Maroney, M. J.; Lovley, D. R., Biochemical characterization of purified OmcS, a *c*-type cytochrome required for insoluble Fe(III) reduction in *Geobacter sulfurreducens*. *Biochim. Biophys. Acta* **2011,** *1807* (4), 404-412.

78. Leang, C.; Qian, X. L.; Mester, T.; Lovley, D. R., Alignment of the *c*-Type Cytochrome OmcS along Pili of *Geobacter sulfurreducens*. *Appl. Environ. Microbiol.* **2010,** *76* (12), 4080-4084.

79. Summers, Z. M.; Fogarty, H. E.; Leang, C.; Franks, A. E.; Malvankar, N. S.; Lovley, D. R., Direct Exchange of Electrons Within Aggregates of an Evolved Syntrophic Coculture of Anaerobic Bacteria. *Science* **2010,** *330* (6009), 1413-1415.

80. Okamoto, A.; Saito, K.; Inoue, K.; Nealson, K. H.; Hashimoto, K.; Nakamura, R., Uptake of self-secreted flavins as bound cofactors for extracellular electron transfer in Geobacter species. *Energy Environ. Sci.* **2014,** *7* (4), 1357-1361.

81. Mitchell, A. C.; Peterson, L.; Reardon, C. L.; Reed, S. B.; Culley, D. E.; Romine, M. R.; Geesey, G. G., Role of outer membrane c-type cytochromes MtrC and OmcA in *Shewanella oneidensis* MR-1 cell production, accumulation, and detachment during respiration on hematite. *Geobiology* **2012,** *10* (4), 355-370.
82. Neal, A. L.; Bank, T. L.; Hochella, M. F.; Rosso, K. M., Cell adhesion of Shewanella oneidensis to iron oxide minerals: Effect of different single crystal faces. *Geochem. Trans.* **2005,** *6* (4), 77-84.
83. Song, F.; Koo, H.; Ren, D., Effects of Material Properties on Bacterial Adhesion and Biofilm Formation. *J. Dent. Res.* **2015,** *94* (8), 1027-1034.
84. Friedlander, R. S.; Vlamakis, H.; Kim, P.; Khan, M.; Kolter, R.; Aizenberg, J., Bacterial flagella explore microscale hummocks and hollows to increase adhesion. *Proc. Natl. Acad. Sci. U.S.A.* **2013,** *110* (14), 5624-5629.
85. Bos, R.; van der Mei, H. C.; Busscher, H. J., Physico-chemistry of initial microbial adhesive interactions - its mechanisms and methods for study. *FEMS Microbiol. Rev.* **1999,** *23* (2), 179-230.
86. Lusk, B. G.; Peraza, I.; Albal, G.; Marcus, A. K.; Popat, S. C.; Torres, C. I., pH Dependency in Anode Biofilms of *Thermincola ferriacetica* Suggests a Proton-Dependent Electrochemical Response. *J. Am. Chem. Soc.* **2018,** *140* (16), 5527-5534.
87. Mehta, T.; Coppi, M. V.; Childers, S. E.; Lovley, D. R., Outer membrane *c*-type cytochromes required for Fe(III) and Mn(IV) oxide reduction in *Geobacter sulfurreducens*. *Appl. Environ. Microbiol.* **2005,** *71* (12), 8634-8641.
88. Jain, A.; Gazzola, G.; Panzera, A.; Zanoni, M.; Marsii, E., Visible spectroelectrochemical characterization of *Geobacter sulfurreducens* biofilms on optically transparent indium tin oxide electrode. *Electrochim. Acta* **2011,** *56* (28), 10776-10785.
89. Heidelberg, J. F. *et al,* Genome sequence of the dissimilatory metal ion-reducing bacterium *Shewanella oneidensis*. *Nat .Biotechnol.* **2002,** *20* (11), 1118-1123.
90. Micsonai, A.; Wien, F.; Kernya, L.; Lee, Y. H.; Goto, Y.; Refregiers, M.; Kardos, J., Accurate secondary structure prediction and fold recognition for circular dichroism spectroscopy. *Proc. Natl. Acad. Sci. U.S.A.* **2015,** *112* (24), E3095-E3103.
91. Micsonai, A.; Wien, F.; Bulyaki, E.; Kun, J.; Moussong, E.; Lee, Y. H.; Goto, Y.; Refregiers, M.; Kardos, J., BeStSel: a web server for accurate protein secondary structure prediction and fold recognition from the circular dichroism spectra. *Nucleic Acids Res.* **2018,** *46* (W1), W315-W322.

Chapter
4

Control of reverse extracellular electron transport

In chapter 2 and 3, the author has examined the mechanisms of flavin-mediated enhancement of non-equilibrium extracellular electron export reaction through OM *c*-Cyts in *S. oneidensis* MR-1. While the electron export mediated by flavin is a universal reaction, the reverse electron flow, that is cathodic electron flow termed extracellular electron uptake (EEU), occurs in not all kinds of EET-capable bacteria. For example, the OM *c*-Cyts in *S. oneidensis* MR-1 conduct EEU as fast as EET process [1-2], however, reverse electron flux through OM *c*-Cyts in another model EET-capable bacteria, *Geobacter sulfurreducens* PCA, is limited to be about 10 times lower than that of EET like a "diode" [3-6](Figure 4-1). Considering that the mechanisms dictating uni- or bi-directional electron flow through molecules under non-equilibrium condition potentially improves the efficiency and stability of molecular computational technologies, unraveling the EEU mechanisms through OM *c*-Cyts may contribute to the understanding and development of molecular electronics as well as biological electron transport reactions [7-8]. Since in chapter 2 and 3, the author has found that the flavin analogues possessing N(5) are the key to control the EET process, in this chapter 4, the unidirectional and bidirectional electron transport mechanisms in OM *c*-Cyts of *S. oneidensis* MR-1 and *G. sulfurreducens* PCA were examined using N(5) molecules. After the investigation of electron transport property of OM *c*-Cyts in *S. oneidensis* MR-1 and *G. sulfurreducens*

PCA in chapter 4-1 and 4-2, the author further developed a novel technique to estimate enzyme activity inside the bacterial cells by controlling the EEU kinetics in chapter 4-3.

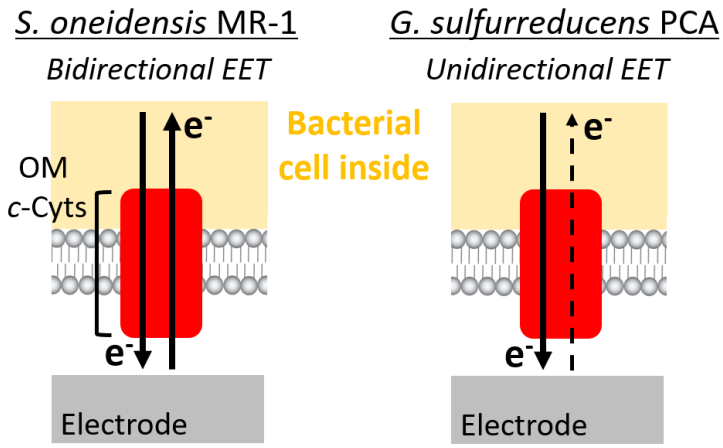

Figure 4-1. Bi- or uni- directional EET through OM *c*-Cyts in *S. oneidensis* MR-1 and *G. sulfurreducens* PCA

4.1

Rate regulation of extracellular electron uptake in *S. oneidensis* MR-1 as a model system of bidirectional electron transport

4.1.1 Introduction

Microbial conversion from electrical energy to a desired product, electrosynthesis, occurs with intercellular metabolic enzymatic reactions driven by an electrode as a metabolic electron donor [9-10], which is utilized for bioremediation by reduction of heavy metals [11] and carbon dioxide to organic carbon compounds for biofuels or fuel precursors using renewable sources of electricity [12]. Gaseous hydrogen generated by electrolysis serves as electron carrier in number of systems, but excessive low electrode potential for hydrogen evolution make the process inefficient [9-10, 13]. To this end, direct microbial electron uptake process, EEU, is key factor to increase the efficiency for microbial electrosynthesis [9, 14]. *S. oneidensis* MR-1 is a model system to conduct EEU through the OM *c*-Cyts by posing cathodic potential enough to drive reduction reaction of metabolite. For example, the application of −0.45 V (vs SHE) to *S. oneidensis* MR-1 drives reduction reaction of fumarate into succinate. Towards development of microbial electrosynthesis, methodologies to accelerate and regulate EEU processes are required.

The rate of EEU mediated by OM *c*-Cyts is enhanced by the presence of small redox molecules that act as either shuttles [15] or bound cofactors [16]. Although several electron shuttles have been identified to date,[15, 17-18] only riboflavin (RF) is known to

function as non-covalently bound redox active centers in OM *c*-Cyts during EEU process.[19-21] The EEU process are initiated by one-electron redox cycling of RF between semiquinone (Sq) and hydroquinone (Hq) at the electrode surface. Hq transport electrons to bound OmcA, and subsequently reduce intracellular molecules. The identification and characterization of alternative cofactor molecules is important for understanding the acceleration mechanisms of EEU mediated by OM *c*-Cyts, particularly the kinetics and molecular interactions between noncovalent flavin cofactors and the binding pocket of MtrC and OmcA protein.

In the present study, the author examined the potential of compounds other than RF to function as bound redox cofactors in OmcA using whole-cell electrochemical assays performed under cathodic conditions. Here, two flavin analogues were selected as potential cofactor of OmcA protein, safranin (Saf) with N(5) and anthraquinone-1-sulfonate (α-AQS) without N(5) (Figure 4-2). Their EET kinetics and binding affinity with OmcA were evaluated to obtain strategies to design cofactors for controlling the rate of EEU.

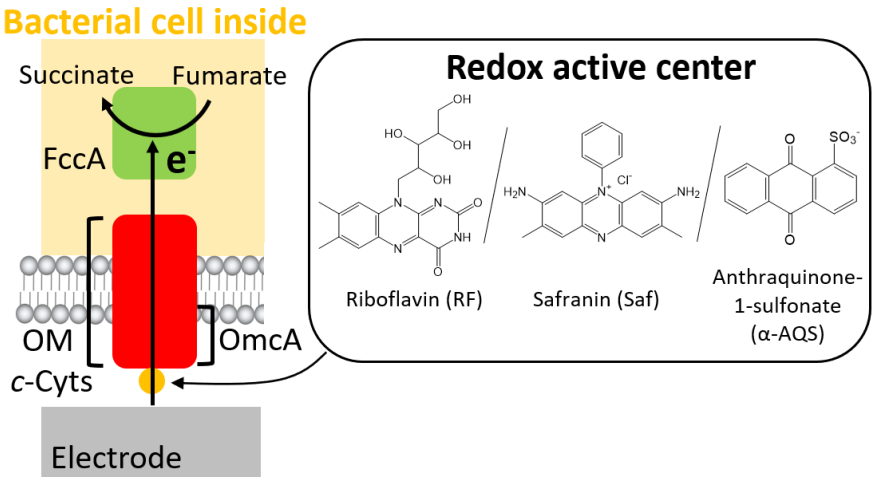

Figure 4-2. EEU of *S. oneidensis* MR-1 with flavin analogues

4.1.2 Methods

Electrode-immobilized biofilm construction and electrochemical measurement

Electrochemical experiments were conducted under cathodic conditions after the formation of a monolayer biofilm *S. oneidensis* MR-1 and its mutants in electrochemical reactors as described in chapter 2-1. After confirming the formation of a biofilm on an ITO electrode by in-situ confocal fluorescence microscopy, the supernatant in the electrochemical cell was replaced with anaerobic DM containing 50 mM fumarate as an electron acceptor, and the electrode potential was shifted to −0.45 V to promote the donation of electrons to microbes. Differential pulse (DP) voltammetry was conducted using an automatic polarization system (VMP3, Bio Logic Co.) and the following conditions: 5.0 mV pulse increments, 50 mV pulse amplitude, 300 ms pulse width, and a 5.0 s pulse period. Charging current subtraction was performed using the open source program SOAS by fitting the baseline from regions sufficiently far from the target reduction peaks and assuming that continual charging current flows throughout the peak region.[22]

Calculation of current enhancement factor (β) using dissociation constant (K_d)

When the cathodic current (I_c) is proportionally related to the amount of redox cofactor binding, the normalized enhancement factor (β) is defined as follows:

$$\beta = \frac{I_C}{[\mathrm{PL}]} \quad (\mathrm{Eq}\ 4-1)$$

For the calculation of β, the dissociation constant (K_d) for complex formation between the non-covalent redox cofactors and OM *c*-Cyts was estimated as described in chapter

2-1. K_d was estimated from the cathodic current (I_c) and the reduction peak current in DP voltammograms before and after the addition of each redox molecule. Using K_d, β can be described as follows:

$$\beta = \frac{([\mathrm{L}] + \mathrm{K_d})I_C}{[\mathrm{L}]([\mathrm{P}] + [\mathrm{PL}])} \quad (\mathrm{Eq}\ 4-2)$$

where [P] is the concentration of OM *c*-Cyts, [L] is the concentration of unbound RF, Saf or α-AQS in solution, and [PL] is the concentration of the OM *c*-Cyts complex with these molecules. To compare β among the different redox molecules, [L] was set as 2.0 μM and the sum of [P] and [PL] was assumed to be constant in the uniform monolayer biofilm of *S. oneidensis* MR-1.

4.1.3 Results and discussion

Saf and α-AQS enhance extracellular electron uptake as redox active centers in OmcA

To determine if Saf and α-AQS can function as redox cofactors in OM *c*-Cyts and enhance the rate of EET, the author examined cathodic current production for fumarate reduction in the presence of Saf and α-AQS at a concentration of 2.0 μM, in which bound cofactors of OmcA strongly enhances EEU but not as shuttling redox mediators as described in chapter 2. In the presence of 50 mM fumarate as the sole electron acceptor, a *S. oneidensis* MR-1 biofilm generated a cathodic current (I_c) of approximately –2.5 μA at –0.45 V (vs. SHE). However, upon the addition of 2.0 μM Saf, an immediate increase in I_c comparable to that resulting from the addition of 2.0 μM RF was detected (Figure 4-3). Although the increase was markedly less compared to the systems supplemented with Saf or RF, the addition of α-AQS also led to an enhancement in I_c. These results suggest that Saf and α-AQS enhance the rate of electron uptake by OM *c*-Cyts by serving as redox active centers, as has been demonstrated for RF.

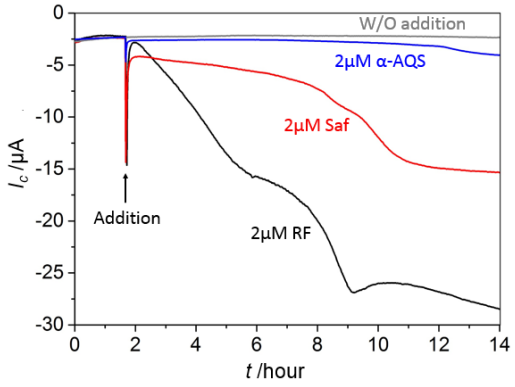

Figure 4-3. Time course for cathodic current production (I_c) from the biofilm of *S. oneidensis* MR-1 in the presence of 50 mM fumarate on an ITO electrode at −0.45 V (vs SHE). Arrow indicates the point at which 2.0 μM Saf, α-AQS, or RF was added to each batch. The same tendency was reproduced in at least three separate experiments.

The electrochemical properties of Saf and α-AQS

To examine the electrochemical properties of Saf and α-AQS in the monolayer biofilm of *S. oneidensis* MR-1, DP voltammetry was conducted during the course of the I_c measurement (Figure 4-4, 5, 6). After the addition of 4.0 μM Saf to the electrochemical reactor containing an *S. oneidensis* MR-1 monolayer biofilm, the peak cathodic current was observed at −0.45 V vs SHE ($I_{-0.45}$) (Figure 4-4a) and increased with increasing Saf concentration (Figure 4-5a), indicating that the cathodic peak at −0.45 V ($I_{-0.45}$) is assignable to the redox reaction mediated by Saf. The half-width potential ($\Delta E_{p/2}$) for $I_{-0.45}$ was approximately 190 mV (Figure 4-4a), which is close to the characteristics of the one-electron redox reaction in bound RF with OmcA under cathodic conditions.[2] In contrast, the two-electron redox reaction of unbound Saf in a cell-free system has $\Delta E_{p/2}$ and E_p values of approximately 75 mV and –0.30 V, respectively (Figure 4-4a). These redox profiles strongly suggest that Saf mediates one-electron redox reactions in *S. oneidensis* MR-1 biofilms, similar to bound RF cofactors in OmcA [2]. In addition, DP voltammograms of α-AQS in the presence or absence of biofilm showed redox profiles characteristic of one- or two-electron redox reactions, respectively ((Figure 4-4b and 4-5b). These results indicate that both Saf and α-AQS are able to mediate one-electron reactions in MR-1 biofilms, as has been reported for RF as a bound cofactor in OmcA.

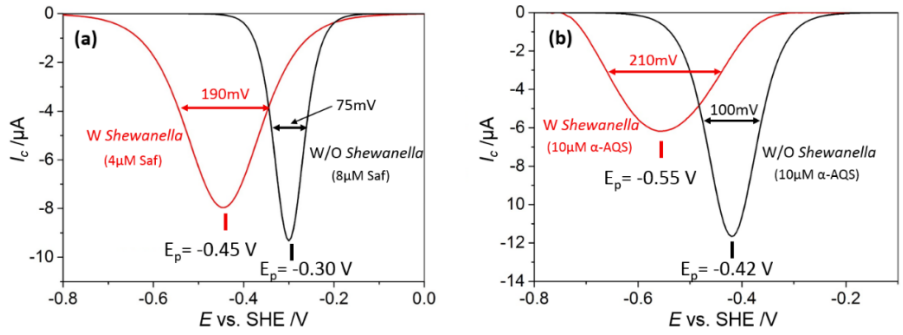

Figure 4-4. Baseline-subtracted differential pulse (DP) voltammograms for monolayer biofilm of *S. oneidensis* MR-1 (red line) and cell-free electrolyte (black line) in the presence of (a) Saf and (b) α-AQS at a concentration of 4.0 μM on an ITO electrode surface. The same tendency was reproduced in three separate experiments.

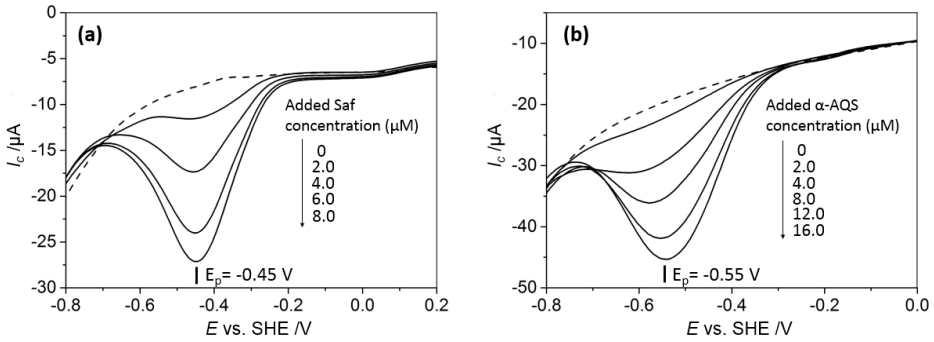

Figure 4-5. DP voltammograms for monolayer biofilms of *S. oneidensis* MR-1 on an ITO electrode surface in the absence (dotted line) and presence of Saf at several different concentrations (solid line) (a), in the absence (dotted line) and presence of α-AQS at several different concentrations (solid line) (b).

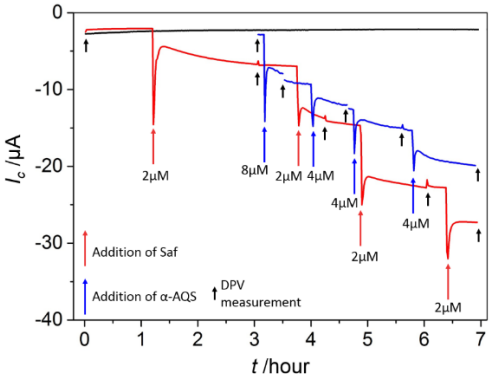

Figure 4-6. I_c from biofilms of *S. oneidensis* MR-1 in the presence of 50 mM fumarate on an ITO electrode at −0.45 V (vs. SHE). Red and blue arrows indicate the points at which Saf and α-AQS were added into the reactor, respectively. Black arrows indicate the timings of DPV measurements.

To examine the interaction between OM *c*-Cyts and Saf or α-AQS in biofilms, the author used mutant strains of *S. oneidensis* MR-1 that lack either OmcA (Δ*omcA*) or MtrC (Δ*mtrC*). In the DP voltammogram for the Δ*omcA* biofilm in the presence of Saf, an approximately 90 mV positive shift in the redox signal compared to that for the wild-type (WT) system was observed (Figure 4-7a), indicating that OmcA interacts with Saf in the biofilm. However, the negative shift (~60 mV) in the peak potential of unbound Saf suggests that Saf interacts with not only OmcA, but also other OM *c*-Cyts, such as MtrC, in MR-1 cells. In contrast, a negligible peak shift was observed in the DP voltammograms for α-AQS in the presence or absence of Δ*omcA* biofilms (Figure 4-7b), suggesting that α-AQS specifically associates with OmcA protein. In addition, the I_c of the Δ*mtrC* monolayer biofilm in the presence of Saf was approximately 15% lower than that for the WT biofilm, whereas comparable values between Δ*mtrC* and WT were detected in the systems supplemented with α-AQS (Figure 4-8). Taken together, these results strongly suggest that Saf functions as a bound cofactor in OM *c*-Cyts of MR-1, mainly in OmcA, but also in MtrC, and that α-AQS specifically interacts with OmcA to enhance microbial cathodic electron uptake.

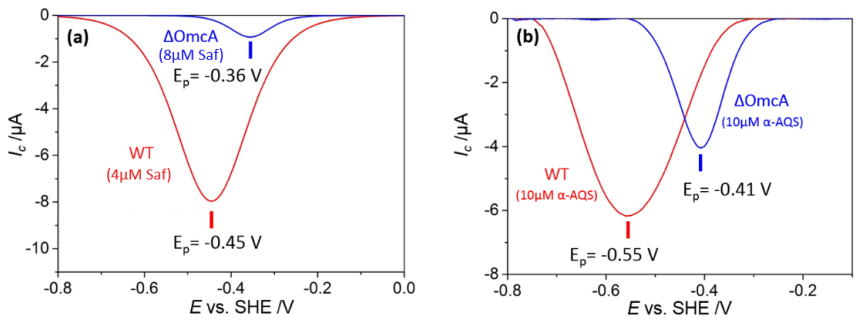

Figure 4-7. Baseline-subtracted DP voltammograms for monolayer biofilm of WT (red line) and Δ*omcA* (blue line) in the presence of (a) Saf and (b) α-AQS The same tendency was reproduced in three separate experiments.

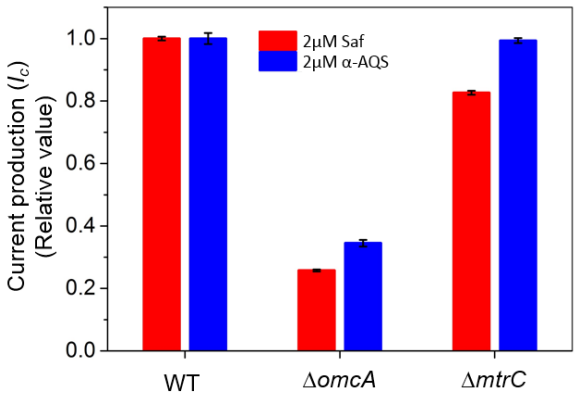

Figure 4-8. I_c from biofilms of WT, Δ*omcA*, and Δ*mtrC* strains in the presence of 50 mM fumarate on an ITO electrode at −0.45 V (vs. SHE). Red and blue bars represent I_c from two independent experiments in the presence of 2.0 μM Saf and α-AQS, respectively. I_c is normalized as WT = 1.0.

We also examined the contribution of the cathodic reaction of Saf and α-AQS to I_c in the presence of the MR-1 biofilm by plotting I_c against $I_{-0.45}$ and $I_{-0.55}$, which correspond to the relative amount of Saf and α-AQS, respectively. In the course of current generation, we examined the effects of several different concentrations of Saf and α-AQS in the electrochemical system and performed DP voltammetry at each concentration (Figure 4-9). I_c exhibited a clear negative correlation with both $I_{-0.45}$ and $I_{-0.55}$, giving square of the correlation coefficient values of 0.997 and 0.995, respectively. These results indicate that complex formation of either Saf or α-AQS with OM *c*-Cyt proteins enhances the rate of EEU from the electrode. In addition, these results also suggest that the rate-determining factor for I_c is the number of polycyclic molecules bound to OM *c*-Cyts within biofilms formed at the electrode surface under the present experimental conditions.

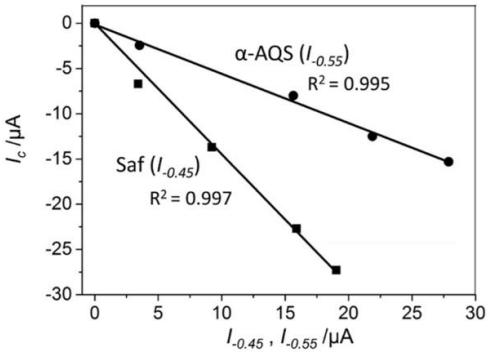

Figure 4-9. Plots of I_c at an electrode potential of −0.45 V (vs SHE) against the peak current of Saf and α-AQS (Saf: E_p = −0.45 V vs SHE, α-AQS: E_p = −0.55 V vs SHE). The squares of the correlation coefficients include the point of origin.

Quantitative comparison of binding affinity to OM *c*-Cyts and EET kinetics for RF, Saf and α-AQS

To obtain insight into the factors controlling the interaction between OM *c*-Cyts and the redox molecules, RF, Saf and α-AQS, the author next compared the dissociation constant (K_d) between OM *c*-Cyts and each polycyclic redox molecule based on the observed concentration dependency for the peak currents in DP voltammograms, as described in Experimental Section (Table 4-1). Notably, RF and Saf possess N(5) in their backbone, but α-AQS does not, suggesting that N(5) is critical for stabilizing one-electron reduced Sq cofactors to accelerate EEU process. This is consistent with the results obtained in chapter 2; the stabilization of Sq state in anodic condition requires N(5) in flavin backbone.

Table 4-1. Dissociation constant (K_d) for each molecule.

	K_d /μM
Saf	18.1±4.4
α-AQS	29.5±1.8
RF	15.8±0.4

The author also compared the enhancement factor (β), EET kinetics among single molecules of RF, Saf and α-AQS, based on the I_c and K_d for each molecule as described in Method Section. Because the molecules with a more positive redox potential showed higher β values (the β for Saf and α-AQS were approximately 60% and 14%, respectively, of the β for RF) (Figure 4-10), it appears that electron transfer from the electrode to these redox molecules is the slowest reaction for cathodic fumarate reduction. This speculation is in good agreement with the observed linear relationship between I_c and reduction peak current in DP voltammograms of *S. oneidensis* MR-1 biofilms in the presence of these redox molecules ($I_{-0.45}$ or $I_{-0.55}$) (Figure 4-9), because these data suggest that the reduction rate of these molecules determines the rate of cathodic fumarate reduction. Therefore, it can be expected that flavin analogues with higher redox potentials than RF have a potential to enhance the rate of EEU. Since the relationship of pK_a value and the EEU kinetics is still open question, it would be of great interest to test the β value using various flavin analogues with different pK_a.

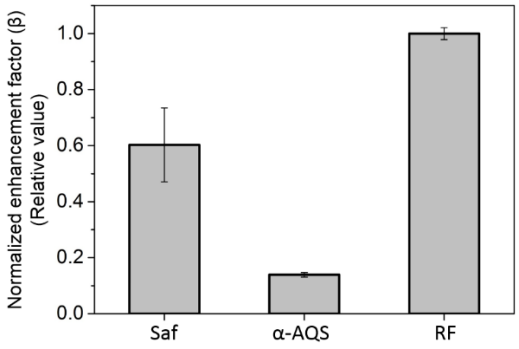

Figure 4-10. Normalized current enhancement factor (β) for Saf, α-AQS, and RF calculated from at least two separate experiments

4.1.4 Conclusion

In this work, the author demonstrated that two flavin analogues, Saf and α-AQS, accelerate non-equilibrium EEU process in *S. oneidensis* MR-1 by functioning as bound redox cofactors in the OM *c*-Cyt protein, OmcA. This finding indicates that the binding site in OmcA for RF is sufficiently flexible to accept other flavin analogues in cathodic condition as well as anodic condition. In addition, the data for K_d suggest that the N(5) in their backbone is important for the affinity of non-covalent redox cofactors towards OM *c*-Cyts, a property that may be utilized as a strategy for controlling the rate of EET. Thus, the findings from this study provide an approach for designing electrocatalysts that mediate EEU towards microbial electrosynthesis. Furthermore, because the flavin-binding pocket in OM *c*-Cyts is also found in another model iron-reducing bacterium, *G. sulfurreducens* PCA, this approach may also be applicable to processes involving *G. sulfurreducens* PCA,[23] which is an important species in industrial bioelechemical reactors.[3]

4.2

Rate regulation of extracellular electron uptake in *G. sulfurreducens* PCA as a model system of unidirectional electron transport

4.2.1 Introduction

Microbial EEU process is applicable for production of various compounds and immobilization of heavy metals as bioremediation. *Geobacter sulfurreducens* PCA is capable of the formation of electrically conductive biofilm matrix [3, 24], which makes electrical connection from the electrode to even cells without direct contact with the electrode surface [25]. Combined with EEU capability via OM *c*-Cyts, the conductive matrix enables *G. sulfurreducens* PCA to produce the highest anodic current production among the strains isolated so far. Because electronic measurements have shown electron conduction through biofilm and the bioengineering is available for the *G. sulfurreducens* PCA [26-27], the biofilm has high potential as a platform of microbial electrosynthesis. However, as for the EEU reaction, the current density drastically decreases, typically over 10 times [3-4], suggesting that the suppression of electron uptake via OM *c*-Cys from the conductive matrix occurs specifically under cathodic condition. Although it has been shown that the alteration in outer-surface components gradually proceeds during cathodic condition [5-6], the mechanism for the suppression of electron uptake in *G. sulfurreducens* PCA has not been identified in molecular-level.

The suppression of EEU is distinct from that in another model iron-reducing

bacterium, *S oneidensis* MR-1, which showed high EEU kinetics comparable with anodic EET kinetics. In *S. oneidensis* MR-1, cathodic reaction proceeds with the almost identical rate with that in anodic reaction, where electron transport processes are mediated by flavin analogues with N(5) such as RF and Saf as cofactors in OM *c*-Cyts as described in chapter 4-1. Meanwhile, the research group of the author recently found that RF binds with OM *c*-Cyts as a non-covalent cofactor and constitute the conduits for electron export from *G. sulfurreducens* PCA to anode [23]. In this chapter 4-2, the author examined two hypotheses, 1. RF and flavin analogues with N(5) in their backbone potentially mediate electron uptake reaction as well in *G. sulfurreducens* PCA, and 2. cathodic current suppression is due to the dissociation of RF from OM *c*-Cyts under cathodic condition.

Electronic properties of OM *c*-Cyts in *Geobacter* have been studied mostly in the thick biofilm [28-29]. However, because those experiments potentially cannot distinguish inter and extracellular electron transport, ex-situ measurements for the biofilm conductivity, e.g. isolation of nano filaments, have been conducted [26, 30]. Here, the author prepared a monolayer biofilm of *Geobacter sulfurreducens* PCA strain to specifically monitor the interfacial electron transfer of OM *c*-Cyts to the electrode, and explored the role of RF for the asymmetric electron flow via OM *c*-Cyts in *G. sulfurreducens* PCA (Figure 4-11).

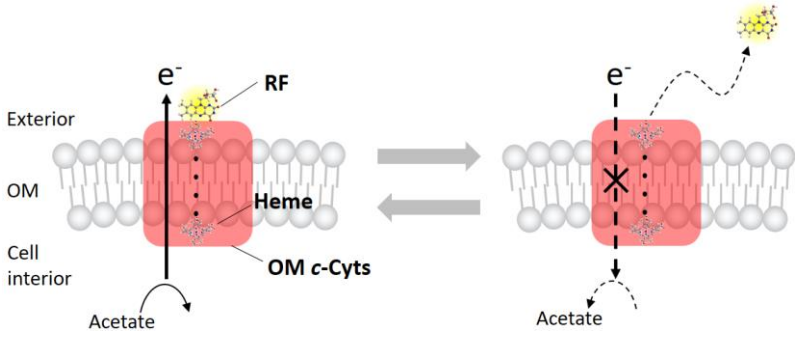

Figure 4-11. Schematic illustration of asymmetric electron flow through OM *c*-Cyts in *G. sulfurreducens* PCA dictated by association/dissociation of RF cofactor.

4.2.2 Methods

Bacterial strains and growth conditions

G. sulfurreducens PCA and the mutant lacking omcB, omcE, omcS, and omcT (*ΔomcBEST*) were cultured anaerobically at 30 °C for 120 h in 100 mL PSN medium (1.68 gL^{-1} $NaHCO_3$, 0.02 gL^{-1} $CaCl_2 \cdot 2H_2O$, 0.54 gL^{-1} NH_4Cl, 0.02 gL^{-1} $MgCl_2 \cdot 6H_2O$, 0.02 gL^{-1} $MgSO_4 \cdot 7H_2O$, 0.14 gL^{-1} KH_2PO_4, 4.76 gL^{-1} HEPES, 0.1 gL^{-1} yeast extract, 0.1 mL trace element solution (10mM $FeCl_2$, 1mM $CoCl_2$, 1 mM $MnCl_2 \cdot 4H_2O$, 1 mM $ZnCl_2$, 0.1 mM H_3BO_3, 0.1 mM $NiCl_2$, 0.1 mM $AlCl_3$, 0.1 mM $Na_2MoO_4 \cdot 2H_2O$, 0.01 mM $CuCl_2$), and 1 μL Se/W solution (1 mM Na_2SeO_3, 1 mM $Na_2WO_4 \cdot H_2O$)), supplemented with 20 mM acetate as a carbon source and 80 mM fumarate as an electron acceptor.

Formation of a biofilm of *G. sulfurreducens* PCA on an ITO electrode

A biofilm of *G. sulfurreducens* PCA was formed on an indium tin-doped oxide (ITO) substrate in the same electrochemical reactor as that in chapter 2. 4.0 mL PSN supplemented 10 mM acetate was deaerated by bubbling with N_2 and added to the electrochemical reactor as an electrolyte. The reactor was maintained at 30 °C and was not agitated during the measurements. A cell suspension of *G. sulfurreducens* PCA was used for biofilm formation after washing three times with PSN medium by centrifugation for 10 min at 4,000 x g. The concentration of the cell suspension in the electrochemical reactor was determined by measuring the optical density at 600 nm (OD_{600}) and adjusted to OD_{600} = 0.5. The cell suspension was cultivated on the ITO electrode, which was poised at a potential of +0.4 V versus SHE using an automatic polarization system (VMP3, Bio Logic) for 40 h.

Electrochemical measurement of *G. sulfurreducens* PCA biofilm

After formation of a biofilm, the supernatant in the electrochemical reactor was then removed and replaced with anaerobic PSN after washing a biofilm twice with anaerobic PSN. The electrode potential was shifted to −0.45 V versus SHE to promote the donation of electrons to microbes. Differential pulse (DP) voltammetry was conducted using an automatic polarization system (VMP3, Bio Logic) under the following conditions: 5.0 mV pulse increments, 50 mV pulse amplitude, 300 ms pulse width, and a 5.0 s pulse period. Charging current subtraction was performed using the open source program SOAS by fitting the baseline from regions sufficiently far from the target reduction peaks and assuming that continual charging current flows throughout the peak region [22].

Imaging of *G. sulfurreducens* PCA biofilm by confocal fluorescence microscopy

A biofilm of *G. sulfurreducens* PCA formed on ITO electrode, which was poised at a potential of +0.4 V versus SHE for 40 h, was stained with DAPI (4',6-diamidino-2-phenylindole) using a 0.5 μg/ml solution after gentle wash with phosphate buffer. Microscopic observation was performed on a confocal laser scanning microscope (Fluoview FV1000, Olympus) using a 100× oil-immersion objective lens.

Quantification of nitrate, nitrite and ammonium ions from *G. sulfurreducens* PCA during −0.45 V (versus SHE) application by ion chromatography

200 μL of supernatant in the electrochemical reactor was collected during −0.45 V (versus SHE) application on a monolayer biofilm of *G. sulfurreducens* PCA. After centrifugation for 10 min at 4,000 x g and filtration, the supernatant was diluted 100 times prior to

analysis. Especially in the case of cation chromatography, the supernatant was diluted by 7.30 gL^{-1} TAPS buffer at pH = 8.00 for keeping ionization ratio of ammonium in every sample. The concentration of nitrate, nitrite, and ammonium in the supernatant was quantified using an ion chromatograph system (Shimadzu, HIC-20A*super*). Shim-pack IC-A3 (Shimadzu) and Shim-pack IC-C4 (Shimadzu) were used as the column for analysis in anion chromatography and cation chromatography, respectively. The temperature was kept at 40 °C and 45 °C, with the flow rate of 1.2 mL/min and 1.0 mL/min, respectively. The mobile phase was composed of 1.11 gL^{-1} *p*-hydroxy benzoic acid, 0.67 gL^{-1} Bis-Tris, and 3.09 gL^{-1} boric acid in anion chromatograph system, and 0.23 gL^{-1} oxalic acid and 0.40 gL^{-1} 18-crown-6 in cation chromatograph system. The retention time of nitrate, nitrite, and ammonium were about 8.43 min, 5.93 min, and 5.90 min. The standard curve exhibited squares of the correlation coefficients as 0.999 in every ion in the target concentration range.

Estimation of dissociation constant (K_d) for complex formation between OM enzymes in *G. sulfurreducens* PCA and redox molecules

K_d can be estimated from the peak intensity at different concentration of redox molecules. When the peak intensity increased about α times with increase of the concentration of redox molecules from $[L]_1$ to $[L]_2$, K_d can be described as below, assuming the sum of [P] and [PL] is constant throughout the measurement as described in chapter 4-1:

$$\alpha - 1 = K_d \left(\frac{1}{[L]_1} - \frac{\alpha}{[L]_2} \right) \quad (\text{Eq } 4-3)$$

The author estimated the K_d from the plot of $\alpha - 1$ against $\frac{1}{[L]_1} - \frac{\alpha}{[L]_2}$, in the range of 4~24 μM RF and safranin.

4.2.3 Results and discussion

Comparison of cathodic current with anodic one in monolayer biofilm of *G. sulfurreducens* PCA

To form a monolayer biofilm of *G. sulfurreducens* PCA, we inoculated the cells on an indium tin-doped oxide (ITO) electrode poised at +0.40 V (vs SHE) to a cell suspension of *G. sulfurreducens* PCA at OD_{600} = 0.5 with 10 mM acetate as sole electron donor. During potential application, almost constant anodic current of approximately 20 μA was observed (Figure 4-12a). After 40 hours, confocal fluorescence microscopy showed 3D image in which *G. sulfurreducens* PCA stained by DAPI (4',6-diamidino-2-phenylindole) forms a homogeneous monolayer biofilm on ITO electrode (Figure 4-12b). In order to monitor the EEU process through OM *c*-Cyts expressed during anodic condition, we switched the applied potential to −0.45 V just after exchanging the supernatant with fresh anaerobic PSN medium containing 50 mM nitrate as sole electron acceptor for *G. sulfurreducens* PCA [31]. Consistent with a previous report using *Geobacer soli* [5], cathodic current (I_c) was largely suppressed to approximately −0.3 μA compared with anodic current (Figure 4-12a). Linear sweep (LS) voltammograms for a monolayer biofilm further demonstrate the suppression of electron uptake and asymmetric electron flow in *G. sulfurreducens* PCA (Figure 4-12c). While negative faradaic resistance was observed around −0.1 V in both scan direction as reported previously [32], potential scan to the positive direction showed onset potential around −0.3 V for clear acetate oxidation current and potential scan to opposite direction exhibited much smaller nitrate reduction current. These results demonstrate that the rate of electron uptake reaction or metabolism is slower for nitrate reduction compared with anodic condition.

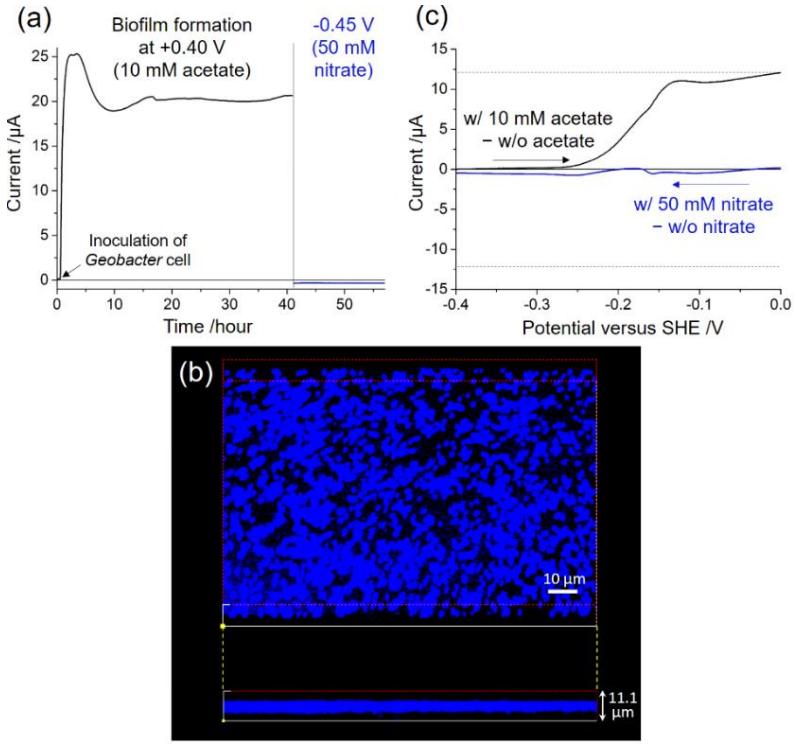

Figure 4-12. Characterization of *G. sulfurreducens* PCA biofilm formed on an indium tin-doped oxide (ITO) electrode. (a) Time course for current production from *G. sulfurreducens* PCA inoculated on an ITO electrode. After potential application at +0.40 V (versus SHE) for 40 hours in the presence of PSN medium containing 10 mM acetate (black line), the supernatant was exchanged with fresh anaerobic PSN medium containing 50 mM nitrate followed by potential switching to −0.45 V (blue line). (b) 3D image of *G. sulfurreducens* PCA biofilm on an ITO electrode used in this study. (c) Linear sweep (LS) voltammograms for *G. sulfurreducens* PCA biofilm on an ITO electrode at a scan rate of 1.0 mVs^{-1}. The black and blue lines represent the LS voltammograms in the presence of 10 mM acetate and 50 mM nitrate respectively, followed by subtraction of the LS voltammogram in the absence of any electron donor or acceptor. Black arrows indicate the direction of potential scanning.

Riboflavin increases the rate of electron uptake in *G. sulfurreducens* PCA

Assuming that RF dissociation from OM *c*-Cyts in cathodic condition decrease the rate of electron uptake, one can expect the high concentration of RF would promote

the RF-binding to OM *c*-Cyts, and increase the cathodic current production. Therefore, the author tested the effect of RF addition on I_c from *G. sulfurreducens* PCA formed on an ITO electrode applied at −0.45 V. As expected, the supplementation of 4.0 μM RF to a monolayer biofilm on an ITO electrode immediately increased the I_c (Figure 4-13). The I_c further shows enhancement with higher concentration of RF in cathodic condition exhibiting about 30 times increase (−9.0 μA) in the presence of 16 μM RF (Figure 4-13). In contrast to the observations, the current increase by RF addition is strictly inhibited in anodic condition [23], because the OM *c*-Cyts are occupied by RF in the physiological concentration range (about 50 nM) [33]. The author also quantified the concentration of nitrate in the supernatant by ion chromatography and confirmed that nitrate is reduced associated with cathodic current production. As shown in Figure 4-14, the amount of nitrate in the supernatant clearly decreased with the time of potential application at −0.45 V, and the consumption rate was higher in the presence of 20 μM RF than that of 10 μM RF. These results strongly suggest that the cathodic current suppression is not caused by the shortage of enzymes required for nitrate reduction but the low affinity of RF, resulting in dissociation from OM *c*-Cyts during EEU reaction.

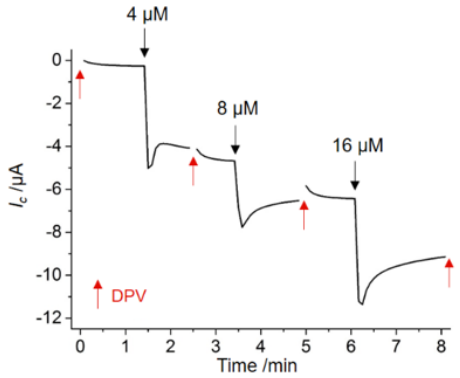

Figure 4-13. Time course for I_c from a biofilm of *G. sulfurreducens* PCA on an ITO electrode at −0.45 V (versus SHE). Black arrows indicate the timings for RF addition to each reactor. The concentrations of RF in the reactor are written by the arrows. Red arrows indicate the timings at which differential pulse (DP) voltammetry was conducted.

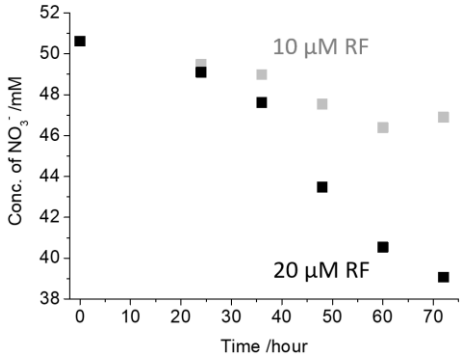

Figure 4-14. Quantification of products from a biofilm of *G. sulfurreducens* PCA during −0.45 V application by ion chromatography.

To confirm the rate-limiting process for I_c generation is assignable to the redox reaction of RF, we performed differential pulse (DP) voltammetry conducted at different RF concentration during I_c production (Figure 4-15). All the DP voltammograms depicted three cathodic peaks (Figure 4-15b). While the intensity of two signals with the peak potential (E_p) of −0.13 V and −0.05 V are inversely decreased by time, only one peak at −0.39 V ($I_{-0.39}$) increased with the concentration of RF and was not observable before addition of RF, indicating that the redox species at E_p of −0.39 V is assignable to RF (Figure 4-15). The observed E_p at −0.39 V is about 0.17 V more negative than the E_p for RF in cell-free electrolyte (Figure 4-15d), demonstrating that RF changes its redox property by the interaction with the biofilm of *G. sulfurreducens* PCA. Importantly, the $I_{-0.39}$ showed linear correlation with the I_c passing through the point of origin with the squares of the correlation coefficients of 0.98 (Figure 4-15a inset). Given $I_{-0.39}$ represents the amount of RF at the interface between *G. sulfurreducens* PCA and cathode, the nitrate reduction is likely predominantly driven by the electron supply via the redox cycling of RF at E_p of −0.39 V. Notably, since the redox potential shift of RF is almost identical with RF binding with OM *c*-Cyts in anodic condition and that in *S. oneidensis* MR-1 as

described in chapter 4-1, OM *c*-Cyts may work as the binging scaffold for RF as with the anodic condition.

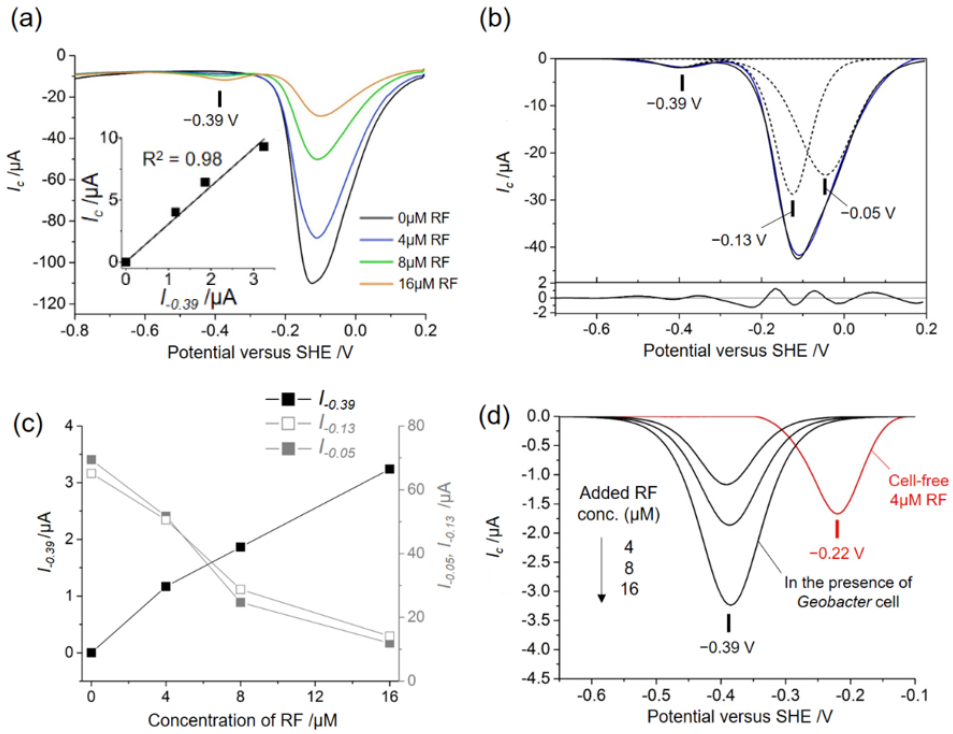

Figure 4-15. DP voltammetry conducted during cathodic current production from a biofilm of *Geobacter* in the presence of 50 mM nitrate on an ITO electrode. (a) DP voltammetry conducted at timings red arrows indicate in Figure 4-13. The inset represents plots of I_c against the peak current assignable to bound RF ($I_{-0.39}$). Both the horizontal and vertical axes are indicated as absolute value. The squares of the correlation coefficients include the point of origin. (b) An example for deconvolution of DP voltammogram. Blue and black line show the base-line subtracted DP voltammogram for *G. sulfurreducens* PCA in the presence of 8.0 μM RF (obtained from (a)) and fitted line composed of 3 peaks represented by dotted lines [E_p = −0.39 V, −0.13 V, and −0.05 V], respectively. Lower column represents the difference between blue and black line. (c) The peak current with E_p of −0.39 V ($I_{-0.39}$), −0.13 V ($I_{-0.13}$), and −0.05 V ($I_{-0.05}$) obtained from deconvolution of DPV in (a) against the duration time for the constant potential application at −0.45 V. (d) The base-line subtracted DP voltammograms for RF in the presence of *G. sulfurreducens* PCA after the deconvolutions demonstrated in (b). Red line represents the reduction peak for RF in cell-free electrolyte depicted as a comparison.

Bidirectional EET through RF-bound OM *c*-Cyts

To specifically examine the electron uptake pathway, we used the quadruple mutant for *omcB*, *omcE*, *omcS*, and *omcT* (*ΔomcBEST*), which are the major OM *c*-Cyts acting as binding scaffold for RF in anodic condition [23]. Although comparable I_c was observed for *ΔomcBEST* with wild-type (WT) before addition of RF, RF addition showed much less enhancement in I_c for *ΔomcBEST* (Figure 4-16a). Furthermore, the reduction peak of the RF in a biofilm of *ΔomcBEST* showed distinct E_p (−0.24 V) from that in WT and almost identical with that of cell-free RF (−0.22 V) (Figure 4-16b and 4-14d), demonstrating that the OmcB, OmcE, OmcS, or OmcT protein specifically interacts with RF at the cathode as with the anodic condition. Use of the same OM *c*-Cyts as the binding scaffold for RF in both anodic and cathodic EET implies that RF-bound OM *c*-Cyts bidirectionally transfer electrons. Thus, the asymmetric electron flow of *G. sulfurreducens* PCA is suggested to be solely dictated by the biased affinity of RF with OM *c*-Cyts in electron uptake and export (Figure 4-11).

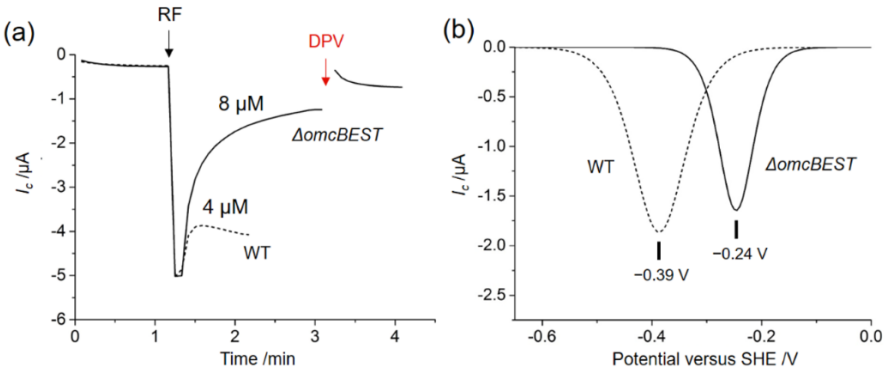

Figure 4-16. (a) Time course for I_c from a biofilm of *ΔomcBEST* (solid line) on an ITO electrode at −0.45 V (versus SHE). The I_c from wild-type (WT, broken line) is the same I_c profile indicated in Figure 4-14 as comparison. Black and red arrow indicates the timings of RF addition and DPV measurement, respectively. (b) Base-line subtracted DP voltammograms of RF in the presence of *ΔomcBEST* (solid line) and WT (dotted line). The concentration of RF in the reactor is 8.0 μM.

Since the amount of bound RF correlates with the reduction peak current at E_p of −0.39 V, the binding affinity of RF can be estimated as previously described as chapter 4-1 [33]. While the dissociation constant (K_d) for the formation of bound RF to OM c-Cyts in anodic condition is about 3 nM [33], the K_d under the cathodic condition was estimated to be 14.5 ± 1.0 μM (Table 4-2 and Figure 4-17). Namely, the binding affinity of RF largely decreased under cathodic condition. Because the I_c linearly increases with the complex formation of RF-bound OM *c*-Cyts (Figure4-15a inset), the author examined if the K_d difference could sufficiently explain the large difference in anodic and cathodic current. When it is assumed that the K_d under the cathodic condition is the same with that under anodic condition, 3 nM (Table 4-3), and the I_c linearly increases with the amount of bound RF, the I_c reaches approximately −16 μA, which is comparable current value with anodic condition (Figure 4-12a), demonstrating that the low stability of bound RF under cathodic condition is sufficient to account for the observed suppression of EEU and asymmetric electron flow in *G. sulfurreducens* PCA.

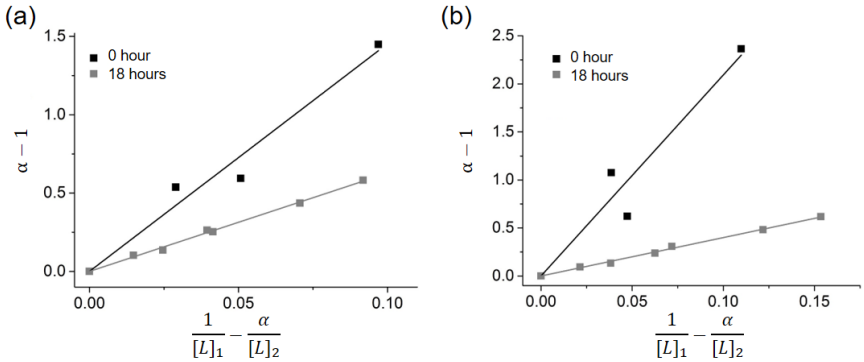

Figure 4-17. Estimation of dissociation constant (K_d) for complex formation between membrane proteins and RF (a) or safranin (b) just after switching from anodic cultivation (black plots and line) and after continuous potential application at −0.45 V for 18 hours (gray plots and line). K_d was estimated via linear regressions, setting $\frac{1}{[L]_1} - \frac{\alpha}{[L]_2}$ and $\alpha -$

1 as horizontal and vertical axis, respectively as described in eq. 2 in Supplementary Methods. The linear regressions are as follows; RF at t = 0 hour: b = 14.5a, R^2 = 0.967; RF at t = 18 hours: b = 6.3a, R^2 = 0.997; safranin at t = 0 hour: b = 20.9a, R^2 = 0.924; safranin at t = 18 hours: b= 4.0a, R^2 = 0.996. The squares of the correlation coefficients were estimated by adding the point of origin.

Table 4-2. Dissociation constants (K_d) for complex formation between OM enzymes of *G. sulfurreducens* PCA and riboflavin (RF) and safranin under cathodic condition

Cofactor	**Time for potential application at −0.45 V (versus SHE)**	**Dissociation constant (K_d)**
RF	0 hour	14.5 ± 1.0 μM
RF	18 hours	6.3 ± 0.1 μM
Safranin	0 hour	20.9 ± 2.1 μM
Safranin	18 hours	4.0 ± 0.1 μM

*Quoted from ref.[33].

Table 4-3. Dissociation constants (K_d) for complex formation between OM enzymes of *G. sulfurreducens* PCA or *S. oneidensis* MR-1 and riboflavin (RF)

	***Geobacter sulfurreducens* PCA**	***Shewanella oneidensis* MR-1**
Anode	3 nM[a]	ca. 10 μM[b]
Cathode	Listed in Table 4-2	15.8 μM[c]

a: Quoted from ref. [33], b: [16], and c: chapter 4-1.

While *S. oneidensis* MR-1 also proceeds bidirectional EET through OM *c*-Cyts, where the binding affinity of flavin is dictated by reductive cleavage of disulfide bond [34], however, amino acid sequences show no disulfide bond in the OmcBEST in *G. sulfurreducens* PCA, demonstrating that OmcBEST have other binding mechanism. Although it is still unclear how the binding of RF is dictated in molecular-level, it is reasonable that OmcBEST utilize different recognition mechanism. Actually, RF coordination corresponding with cleavage of disulfide bond in MtrC is proposed to be a

mechanism to respond to changes in oxygen levels of oxic/anoxic environment [34]. Since *Geobacter* species are strict anaerobe, dictation of RF binding should be linked with not oxygen, but other redox species, ex. OmcBEST. Therefore, the binding affinity of RF may be regulated by other system, such as conformational change of OmcBEST triggered by redox state of hemes. It is of great interest to investigate the molecular recognition mechanisms for RF binding by further biochemical experiments, e.g., amino acid substitution.

Why *G. sulfurreducens* PCA selected dissociation of flavins as a mechanism for diode-like electron transport through OM *c*-Cyts?

Then why OM *c*-Cyts utilizes the binding affinity of RF for diode-like asymmetric EET? Instead of RF affinity, downhill energy landscape of heme cofactors along EET pathway seems to facilitate only electron export, resulting in asymmetric electron flow. For example, a recent report proposed that a terminal cytochrome *c* in an OM *c*-Cyts complex in *S. oneidensis*, MtrF, has hemes with downhill energy landscape from cell interior to exterior [35]. Also, electrochemical analysis showed that a homologue of MtrF, MtrC has higher redox potential than MtrA protein located to the side of cell interior, demonstrating that the EET pathway through MtrCAB complex is downhill [36]. Although these downhill energetics through OM *c*-Cyts seem to proceed diode-like EET, however, in reality, electrons are reversibly transported through OM *c*-Cyts at almost identical rate between export and uptake, probably due to the acceleration of electron transport under non-equilibrium condition as demonstrated in chapter 2 and 3. Notably, electrons can be transported even in uphill reaction in biological system under non-equilibrium condition [37], thus, downhill energetics inside OM *c*-Cyts would not sufficiently suppress electron

uptake process. In that sense, physical detachment of RF from OM *c*-Cyts is a rational strategy to suppress electron uptake and achieve asymmetric EET. Therefore, this dissociation-based diode-like response possibly control the kinetics of biological electron transfer reactions in various microbial strains. Indeed, the gene cluster for porin-cytochrome protein complex (pcc) including *omcB*, which is a part of OM *c*-Cyts suggested to bind with RF in this study, is identified in all sequenced *Geobacter* species [38]. Also, the pcc gene cluster is distributed in a variety of phyla such as sulfur-reducing bacteria and anammox bacteria with significant implications for elemental cycles in the ocean [38-39].

EEU suppression in *G. sulfurreducens* PCA is constitutive

Further analyses revealed the suppression of electron uptake is constitutive feature in *G. sulfurreducens* PCA. While the present study has focused on the OmcBEST for insight into the electron uptake process in anodic biofilm, it has been the consensus that electrons are imported by different membrane proteins from the OM *c*-Cyts which export electrons in *G. sulfurreducens* PCA. This model has mainly been supported by the gene expression profile and minimal effect of deletion of OM *c*-Cyts on cathodic current after a few days of cathodic condition [6]. Since the I_c measurements and DP voltammetry in this study were conducted just after switching from anodic condition (Short time cathodic condition, SC condition), the apparent difference in cathodic electron carrier possibly originates from the duration time of cathodic potential application. Electrochemical analysis after constant potential application at −0.45 V for 18 hours (Long time cathodic condition, LC condition) clarified this point. Distinct from SC condition, the I_c from *ΔomcBEST* was largely enhanced by RF addition, which is

comparable with WT in LC condition (Figure 4-18a). Also, the reduction peak of bound RF shifted to E_p of −0.34 V in both WT and *ΔomcBEST* (Figure 4-18b), demonstrating that other outer-surface components than OmcBEST alternatively binds with RF. Notably, instead of the $I_{-0.39}$, the $I_{-0.34}$ proportionally increased with the I_c passing through the original point in LC condition (Figure 4-18c), demonstrating that electrons are injected via the RF-bound alternative OM enzymes, not OmcBEST. The K_d for the RF binding in LC condition was distinct from that of OmcBEST but still over 1000 times larger than that in anodic condition, estimated to be 6.3 ± 0.1 μM (Table 4-2 and Figure 4-17), which further confirms that RF interact with the alternative membrane proteins and demonstrates that the high capability of *G. sulfurreducens* PCA for electron uptake is hindered by the significantly lower affinity of RF even after alteration in membrane proteins under cathodic condition. The DP voltammograms conducted every 3 hours during potential application at −0.45 V recorded the appearance of reduction peak at −0.34 V and disappearance of that at −0.39 V taking about 6 hours (Figure 4-18d), which is short enough to alter the outer-surface components and gene expressions in previous studies [6].

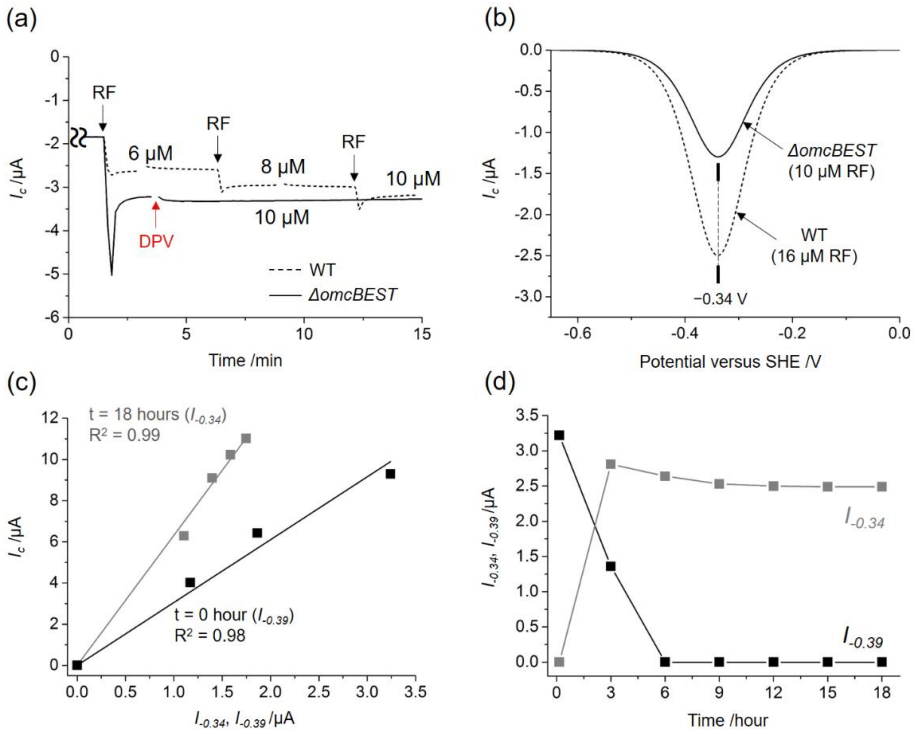

Figure 4-18. Change in extracellular electron uptake pathway after continuous cathodic potential application. Time course for I_c from a biofilm of *ΔomcBEST* (solid line) on an ITO electrode at −0.45 V (versus SHE) after 18 hours cathodic cultivation (LC condition). Black arrows indicate the timings for RF addition to each reactor. The concentration of RF in the reactors are indicated. The I_c from WT (broken line) is normalized to the data point just prior to the addition of RF in the solid line data for comparison. The reactors contain 4.0 μM RF prior to the measurement. (b) Base-line subtracted DP voltammograms of RF in the presence of *ΔomcBEST* and WT in LC condtion. (c) Plots of I_c against the peak current assignable to bound RF. Black plots represent the I_c in SC condition against the $I_{-0.39}$ and gray plots represent the I_c in LC condition against the $I_{-0.34}$. Both the horizontal and vertical axes are indicated as absolute value. The squares of the correlation coefficients include the point of origin. (d) The peak current assignable to RF in DP voltammograms against the time for the continuous potential application at −0.45 V (versus SHE). The vertical axis is indicated as absolute value.

Control of EEU kinetics by a flavin analogue

Biological system has utilized the redox characteristics of flavin molecule to dictate electron transport reactions with a variety of mechanisms, e.g. electron bifurcation, confurcation, and proton coupled electron transport, of which kinetics are solely regulated by the energetics of sequential redox reactions. On the other hand, the native diode-like characteristics of flavin-OM enzyme association observed in this study is controlled by the binding affinity. This novel insight into flavin-based biological electron transport reactions would enable to control the native biological diode; alteration in affinity of RF cofactor by molecular design would control the rate of bidirectional EET. In order to test the flexibility of binding affinity, a monolayer biofilm of *G. sulfurreducens* PCA was supplemented by a flavin analogue, safranin, which acts as alternative cofactor of OM *c*-Cyts in *S. oneidensis* MR-1 as described in chapter 4-1. As expected, the addition of 4.0 μM safranin to electrochemical reactor containing a biofilm of *G. sulfurreducens* PCA resulted in immediate increase of I_c to the similar extent with RF (Figure 4-19), exhibiting the evidences for the binding with *G. sulfurreducens* PCA, namely, negative shift in E_p compared with that in cell-free electrolyte as the same with RF (E_p = −0.43 V in the presence of a biofilm, and −0.31 V in cell-free electrolyte) (Figure 4-20). These data indicate that safranin acts as a binding cofactor instead of RF accelerating the EEU. The K_d for bound safranin was estimated to be 20.9 ± 2.1 μM (Table 4-2 and Figure 4-20). This clear difference of affinity between RF and safranin demonstrates that molecular design of cofactor potentially alters the affinity with OM *c*-Cyts of *G. sulfurreducens* PCA and control the kinetics and bias of diode-like EET.

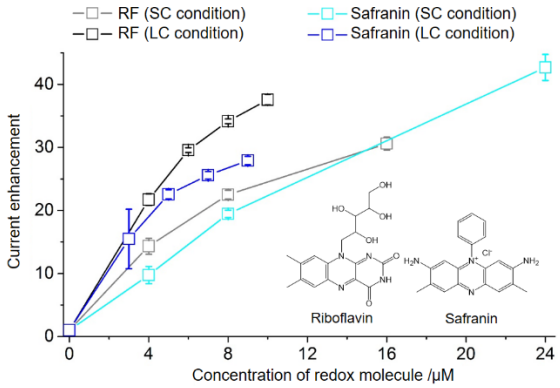

Figure 4-19. Cathodic current enhancement by addition of RF or safranin to a biofilm of *G. sulfurreducens* PCA in the presence of 50 mM nitrate on an ITO electrode. Enhancement in cathodic current production (I_c) by addition of RF or safranin compared to that without supplementation of redox molecules (−0.3 μA) were plotted against the concentration of RF or safranin. I_c was observed in SC condition (gray and light blue plots) and LC condition (black and blue plots). Error bars represent the fluctuations of I_c during each experiment. The chemical structures of RF and safranin are indicated.

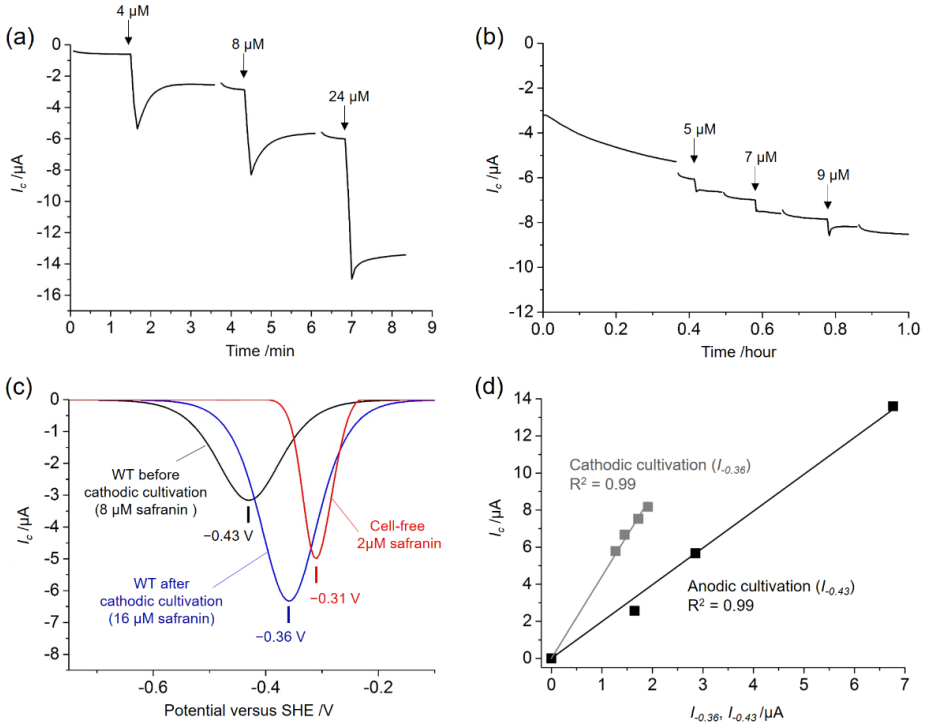

Figure 4-20. The effect of safranin on a biofilm of *G. sulfurreducens* PCA in the presence of 50 mM nitrate on an ITO electrode. Time course for I_c from a biofilm of *G. sulfurreducens* PCA on an ITO electrode at −0.45 V just after switching from anodic cultivation (a) and after continuous potential application at −0.45 V for 18 hours (b). Black arrows indicate the timings for safranin addition to each reactor. The concentrations of safranin in the reactor are written by the arrows. The reactor in (b) contains 3.0 μM safranin before the measurement. (c) The base-line subtracted DP voltammograms for safranin in the presence of a biofilm of *G. sulfurreducens* PCA just after switching from anodic potential application (black line), after continuous potential application at −0.45 V for 18 hours (blue line), and in a cell-free electrolyte (red line). (d) Plots of the I_c during potential application at −0.45 V against $I_{-0.36}$ after potential application at −0.45 V for 18 hours (black plots) and $I_{-0.43}$ just after switching from anodic condition (gray plots). Both the horizontal and vertical axes represent absolute value. The squares of the correlation coefficients include the point of origin.

4.2.4 Conclusion

In this work, the author demonstrated the low affinity of RF cofactor to OM enzymes causes the suppression of electron uptake in *G. sulfurreducens* PCA, highlighting the large potential for the use of the combination of *G. sulfurreducens* PCA and designed redox cofactors towards bioelectrosynthesis. The author also showed that high and low affinity of RF in anodic and cathodic condition, respectively, provides strong bias to the direction of electron flow in multilayer biofilms of *G. sulfurreducens* PCA. Considering that electrons can be transported even in uphill reaction in biological system under non-equilibrium condition [37], modulation of binding affinity of redox cofactor, RF, from OM *c*-Cyts would be a rational strategy to form efficient uni-directional electron flow like diode. This insight may contribute to the understanding and development of molecular diode as a component in future molecular electronics. Furthermore, the gene cluster for porin-cytochrome protein complex (pcc) including *omcB*, which is suggested to bind with RF in this study, is identified in all sequenced *Geobacter* species [38]. Furthermore, the pcc gene cluster is distributed in a variety of phyla such as sulfur-reducing bacteria and anammox bacteria with significant implications for elemental cycles in the ocean [38-39]. Therefore, the regulation of electron flow direction with use of cofactor molecules may be more widely distributed mechanism in a variety of EET-related microbial ecology than previously thought.

4.3

Shewanella as a platform of electrochemical enzyme assay *in vivo*

4.3.1 Introduction

Bacterial metabolisms and respirations are composed of sequential enzymatic redox reactions. The redox-chemistry-based enzymatic activity dictates the energy conversion efficiency in microbial life. Thus, quantification of redox enzymatic activity has a vital role in development of drugs and biotechnologies including biosensors[40], biofuel cells[41], biocatalysts[42], and biomolecular electronics[43] as well as elucidation of bacterial energy acquisition mechanisms[44]. Enzymatic activity has been examined in isolated and purified system *in vitro* over 100 years[45-46], however, living cell inside has potentially different condition from that *in vitro*, e.g. macromolecular crowding effect, pH, and ionic strength and so on[47-49]. Therefore, a new technique to obtain enzymatic activities and kinetics in living system *in vivo* is required.

Electrochemistry is one of the most direct and strong technique to examine the redox enzymatic kinetics, which monitors the electron flux associated with redox reactions. Due to its high sensitivity, the kinetics of a variety of redox enzymes immobilized on electrodes have been characterized *in vitro*[44]. An iron-reducing bacterium, *S. oneidensis* MR-1, is capable of forming OM *c*-Cyts as an electronic conduit between cell inside and electrode[36, 50], thus, the activity of redox enzyme in living system can potentially be monitored through the current production from *S. oneidensis* MR-1.

However, it is challenging to directly assess the enzymatic reaction kinetics from current production, due to the strictly limited electron flux through OM *c*-Cyts[16, 51], which neglects the faster enzymatic reactions than that in OM *c*-Cyts.

Here, the author accelerated the electron transport through OM *c*-Cyts by addition of RF acting as a binding redox cofactor as described in chapter 4-1, and thereby, established the novel electrochemical enzyme assay *in vivo* (Figure 4-22), which does not require any marking and gene modification to target protein and microbes.

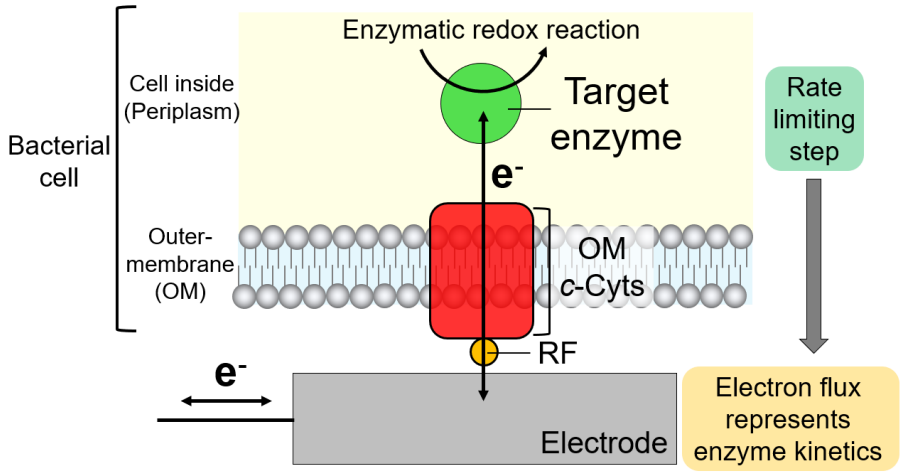

Figure 4-21. Concept of *in vivo* electrochemical enzyme assay.

4.3.2 Methods

Electrode-immobilized biofilm construction and electrochemical measurement

Electrochemical experiments were conducted under cathodic conditions after the formation of a monolayer biofilm *S. oneidensis* MR-1 in the same condition as that in chapter 4-1. After confirming the formation of a biofilm on an ITO electrode by in-situ confocal fluorescence microscopy, the supernatant in the electrochemical cell was replaced with anaerobic DM containing 10 μM RF. Cyclic voltammetry was conducted with a scan rate of 10 mVs^{-1}, which is slow enough to support nitrite diffusion [52].

4.3.3 Results and discussion

Electrochemical observation of cathodic electron flow through RF-bound OM *c*-Cyts

In order to prove the concept of electrochemical enzyme assay *in vivo*, the author first examined the activity of periplasmic NrfA protein, which is the sole nitrite reductase in *S.oneidensis* MR-1[53-54]. A monolayer biofilm of *S.oneidensis* MR-1 was formed on an ITO electrode using 3-electrode system, and subsequently the supernatant was anaerobically replaced with fresh defined medium containing nitrite. 10 μM RF was added to the electrochemical reactor, which potentially accelerates the electron transport through OM *c*-Cyts over 50 times as described in chapter 4-1 [2]. The cyclic voltammetry (CV) of a monolayer biofilm showed a clear cathodic current with an onset potential with −0.23 V (vs SHE) corresponding with RF binding with OM *c*-Cyts (Figure 4-22b). Although cathodic current was observed without addition of nitrite probably due to the reduction of metabolites inside the cell and hydrogen evolution reaction on an ITO electrode as reported previously, the limiting current increased depending on the concentration of nitrite, suggesting that nitrite is reduced by the up-taken electrons through RF-bound OM *c*-Cyts. It was confirmed that nitrite in the absence of biofilm showed no catalytic current, indicating that the increase of cathodic limiting current is not attributed to abiotic reactions on ITO electrode surface (Figure 4-23). Furthermore, removal of RF from biofilm dissipated the catalytic nitrite reduction current (Figure 4-23a and 24). Taken together, these data demonstrate that a monolayer biofilm of *S.oneidensis* MR-1 on an ITO electrode exhibits nitrite reduction current through RF-bound OM *c*-Cyts as illustrated in Figure 4-21.

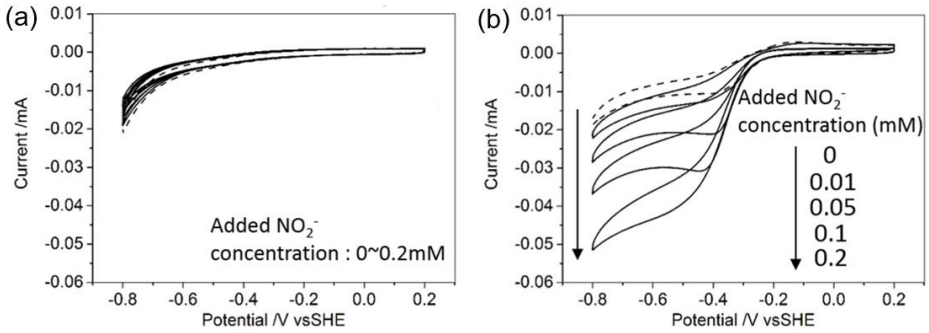

Figure 4-22. Catalytic current production from a monolayer biofilm of *S. oneidensis* MR-1 before (broken line) and after (solid line) the addition of 10, 50, 100, 200 μM NO_2^- in cyclic voltammetry (CV) in the absence (a) and presence (b) of 10 μM riboflavin (RF). The scan rate is $10mVs^{-1}$.

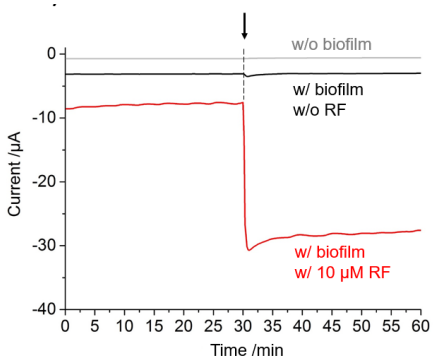

Figure 4-23. Time course change of cathodic current production from ITO electrodes at −0.45 V vs SHE in the absence of biofilm (gray), in the presence of biofilm (black), and in the presence of both biofilm and 10 μM RF. The black arrow indicates the timing of 100 μM NO_2^- addition.

Quantification of intracellular enzyme kinetics by electron flux

To directly test the link between cathodic current and NrfA activity inside *S.oneidensis* MR-1 cells, the author plotted the limiting current against the concentration of nitrite in the electrochemical reactor, assuming the cathodic current production at −0.8 V vs SHE to be the limiting current of nitrite reduction reaction inside the cell. The plots showed that the limiting current increased dependent on nitrite concentration up to 400 μM, however, the magnitude of limiting current started to decrease with more concentration

of nitrite (Figure 4-24). This profile is characteristic to enzymes with substrate inhibition, consistent with NrfA protein in *S.oneidensis* MR-1 suffering with inhibition at higher concentration of nitrite[52]. Therefore, the Michaelis-Menten parameters for nitrite reduction in *S.oneidensis* MR-1 cells were estimated based on a model in which a second substrate molecule binds to inhibit the enzyme (Equation 4-4).

$$v = \frac{V_{max}[S]}{K_M + [S](1 + [S]/K_i)} \qquad (\text{Eq } 4-4)$$

where K_M and K_i are the Michaelis constant and the inhibition constant, and V_{max} and [S] are maximum turnover rate and nitrite concentration, respectively. From this inhibition model, the K_M and K_i were estimated to be 55 μM and 20 mM, respectively (Table 4-4). These parameters are almost identical with that of NrfA immobilized on electrodes, 54 ± 12 μM for K_M and 18 ± 4 mM for K_i (Table 4-4). This quantitative correspondence of catalytic behavior as well as substrate inhibition with NrfA activity demonstrates that this analytical framework successfully provides the electrochemical enzymatic activity *in vivo*. Additionally, comparison of limiting current from biofilm with purified NrfA protein enables quantification of NrfA inside the cell. Assuming that the catalytic rate of NrfA is identical between *in vitro* and *in vivo* conditions, the amount of NrfA in the biofilm of *S.oneidensis* MR-1 was estimated to be 5.3×10^{-9} mol.

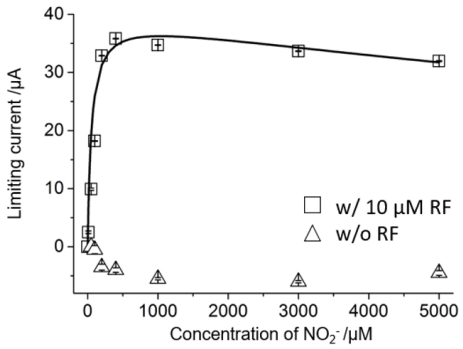

Figure 4-24. The dependence of cathodic limiting current from a monolayer biofilm of *S. oneidensis* MR-1 in CV on the concentration of NO_2^-. Those data are subtracted by the limiting current in the absence of NO_2^-. The square and triangle plots represent the data in the presence and absence of 10 μM RF, respectively. The error bars represent the mean±SEM obtained from three individual experiments. The line represents the enzymatic activity of purified NrfA reported in ref. [52] (K_M = 54 μM and K_i = 18 mM) assuming that the total amount of NrfA in the biofilm of *S. oneidensis* MR-1 is 5.3×10^{-9} mol.

Table 4-4. Comparison of Michaelis-Menten parameters estimated in our electrochemical enzyme assay *in vivo* with reported ones *in vitro*.

	In vivo	***In vitro***
K_M (NrfA) /μM	55	54 ± 12[a]
K_i (NrfA) /mM	20	18 ± 4[a]
K_M (FccA) /mM	1.0	0.021, 0.006[b]

a: Quoted from [52], b: Quoted from [55-56].

Advantages of enzyme assay *in vivo*

In addition to its easy and simple procedure without any electrode modification nor multi-step preparations, the electrochemical enzyme assay *in vivo* has an advantage compared to *in vitro* techniques; although *in vitro* approaches require precise medium condition to reproduce *in vivo*-like environment, the kinetics estimated in the assay automatically

reflects the physiological condition regardless of medium components. In Figure 4-25a, the dependence of limiting current of nitrite reduction of NrfA *in vivo* on the buffer concentrations was examined. While buffer concentration critically affects enzymatic activity *in vitro*, the removal of HEPES buffer in our system had scarce suppression on cathodic current. Considering that an antibiotic, polymyxin B, which forms pores in membrane, caused activity loss of NrfA by buffer removal (Figure 4-25b), the OM may protect NrfA from the buffer shock in electrochemical enzyme assay *in vivo*. Besides, other redox enzyme inside *S. oneidensis* MR-1, FccA, which catalyze fumarate reduction reaction, shows distinct enzymatic activity *in vitro*. While the K_M value of FccA in *Shewanella* species to be 0.021 mM[55] or 0.006 mM[56], our assay revealed that FccA has 1.0 mM of K_M *in vivo*, which is two orders of magnitude difference from *in vitro* (Table 4-4 and Figure 4-26). Given that FccA in *S. oneidensis* MR-1 reduce fumarate binding with heme protein, CymA[57-58], the difference would suggest that inter-proteins interaction affects the activity and reaction mechanisms of FccA. While additional studies are required to determine the specific mechanisms differentiating the reaction kinetics of FccA *in vivo* from *in vitro*, those data strongly suggest that the electrochemical enzyme assay *in vivo* reflects the physiological condition, which is potentially missed in purified system.

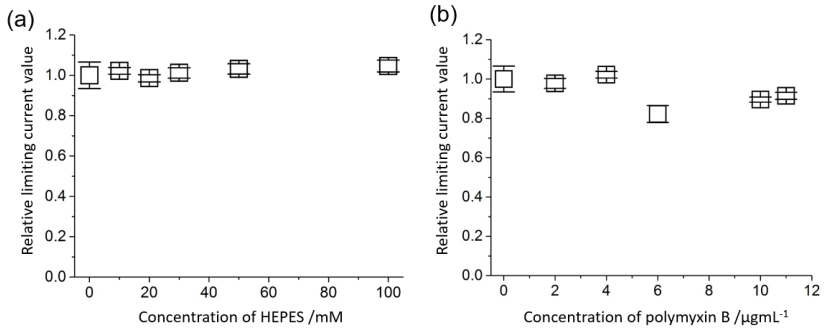

Figure 4-25. The dependence of limiting currents from a monolayer biofilm of *S. oneidensis* MR-1 on the concentration of HEPES buffer (a) and polymyxin B (b) contained in the medium. The medium contains 10 μM RF and 100 μM NO_2^-, and HEPES was removed in (b). The data were normalized by the limiting current in the presence of 30 mM HEPES in (a) and that in the absence of both HEPES and polymyxin B in (b), respectively. The error bars represent the mean±SEM obtained from three individual experiments.

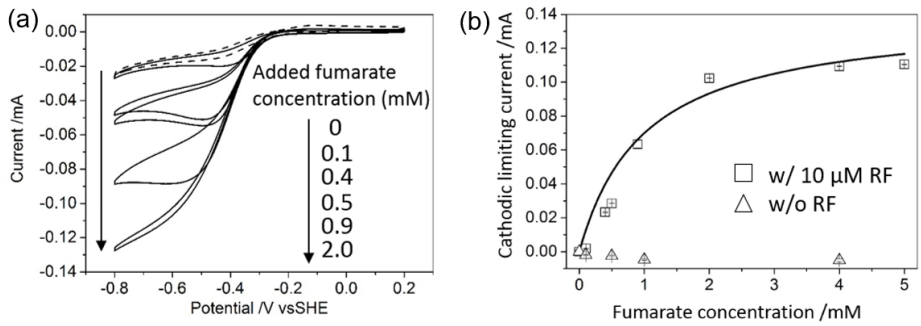

Figure 4-26. (a) Catalytic current production from a monolayer biofilm of *S. oneidensis* MR-1 in the presence of 10 μM RF before (broken line) and after (solid line) the addition of 0.1, 0.4, 0.5, 0.9, and 2.0 mM fumarate in (CV). The scan rate is $10mVs^{-1}$. The dependence of cathodic limiting current from a monolayer biofilm of *S. oneidensis* MR-1 in CV on the concentration of fumarate. Those data are subtracted by the limiting current in the absence of fumarate. The square and triangle plots represent the data in the presence and absence of 10 μM RF, respectively. The error bars represent the mean±SEM obtained from three individual experiments. The line represents the enzymatic activity with K_M of 1.0 mM.

4.3.4 Conclusion

In conclusion, the author established a novel platform of electrochemical enzyme assay *in vivo* applicable to a variety of redox enzymes in plants as well as bacteria. By virtue of *in vivo* assay, the analytical framework guarantees appropriate physiological condition for activity assay. It is anticipated that the present technique to be a basis for enzyme assay as protein film voltammetry has played a vital role in enzymatic mechanistic studies and drug designing.

References in chapter 4

1. Ross, D. E.; Flynn, J. M.; Baron, D. B.; Gralnick, J. A.; Bond, D. R., Towards Electrosynthesis in *Shewanella*: Energetics of Reversing the Mtr Pathway for Reductive Metabolism. *Plos One* **2011,** *6* (2).
2. Okamoto, A.; Hashimoto, K.; Nealson, K. H., Flavin Redox Bifurcation as a Mechanism for Controlling the Direction of Electron Flow during Extracellular Electron Transfer. *Angew. Chem. Int. Ed.* **2014,** *53* (41), 10988-10991.
3. Bond, D. R.; Lovley, D. R., Electricity production by *Geobacter sulfurreducens* attached to electrodes. *Appl. Environ. Microbiol.* **2003,** *69* (3), 1548-1555.
4. Gregory, K. B.; Bond, D. R.; Lovley, D. R., Graphite electrodes as electron donors for anaerobic respiration. *Environ. Microbiol.* **2004,** *6* (6), 596-604.
5. Yang, G.; Huang, L.; You, L.; Zhuang, L.; Zhou, S., Electrochemical and spectroscopic insights into the mechanisms of bidirectional microbe-electrode electron transfer in *Geobacter soli* biofilms. *Electrochem. Commun.* **2017,** *77*, 93-97.
6. Strycharz, S. M.; Glaven, R. H.; Coppi, M. V.; Gannon, S. M.; Perpetua, L. A.; Liu, A.; Nevin, K. P.; Lovley, D. R., Gene expression and deletion analysis of mechanisms for electron transfer from electrodes to *Geobacter sulfurreducens*. *Bioelectrochemistry* **2011,** *80* (2), 142-150.
7. Diez-Perez, I.; Hihath, J.; Lee, Y.; Yu, L. P.; Adamska, L.; Kozhushner, M. A.; Oleynik, I. I.; Tao, N. J., Rectification and stability of a single molecular diode with controlled orientation. *Nat. Chem.* **2009,** *1* (8), 635-641.
8. Aradhya, S. V.; Venkataraman, L., Single-molecule junctions beyond electronic transport. *Nat. Nanotechnol.* **2013,** *8* (6), 399-410.
9. Rabaey, K.; Rozendal, R. A., Microbial electrosynthesis - revisiting the electrical route for microbial production. *Nat. Rev. Microbiol.* **2010,** *8* (10), 706-716.
10. Thrash, J. C.; Coates, J. D., Review: Direct and indirect electrical stimulation of microbial metabolism. *Environ. Sci. Technol.* **2008,** *42* (11), 3921-3931.
11. Gregory, K. B.; Lovley, D. R., Remediation and recovery of uranium from contaminated subsurface environments with electrodes. *Environ. Sci. Technol.* **2005,** *39* (22), 8943-8947.
12. Nevin, K. P.; Woodard, T. L.; Franks, A. E.; Summers, Z. M.; Lovley, D. R., Microbial Electrosynthesis: Feeding Microbes Electricity To Convert Carbon Dioxide and Water to Multicarbon Extracellular Organic Compounds. *Mbio* **2010,** *1* (2).
13. Christodoulou, X.; Velasquez-Orta, S. B., Microbial Electrosynthesis and Anaerobic Fermentation: An Economic Evaluation for Acetic Acid Production from CO_2 and CO. *Environ. Sci. Technol.* **2016,** *50* (20), 11234-11242.

14. Choi, O.; Sang, B. I., Extracellular electron transfer from cathode to microbes: application for biofuel production. *Biotechnol. Biofuels.* **2016,** *9*.
15. Lovley, D. R., Bug juice: harvesting electricity with microorganisms. *Nat. Rev. Microbiol.* **2006,** *4* (7), 497-508.
16. Okamoto, A.; Hashimoto, K.; Nealson, K. H.; Nakamura, R., Rate enhancement of bacterial extracellular electron transport involves bound flavin semiquinones. *Proc. Natl. Acad. Sci. U.S.A.* **2013,** *110* (19), 7856-7861.
17. Jiang, J.; Kappler, A., Kinetics of microbial and chemical reduction of humic substances: Implications for electron shuttling. *Environ. Sci. Technol.* **2008,** *42* (10), 3563-3569.
18. Wu, Y. D.; Liu, T. X.; Li, X. M.; Li, F. B., Exogenous Electron Shuttle-Mediated Extracellular Electron Transfer of *Shewanella putrefaciens* 200: Electrochemical Parameters and Thermodynamics. *Environ. Sci. Technol.* **2014,** *48* (16), 9306-9314.
19. Clarke, T. A.; Edwards, M. J.; Gates, A. J.; Hall, A.; White, G. F.; Bradley, J.; Reardon, C. L.; Shi, L.; Beliaev, A. S.; Marshall, M. J.; Wang, Z.; Watmough, N. J.; Fredrickson, J. K.; Zachara, J. M.; Butt, J. N.; Richardson, D. J., Structure of a bacterial cell surface decaheme electron conduit. *Proc. Natl. Acad. Sci. U.S.A.* **2011,** *108* (23), 9384-9.
20. Edwards, M. J.; Hall, A.; Shi, L.; Fredrickson, J. K.; Zachara, J. M.; Butt, J. N.; Richardson, D. J.; Clarke, T. A., The Crystal Structure of the Extracellular 11-heme Cytochrome UndA Reveals a Conserved 10-heme Motif and Defined Binding Site for Soluble Iron Chelates. *Structure* **2012,** *20* (7), 1275-1284.
21. Edwards, M. J.; Baiden, N. A.; Johs, A.; Tomanicek, S. J.; Liang, L.; Shi, L.; Fredrickson, J. K.; Zachara, J. M.; Gates, A. J.; Butt, J. N.; Richardson, D. J.; Clarke, T. A., The X-ray crystal structure of Shewanella oneidensis OmcA reveals new insight at the microbe-mineral interface. *FEBS Lett* **2014,** *588* (10), 1886-90.
22. Fourmond, V.; Hoke, K.; Heering, H. A.; Baffert, C.; Leroux, F.; Bertrand, P.; Leger, C., SOAS: A free program to analyze electrochemical data and other one-dimensional signals. *Bioelectrochemistry* **2009,** *76* (1-2), 141-147.
23. Okamoto, A.; Saito, K.; Inoue, K.; Nealson, K. H.; Hashimoto, K.; Nakamura, R., Uptake of self-secreted flavins as bound cofactors for extracellular electron transfer in *Geobacter* species. *Energy Environ. Sci.* **2014,** *7* (4), 1357-1361.
24. Reguera, G.; McCarthy, K. D.; Mehta, T.; Nicoll, J. S.; Tuominen, M. T.; Lovley, D. R., Extracellular electron transfer via microbial nanowires. *Nature* **2005,** *435* (7045), 1098-1101.
25. Liu, Y.; Bond, D. R., Long-Distance Electron Transfer by *G. sulfurreducens*

Biofilms Results in Accumulation of Reduced *c*-Type Cytochromes. *Chemsuschem* **2012,** *5* (6), 1047-1053.

26. Malvankar, N. S.; Vargas, M.; Nevin, K. P.; Franks, A. E.; Leang, C.; Kim, B. C.; Inoue, K.; Mester, T.; Covalla, S. F.; Johnson, J. P.; Rotello, V. M.; Tuominen, M. T.; Lovley, D. R., Tunable metallic-like conductivity in microbial nanowire networks. *Nat. Nanotechnol.* **2011,** *6* (9), 573-579.

27. Borole, A. P.; Reguera, G.; Ringeisen, B.; Wang, Z. W.; Feng, Y. J.; Kim, B. H., Electroactive biofilms: Current status and future research needs. *Energy Environ. Sci.* **2011,** *4* (12), 4813-4834.

28. Snider, R. M.; Strycharz-Glaven, S. M.; Tsoi, S. D.; Erickson, J. S.; Tender, L. M., Long-range electron transport in *Geobacter sulfurreducens* biofilms is redox gradient-driven. *Proc. Natl. Acad. Sci. U.S.A.* **2012,** *109* (38), 15467-15472.

29. Steidl, R. J.; Lampa-Pastirk, S.; Reguera, G., Mechanistic stratification in electroactive biofilms of *Geobacter sulfurreducens* mediated by pilus nanowires. *Nat. Commun.* **2016,** *7*.

30. Malvankar, N. S.; Vargas, M.; Nevin, K.; Tremblay, P. L.; Evans-Lutterodt, K.; Nykypanchuk, D.; Martz, E.; Tuominen, M. T.; Lovley, D. R., Structural Basis for Metallic-Like Conductivity in Microbial Nanowires. *Mbio* **2015,** *6* (2).

31. Knoche, K. L.; Renner, J. N.; Gellett, W.; Ayers, K. E.; Minteer, S. D., A Self-Sufficient Nitrate Groundwater Remediation System: *Geobacter Sulfurreducens* Microbial Fuel Cell Fed by Hydrogen from a Water Electrolyzer. *J. Electrochem. Soc.* **2016,** *163* (7), F651-F656.

32. Matsuda, S.; Liu, H.; Kato, S.; Hashimoto, K.; Nakanishi, S., Negative Faradaic Resistance in Extracellular Electron Transfer by Anode-Respiring *Geobacter sulfurreducens* Cells. *Environ. Sci. Technol.* **2011,** *45* (23), 10163-10169.

33. Okamoto, A.; Nakamura, R.; Nealson, K. H.; Hashimoto, K., Bound Flavin Model Suggests Similar Electron-Transfer Mechanisms in *Shewanella* and *Geobacter*. *Chemelectrochem* **2014,** *1* (11), 1808-1812.

34. Edwards, M. J.; White, G. F.; Norman, M.; Tome-Fernandez, A.; Ainsworth, E.; Shi, L.; Fredrickson, J. K.; Zachara, J. M.; Butt, J. N.; Richardson, D. J.; Clarke, T. A., Redox Linked Flavin Sites in Extracellular Decaheme Proteins Involved in Microbe-Mineral Electron Transfer. *Sci. Rep.* **2015,** *5*, 11677.

35. Watanabe, H. C.; Yamashita, Y.; Ishikita, H., Electron transfer pathways in a multiheme cytochrome MtrF. *Proc. Natl. Acad. Sci. U.S.A.* **2017,** *114* (11), 2916-2921.

36. Hartshorne, R. S.; Reardon, C. L.; Ross, D.; Nuester, J.; Clarke, T. A.; Gates, A. J.; Mills, P. C.; Fredrickson, J. K.; Zachara, J. M.; Shi, L.; Beliaev, A. S.; Marshall, M. J.;

Tien, M.; Brantley, S.; Butt, J. N.; Richardson, D. J., Characterization of an electron conduit between bacteria and the extracellular environment. *Proc. Natl. Acad. Sci. U.S.A.* **2009,** *106* (52), 22169-22174.

37. Chen, I. P.; Mathis, P.; Koepke, J.; Michel, H., Uphill electron transfer in the tetraheme cytochrome subunit of the Rhodopseudomonas viridis photosynthetic reaction center: Evidence from site-directed mutagenesis. *Biochemistry* **2000,** *39* (13), 3592-3602.

38. Shi, L.; Fredrickson, J. K.; Zachara, J. M., Genomic analyses of bacterial porin-cytochrome gene clusters. *Front. Microbiol.* **2014,** *5*.

39. Kuypers, M. M. M.; Sliekers, A. O.; Lavik, G.; Schmid, M.; Jorgensen, B. B.; Kuenen, J. G.; Damste, J. S. S.; Strous, M.; Jetten, M. S. M., Anaerobic ammonium oxidation by anammox bacteria in the Black Sea. *Nature* **2003,** *422* (6932), 608-611.

40. Zhu, C. Z.; Yang, G. H.; Li, H.; Du, D.; Lin, Y. H., Electrochemical Sensors and Biosensors Based on Nanomaterials and Nanostructures. *Anal. Chem.* **2015,** *87* (1), 230-249.

41. Barton, S. C.; Gallaway, J.; Atanassov, P., Enzymatic biofuel cells for Implantable and microscale devices. *Chem. Rev.* **2004,** *104* (10), 4867-4886.

42. Cracknell, J. A.; Vincent, K. A.; Armstrong, F. A., Enzymes as working or inspirational electrocatalysts for fuel cells and electrolysis. *Chem. Rev.* **2008,** *108* (7), 2439-2461.

43. Bostick, C. D.; Mukhopadhyay, S.; Pecht, I.; Sheves, M.; Cahen, D.; Lederman, D., Protein bioelectronics: a review of what we do and do not know. *Rep. Prog. Phys.* **2018,** *81* (2).

44. Leger, C.; Bertrand, P., Direct electrochemistry of redox enzymes as a tool for mechanistic studies. *Chem. Rev.* **2008,** *108* (7), 2379-2438.

45. Michaelis, L.; Menten, M. L., The kenetics of the invertin action. *Biochem Z* **1913,** *49*, 333-369.

46. Johnson, K. A., A century of enzyme kinetic analysis, 1913 to 2013. *FEBS Lett.* **2013,** *587* (17), 2753-2766.

47. van Eunen, K.; Bakker, B. M., The importance and challenges of *in vivo*-like enzyme kinetics. *Perspectives in Science* **2014,** *1* (1-6), 126-130.

48. Ellis, R. J., Macromolecular crowding: obvious but underappreciated. *Trends. Biochem. Sci.* **2001,** *26* (10), 597-604.

49. García-Contreras, R.; Vos, P.; Westerhoff, H. V.; Boogerd, F. C., Why *in vivo* may not equal *in vitro*–new effectors revealed by measurement of enzymatic activities under the same *in vivo*-like assay conditions. *FEBS J.* **2012,** *279* (22), 4145-4159.

50. Edwards, M. J.; White, G. F.; Lockwood, C. W.; Lawes, M. C.; Martel, A.; Harris,

G.; Scott, D. J.; Richardson, D. J.; Butt, J. N.; Clarke, T. A., Structural modeling of an outer membrane electron conduit from a metal-reducing bacterium suggests electron transfer via periplasmic redox partners. *J. Biol. Chem.* **2018,** *293* (21), 8103-8112.

51. Liu, H. A.; Newton, G. J.; Nakamura, R.; Hashimoto, K.; Nakanishi, S., Electrochemical Characterization of a Single Electricity-Producing Bacterial Cell of *Shewanella* by Using Optical Tweezers. *Angew. Chem. Int. Ed.* **2010,** *49* (37), 6596-6599.

52. Judd, E. T.; Youngblut, M.; Pacheco, A. A.; Elliott, S. J., Direct Electrochemistry of Shewanella oneidensis Cytochrome *c* Nitrite Reductase: Evidence of Interactions across the Dimeric Interface. *Biochemistry* **2012,** *51* (51), 10175-10185.

53. Heidelberg, J. F.; Paulsen, I. T.; Nelson, K. E.; Gaidos, E. J.; Nelson, W. C.; Read, T. D.; Eisen, J. A.; Seshadri, R.; Ward, N.; Methe, B.; Clayton, R. A.; Meyer, T.; Tsapin, A.; Scott, J.; Beanan, M.; Brinkac, L.; Daugherty, S.; DeBoy, R. T.; Dodson, R. J.; Durkin, A. S.; Haft, D. H.; Kolonay, J. F.; Madupu, R.; Peterson, J. D.; Umayam, L. A.; White, O.; Wolf, A. M.; Vamathevan, J.; Weidman, J.; Impraim, M.; Lee, K.; Berry, K.; Lee, C.; Mueller, J.; Khouri, H.; Gill, J.; Utterback, T. R.; McDonald, L. A.; Feldblyum, T. V.; Smith, H. O.; Venter, J. C.; Nealson, K. H.; Fraser, C. M., Genome sequence of the dissimilatory metal ion-reducing bacterium *Shewanella* oneidensis. *Nat. Biotechnol.* **2002,** *20* (11), 1118-1123.

54. Cruz-Garcia, C.; Murray, A. E.; Klappenbach, J. A.; Stewart, V.; Tiedje, J. M., Respiratory nitrate ammonification by *Shewanella oneidensis* MR-1. *J. Bacteriol.* **2007,** *189* (2), 656-662.

55. Morris, C. J.; Black, A. C.; Pealing, S. L.; Manson, F. D. C.; Chapman, S. K.; Reid, G. A.; Gibson, D. M.; Ward, F. B., Purification and Properties of a Novel Cytochrome - Flavocytochrome-*C* from *Shewanella-putrefaciens*. *Biochem. J.* **1994,** *302*, 587-593.

56. Pealing, S. L.; Cheesman, M. R.; Reid, G. A.; Thomson, A. J.; Ward, F. B.; Chapman, S. K., Spectroscopic and Kinetic-Studies of the Tetraheme Flavocytochrome-*C* from *Shewanella-putrefaciens* Ncimb400. *Biochemistry* **1995,** *34* (18), 6153-6158.

57. Marritt, S. J.; McMillan, D. G. G.; Shi, L.; Fredrickson, J. K.; Zachara, J. M.; Richardson, D. J.; Jeuken, L. J. C.; Butt, J. N., The roles of CymA in support of the respiratory flexibility of *Shewanella oneidensis* MR-1. *Biochem. Soc. Trans.* **2012,** *40*, 1217-1221.

58. McMillan, D. G. G.; Marritt, S. J.; Firer-Sherwood, M. A.; Shi, L.; Richardson, D. J.; Evans, S. D.; Elliott, S. J.; Butt, J. N.; Jeuken, L. J. C., Protein-Protein Interaction Regulates the Direction of Catalysis and Electron Transfer in a Redox Enzyme Complex. *J. Am. Chem. Soc.* **2013,** *135* (28), 10550-10556.

Chapter
5

Summary and perspective

Summary

In this thesis, the mechanisms in flavin-mediated EET enhancement has been examined using microbio-electrochemistry. Because the rate enhancement of EET conflicts with the energetics of electron, in chapter 2, the author focused on a possible role of counter cation, proton. Since whole-cell approaches limit accesses to molecular-level information regarding specific enzymes, a variety of techniques were combined with microbio-electrochemistry, e.g. replacement of flavin to molecularly designed analogues to bind with OM *c*-Cyts, solvent kinetic isotope effect (KIE) on EET using deuterated water, and impact of pH on EET kinetics. As a result, it was revealed that proton transport reaction is coupled with EET through OM *c*-Cyts, and flavin likely enhances the rate of EET by acceleration of coupled proton transport. This novel proton-coupling property will possibly make the OM *c*-Cyts complex a model system for studying biological proton-coupled electron transfer reactions *in vivo*, and expand the available strategies to control the kinetics of EET. Especially, molecular-level insight has also been obtained, i.e. protonation reaction of the nitrogen atom at position 5 (N(5)) of flavin is critical for EET acceleration. Because electron free energy has been a focal point in EET mechanisms, directly linking EET kinetics to basicity of N(5) would provide novel strategies for control of EET-associated biological reactions by adjustment of the pK_a value as well as the redox potential of flavin analogues.

Furthermore, the finding of proton coupling property provides novel insight into ecophysiology of EET-capable bacteria. In chapter 2, further microbio-electrochemical analysis showed that proton gradient is not formed during EET-respiration, suggesting that proton export to cell exterior via OM limits the rate of EET. While this possibility should be further explored in biochemical approaches like proteoliposomal system, if true, the EET process may represent a novel form of respiratory metabolism, in which rapid electron outflow associated with proton export across the OM sustains the regeneration of NAD^+ to promote substrate-level phosphorylation. Considering respiration process drives chemiosmotic ATP formation and fermentation expels protons in the form of hydrogen or reduced organics for ATP formation, EET-coupled metabolism could be categorized in neither anaerobic respiration nor fermentation processes.

In chapter 3, the EET mechanisms were investigated from the viewpoint of geometry and redox state of hemes in OM *c*-Cyts. Although coupled proton transport reaction limits the rate of EET, potential proton pathways have not been identified in the crystal structures of OM *c*-Cyts. To test a possible structural change in intact cell, in chapter 3, the author examined the heme geometry of OM *c*-Cyts in intact cell at various conditions and discussed about possible EET mechanisms via rearranged hemes centers. In detail, the author developed a novel methodology to monitor the inter-heme interaction in a unit of OM *c*-Cyts, MtrC protein, in intact cell, termed whole-cell circular dichroism (CD) difference spectroscopy. Comparisons of MtrCs in purified and native systems showed that the heme geometry in reduced MtrC can be altered by interactions with cellular components and extacellular minerals, suggesting that *in vivo*-specific structural change would potentially form novel hydrogen-bond networks for proton pathways.

Notably, the results in chapter 3 showed that the changes in CD spectra are linked with EET kinetics, indicating that the rate-limiting proton pathway is involved in local environments of hemes in MtrC. Since flavin may enhance the EET rate by acceleration of coupled proton transport, it is reasonable that binding reaction of flavin causes reorganization of hydrogen-bond networks. However, the whole-cell CD spectra of *S. oneidensis* MR-1 in the presence of flavin without electron flow was almost identical with that in the absence of flavin. In contrast, bound flavin changed the CD specra specifically during electron flow, suggesting that the redox state of hemes in MtrC occur only under non-equilibrium condition. Considering that the redox state of hemes in MtrC alters organization of surrounding amino residues in the level of secondary structure as demonstrated in far-UV CD spectroscopy, it is likely that electron flow initiates reorganization of proton pathway in flavin-bound OM *c*-Cyts to accelerate EET. Given that the electron transport mechanisms in proteins have been discussed using crystal structures (in oxidized condition) based on the assumption that protein structures are scarcely affected by *in vivo* specific environments such as cellular components and electron flow, the whole-cell CD difference spectroscopy applicable to intact cells is an important first step in pioneering biological electron transfer providing insights into potential structural change in intact cell.

The author has found that bound flavin controls kinetics of EET associated with structural change of OM *c*-Cyts in chapter 2 and 3. Furthermore, in chapter 4, it was revealed that bound flavin dictates the direction of electron flow through OM *c*-Cyts, i.e. forward and reverse electron transport. While the electron export mediated by flavin is a universal reaction, the reverse electron flow occurs in not all kinds of EET-capable bacteria. For example, the OM *c*-Cyts in *S. oneidensis* MR-1 conduct bidirectional EET,

however, reverse electron flux through OM *c*-Cyts in another model EET-capable bacteria, *G. sulfurreducens* PCA, is limited to be about 10 times lower than that of electron export like a "diode". The mechanisms to dictate the direction of EET has been unclear, hindering development of biotechnologies utilizing cathodic EET. The microbio-electrochemical analysis revealed that the cathodic current suppression in *G. sulfurreducens* PCA is due to the dissociation of flavin from OM *c*-Cyts under cathodic condition. The bidirectional EET of *S. oneidensis* MR-1 is realized by the comparable binding affinity in the complex formation of flavocytochromes under cathodic condition with that under anodic condition, and significantly weaker binding affinity under cathodic condition made the diode-like EET property of *G. sulfurreducens* PCA. Thus, this may suggest that molecular design of flavin analogues with different dissociation constant may enable to control the electronic property of OM *c*-Cyts including the kinetics and the direction of EET switching conductive and diode-like response. While significant improvement of binding affinity has not been achieved in this thesis, flavin analogues containing N(5) were confirmed to be bound with OM *c*-Cyts in both *S. oneidensis* MR-1 and *G. sulfurreducens* PCA with distinct binding affinity from flavins under cathodic condition. Thus, molecular design of flavin analogues have potential to control and enhance the rate of cathodic EET.

Taken together, this thesis revealed the mechanisms underlying flavin-mediated EET enhancement in intact cells. Those data provide fundamental insight into biological electron transport reaction *in vivo*, with major implications for understanding and controlling the EET-based bacterial respiration.

Perspective

Development of power-generating biochemical production system

The activation of substrate-level phosphorylation and regeneration of NAD^+ associated with EET-linked respiration indicated in chapter 2 have an impact not only on the EET kinetics but also development of bio-technologies. While microbial fuel cells (MFCs), which decompose and clean waste water generating electrical energy, has been developed as an emerging environmental biotechnology, other techniques have not yet been used as practical stage. Although microbial electrosynthesis (MES) has been developed as a technology to produce bio-fuels and bio-chemicals, MES is operated under reverse EET, i.e. electrical energy input is required to drive chemical synthesis inside EET-capable bacteria [1-2]. One of the reasons for the scarce applications other than MFC utilizing bacteria on anode is the limited number of biomolecules catalyzed by respiration-based EET. Catabolites after anodic EET-coupled respiration is usually limited to carbon dioxide, succinate, and acetate [3]. However, the results herein demonstrated that the EET-associated metabolism of *S. oneidensis* MR-1 proceeds based on the energetics of fermentation. Considering that fermentation can catalyze a variety of bioreactions, gene-engineered *S. oneidensis* MR-1 strains or other bacteria to conduct EET through OM *c*-Cyts may potentially conduct both current generation and biochemical production. Given that the functionalization of *Escherichia coli* as EET-capable bacteria has been realized [4-5], the development of "power-generating biochemical production" could possibly be realized. Since this is a heterogeneous system, the cost for separation between produced biochemicals and bacterial cells can be saved compared with general homogeneous biotechnologies. In addition, since regeneration of NAD^+ is connected with EET rate,

acceleration of EET by flavins or N(5) molecules may help to improve the efficiency of this system. These are great advantages of this “power-generating biochemical production” system. The author hope that this study helps development of such novel biotechnologies.

Control of EET-linked bacterial respiration by flavin analogues with N(5)

One of the achievements in this thesis is to find a strategy to control and enhance the rate of both anodic and cathodic EET by molecular design of flavin analogues. Basicity of N(5) in flavin backbone and binding affinity with OM *c*-Cyts were the keys for the EET rate enhancement. Notably, the flavin analogues works as cofactor not only in *S. oneidensis* MR-1 but also another model bacterium, *G. sulfurreducens* PCA. Thus, this would be a promising strategy for enhancment of power generation in biotechnologies utilizing EET-capable bacteria such as MFC, MES and “power-generating biochemical production” system.

The respiratory control of EET-capable pathogens and gut bacteria might be also possible in future. In addition, the proposed proton export model in chapter 2 could be linked with oral diseases such as gingivitis and periodontitis promoting the dissolution of teeth caused by oral biofilm. One of the central mechanisms of teeth dissolution is acidification of teeth surface caused by biofilm. Given that some of the bacteria in the oral biofilm have an ability to conduct EET as reported by G. Wanger *et al* [6], the acidification of teeth surface caused by biofilm would potentially be related with proton export associated with EET, which is under investigation using a model oral bacterium, *Streptococcus mutans* (*Unpubilshed*). The control of EET rate by molecular design of flavin analogues may have a potential to contribute on the therapeutics of oral disease.

Understanding of EET mechanisms in molecular-level

This thesis developed several techniques to reveal EET mechanisms in intact cell, e.g. the methodology to test KIE on EET using intact cells, to replace flavin cofactor to its analogues binding with OM *c*-Cyts, and to obtain CD spectra of MtrC from whole-cell. Given that all of these techniques can potentially be used with other EET-capable bacteria and mutant strains of *S. oneidensis* MR-1 lacking or replacing some amino acids in OM *c*-Cyts, the proton-coupled EET mechanisms would be further investigated. Especially, since detailed mechanisms on the level of amino acids interaction have not been obtained in this thesis, it would be of great interest to combine those method with biochemical approaches such as point mutation towards understanding of biological electron transport *in vivo*.

Nonlinear optical techniques to study bacterial electron transport mechanisms and to screen electroactive bacteria

This study revealed that OM *c*-Cyts have extraordinarily large Soret CD intensity, which stems from strong electronic transition dipole reflecting the geometry of hemes. The combination of CD and electrochemistry provided insight into OM *c*-Cyts during EET. However, CD is not specific for electrode surface, thus, the electrochemical CD spectra includes the information of OM *c*-Cyts passing electrons among cells. In order to truly reveal the act of OM *c*-Cyts at cell/electrode interface, technical improvement would be required. Given that nonlinear optical techniques, second harmonic generation (SHG) or sum frequency generation (SFG), can probe the electronic transition dipole of molecules with surface-specificity due to the intrinsic symmetry constraints on the nonlinear process [7-8], those optical techniques are promising candidates to analyze heme geometry in OM

c-Cyts during EET. The combination of those optical techniques with electrochemistry may expand the methodology to reveal EET process occurring at cell/electrode interface. Especially, recent studies have used SHG and SFG to detect low concentrations of biomolecules such as proteins and peptides on artificial membranes [9-10], supporting the feasibility of those optical techniques.

Cultivatable bacteria in isolated form is limited within 1% in total bacteria on the earth [11]. While recent studies are revealing the large distribution of EET-capable bacteria in a variety of environment, whole-picture of EET-capable bacteria on bacterial community and the impact of EET on ecophysiology is still under debate. Although lots of methods have been develop to isolate bacteria and assess their EET-capability e.g. isolation of bacteria on minerals or electrodes [12-13], most of those techniques require growth process, which problematically limits the possibility to detect hardly cultivatable bacteria. Since nonlinear optical techniques have a potential to elucidate electron transport membrane proteins like OM *c*-Cyts, they would be promising technologies to screen EET-capable bacteria from bacterial consortia even without growth step as well as to reveal EET mechanisms. Furthermore, transient light of SHG can be used to detect bacterial cell surface molecules even without contact with electrode surface [14-15]. Thus, electroactive bacteria utilizing not electrode but other bacterial cells as electron donor/acceptor, i.e. direct inter-species electron transport (DIET) -capable bacteria, can also be investigated. Those bacteria utilize electron transport proteins not for mineral-based respiration but for respiration in bacterial syntrophy [16-18]. Considering that recent studies demonstrate the importance of DIET from the viewpoint of bacterial ecophysiology, environmental issues, and industrial applications [19-20], the use of SHG would have implications to a variety of research field related to EET- or DIET- capable

bacteria.

Controlling thickness of electroactive biofilm by redox molecules

In chapter 4, it was revealed that the binding affinity of flavin dictates the direction of electron flow through OM *c*-Cyts. This finding may have implications to physiology in electroactive biofilm formation, providing a strategy to control or remove electroactive biofilm. Given that electroactive biofilm has affected iron corrosion, oral diseases as well as EET-based biotechnologies, the control of biofilm is important subject in industrial applications.

In case of an EET-capable bacterium, *G. sulfurreducens* PCA, thick biofilms with conductive matrix to transport electron more than 10 μm long are formed, which enables cells to rapidly respire with solid electron acceptors even without direct contact to the electrode [21-22]. Rachel M. Snider *et al.* have shown that long-range electron conduction in *Geobacter* biofilm is driven by redox gradient where electrons are hopping among redox centers in the matrix of biofilm [22]. One of the unexpected observations for redox gradient model is that the redox species mediating biofilm conduction have highly negative redox potential peaked at around −0.33 V [versus the standard hydrogen electrode (SHE)]. Because intracellular energy level in iron-reducing bacteria connects with extracellular redox environment via biological electron conductor of OM *c*-Cyts, more negative potential than the redox potential of NAD^+/NADH causes electron backflow into *Geobacter* cells, which potentially reverses the respiratory acetate oxidation in the cytoplasm and inhibit current generation. However, in reality, thick biofilm of *Geobacter* can sustain the microbial respiration without respiratory inhibition [23-24]. In that sense, the flavin-based dictation of EET direction may have a role in

continuing electron export with suppression of electron backflow through OM *c*-Cyts. Indeed, *S. oneidensis* MR-1 forms relatively thin biofilm compared with *G. sulfurreducens* PCA, probably because *S. oneidensis* MR-1 is unable to suppress electron backflow by flavin dissociation. Thus, design of redox molecules to enhance electron back flow may remove thick electroactive biofilm. It is of great interest to test the effect of redox molecules on biofilm morphology using microscopic techniques.

References in chapter 5

1. Choi, O.; Sang, B. I., Extracellular electron transfer from cathode to microbes: application for biofuel production. *Biotechnol. Biofuels.* **2016,** *9*, 11.
2. Rabaey, K.; Rozendal, R. A., Microbial electrosynthesis - revisiting the electrical route for microbial production. *Nat. Rev. Microbiol.* **2010,** *8* (10), 706-716.
3. Newton, G. J.; Mori, S.; Nakamura, R.; Hashimoto, K.; Watanabe, K., Analyses of Current-Generating Mechanisms of *Shewanella loihica* PV-4 and *Shewanella oneidensis* MR-1 in Microbial Fuel Cells. *Appl. Environ. Microbiol.* **2009,** *75* (24), 7674-7681.
4. Jensen, H. M.; Albers, A. E.; Malley, K. R.; Londer, Y. Y.; Cohen, B. E.; Helms, B. A.; Weigele, P.; Groves, J. T.; Ajo-Franklin, C. M., Engineering of a synthetic electron conduit in living cells. *Proc. Natl. Acad. Sci. U.S.A.* **2010,** *107* (45), 19213-19218.
5. Jensen, H. M.; TerAvest, M. A.; Kokish, M. G.; Ajo-Franklin, C. M., CymA and Exogenous Flavins Improve Extracellular Electron Transfer and Couple It to Cell Growth in Mtr-Expressing *Escherichia coli*. *ACS Synth. Biol.* **2016,** *5* (7), 679-688.
6. Wanger, G.; Gorby, Y.; El-Naggar, M. Y.; Yuzvinsky, T. D.; Schaudinn, C.; Gorur, A.; Sedghizadeh, P. P., Electrically conductive bacterial nanowires in bisphosphonate-related osteonecrosis of the jaw biofilms. *Oral Surg. Oral Med. Oral Pathol. Oral Radiol* **2013,** *115* (1), 71-8.
7. Stoller, P.; Celliers, P. M.; Reiser, K. M.; Rubenchik, A. M., Quantitative second-harmonic generation microscopy in collagen. *Appl. Opt.* **2003,** *42* (25), 5209-19.
8. Zaera, F., Probing liquid/solid interfaces at the molecular level. *Chem. Rev.* **2012,** *112* (5), 2920-86.
9. Tran, R. J.; Sly, K. L.; Conboy, J. C., Applications of Surface Second Harmonic Generation in Biological Sensing. *Annu. Rev. Anal. Chem.* **2017,** *10* (1), 387-414.
10. Moree, B.; Connell, K.; Mortensen, R. B.; Liu, C. T.; Benkovic, S. J.; Salafsky, J., Protein Conformational Changes Are Detected and Resolved Site Specifically by Second-Harmonic Generation. *Biophys. J.* **2015,** *109* (4), 806-15.
11. Whitman, W. B.; Coleman, D. C.; Wiebe, W. J., Prokaryotes: the unseen majority. *Proc. Natl. Acad. Sci. U.S.A.* **1998,** *95* (12), 6578-83.
12. Jangir, Y.; French, S.; Momper, L. M.; Moser, D. P.; Amend, J. P.; El-Naggar, M. Y., Isolation and Characterization of Electrochemically Active Subsurface Delftia and Azonexus Species. *Front. Microbiol.* **2016,** *7*, 756.
13. Yoon, S. M.; Choi, C. H.; Kim, M.; Hyun, M. S.; Shin, S. H.; Yi, D. H.; Kim, H. J., Enrichment of electrochemically active bacteria using a three-electrode electrochemical cell. *J. Microbiol. Biotechnol.* **2007,** *17* (1), 110-5.

14. Zeng, J.; Eckenrode, H. M.; Dounce, S. M.; Dai, H. L., Time-resolved molecular transport across living cell membranes. *Biophys. J.* **2013,** *104* (1), 139-45.
15. Rao, Y.; Kwok, S. J.; Lombardi, J.; Turro, N. J.; Eisenthal, K. B., Label-free probe of HIV-1 TAT peptide binding to mimetic membranes. *Proc. Natl. Acad. Sci. U.S.A.* **2014,** *111* (35), 12684-8.
16. McGlynn, S. E.; Chadwick, G. L.; Kempes, C. P.; Orphan, V. J., Single cell activity reveals direct electron transfer in methanotrophic consortia. *Nature* **2015,** *526* (7574), 531-U146.
17. Wegener, G.; Krukenberg, V.; Riedel, D.; Tegetmeyer, H. E.; Boetius, A., Intercellular wiring enables electron transfer between methanotrophic archaea and bacteria. *Nature* **2015,** *526* (7574), 587-U315.
18. Scheller, S.; Yu, H.; Chadwick, G. L.; McGlynn, S. E.; Orphan, V. J., Artificial electron acceptors decouple archaeal methane oxidation from sulfate reduction. *Science* **2016,** *351* (6274), 703-707.
19. Dube, C. D.; Guiot, S. R., Direct Interspecies Electron Transfer in Anaerobic Digestion: A Review. *Adv. Biochem. Eng. Biotechnol.* **2015,** *151*, 101-15.
20. Zhou, Y.; Schideman, L.; Zheng, M.; Martin-Ryals, A.; Li, P.; Tommaso, G.; Zhang, Y., Anaerobic digestion of post-hydrothermal liquefaction wastewater for improved energy efficiency of hydrothermal bioenergy processes. *Water Sci. Technol.* **2015,** *72* (12), 2139-47.
21. Reguera, G.; Nevin, K. P.; Nicoll, J. S.; Covalla, S. F.; Woodard, T. L.; Lovley, D. R., Biofilm and nanowire production leads to increased current in *Geobacter sulfurreducens* fuel cells. *Appl. Environ. Microbiol.* **2006,** *72* (11), 7345-7348.
22. Snider, R. M.; Strycharz-Glaven, S. M.; Tsoi, S. D.; Erickson, J. S.; Tender, L. M., Long-range electron transport in *Geobacter sulfurreducens* biofilms is redox gradient-driven. *Proc. Natl. Acad. Sci. U.S.A.* **2012,** *109* (38), 15467-15472.
23. Marsili, E.; Sun, J.; Bond, D. R., Voltammetry and Growth Physiology of *Geobacter sulfurreducens* Biofilms as a Function of Growth Stage and Imposed Electrode Potential. *Electroanal.* **2010,** *22* (7-8), 865-874.
24. Bond, D. R.; Strycharz-Glaven, S. M.; Tender, L. M.; Torres, C. I., On Electron Transport through *Geobacter* Biofilms. *Chemsuschem* **2012,** *5* (6), 1099-1105.

Acknowledgement

This work was conducted under the supervision of Prof. Hiroyuki Noji from April 2016 to March 2019. Firstly, I owe my deepest gratitude to Prof. Hiroyuki Noji for providing me an opportunity to study, and Dr. Akihiro Okamoto for his daily fruitful discussions and instructions for the research. I would like to express my gratitude to President Dr. Kazuhito Hashimoto for giving me comments about scientific research and providing me a change to conduct research in NIMS. I have learned a lot from them, and their scientific insight, research vision, and attractive presentation have been very important guidance for me. This work was conducted with the research help of Prof. Kazuyuki Ishii, Prof. Hiroshi Ishikita, Prof. Kenneth H. Nealson, Prof. Liang Shi, Dr. Keisuke Saito, Dr. Thomas A. Clarke, Dr. Shingo Hattori, Dr. Shafeer Kalathil, Ms. Punthira Chinotaikul, and Mr. Junki Saito. I express my thanks to all of them. I am really thankful to Prof. Kohei Uosaki, Prof. Hidenori Noguchi, Dr. Ken Sakaushi, and Dr. Shogo Miyoshi for their critical comment and suggestions during seminars and daily discussions, and to all the members in the Program for Leading Graduate Schools (MERIT) and Dr. Okamoto's group for fruitful discussion. I thank MERIT program and the Japan Society for the Promotion of Science (JSPS) for financial support. Finally, my heartfelt appreciation goes to my family and friends, who always supported and encouraged me to complete this work.

February 9th, 2019

Yoshihide Tokunou

List of publications

Chapter 2

1. "Basicity of N(5) in semiquinone dictates the rate of respiratory electron outflow"
   Y. Tokunou, K. Saito, R. Hasegawa, K. H. Nealson, K. Hashimoto, H. Ishikita, and A. Okamoto
   Under review
2. "Electrochemical Detection of Deuterium Kinetic Isotope Effect on Extracellular Electron Transport in *Shewanella oneidensis* MR-1"
   Y. Tokunou, K. Hashimoto, and A. Okamoto
   J. Vis. Exp, **2018**, *e57584*, 1-9.
3. "Proton Transport in the Outer-Membrane Flavocytochrome Complex Limits the Rate of Extracellular Electron Transport"
   A. Okamoto**+**, Y. Tokunou**+**, S. Kalathil, K. Hashimoto
   Angew. Chem. Int. Ed., **2017**, *56*, 9082-9086.
   +: Equal contribution
4. "Extracellular Electron Transport Scarcely Accumulates Proton Motive Force in *Shewanella oneidensis* MR-1"
   Y. Tokunou, K. Hashimoto, and A. Okamoto
   Bull. Chem. Soc. Jpn, **2015**, *88*, 690–692.
5. "Cation-limited Kinetic Model for Microbial Extracellular Electron Transport via an Outer Membrane Cytochrome *c* Complex"
   A. Okamoto, Y. Tokunou, and J. Saito
   Biophys. Physicobiol, **2016**, *13*, 71-76.

Chapter 3

6. "Whole-Cell Circular Dichroism Difference Spectroscopy Reveals an *In Vivo*-Specific Deca-Heme Conformation in Bacterial Surface Cytochromes"
   Y. Tokunou, P. Chinotaikul, S. Hattori, T. A. Clarke, L. Shi, K. Hashimoto, K. Ishii, and A. Okamoto
   Chem. Commun., **2018**, *54,* 13933-13936. **[Front Back Cover]**
7. "Geometrical Changes in the Hemes of Bacterial Surface *c*-type Cytochromes Reveal Flexibility in their Binding Affinity with Minerals"
   Y. Tokunou, and A. Okamoto
   Langmuir, **2018**, *in-press*, 10.1021/acs.langmuir.8b02977, **[Supplementary Cover]**

8. “Biological Electron Flow Self-Organization Via Structural Changes in Membrane-bound *c*-Type Cytochrome”
   Y. Tokunou, and A. Okamoto
   To be submitted.

Chapter 4

9. “Acceleration of Extracellular Electron Transfer by Alternative Redox Molecules to Riboflavin for Outer-Membrane Cytochrome *c* of *Shewanella oneidensis* MR-1”
   Y. Tokunou, K. Hashimoto, and A. Okamoto
   J. Phys. Chem. C, **2016**, *120 (29),* 16168-16173.
10. “Riboflavin-Cytochrome Complex on Outer-Membrane Functionalizes *Geobacter* cells as Microbial Diode”
    Y. Tokunou, and A. Okamoto
    To be submitted.
11. “*Shewanella* as a platform of electrochemical enzyme assay *in vivo*”
    Y. Tokunou, K. Hashimoto and A. Okamoto
    To be submitted.

Other publications

1. “Direct Extracellular Electron Transport of Cyanobacteria on Carbon felts and ITO Electrodes”
   Y. Tokunou, R. V. Lemos, M. Bustalinio, A. Okamoto, P. Ledezma, and S. Freguia
   To be submitted.
2. “Nitrate reduction by *Geobacter sulfurreducens*”
   Y. Sorimachi, Y. Tokunou, and A. Okamoto
   To be submitted.